Université Joseph Fourier

THÈSE

Pour obtenir le grade de

DOCTEUR DE L'UNIVERSITÉ DE GRENOBLE

Spécialité : **Physique Subatomique et Astroparticules**

Arrêté ministériel : 7 août 2006

Présentée par

Xiaohu SUN

Thèse dirigée par **Annick LLERES**

préparée au sein **Laboratoire de Physique Subatomique et de Cosmologie de Grenoble (LPSC)**
et de **École Doctorale de Physique de Grenoble**

Top polarization measurement in single top quark production with the ATLAS detector

Thèse soutenue publiquement le **1 octobre 2013**,
devant le jury composé de :

Mr, Christophe Furget
Prof. Université Joseph Fourier, Président
Mr, Frédéric Déliot
Dr. CEA/IRFU Saclay, Rapporteur
Mr, Cunfeng Feng
Prof. Shandong University, Rapporteur
Mrs, Viola Sordini
Dr. IPN Lyon, Examinateur
Mr, Mossadek Talby
Prof. CPP Marseille, Examinateur
Mrs, Annick Lleres
Dr. LPSC Grenoble, Directeur de thèse

Acknowledgments

I thank my supervisor Annick Lleres for helping me to start my life and work in France. It is her who guided me into the exciting field of polarization in top quark physics two years ago and provided technical supports on programming all the time as well as examined the thesis manuscript times and times again in this summer.

I am grateful to my referees Frédéric Déliot and Cunfeng Feng as well as other members in my jury Christophe Furget, Viola Sordini and Mossadek Talby, for their tremendous work on examining my manuscripts and giving comments as well as attending my defense.

I should also thank the ATLAS group in LPSC for all the help on work. In particular, I would like to express my special thanks to Arnaud Lucotte, Benoit Clement and Julien Donini for their patience and guidance on physics as well as statistics during my analysis work.

I am really thankful to the collaborators working in single top group on ATLAS: Dominic Hirschbuehl, Reinhard Schwienhorst, Muhammad Alhroob, Jenny Holzbauer, Jin Wang, Barbara Alvarez Gonzalez and Joseph Boudreau for the inspiring discussions and supports in the past three years.

Je vais remercier mes amis Quentin et Lilian pour les histoires drôles dont nous avons parlé et les sports de montagne nous avons fait ensemble. Je remercie également mes amis Francesca et Jonathan pour la délicieuse crêpe au sarrazin et le beau voyage pour le mariage de Cate à Ferrara.

Vorrei anche ringraziare la mia amica Cate che mi ha aiutato e ha sostenuto negli ultimi due anni del mio lavoro, la mia vita e la mia curiosità per la cultura italiana, così come il marito Michele, un uomo pieno di passione, che non mancava mai di preparami un delizioso piatto napoletana caldo ogni volta che andavo a casa loro.

我要感谢我的前女友吴梦晴，为了在我写论文初期那些美好的回忆。

最后，我不能忘记感谢我的父母，是他们的支持和鼓励，让我坚定信念，勇敢地沿着自己的路走下去，迎接新的挑战。

Contents

1 Introduction **9**

2 The Standard Model **15**
2.1 The Yang-Mills theory 15
2.2 Boson and fermion fields 16
2.3 The Higgs boson field 18
2.3.1 The Higgs mechanism 18
2.3.2 Generation of boson masses 19
2.3.3 Generation of fermion masses 20
2.3.4 The CKM matrix 21
2.3.5 Higgs boson searches at the LHC 24

3 Top quark physics **27**
3.1 Quantum chromodynamics 27
3.1.1 Perturbative theory 27
3.1.2 Asymptotic freedom and confinement 28
3.2 Proton-proton collisions 29
3.2.1 Top quark production cross section 30
3.2.2 Parton distribution functions 31
3.3 Top quark decay 32
3.4 Top quark pair production 33
3.5 Single top quark production 34
3.5.1 Production channels 34
3.5.2 Theoretical cross sections 36
3.5.3 Discovery at the Tevatron 37
3.5.4 Measurements at the LHC 38
3.6 Anomalous coupling constraints in single top quark production 39
3.6.1 Wtb anomalous couplings 39
3.6.2 Constraints with cross sections 40
3.6.3 Constraints with W boson helicity fractions 40
3.6.4 Constraints with W boson polarization observables 42
3.6.5 Top quark polarization 45
3.7 Searches for new physics in single top quark production 48
3.7.1 Extra vector boson - W' 48
3.7.2 New fermion - b^*-quark 49

3.7.3 New coupling - FCNC process . . . 50

4 The ATLAS detector 53
4.1 Basic definitions in high-energy experiments . . . 53
4.2 The LHC . . . 55
4.2.1 The accelerator complex . . . 55
4.2.2 The seven experiments . . . 56
4.3 The ATLAS detector . . . 58
4.4 Magnet system . . . 59
4.5 Inner detector . . . 60
4.5.1 Inner subdetectors . . . 61
4.5.2 Tracking and vertexing performance . . . 62
4.6 Calorimeters . . . 64
4.6.1 Electromagnetic calorimeter . . . 64
4.6.2 Hadronic calorimeters . . . 66
4.6.3 Calorimeter performance . . . 66
4.7 Muon spectrometer . . . 67
4.7.1 Muon chambers . . . 68
4.7.2 Muon spectrometer performance . . . 69
4.8 Forward detectors . . . 70
4.9 The trigger system . . . 71
4.9.1 The motivation for a trigger system . . . 71
4.9.2 The ATLAS tree-level trigger system . . . 72
4.9.3 The trigger chains and streams . . . 74

5 Physics object reconstruction 77
5.1 Electrons . . . 77
5.1.1 Trigger . . . 77
5.1.2 Reconstruction . . . 78
5.1.3 Identification . . . 79
5.1.4 Energy scale . . . 81
5.1.5 Energy resolution . . . 86
5.1.6 Efficiency . . . 88
5.2 Muons . . . 91
5.2.1 Reconstruction . . . 91
5.2.2 Reconstruction efficiency . . . 92
5.2.3 Momentum resolution . . . 94
5.3 Jets . . . 98
5.3.1 Reconstruction . . . 98
5.3.2 Energy scale . . . 102
5.4 Missing transverse momentum . . . 103
5.5 Luminosity measurement . . . 105
5.6 Data quality . . . 107

6 Simulations and data **109**
6.1 Event topology and simulations . . . 109
6.1.1 Single top quark t-channel . . . 110
6.1.2 Single top quark backgrounds . . . 112
6.1.3 Top quark pair background . . . 112
6.1.4 W+jets backgrounds . . . 113
6.1.5 Z+jets and diboson backgrounds . . . 114
6.1.6 QCD multijet backgrounds . . . 114
6.1.7 Monte Carlo samples . . . 115
6.1.8 Pileup simulations . . . 116
6.2 Data . . . 116

7 Simulations with PROTOS **121**
7.1 Top quark polarization . . . 121
7.2 Generator validation . . . 122
7.3 PROTOS samples . . . 122
7.3.1 Anomalous coupling configuration . . . 122
7.3.2 Vertex configuration . . . 127
7.3.3 Generated samples . . . 129
7.3.4 Energy configuration . . . 133
7.4 W boson polarization . . . 133

8 Event selection **139**
8.1 Object selections . . . 139
8.2 Event selections . . . 141
8.2.1 Event preselection . . . 141
8.2.2 Signal event selection . . . 142
8.2.3 Event selections for background estimates . . . 143
8.3 Top quark reconstruction . . . 143
8.4 QCD multijet background estimation . . . 144
8.4.1 Electron channel . . . 145
8.4.2 Muon channel . . . 147
8.5 $W + jets$ background estimation . . . 149
8.6 Event yields . . . 152
8.6.1 Preselection . . . 152
8.6.2 Signal selection . . . 154
8.7 Kinematic distributions . . . 156
8.7.1 Pretag distributions . . . 156
8.7.2 Tag distributions . . . 156
8.7.3 Signal distributions . . . 156

9 Top quark polarization measurement **161**
9.1 Angular distributions at parton level . . . 162
9.2 Angular distributions at reconstruction level . . . 164
9.3 Corrections on reconstructed distributions . . . 168

9.4 Migration and efficiency corrections . . . 171
9.4.1 Migration matrix . . . 171
9.4.2 Efficiencies . . . 174
9.5 Unfolding methods . . . 174
9.5.1 Ordinary unfolding . . . 175
9.5.2 Iterative unfolding . . . 178
9.6 Folding method . . . 187
9.7 Systematic uncertainties . . . 191
9.7.1 Theoretical uncertainties . . . 191
9.7.2 Detector uncertainties . . . 192
9.7.3 Background uncertainties . . . 194
9.7.4 Pseudo-experiments . . . 194
9.7.5 Expected systematic uncertainties . . . 196
9.7.6 Observed systematic uncertainties . . . 196
9.8 Polarization measurements . . . 197
9.8.1 Expected measurements . . . 197
9.8.2 Observed measurements . . . 200
9.8.3 Cross section measurements . . . 204
9.9 Conclusion . . . 207

10 Conclusion **209**

A Simulations with PROTOS **211**
A.1 Energy configuration . . . 211

B Event selection **215**
B.1 PRETAG kinematic distributions . . . 215
B.2 TAG kinematic distributions . . . 215
B.3 Signal kinematic distributions . . . 215

Chapter 1

Introduction

In this introductory chapter, please let me first present a fairly brief introduction to particle physics and to the Standard Model with more attentions on the evolution of our knowledge on fundamental elements and the indispensable new technologies driving the blooms in physics from time to time.

> By convention there is color,
> By convention sweetness,
> By convention bitterness,
> But in reality there are atoms and space
>
> -Democritus (circa 400 B.C.E.)

Democritus proposed the idea of atom in the ancient Greece almost 2500 years ago[1]. Not long after that, the idea of atom was commonly opposed by people including Aristotle due to the lack of scientific proof, but the idea itself encourages to divide matters into smaller and smaller components till the fundamental indivisible elements. These elements constitute all the matters in the Universe. The poor technology at that ancient time limited people to pursue the scientific proof supporting the idea of atom, but the human being never gave up looking into matters and probing the fundamental constituents by inventing new machines or detectors from generation to generation. Great efforts have been made to explore the fundamental elements for centuries.

Up to the end of the 19th century, the first most scientific picture of the fundamental elements in the Universe was drawn by chemists. At that moment, the smallest known units are the elements of the Mendeleev's periodic table, as shown in Figure 1-1. The Universe is all made of these elements perfectly and satisfyingly. But at the same time, one may doubt, "Are there too many fundamental elements?" by looking at the hundreds of elements in the table. The question did not last longer. In 1898, Joseph Thompson discovered that cathode rays are electrons, which turned out to be a fundamental element at that moment and still remains indivisible till now. This discovery challenged the elements in the periodic table as the fundamental units

[1]This idea coincided with a similar declaration by an Indian philosopher Kanada around the same time

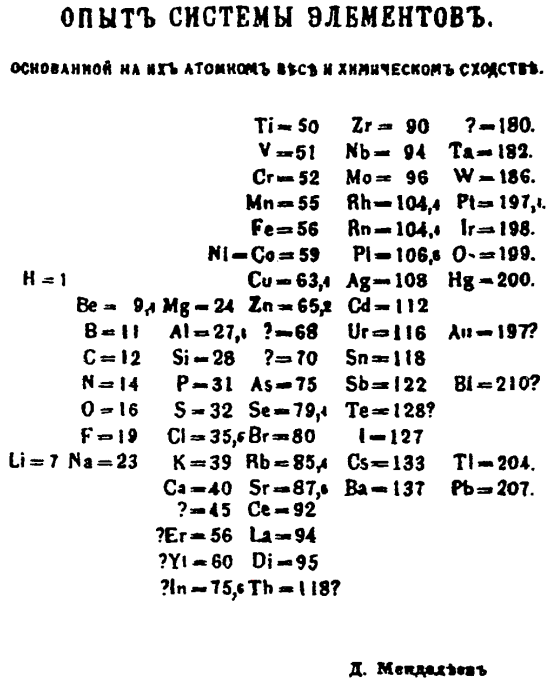

ОПЫТЪ СИСТЕМЫ ЭЛЕМЕНТОВЪ.

ОСНОВАННОЙ НА ИХЪ АТОМНОМЪ ВѢСѢ И ХИМИЧЕСКОМЪ СХОДСТВѢ.

			Ti = 50	Zr = 90	? = 180.
			V = 51	Nb = 94	Ta = 182.
			Cr = 52	Mo = 96	W = 186.
			Mn = 55	Rh = 104,4	Pt = 197,1.
			Fe = 56	Ru = 104,4	Ir = 198.
			Ni = Co = 59	Pl = 106,6	O = 199.
H = 1			Cu = 63,4	Ag = 108	Hg = 200.
	Be = 9,4	Mg = 24	Zn = 65,2	Cd = 112	
	B = 11	Al = 27,4	? = 68	Ur = 116	Au = 197?
	C = 12	Si = 28	? = 70	Sn = 118	
	N = 14	P = 31	As = 75	Sb = 122	Bi = 210?
	O = 16	S = 32	Se = 79,4	Te = 128?	
	F = 19	Cl = 35,6	Br = 80	I = 127	
Li = 7	Na = 23	K = 39	Rb = 85,4	Cs = 133	Tl = 204.
		Ca = 40	Sr = 87,6	Ba = 137	Pb = 207.
		? = 45	Ce = 92		
		?Er = 56	La = 94		
		?Yt = 60	Di = 95		
		?In = 75,6	Th = 118?		

Д. Менделѣевъ

Figure 1-1: Mendeleev's periodic table in 1869. This is how people saw the Universe in the end of the 19th century.

in the Universe. As a result, this event is commonly regarded as the starting point of particle physics. The subatomic era began.

However, at the same time of appreciating the amazing discovery by Thompson, one should never forget to credit the invention of the vacuum pump by Otto von Guericke and the invention of the Crookes tube by William Crookes, which made it possible to produce cathode rays.

At the turn of the 19th century, new theories were proposed and quantum mechanics started to be established triggered by explaining blackbody radiation in the context of quantized energy emission from Max Planck [1] in 1900, answering the wave-particle duality of the light from Albert Einstein [2] in 1905, and generalizing wave-particle duality by suggesting that particles of matter are also wavelike from Louis de Broglie [3] in 1924. Later, in 1911, a concentrated positive nucleus was proved inside an atom by Ernest Rutherford leading to the Rutherford model of the atom. This model tells that an atom consists of a very small charged nucleus containing much of the atom's mass and low-mass electrons orbiting the nucleus. This model completely broke the nice picture drawn by the elements from the periodic table as the fundamental units in the Universe in the end of the 19th century. In 1919, the proton was discovered by Ernest Rutherford via the nuclear reaction $^{14}N + \alpha \rightarrow ^{17} O + p$, and later, the neutron was discovered by James Chadwick in 1932.

Back to the 1910's, Charles Wilson invented the cloud chamber containing a supersaturated vapor of water or alcohol, which allows to capture the track of charged particles. Since then, new particles were discovered one by one in a very short period

benefiting from this powerful machine. The first "antiparticle" positron was a good example. It was discovered by Carl Anderson in 1932 when letting cosmic rays pass through a lead plate inside a cloud chamber surrounded by a magnet. The ion trail left by each positron appeared with a curvature matching the mass-to-charge ratio of an electron, but the direction showed that its charge is positive. The muon [2] was discovered in 1937 by Seth Neddermeyer, Carl Anderson, Jabez Street, and Elmer Stevenson using the cloud chamber measurements of cosmic rays. Till the 1950's, hadrons, like pions and kaons, were all successfully discovered by the cloud chamber.

Naively, at that moment, one regarded the newly discovered hadrons as the fundamental particles. But given the big amount of hadrons discovered in that short time, one got confused again, in such a way that Wolfgang Pauli exclaimed "Had I foreseen that, I would have gone into botany". "Are they fundamental particles?", one had to ask themselves when looking at the blackboard filled with various hadrons. The situation looked like what had happened almost half a century ago when people were satisfied and also confused with the fruitful achievements after identifying more than one hundred elements in the periodic table. The most knotty work at that moment was no more than classifying all the hadrons and figuring out if they have substructures. After so many failed models, the quark model in its modern form was formed by Murray Gell-Mann, Kazuhiko Nishijima and George Zweig in 1964. Afterwards, it was validated by the continuous discoveries of the up quark, the down quark, and the strange quark at SLAC (Stanford Linear Accelerator Center) in 1969. The picture of the fundamental elements was refreshed.

Later on, new detectors were invented, bringing another bloom of the particle discoveries. The bubble chamber was invented by Donald Glaser for tracking in the 1950's. This chamber allows to observe what happens in high energy beam collisions thus paving the way for many important discoveries. The multi-wire chamber was invented by Georges Charpak for tracking in the 1960's. This chamber improved the detection rate from only one or two particles per second by the earlier bubble chamber to around 1000 particles per second. This advancement brought particle detection into a new era with high event rates suiting the high luminosities delivered by colliders. This chamber was immediately used in high energy physics and its design was adopted and improved in the trackers that came later even till today. In 1974, the J/ψ meson was discovered independently by the groups headed by Burton Richter and Samuel Ting, proving the existence of the charm quark. One year after, the tau lepton was discovered by a group headed by Martin Perl, followed by the discovery of the bottom quark at Fermilab (Fermi National Accelerator Laboratory) in 1977. Then in the 1980's, the gluon, W and Z bosons were discovered on colliders by the UA1 and UA2 collaborations. In 1995, the top quark was finally discovered at Fermilab, and in 2000, the tau neutrino was also discovered there.

All these particles discovered through the last century make up the most complete theory framework till now, the Standard Model, which was proposed by Steven Weinberg [5], Sheldon Glashow [6] and Abdus Salam [7] in 1967 and improved later. The

[2]The electron neutrino (postulated by Wolfgang Pauli in 1930) and the muon neutrino (postulated in the 1940s) were discovered separately in 1956 and 1962 from nuclear interactions.

Matter constituents (Fermions, spin = $\frac{1}{2}$)					
Leptons			Quarks		
Flavor	Mass (GeV)	Charge	Flavor	Mass (GeV)	Charge
$\begin{pmatrix}\nu_e\\ e\end{pmatrix}$	$< 2 \times 10^{-9}$ 0.000511	0 -1	$\begin{pmatrix}u\\ d\end{pmatrix}$	0.0023 0.0048	$\frac{2}{3}$ $-\frac{1}{3}$
$\begin{pmatrix}\nu_\mu\\ \mu\end{pmatrix}$	< 0.00019 0.106	0 -1	$\begin{pmatrix}c\\ s\end{pmatrix}$	1.275 0.095	$\frac{2}{3}$ $-\frac{1}{3}$
$\begin{pmatrix}\nu_\tau\\ \tau\end{pmatrix}$	< 0.0182 1.777	0 -1	$\begin{pmatrix}t\\ b\end{pmatrix}$	173.5 4.18	$\frac{2}{3}$ $-\frac{1}{3}$

Table 1.1: Properties of the leptons and quarks which constitute the matter world. All properties are obtained from [4].

Force carriers (Bosons, spin = 1)			
Interaction	Flavor	Mass (GeV)	Charge
Electroweak	γ	$< 1 \times 10^{-27}$	$< 1 \times 10^{-35}$
	W^-	80.385	-1
	W^+	80.385	1
	Z^0	91.1876	0
Strong	g	0	0

Table 1.2: Properties of the bosons which carry the forces among the constituents. All properties are obtained from [4].

known fundamental elements in our time are listed with their properties in Table 1.1 for the fermions that constitute the matter world, and in Table 1.2 for the bosons that are responsible for the interactions between the matter constituents, leaving the only missing piece in the Standard Model: the Brout-Englert-Higgs boson, commonly known as the Higgs boson. In the summer of 2012, both ATLAS and CMS collaborations reported the discovery at the LHC of a Higgs-like boson, which exhibits most of the predicted characteristics of the searched Higgs boson.

Besides the search for the Higgs boson, one of the main interesting fields at the LHC concerns the top quark physics. In the framework of the Standard Model, the

top quark, the last discovered quark, is the heaviest elementary particle found so far. Its large mass (around 173 GeV), which is of the same order of magnitude as the electroweak spontaneous symmetry breaking scale ($\approx$ 246 GeV), can provide further insights into the electroweak theory. In particular, the single top quark production, which proceeds via electroweak interaction, allows precise measurements within the Standard Model as well as searches of new physics (i.e. beyond the Standard Model), such as the production of new particles like an extra vector boson W' or a new quark b^* [8, 9, 10, 11, 12, 13, 14]. Single top quark production cross sections provide a direct measurement of the V_{tb} element of the Cabibbo-Kobayashi-Maskawa quark-mixing matrix [15, 16], while the polarization measurements with single top quarks are powerful probes of the electroweak production and decay properties of the top quark. Furthermore, measurements of the top quark and W boson polarization observables provide meaningful contraints on anomalous couplings in the Wtb vertex.

This document focuses on the top quark polarization and discusses the various possible methods to perform robust and precise measurements. It starts from an introduction to the Standard Model in Chapter 2, with a discussion on the generation of the boson and fermion masses, as well as the Cabibbo-Kobayashi-Maskawa quark-mixing matrix derived from the Higgs mechanism, followed by a detailed description dedicated to the top quark physics in Chapter 3, covering both the strong and electroweak productions, with a particular interest on the polarization measurements in single top quark production. To achieve the challenging physics goals, the ATLAS detector used by the measurement is introduced in Chapter 4, with in particular a description of the inner part of the detector and a discussion of its performances. Benefiting from the good performances of the detector, a detailed presentation on the well-reconstructed physics objects is given in Chapter 5. Then, an overview of the phenomenology of the single top quark events and their backgrounds, is presented in Chapter 6, associated to a presentation of the corresponding simulations and data. Following this, the studies carried out with Monte Carlo simulations, dedicated to the parton-level polarization, are presented in Chapter 7. Based on the phenomenology of the signal events, the event selection and data-driven background estimates are presented in Chapter 8. Utilizing the reconstructed objects and single top quark events, the polarization measurements are performed with several methods, based on unfolding and folding techniques, all the methods being validated through various checks and comparisons, which are presented in the first part of Chapter 9. Then, the measurements, together with their uncertainties obtained from the expectations, are discussed in the second part of Chapter 9 and the final measurement extracted from the data using the most precise method is reported in the last part of this chapter. Finally, all the presented studies and results are summarized in Chapter 10, which also gives some perspectives on the future single top quark polarization measurements.

Chapter 2

The Standard Model

The Standard Model (SM) is built on quantum field theory. It describes all the bosons and fermions known by now as well as their interactions, including electromagnetic, weak and strong forces, with a simple Lagrangian. The Yang-Mills gauge theory proposed the idea that the Lagrangian should be invariant with the local gauge transformations. However, it does not explain the origin of particle masses, since the gauge symmetry forbids any masses for bosons or fermions. This is solved by introducing a spontaneous symmetry breaking via the Brout-Englert-Higgs mechanism.

In this chapter, a discussion on the construction of the Standard Model Lagrangian is presented following [17]. The Yang-Mills gauge theory as a basic building block of the Standard Model is introduced in Section 2.1. The Standard Model Lagrangian for bosons and fermions is introduced in Section 2.2. The Higgs mechanism is discussed in Section 2.3 including the mechanism itself, the origin of the masses for bosons and fermions, and the Cabibbo-Kobayashi-Maskawa (CKM) matrix required by the fermion mass generation.

2.1 The Yang-Mills theory

The Yang-Mills gauge theory was first initiated in 1954 in a publication on the $SU(2)$ isospin invariance of the proton-neutron system and was developped in the 1960's [18]. Regardless of the unclear mathematical foundations in the theory, the Yang-Mills gauge theory helps the Standard Model to unify weak, electromagnetic and strong forces, which will be shown in the following.

Assuming T^a $(a = 1, 2...N)$ as generators of a Lie group $\mathcal{G}$, a gauge transformation acting on a set of Dirac fermions can be written as:

$$\Psi(x) \rightarrow e^{i\alpha^a(x)T^a}\Psi(x) \tag{2.1}$$

with $\alpha^a(x)$ defined as a local transformation parameter. The transformation will make $\partial_\mu\Psi(x)$ generate a term due to $\alpha^a(x)$ making the free Lagrangian for a set of Dirac spinors not invariant. However, to keep the gauge invariance of the Lagrangian,

one needs to replace the normal partial derivative by a covariant derivative:

$$D_\mu = \partial_\mu + igT^a A^a_\mu(x) \tag{2.2}$$

where $A^a_\mu(x)$ is introduced as a vector boson field with the coupling strength g to the fermion field. In this way, the gauge invariant Lagrangian can be written as (from now on, the field will always assume the space-time dependence):

$$\mathcal{L}_F = i\bar{\Psi}\gamma^\mu D_\mu \Psi. \tag{2.3}$$

To keep the local gauge invariance, the Yang-Mills theory spontaneously introduces a vector boson field to interact with the fermion field. This will be applied in the Standard Model where the vector bosons such as $W^\pm$, Z, γ and gluon are demanded by a certain gauge symmetry.

The Lagrangian of the newly introduced gauge vector boson field can be written as:

$$\mathcal{L}_G = -\frac{1}{4} F^{a\mu\nu} F^a_{\mu\nu} \tag{2.4}$$

with:

$$F^a_{\mu\nu} = \partial_\mu A^a_\nu - \partial_\nu A^a_\mu - g f^{abc} A^b_\mu A^c_\nu \tag{2.5}$$

where f^{abc} are the structure constants of $\mathcal{G}$, such that $[T^a, T^b] = i f^{abc} T^c$, and g is the coupling strength between the gauge boson and the fermion fields.

The gauge invariance is thus preserved and a new vector boson is introduced due to this local gauge invariance. Nevertheless, the gauge invariance still forbids any mass term in the Lagrangians of either fermion or gauge boson fields.

2.2 Boson and fermion fields

The Standard Model symmetry inherits the local gauge invariance from the Yang-Mills theory and specifies the local transformation group as $SU(3)_C \times SU(2)_L \times U(1)_Y$. The $SU(3)_C$ gauge symmetry introduces the strong interaction via the eight gauge bosons G^a_μ (gluons) coupled to the colors. The $SU(2)_L \times U(1)_Y$ gauge symmetries introduce the combined electromagnetic and weak interactions. The $SU(2)_L$ gauge symmetry introduces three gauge bosons W^i_μ, coupled to the weak isospin, while the $U(1)_Y$ gauge symmetry introduces one gauge boson B_μ, coupled to the weak hypercharge. The Lagrangian of the gauge boson fields is thus written as:

$$\mathcal{L}_G = -\frac{1}{4} B_{\mu\nu} B^{\mu\nu} - \frac{1}{4} W^i_{\mu\nu} W^{i\mu\nu} - \frac{1}{4} G^a_{\mu\nu} G^{a\mu\nu} \tag{2.6}$$

with

$$B_{\mu\nu} = \partial_\mu B_\nu - \partial_\nu B_\mu \tag{2.7}$$

$$W^i_{\mu\nu} = \partial_\mu W^i_\nu - \partial_\nu W^i_\mu - g_2 \epsilon^{ijk} W^j_\mu W^k_\nu \tag{2.8}$$

$$G^a_{\mu\nu} = \partial_\mu G^a_\nu - \partial_\nu G^a_\mu - g_3 f^{abc} G^b_\mu G^c_\nu \tag{2.9}$$

where $g_2,\ g_3$ are the gauge coupling strengths and $\epsilon^{ijk},\ f^{abc}$ the structure constants for $SU(2)$ and $SU(3)$ respectively. The $W^{\pm}$, Z and γ bosons will be generated by mixing the pure electroweak gauge bosons B_μ and W^i_μ when the Higgs boson is introduced.

With the newly introduced gauge bosons, one can construct the covariant derivatives like what is done with the Yang-Mills theory:

$$D_\mu = \partial_\mu + ig_1\frac{Y}{2}B_\mu + ig_2\tau^j W^j_\mu + ig_3\lambda^a G^a_\mu \tag{2.10}$$

where g_1, g_2, g_3 are coupling strengths for each interaction, Y is associated to the weak hypercharge of the fermion, τ^j are the generators of $SU(2)$, and λ^a the generators of $SU(3)$. The weak hypercharge is defined by $Q = T_3 + \frac{Y}{2}$, where Q is the electric charge and T_3 the third component of the weak isospin. Using this covariant derivative instead of the normal derivatives ∂_μ, one can construct the Lagrangian for fermions with gauge invariance under the group $SU(3)_C \times SU(2)_L \times U(1)_Y$:

$$\begin{aligned}\mathcal{L}_F = \sum_i (&\bar{Q^L_i} i\gamma^\mu D_\mu Q^L_i + \bar{u^R_i} i\gamma^\mu D_\mu u^R_i + \bar{d^R_i} i\gamma^\mu D_\mu d^R_i \\ &+ \bar{L^L_i} i\gamma^\mu D_\mu L^L_i + \bar{e^R_i} i\gamma^\mu D_\mu e^R_i)\end{aligned} \tag{2.11}$$

where left-chiral fermions are grouped in weak isospin doublets running over the three families:

$$Q^L_{1,2,3} = \begin{pmatrix} u \\ d \end{pmatrix}^L, \begin{pmatrix} c \\ s \end{pmatrix}^L, \begin{pmatrix} t \\ b \end{pmatrix}^L \tag{2.12}$$

$$L^L_{1,2,3} = \begin{pmatrix} \nu_e \\ e \end{pmatrix}^L, \begin{pmatrix} \nu_\mu \\ \mu \end{pmatrix}^L, \begin{pmatrix} \nu_\tau \\ \tau \end{pmatrix}^L \tag{2.13}$$

and right-chiral fermions are weak isospin singlets:

$$u^R_{1,2,3} = u^R, c^R, t^R \tag{2.14}$$

$$d^R_{1,2,3} = d^R, s^R, b^R \tag{2.15}$$

$$e^R_{1,2,3} = e^R, \mu^R, \tau^R. \tag{2.16}$$

There is no right-chiral neutrino due to its zero mass in the minimal Standard Model.

In the Lagrangian 2.11, the terms in the first line describe the kinematics for quark fields in electroweak couplings including the favored left-handed couplings with $SU(2)_L \times U(1)_Y$ gauge symmetry and the right-handed couplings with only $U(1)_Y$ gauge symmetry. The terms in the second line of the Lagrangian 2.11 describe the kinematics for lepton fields in the same manner as the quark fields. The terms in the last line of the Lagrangian 2.11 describe the kinematics for quark fields. There is still no mass terms in the Lagrangian, since the gauge symmetry forbids mass terms for either gauge bosons in Equation 2.6 or fermions in Equation 2.11.

2.3 The Higgs boson field

2.3.1 The Higgs mechanism

The Brout-Englert-Higgs mechanism was proposed in the 1960's, to solve the mass problem in the Standard Model Lagrangian by introducing a scalar field called the Higgs field [19, 20]. A spontaneous symmetry-breaking takes place and leads to a non-zero vacuum state but still keeps the Lagrangian invariant under the local gauge transformations. The Higgs field is a weak isospin scalar field in a $SU(2)$ doublet written as:

$$\Phi = \begin{pmatrix} \phi^+ \\ \phi^0 \end{pmatrix}. \tag{2.17}$$

The corresponding Lagrangian reads:

$$\mathcal{L} = (D^\mu \Phi)^\dagger (D_\mu \Phi) - \mu^2 \Phi^\dagger \Phi - \lambda (\Phi^\dagger \Phi)^2 \tag{2.18}$$

with the covariant derivative:

$$D_\mu = \partial_\mu + i g_1 \frac{1}{2} B_\mu + i g_2 \tau^j W_\mu^j \tag{2.19}$$

where B^μ and W^μ are the gauge fields with coupling strengths g_1 and g_2, as used in the Lagrangian expressed by Equation 2.6. In Equation 2.18, the covariant derivative term describes the kinematics of the Higgs field, while the remainings are the potential term indicating the mass and a self-interaction of the Higgs field. The spontaneous symmetry breaking is realized by assuming $\mu^2 < 0$ and letting $\lambda > 0$. In this way, one can derive a vacuum expectation value (vev) that is not zero regarding the minimum potential shown in Figure 2-1 such as:

$$< \Phi >_0 = < 0|\Phi|0 > = \frac{1}{\sqrt{2}} \begin{pmatrix} 0 \\ \nu \end{pmatrix} \tag{2.20}$$

$$\text{where} \quad \nu = \sqrt{-\frac{\mu^2}{\lambda}}. \tag{2.21}$$

Therefore the Higgs field can be written as (around the vev):

$$\Phi = \frac{1}{\sqrt{2}} \begin{pmatrix} 0 \\ h + \nu \end{pmatrix} \tag{2.22}$$

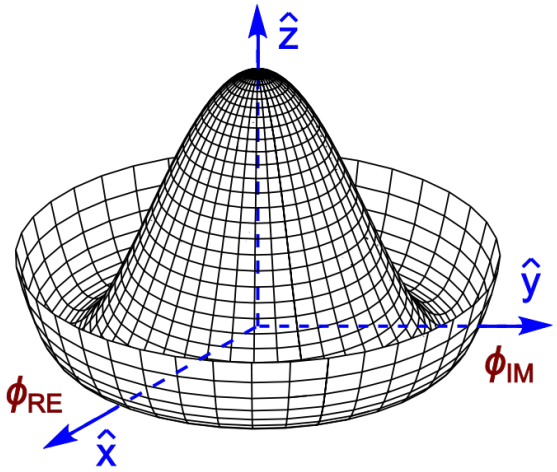

Figure 2-1: Demonstration for the potential of the Higgs scalar field. The minimum potential gives a non-zero vacuum expectation value.

2.3.2 Generation of boson masses

Inserting the Higgs field into the covariant derivative term of the the Higgs Lagrangian (Equation 2.18) allows to derive the gauge boson mass related terms as follows:

$$\begin{aligned}\mathcal{L} = &-(\frac{2\lambda\nu^2}{2})h^2 + (\frac{g_2\nu}{2})^2 W^{+\mu}W^-_\mu \\ &+ (\frac{\nu}{2})^2(g_2W^3_\mu - g_1B_\mu)(g_2W^{3\mu} - g_1B^\mu)\end{aligned} \tag{2.23}$$

with the charge eigenstates of the weak gauge boson $W^\pm_\mu$ defined by $W^{1,2}_\mu$:

$$W^\pm_\mu = \frac{1}{\sqrt{2}}(W^1_\mu \mp W^2_\mu). \tag{2.24}$$

Therefore one gets the mass for the $W^\pm_\mu$ bosons:

$$m_{W^\pm} = \frac{g_2\nu}{2}. \tag{2.25}$$

For the neutral-current weak boson Z^0_μ and the electromagnetic boson (photon), the mixture of W^3_μ and B_μ can give their mass eigenstates:

$$\begin{pmatrix} Z^0_\mu \\ A_\mu \end{pmatrix} = \begin{pmatrix} cos\theta_W & -sin\theta_W \\ sin\theta_W & cos\theta_W \end{pmatrix} \begin{pmatrix} W^3_\mu \\ B_\mu \end{pmatrix} \tag{2.26}$$

with the Weinberg angle θ_W defined by:

$$tan\theta_W = \frac{g_1}{g_2}, \quad \text{and} \quad cos\theta_W = \frac{g_2}{\sqrt{g_1^2 + g_2^2}} \tag{2.27}$$

and the masses which are then given by:

$$M_{Z^0} = \frac{\nu\sqrt{g_1^2 + g_2^2}}{2}, \quad M_A = 0. \tag{2.28}$$

The masses of the three massive gauge bosons $W^{\pm}$ and Z^0 come from absorbing the unphysical Goldstone bosons ($\phi_{1,2,3}$) during the calculation of the vacuum expectation value for the Higgs field $\frac{1}{\sqrt{2}}\binom{\phi_1+i\phi_2}{\eta+i\phi_3}$. In this way, the proposed Higgs doublet with four parameters η and $\phi_{1,2,3}$ can be simplified with $\phi_{1,2,3}$ all equal to 0 and $\eta = \nu$ (vev) as shown in Section 2.3.1. Under the spontaneous symmetry-breaking, the gauge symmetry is broken $SU(2)_L \times U(1)_Y \rightarrow U(1)_{EM}$, generating the masses of the gauge bosons $W^{\pm}$ and Z^0 while keeping the photon A massless.

2.3.3 Generation of fermion masses

A Yukawa coupling Lagrangian is introduced to describe the interaction between the scalar Higgs field and the Dirac fermion fields:

$$\begin{aligned}\mathcal{L}_{Yukawa} = &\sum_{n=1}^{3}\sum_{m=1}^{3}(y^e_{nm}\bar{e}^R_n\Phi^\dagger L^L_m + y^{e*}_{nm}\bar{L}^L_m\Phi e^R_n) \\ &+ (y^d_{nm}\bar{d}^R_n\Phi^\dagger Q^L_m + y^{d*}_{nm}\bar{Q}^L_m\Phi d^R_n) \\ &+ (y^u_{nm}\bar{u}^R_n\tilde{\Phi}^\dagger Q^L_m + y^{u*}_{nm}\bar{Q}^L_m\tilde{\Phi}u^R_n)\end{aligned} \tag{2.29}$$

with:

$$\tilde{\Phi} = i\tau^2\Phi^* \tag{2.30}$$

n and m run over the three families of leptons and quarks, respectively, the fermions being all grouped into left-handed doublets and right-handed singlets according to Equations 2.12 to 2.16. The coupling strengths $y^{u,d,e}_{nm}$ can be grouped into three 3×3 matrices $Y_u = \{y^u_{nm}\}$, $Y_d = \{y^d_{nm}\}$, $Y_e = \{y^e_{nm}\}$ for up-type quark, down-type quark and lepton respectively. For example:

$$Y_u = \begin{pmatrix} y^u_{11} & y^u_{12} & y^u_{13} \\ y^u_{21} & y^u_{22} & y^u_{23} \\ y^u_{31} & y^u_{32} & y^u_{33} \end{pmatrix}. \tag{2.31}$$

These matrices operate transformations on weak eigenstates. Due to the non-zero off-diagonal elements in the matrices, one cannot directly obtain the mass terms for fermions with weak eigenstates. Instead, one needs to transform them into mass eigenstates to extract the masses. Constructing four unitary matrices $V^{L,R}_{u,d}$, the coupling matrices Y_u and Y_d can be diagonalized. Since the neutrino mass is assumed to be null in the minimal Standard Model, no diagonalization is required for the lepton.

The diagonalized up-type and the down-type mass matrices are as follows:

$$M_u^{diag} = V_u^{R\dagger} Y_u V_u^L = \begin{pmatrix} \lambda_u & 0 & 0 \\ 0 & \lambda_c & 0 \\ 0 & 0 & \lambda_t \end{pmatrix} \tag{2.32}$$

$$M_d^{diag} = V_d^{R\dagger} Y_d V_d^L = \begin{pmatrix} \lambda_d & 0 & 0 \\ 0 & \lambda_s & 0 \\ 0 & 0 & \lambda_b \end{pmatrix}. \tag{2.33}$$

The corresponding quark fields in weak eigenstates will be transformed into mass eigenstates as follows. The transformation is applied to each element of the weak doublets (Equation 2.12) and singlets (Equations 2.14 and 2.15):

$$u_i^L = V_u^{L\dagger} u_{mass,i}^L, \quad \text{and} \quad u_i^R = u_{mass,i}^R V_u^R \tag{2.34}$$

$$d_i^L = V_d^{L\dagger} d_{mass,i}^L, \quad \text{and} \quad d_i^R = d_{mass,i}^R V_d^R. \tag{2.35}$$

A similar transformation is applied to all three families, with i running over all up-type or down-type quarks. Then, with these diagonalization transformations, one can derive the fermion mass term $\mathcal{L}_{FM}$ from the Yukawa coupling Lagrangian (Equation 2.29) by replacing the weak eigenstates with the mass eigenstates and inserting the Higgs fields (Equation 2.22):

$$\mathcal{L}_{FM} = \sum_i \bar{u}_i^R M_{u,ii} \frac{\nu}{\sqrt{2}} u_i^L + \bar{d}_i^R M_{d,ii} \frac{\nu}{\sqrt{2}} d_i^L. \tag{2.36}$$

The masses of quarks are thus related to the non-zero vacuum expectation value from the Higgs field under the spontaneous symmetry breaking:

$$m_u = \frac{\nu}{\sqrt{2}}\lambda_u, \; m_c = \frac{\nu}{\sqrt{2}}\lambda_c, \; m_t = \frac{\nu}{\sqrt{2}}\lambda_t \tag{2.37}$$

$$m_d = \frac{\nu}{\sqrt{2}}\lambda_d, \; m_s = \frac{\nu}{\sqrt{2}}\lambda_s, \; m_b = \frac{\nu}{\sqrt{2}}\lambda_b. \tag{2.38}$$

As mentioned before, the lepton mass terms are not written in the mass Lagrangians derived from the Yukawa coupling Lagrangian. That is because the leptons do not have mixing due to the massless neutrino assumed in the Standard Model. Therefore, Y_e in Equation 2.29 is naturally diagonal leading to the mass of leptons equal to the corresponding diagonal elements of Y_e.

2.3.4 The CKM matrix

As discussed before, all fermion fields are written by default in the weak eigenstates and are transformed into mass eigenstates in the Yukawa coupling Lagrangian in order to generate fermion masses. It is also interesting to transform them into the mass eigenstates in the electroweak interaction Lagrangian by the same unitary matrices

$V_{u,d}^{L,R}$ using Equations 2.34 and 2.35, since, in experiments, one can only measure the couplings with the mass eigenstates. With unitary transformations, one can rewrite the weak Lagrangian corresponding to $W^{\pm}$ with only left-handed interactions in mass eigenstates as follows:

$$\mathcal{L}_{W^{\pm}} = \frac{-g}{\sqrt{2}}(\bar{u}^L, \bar{c}^L, \bar{t}^L)_{mass}\gamma^{\mu}W_{\mu}^{+}V_u^L V_d^{L\dagger}\begin{pmatrix} d^L \\ s^L \\ b^L \end{pmatrix}_{mass} + \text{h.c.} \tag{2.39}$$

where

$$V_{CKM} \equiv V_u^L V_d^{L\dagger} = \begin{pmatrix} V_{ud} & V_{us} & V_{ub} \\ V_{cd} & V_{cs} & V_{cb} \\ V_{td} & V_{ts} & V_{tb} \end{pmatrix} \tag{2.40}$$

and h.c. stands for the hermitian conjugate of the previous terms. The V_{CKM} matrix is the Cabibbo-Kobayashi-Maskawa (CKM) matrix in the Standard Model [15, 16]. It is a unitary matrix, since both of V_u^L and V_d^L are unitary. Mathematically, the CKM matrix is derived from the unitary matrices to transform the weak eigenstates into the mass eigenstates for left-handed quark fields. Physically, the element V_{ij} in the CKM matrix describes the probability of a transition from one quark flavor i to another quark flavor j. These transitions are proportional to $|V_{ij}|^2$. For example, the term for the interaction of W-t-b is:

$$\mathcal{L}_{Wtb} = -\frac{g}{\sqrt{2}}\bar{b}\gamma^{\mu}W_{\mu}^{-}V_{tb}t + \text{h.c.} \tag{2.41}$$

where g is proportional to the coupling strength g_2 (Equation 2.10) and V_{tb} indicates the strength of the transition between the top and bottom quarks via the weak gauge bosons $W^{\pm}$. Determining V_{tb}, V_{td} and V_{ts} is one of the most important motivations to study single top quark production.

The CKM matrix can be parameterized in several ways. The so-called standard parameterization [21] uses the three mixing angles (θ_{12}, θ_{23}, θ_{13}) and the CP-violating Kobayashi-Maskawa (KM) phase (δ_{13}) [16], while the Wolfenstein parameterization [22, 23, 24] uses another set of parameters λ, A, $\bar{\rho}$, $\bar{\eta}$. The CKM matrix with Wolfenstein parameterization can be written up to $\mathcal{O}(\lambda^4)$ order of calculation as follows:

$$V_{CKM=}\begin{pmatrix} 1-\lambda^2/2 & \lambda & A\lambda^3(\rho - i\eta) \\ -\lambda & 1-\lambda^2/2 & A\lambda^2 \\ A\lambda^3(1-\rho-i\eta) & -A\lambda^2 & 1 \end{pmatrix} + \mathcal{O}(\lambda^4) \tag{2.42}$$

with

$$sin\theta_{12}\lambda = \frac{|V_{us}|}{\sqrt{|V_{ud}|^2 + |V_{us}|^2}}, \quad sin\theta_{23} = A\lambda^2 = \lambda|\frac{V_{cb}}{V_{us}}| \tag{2.43}$$

$$sin\theta_{13}e^{i\delta} = V_{ub}^{*} = A\lambda^3(\rho + i\eta) = \frac{A\lambda^3(\bar{\rho} + i\bar{\eta})\sqrt{1 - A^2\lambda^4}}{\sqrt{1-\lambda^2}[1 - A^2\lambda^4(\bar{\rho} + i\bar{\eta})]} \tag{2.44}$$

where $\bar{\rho}$ and $\bar{\eta}$ are actually expanded with different orders of λ. For example, $\bar{\rho} = \rho(1-\lambda^2/2+...)$. This parameterization ensures $\bar{\rho}+i\bar{\eta} = -(V_{ud}V_{ub}^*)/(V_{cd}V_{cb}^*)$. Considering the unitarity of the matrix within the Standard Model framework, one has several constraints, among which:

$$V_{ud}V_{ub}^* + V_{cd}V_{cb}^* + V_{td}V_{tb}^* = 0. \tag{2.45}$$

One can draw a triangle from the equation above in the complex plane with three sides of $V_{ud}V_{ub}^*$, $V_{cd}V_{cb}^*$, $V_{td}V_{tb}^*$. Conventionally, one renormalizes the triangle sides divided by $V_{cd}V_{cb}^*$:

$$\frac{V_{ud}V_{ub}^*}{V_{cd}V_{cb}^*} + 1 + \frac{V_{td}V_{tb}^*}{V_{cd}V_{cb}^*} = 0 \tag{2.46}$$

which is equivalent to:

$$(\bar{\rho}+i\bar{\eta}) + (1+i\cdot 0) + (\frac{V_{td}V_{tb}^*}{V_{cd}V_{cb}^*}) = 0. \tag{2.47}$$

It is a unitary triangle with two fixed vertices at $(0,0)$, $(1,0)$ and a free vertex at $(\bar{\rho},\bar{\eta})$ in the complex plane as demonstrated in Figure 2-2(a). Figure 2-2(b) shows the latest contraints in the $\bar{\rho}$, $\bar{\eta}$ plane by using various individual measurements and the global fits performed within the Standard Model framework with dedicated tools such as the frequentist CKMFitter [24, 25] and the Bayesian UTfit [26, 27], which utilize all available variables and the three-generation unitarity required by the Standard Model. The shaded areas indicate the possible $\bar{\rho}$, $\bar{\eta}$ values with 95% confidence level from different measurements. The shared shaded area gives the most precise constraints so far: $\bar{\rho} = 0.131^{+0.026}_{-0.013}$ and $\bar{\eta} = 0.345^{+0.013}_{-0.014}$ [24, 25].

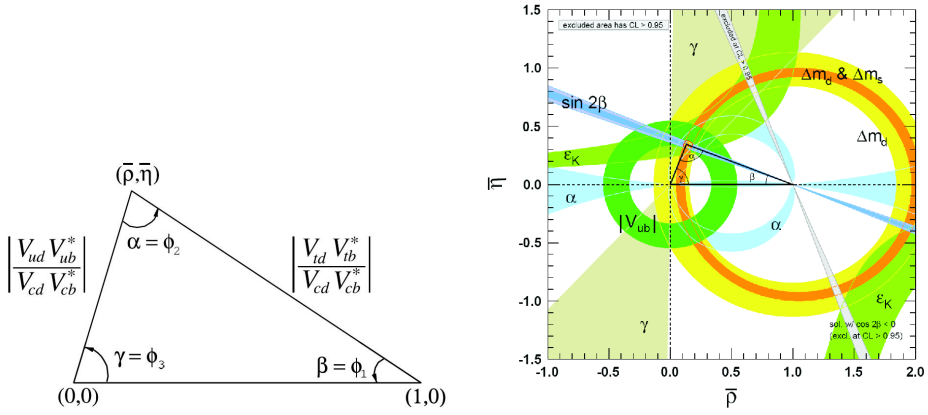

(a) (b)

Figure 2-2: (a) Unitary triangle corresponding to the Wolfenstein parameterization for the CKM matrix. (b) Contraints on the $\bar{\rho}$, $\bar{\eta}$ plane; the shaded areas correspond to a confidence level of 95% [4].

2.3.5 Higgs boson searches at the LHC

The discovery of a Higgs-like boson by both ATLAS and CMS collaborations has been published in the summer of 2012 [28, 29]. The ATLAS collaboration reported a clear evidence for the production of a neutral boson with a measured mass of $126 \pm 0.4(stat.) \pm 0.4(syst.)\ GeV$ with a significance of 5.9 standard deviations corresponding to a background fluctuation probability of 1.7×10^{-9}. The CMS collaboration reported an excess of events observed above the expected background with a local significance of 5.0 standard deviations at a measured mass of $125.3 \pm 0.4(stat.) \pm 0.5(syst.)\ GeV$ indicating a new particle. The searches cover several Higgs boson decay modes including $\gamma\gamma$, ZZ, WW, $\tau^+\tau^-$, $b\bar{b}$, which are all characteristic and productive decay modes in the low mass region. As shown in Figure 2-3(a), the local p-value (p_0) observed by the ATLAS collaboration, assuming that there is no signal, is plotted as a function of the invariant mass of the decay products. The local p-value peak at 126 GeV indicates that a Higgs-like boson may account for the deviation observed with respect to the background-only hypothesis at that mass point. In Figure 2-3(b), the CMS collaboration shows the distribution of the $\gamma\gamma$ invariant mass with an evident bump around the mass of 125 GeV indicating the Higgs-like boson.

The goal of forthcoming studies is to determine the properties of this newly found particle in order to make sure that it is really the Standard Model Higgs boson. From spin studies, both ATLAS and CMS collaborations reported results strongly favoring the assignment $J^P = 0^+$, which supports a 0-spin and an even-parity and excludes a specific model of $J^P = 2^+$ with a confidence level above 99.9% [30, 31].

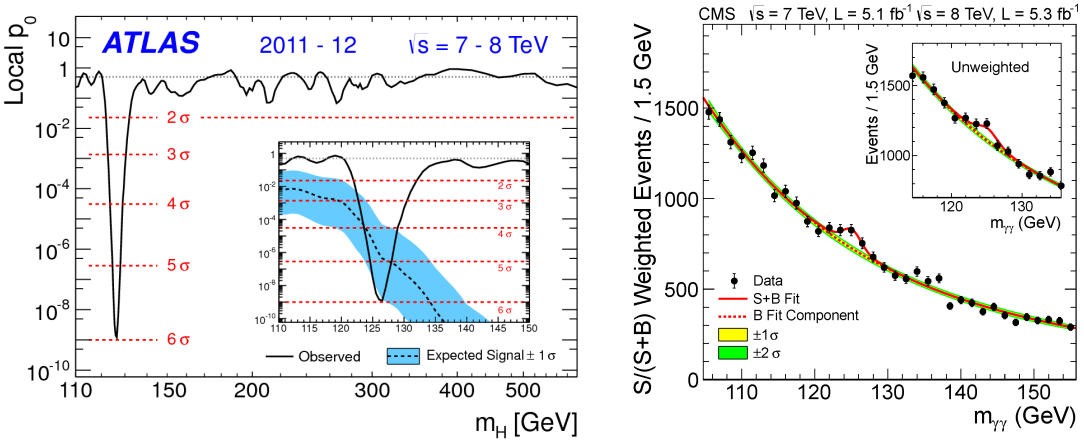

(a) (b)

Figure 2-3: (a) From ATLAS measurements, the observed local p-value (p_0) in the background-only hypothesis (solid line) as a function of the invariant mass of the decay products [28]. The inset plot shows the comparison in the low mass region with the expected p_0 curve (dashed line) under the hypothesis of a Standard Model Higgs boson signal within $\pm 1\sigma$ (blue band). A very small p_0, which is equivalent to a large standard deviation σ, indicates that there is an excess of events due to a non-background contribution (signal). The horizontal red dashed lines indicate the p-values corresponding to significances of 1 σ to 6 σ. (b) From CMS measurements, the diphoton invariant mass distribution with each event weighted by the $S/(S+B)$ value [32], where S and B are the numbers of signal and background events categorized according to a dedicated multivariable classifier, respectively [29]. The lines represent the fitted background and signal components, and the colored bands represent the ± 1 and ± 2 standard deviation uncertainties in the background estimate. The inset shows the central part of the unweighted invariant mass distribution.

Chapter 3

Top quark physics

In this chapter, the quantum chromodynamics is first introduced in Section 3.1 since the strong interaction dominates in hadron collisions, which are then described in Section 3.2 together with the factorization of the cross section calculation. The top quark physics with strong and electroweak interactions is presented in Sections 3.3 to 3.5. The various single top quark observables related to the Wtb vertex are discussed in details in Section 3.6 with a particular interest on the polarization measurements that are able to set constraints on anomalous Wtb couplings. Finally, some new physics searches in single top quark final states are presented in Section 3.7.

3.1 Quantum chromodynamics

The quantum chromodynamics (QCD) describes the strong interaction among quarks and gluons with the $SU(3)_C$ gauge invariance as introduced in Section 2.2. The QCD coupling constant α_s describing the strong interaction can be written as:

$$\alpha_s \equiv \frac{g_3^2}{4\pi} \tag{3.1}$$

where g_3 is the gauge coupling strength (Equation 2.9). In the following, the theory will be introduced according to the value of the coupling constant α_s which is actually a running constant and leads to the two most important features of the QCD theory: asymptotic freedom and confinement, corresponding to perturbative and non-perturbative QCD calculation, respectively.

3.1.1 Perturbative theory

Most of the time, the calculation of a physical observable, such as the production cross section, is not possible to be achieved without approximation either in an analytical way or in a computational way. The perturbative theory provides an approximation in the calculation of physical observables by expanding them into a perturbation series and focusing only on the leading order terms while neglecting all higher order terms.

For example, the cross section σ can be expanded as a function of a parameter α:

$$\sigma(\alpha) = A + B\alpha^k + C\alpha^{k+1} + D\alpha^{k+2} + ... \tag{3.2}$$

α is a coupling strength (such as the strong coupling constant of the Standard Model) and k the starting order of the expansion (usually $k = 2$). The only requirements from the perturbative theory is that α needs to be small in order to make the high order terms vanishing.

Conventionally, the perturbative calculation that considers the terms corresponding to the Feynman diagrams at tree level is called leading order (LO) (for example $\sigma(\alpha)_{LO} = A + B\alpha^k$), while the one that considers one more order of the parameter α is called next-to-leading order (NLO) ($\sigma(\alpha)_{NLO} = A + B\alpha^k + C\alpha^{k+1}$). The two next calculation orders are called next-to-next-to-leading order (NNLO) and next-to-next-to-next-to-leading order (NNNLO), respectively.

3.1.2 Asymptotic freedom and confinement

The strong coupling constant α_s is running as a function of the interaction energy scale, as illustrated in Figure 3-1, as well as as a function of the interaction distance. In Figure 3-1, the open (filled) symbols represent the values of α_s extracted from independent measurements using NLO (NNLO) QCD calculations compared to the predictions of the QCD theory for the combined world average value of α_s at the Z-pole mass. As we can see, the various measurements agree well with the theoretical curve.

The coupling constant α_s strongly decreases when the interaction distance decreases or the energy transfer increases; at very small distance ($\ll 1\ fm$) or at high energy scale ($\gtrsim 1\ GeV$), α_s becomes very small while at large distances or low energy transfers, α_s is very large. At short relative distances, the interactions among quarks and gluons are therefore weak; it is the so-called phenomenon of asymptotic freedom. At large relative distances, the interactions between quarks and gluons get much stronger; it is the so-called phenomenon of confinement.

For the small values of α_s, in the asymptotic freedom regime, one is able to calculate the physical observables by expanding their expressions into perturbative series as functions of α_s. This is the so-called perturbative QCD regime. For the large values of α_s, in the confinement regime, QCD calculations cannot be achieved by the perturbative theory any more. In this case, one solution can be provided by the lattice QCD [1], which is well established but needs a large amount of computing resources. In hadron collisions, one introduces the parton distribution functions to solve the long-distance QCD calculation which will be discussed in the next section. This is the so called non-perturbative QCD regime.

[1] Lattice QCD uses a discrete set of space-time points (called lattice) to reduce the analytically intractable path integrals of the continuum theory to a (very difficult) numerical computation which is usually carried out on supercomputers.

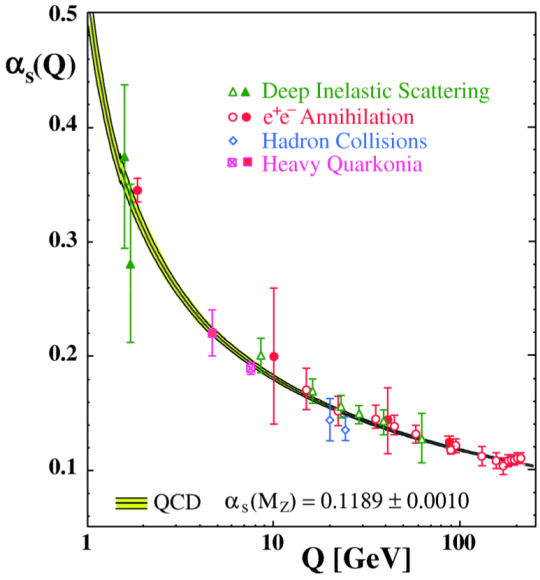

Figure 3-1: Measurements of the strong coupling constant α_s as a function of the interaction energy scale Q. Open symbols indicate resummed NLO and filled symbols NNLO QCD calculations used in the various measurements. The curves correspond to the QCD predictions for the combined world average value of α_s at the Z-pole mass [33].

3.2 Proton-proton collisions

Unlike electron collisions, where two elementary particles interact, proton-proton collisions involve two compounds and cannot be therefore simply described by Feynman diagrams without consideration of the internal structure of the protons. The actually collided elements are not the protons themselves but their partonic constituents, i.e. (valence and sea) quarks and gluons [34].

A proton-proton collision model is sketched in Figure 3-2: it is an example of a quark-gluon scattering leading to a final state consisting of a Z boson decaying into a pair of muons and a hard jet. Two protons are coming at long-distance with their uud valence quarks as well as with their sea quarks ($q\bar{q}$) and gluons whose further contributions to the hard interactions are described by the parton distribution functions (PDFs). Most of the partons of the two colliding protons interact softly and forwardly resulting in so-called underlying events and only a fraction of the partons may interact strongly. In the example given in Figure 3-2, the gluon emitted by a u-quark of one of the protons interacts with a u-quark contained in the other proton to produce a u-quark and a Z boson that then decays into a pair $\mu\bar{\mu}$. This short-distance process is the so-called "hard process" which can be calculated with a set of Feynman diagrams using a perturbative theory.

Before participating to the hard process, the incoming quarks may emit gluons or photons (green wiggled lines in Figure 3-2) which can change the effective energy of the interaction. These are the initial state radiations (ISR). Similarly, the quarks

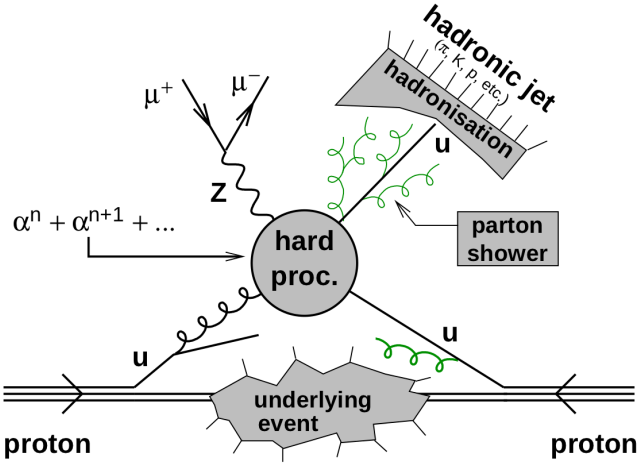

Figure 3-2: Schematic representation of a proton-proton collision, involving a quark-gluon scattering which leads to a final state consisting of a Z boson and a hard jet [35].

produced in the hard process can also emit gluons or photons that deflect the outgoing particles and change their original momentum. These are the final state radiations (FSR).

The produced gluons can emit gluons again and evolve into a hadronic shower around the quark, called parton shower; this parton showering process has a short-distance behavior which can be calculated within the perturbative QCD regime with Feynman diagrams order by order; nevertheless higher order calculations will introduce Feynman diagrams that are not easy to be handled. Within the perturbative QCD theory, the parton shower is instead usually realized by Monte Carlo event generators such as Pythia [36] and Herwig [37].

A quark is a color singlet that is not allowed to exist as a free particle due to the QCD confinement. When two quarks move away from each other, the potential energy via the strong force gets bigger till being strong enough to create new quarks from the vacuum and make up hadrons ($q_1\bar{q}_2$ or $q_1q_2q_3$ states), such that only neutral color states are finally generated. In the end, all produced quarks are confined in hadrons, which will actually decay into a chain of new hadrons. This process is called hadronization.

3.2.1 Top quark production cross section

The factorization theorem [38] allows to factorize the calculations for hadron-hadron collisions into two parts: one is the short-distance interaction described by the hard process of two partons; the other one is the long-distance interaction from the incoming partons that can be described by the parton distribution functions, since it is non-perturbative. For example, the single top quark t-channel cross section σ_{t-ch} for proton-proton collisions at a given center of mass energy $\sqrt{s}$ can be expressed with a

"long-distance" term and a "short-distance" term as follows:

$$\sigma_{t-ch}(s, m_t^2) = \sum_{i,j=g,q,\bar{q}} \int_0^1 dx_i \int_0^1 dx_j \underbrace{f_i(x_i, \mu_f^2) f_j(x_j, \mu_f^2)}_{\text{long-distance part}} \underbrace{\sigma_{ij \to tbj}(s', m_t^2, \mu_f^2, \mu_R^2, \alpha_s^2(\mu_R^2))}_{\text{short-distance part}} \tag{3.3}$$

where $x_{i,j}$ are the momentum transfer fractions for the interacting partons i, j, s' the corresponding fraction of the square of the collision energy s ($s' = s \cdot x_i \cdot x_j$), m_t the top quark mass, μ_f^2 and μ_R^2 the factorization and renormalization energy scales, respectively, and α_s the QCD coupling constant which is a function of the renormalization scale μ_R^2. The physics results should not be dependent on any scales one sets manually. Usually one sets $\mu_f^2 \sim \mu_R^2 \sim Q$, where Q is the energy transfer scale of the process one is interested in.

The "long-distance" term describes the incoming partons in the protons; it is modeled by introducing parton distribution functions for each parton. This term can either enhance or reduce the calculated cross section according to the contents of the colliding hadrons, since different hadrons provide different parton distribution functions. For example, the top-antitop quark production, which will be discussed in Sections 3.4, proceeds via two modes, gg-fusion and $q\bar{q}$-annihilation (Figure 3-5). In $p\bar{p}$ collisions under the center-of-mass energy of around 2 TeV (typically the Tevatron), the $q\bar{q}$-fusion represents 85 % of the total cross section and gg-fusion only 15% due to the large enhancement of the anti-quark distribution function in the colliding anti-proton. One the contrary, in pp collisions under the center-of-mass energy of around 14 TeV (typically the LHC), the $q\bar{q}$-fusion contributes to only 10% of the total $t\bar{t}$ cross section and gg-fusion to 90% due to the large enhancement of the gluon distribution function in the two initial protons.

The "short-distance" term describes the hard process and is determined by the corresponding Feynman diagrams derived from the Standard Model Lagrangians.

3.2.2 Parton distribution functions

The parton distribution functions (PDFs) describe the probability for a quark to carry a given energy fraction x of the whole energy of the hadron. They are constrained experimentally and several parameterizations are available, such as CTEQ [39], HERA [40], MRST/MSTW [41], NNPDF [42]. Figure 3-3 shows for example the parton distribution functions corresponding to the MSTW 2008 sets at NLO precision for the squared energy transfers $Q^2 = 10\ GeV^2$ and $Q^2 = 10^4\ GeV^2$ at the LHC. One can see that at the LHC, the gluon distribution functions are strongly enhanced at small x comparatively to those of the valence or sea quarks.

The distribution for each parton depends on the squared energy transfer Q^2 and its shape can change significantly from one scale to another. The DGLAP (Dokshitzer-Gribov-Lipatov-Altarelli-Parisi) [43] equation governs the evolution of the parton distribution functions along the scale Q^2 and allows to generate them for any scales once they are measured at a given scale. The DGLAP equation for the energy scale evo-

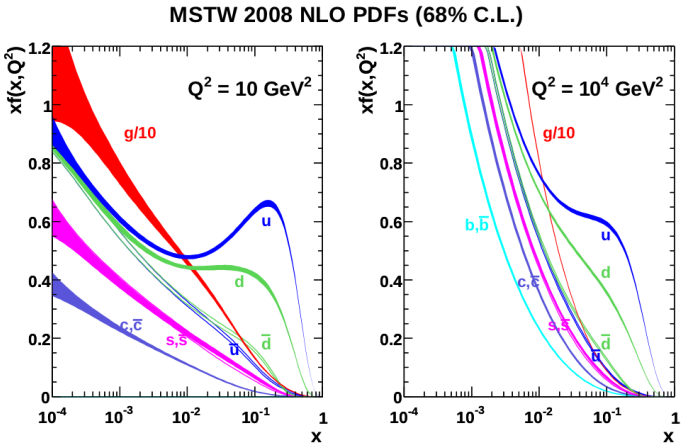

Figure 3-3: Parton distribution functions of the MSTW 2008 NLO set for the squared energy transfers Q^2 of 10 GeV^2 and 10^4 GeV^2 at the LHC.

lution of the parton distribution function of a quark i is:

$$Q^2 \frac{\partial q_i(x,Q^2)}{\partial Q^2} = \frac{\alpha_s(\mu_R^2)}{2\pi} \int_x^1 \frac{dy}{y} [P_{q_i \to q_i g}(\frac{x}{y}) \cdot q_i(y,Q^2) + P_{g \to q_i q_i}(\frac{x}{y}) \cdot g(y,Q^2)] \quad (3.4)$$

where Q^2 is the squared energy transfer, x the energy fraction the parton holds, $q_i(x,Q^2)$ and $g(x,Q^2)$ the distribution functions for quark and gluon which are functions of x and Q^2. The Altarelli-Parisi splitting function $P_{a \to bc}(z)$ represents the probability of a parton a branching into bc with a fraction z of the energy taken by one of its children. Here $P_{q_i \to q_i g}(\frac{x}{y})$ stands for the probability that the quark q_i emits a gluon, while $P_{g \to q_i q_i}(\frac{x}{y}) \cdot g(y,Q^2)$ stands for the probability that a gluon splits into a quark q_i and its anti-quark. The DGLAP equation describes the evolution of the probability, by integrating the parton distribution functions with higher energies, which evolve to this parton distribution function after emitting soft gluons or splitting to quark pairs.

3.3 Top quark decay

Due to its large mass, the top quark has a life time ($\simeq 4 \times 10^{-25} s$) much shorter than the hadronization time scale ($\simeq 28 \times 10^{-25} s$). Consequently, it decays immediately, before the hadronization phase can take place.

Within the Standard Model framework, the top quark decays almost 100 % into a W boson and a down-type quark [44]. Considering the values of the CKM matrix elements which govern this electroweak decay, $V_{tb} = 0.999146^{+0.000021}_{-0.000046}$, $V_{ts} = 0.0404^{+0.0011}_{-0.0005}$, $V_{td} = 0.00867^{+0.00029}_{-0.00031}$ [4], the top quark decays predominantly into a b-quark, as shown in Figure 3-4, since $V_{tb} \gg V_{ts,td}$. The W boson could decay (Figure 3-4) leptonically into a charged lepton and a neutrino ($e\nu$, $\mu\nu$ or $\tau\nu$) or hadronically into two quarks ($q\bar{q}'$). The branching ratio is 0.108 for each lepton flavor while

it is 0.676 for the hadronic mode.

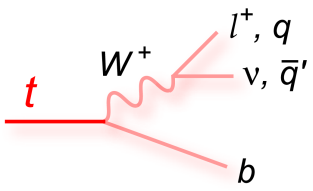

Figure 3-4: Feynman diagram for the electroweak top quark decay with the leptonic and hadronic decays of the W boson.

3.4 Top quark pair production

At hadron colliders, top quarks are predominantly produced in pairs of top (t) and anti-top ($\bar{t}$) quarks via strong interactions as shown in Figure 3-5. $t\bar{t}$ pairs are produced by gluon-gluon fusion, $gg \rightarrow t\bar{t}$, as well as by quark-antiquark fusion, $q\bar{q} \rightarrow t\bar{t}$. Considering the large parton distribution function for gluons in proton-proton collisions at small x and the relatively smaller distribution functions for anti-quarks, the gluon-gluon fusion is much more productive at the LHC than the quark-antiquark fusion; it contributes to around 80%-85% of the total production at the center of mass energy 7-8 TeV and to around 90% at 14 TeV.

The $t\bar{t}$ cross section for pp collisions at the centre of mass energy $\sqrt{s} = 7\ TeV$ is predicted to $\sigma_{t\bar{t}} = 167^{+17}_{-18}\ pb$. This theoretical value is calculated, assuming a top quark mass of 172.5 GeV, at approximate NNLO in QCD with Hathor 1.2 [45] using the MSTW2008 NNLO PDF sets [46]. The theoretical uncertainty incorporates PDF and α_S uncertainties, according to the MSTW prescription [47], added in quadrature to the scale uncertainty and cross checked with the NLO+NNLL calculation [48] as implemented in Top++ 1.0 [49]. The $t\bar{t}$ cross section at the center of mass energy $\sqrt{s} = 8\ TeV$ is predicted at $\sigma_{t\bar{t}} = 238^{+22}_{-24}\ pb$.

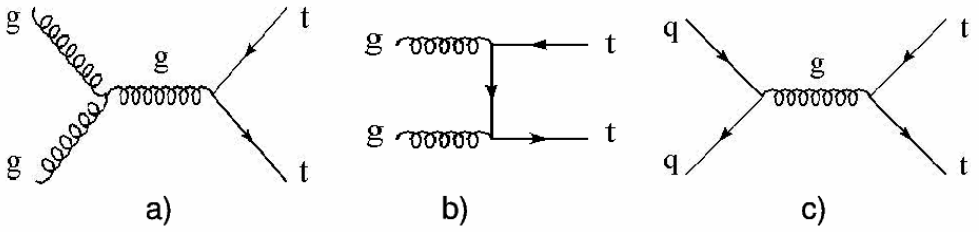

Figure 3-5: Feynman diagrams for top quark pair production in hadron collisions.

Figure 3-6 shows the $t\bar{t}$ cross sections measured in pp (LHC) and $p\bar{p}$ (Tevatron) collisions as a function of the center of mass energy. The CDF and D0 results obtained with $p\bar{p}$ collisions at the center of mass energy of 1.96 TeV are shown on the left-hand side of the figure while the measurements published by the ATLAS collaboration for

pp collisions at center of mass energies of 7 TeV and 8 TeV are presented on the right-hand side of the figure and in the inset.

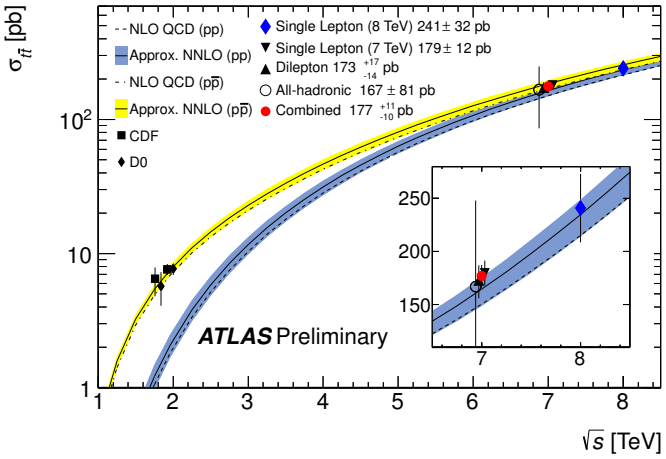

Figure 3-6: Measured cross sections for top quark pair production in hadron colliders (Tevatron and LHC) as a function of the center of mass energy with comparison to theoretical calculations [50].

3.5 Single top quark production

3.5.1 Production channels

Single top quarks are produced by the electroweak interaction involving a Wtb vertex which Lagrangian is described by Equation 2.41. With leading order approximations, we can define conventionally the single top quark production by three mechanisms, which are distinguished by the virtuality of the exchanged W boson. These three sub-processes are t-channel production, Wt associated production and s-channel production.

t-channel production

The dominant t-channel process corresponds to an exchange of a space-like virtual W boson as depicted in Figure 3-7; this W-gluon fusion was firstly proposed by Willenbrock and Dicus in 1986 [51]. In this W-gluon fusion, a gluon splits into two b-quarks, and one of them scatters with an incoming light quark via the exchange of a W boson leading to a final state containing a top quark, a forward light quark (also called spectator quark), and a forward b-quark. In Figure 3-7, there are two Feynman diagrams describing t-channel production: the diagram (a) represents the $2 \to 2$ process whereas diagram (b) represents the $2 \to 3$ process.

Ideally, one could use the $2 \to 3$ diagram to calculate the t-channel cross section but the result is not perturbatively reliable, because the b-quark splitted from a gluon

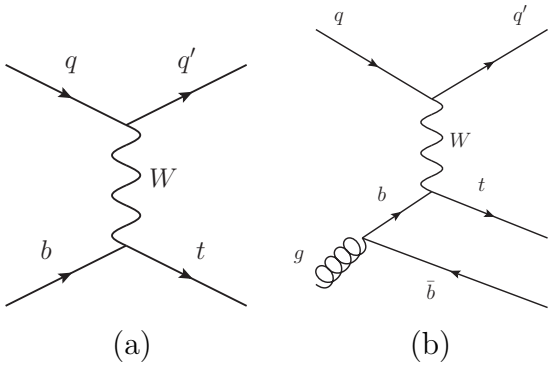

Figure 3-7: Leading order Feynman diagrams for the single top quark t-channel production (a) $2 \to 2$ process and (b) $2 \to 3$ process.

brings a non-perturbative contribution proportional to $\alpha_s log(m_t^2/m_b^2)$ when the b-quark is collinear to the gluon (the b-quark has therefore a low transverse momentum and flies along the direction of the incoming parton). In this case, the perturbative calculation can be restored by the $2 \to 2$ diagram with a parton distribution function introduced for the b-quark in the initial state instead of a gluon splitting. Therefore, t-channel physics is described by two Feynman diagrams: a $2 \to 2$ process where an initial b-quark distribution function is introduced for the physics in the low transverse momentum region of the initial b-quark and a $2 \to 3$ process with a gluon splitting for the physics in the high transverse momentum region of the initial b-quark.

Wt associated production

The sub-leading process at the LHC is the Wt associated production. This process leads to the production of a single top quark in association with a W boson as shown in Figure 3-8(a).

s-channel production

The least productive process at the LHC is the s-channel mode which involves the exchange of a time-like W boson which decays into a top quark and a b-quark as shown in Figure 3-8(b). The virtual W boson is fused from a quark and an anti-quark with different flavors. In pp collisions, the distribution functions of anti-quarks are not as large as the ones of quarks. Consequently, the s-channel is the channel with the smallest cross section in single top quark production, while productions involving gluon initiated process are much likely. The s-channel final state is characterized by two b-quarks, one being associated with the top quark production and the other one coming from the top quark decay.

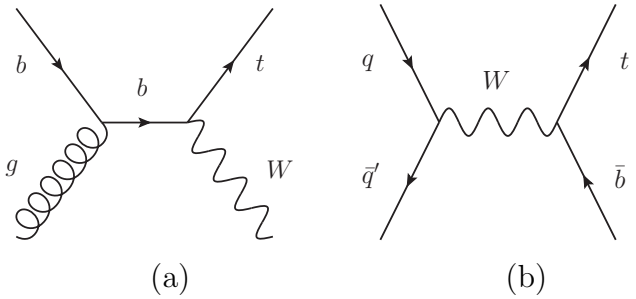

Figure 3-8: Leading order Feynman diagrams for (a) Wt associated production and (b) s-channel single top quark production processes.

3.5.2 Theoretical cross sections

The electroweak t-channel production scales like $1/M_W^2$ which does not depend on the center of mass energy. On the contrary, the strong $t\bar{t}$ process scales like $1/s$ which has a decreasing behavior when the center of mass energy $\sqrt{s}$ goes up. Taking into account the cross section enhancement from a higher center of mass energy, a larger increase of the single top quark electroweak production is therefore expected in hadron colliders with respect to the strong $t\bar{t}$ production. The evolution of the cross section predicted for the three leading order single top quark production modes as a function of the center of mass energy is shown in Figure 3-9. As we can see, the cross section grows very fast with the center of mass energy, in particular for the dominant t-channel process.

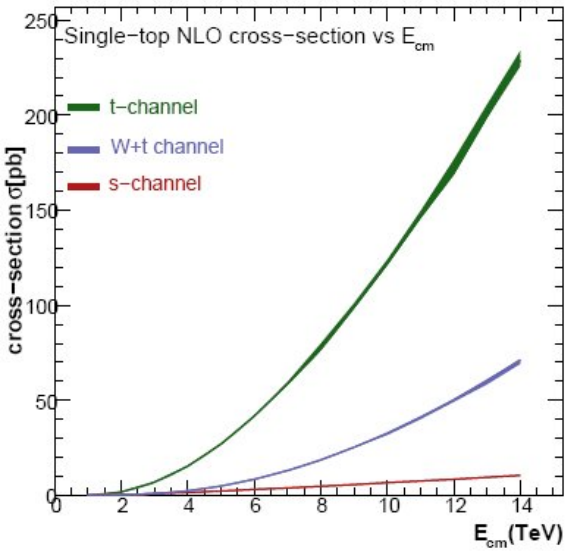

Figure 3-9: Cross sections for the three electroweak production channels of single top quark in proton-proton collisions as a function of the center of mass energy. They are calculated at NLO with MCFM assuming a top quark mass of 172.5 GeV.

The cross sections expected at the Tevatron and LHC colliders for the three single

top quark production channels are reported in Table 3.1. They are given for the center of mass energy of the Tevatron runs ($p\bar{p}$ collisions at 1.96 TeV) and for the center of mass energy of the 2011 LHC runs (pp collisions at 7 TeV). The cross sections expected for the nominal LHC energy (14 TeV) are also listed in the table. In all cases, t-channel is the dominant process. The cross section of the associated production Wt rises from a negligible level at the Tevatron to a detectable level at the LHC due to the enhanced parton density functions of incoming gluons in pp collisions. The s-channel production cross section also grows but to a lesser extent from the Tevatron energy to the LHC energies.

At the center of mass energy of 8 TeV of the 2012 LHC data, the cross sections of the t-channel and Wt processes are expected to increase by a factor of about 40 %, while the s-channel cross section is expected to be increased only by a factor of 20 %.

Channel	Tevatron 1.96 TeV	LHC 7 TeV	LHC 14 TeV
t-channel	2.10	64.6	243.5
Wt	0.27	15.7	84.2
s-channel	1.06	4.63	12.05

Table 3.1: Single top quark cross sections (in pb) of the three single top quark processes calculated for pp (Tevatron) and $p\bar{p}$ (LHC) collisions at different center of mass energies. The top quark mass is assumed to be 172.5 GeV. All cross sections are calculated with the resummation of collinear and soft gluon corrections at next-to-next-to-leading logarithm (NNLL) accuracy yielding approximate next-to-next-to-leading order (NNLO) cross sections [52, 53, 54], except the Tevatron Wt cross section which is calculated with the resummation of threshold soft gluon corrections at next-to-leading logarithm (NNL) accuracy yielding an approximate next-to-next-to-next-to-leading order (NNNLO) cross section [55].

3.5.3 Discovery at the Tevatron

Fourteen years after the discovery of the top quark [56, 57] at the Tevatron, the D0 and CDF collaborations reported in 2009 the first observation of the electroweak production of single top quarks in $p\bar{p}$ collisions at $\sqrt{s} = 1.96\ TeV$ [58, 59]. Both experiments measured an inclusive cross section of the t-channel and s-channel production $\sigma(p\bar{p} \to tb + X, tqb + X)$. The D0 collaboration measured a cross section of $3.94 \pm 0.88\ pb$ with 2.3 fb^{-1} of data corresponding to a significance of 5.0 σ, assuming a top quark mass equal to 170 GeV. The CDF collaboration measured a cross section of $2.3^{+0.6}_{-0.5}\ pb$ with 3.2 fb^{-1} of data corresponding to a significance of 5.9 σ assuming a top quark mass of 175 GeV. Multivariate techniques (boosted decision trees and neural networks) were used in the search of the electroweak single top quark production, since both analyses were strongly dominated by background events (signal-over-background ratio around 0.06).

3.5.4 Measurements at the LHC

t-channel production

Taking advantage of the larger cross sections expected at the LHC at the center of mass energy of 7 TeV, both the ATLAS and CMS collaborations observed the t-channel production. The results extracted from the analysis of a part of the 2011 data are shown in Figure 3-10. The t-channel cross section measured by the ATLAS collaboration is 83 ± 4 $(stat.)$ $^{+20}_{-19}$ $(syst.)$ pb, and the CMS collaboration measured a cross section of 67.2 ± 3.7 $(stat.)$ ± 3.0 $(syst.)$ ± 3.5 $(theor.)$ ± 1.5 $(lum.)$ pb [60]. From the 2012 data recorded at 8 TeV, the t-channel cross sections measured by the ATLAS and CMS collaborations are 95 ± 2 $(stat.)$ ± 18 $(syst.)$ pb [61] and 80.1 ± 5.7 $(stat.)$ ± 11.0 $(syst.)$ ± 4.0 $(lumi.)$ pb [62], respectively.

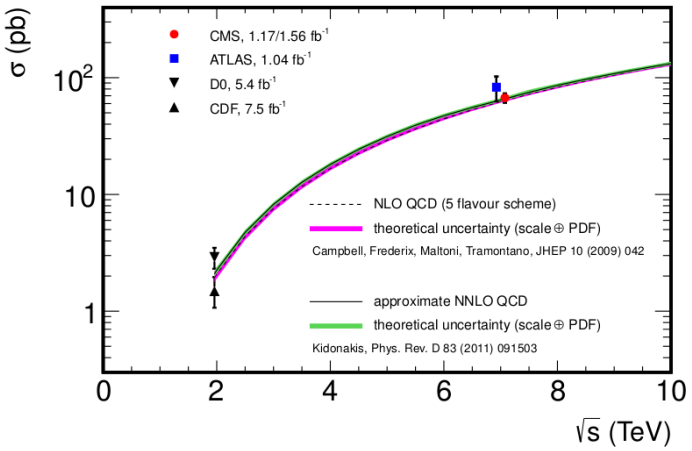

Figure 3-10: Single top quark t-channel cross section measurements as a function of the center of mass energy. The triangles stand for the measurements of the D0 and CDF collaborations at the Tevatron with a center of mass energy of 1.96 TeV; the blue square and the red circle represent respectively the LHC results from the ATLAS and CMS collaborations at a center of mass energy of 7 TeV. The measurements are compared to the theoretical calculations.

Wt associated production

The first evidence of the Wt associated production has been reported by the ATLAS collaboration in 2012 which found a deviation with a significance of 3.3σ with respect to the background-only hypothesis [63]. The CMS collaboration released an evidence of the Wt production mode with a significance of 4.0σ [64].

s-channel production

Only limits on the s-channel production have been set till now since its cross section is very small and its backgrounds very important (a typical signal-over-background ratio of the order of 0.05 is estimated). The best available upper limit is $\sigma_s < 26.5$ pb

at 95% confidence level with the first LHC data collected at the center of mass energy of 7 TeV [65]. This limit corresponds to about 5 times the Standard Model prediction for the s-channel cross section.

3.6 Anomalous coupling constraints in single top quark production

The properties of the top quark such its mass and its charge are usually measured with $t\bar{t}$ events benefiting from their larger production. On the other hand, single top quark production is a powerful probe of the electroweak Wtb vertex since its cross section gives a direct measurement of this coupling [2]. In addition, the produced single top quarks are highly polarized and the measurement of their polarization combined to the measurement of various W boson polarization observables may provide strong constraints on potential anomalous Wtb couplings.

3.6.1 Wtb anomalous couplings

As expressed by Equation 2.41, the Standard Model Lagrangian for the Wtb vertex involves only a vector coupling with left-handed chirality. This standard Lagrangian can be extended by introducing an additional right-handed vector coupling (V_R) as well as left-handed (g_L) and right-handed (g_R) tensor couplings. The most general effective Lagrangian for this extended Wtb vertex can be written as follows [66, 67]:

$$\begin{aligned}\mathcal{L}_{Wtb} = &-\frac{g}{\sqrt{2}}\bar{b}\gamma^{\mu}(V_L P_L + V_R P_R)tW^{-}_{\mu} \\ &+ -\frac{g}{\sqrt{2}}\bar{b}\frac{i\sigma^{\mu\nu}q_{\nu}}{M_W}(g_L P_L + g_R P_R)tW^{-}_{\mu} + h.c.\end{aligned} \tag{3.5}$$

where q is the momentum of the W boson, M_W its mass, g the coupling constant appearing in the standard Wtb Lagrangian and P_L, P_R the left-handed and right-handed projectors.

Within the Standard Model, the left-handed vector coupling V_L is the CKM matrix element V_{tb} (with value $\simeq 1$) discussed in Section 2.3.4, all other couplings V_R, g_L, g_R vanishing at tree level. Beyond the Standard Model configuration, all coupling strengths could be non-zero and even complex in case of CP-violation. Since the Lagrangian given by Equation 3.5 is a general formulation, all new physics effects related to the Wtb vertex are encoded in these four coupling strengths V_L, V_R, g_L and g_R without requiring any additional model assumptions. These four coupling strengths can be constrained by different precise measurements, such as single top quark cross section measurements, W boson polarization measurements as well as top quark polarization measurements, as discussed in the next sections.

[2] V_{tb} can also be probed by B^0-mixing such as B^0_d, B^0_s within the existing theoretical framework.

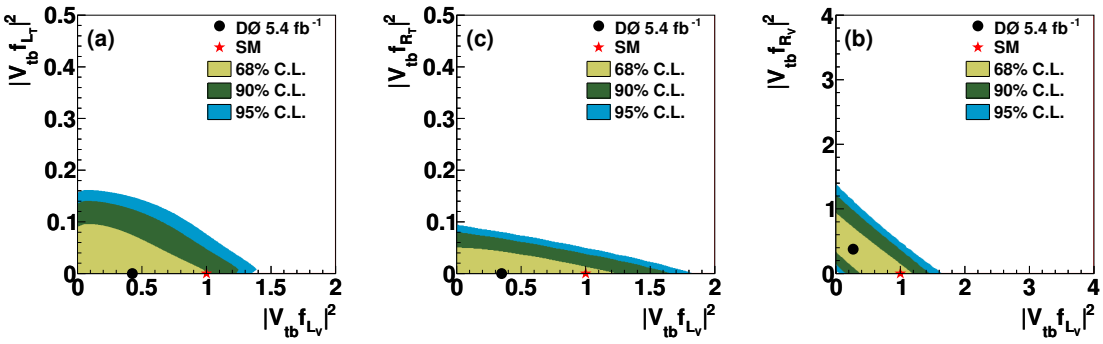

Figure 3-11: Two-dimensional posterior probability density distributions for the anomalous coupling configurations (V_L,V_R), (V_L,g_L) and (V_L,g_R). The black points represent the data and the red stars the Standard Model predictions.

3.6.2 Constraints with cross sections

The D0 collaboration has published in 2012 results on anomalous coupling constraints based on the measured cross sections [68]. The analysis assumed three combinations of single top quark productions mixing the Standard Model coupling V_L with one of the three anomalous couplings (V_R, g_L, g_R). Figure 3-11 shows the two-dimensional probability density distributions obtained from template-fits to the data for the three configurations of anomalous couplings. No significant deviations from the Standard Model expectations are seen. The upper limits extracted on the three anomalous couplings are given in Table 3.2. At 95 % confidence level, upper limits of 0.93, 0.06, and 0.13 were found on $|V_R|^2$, $|g_L|^2$ and $|g_R|^2$, respectively.

Coupling	Upper limit
$\|V_R\|^2$	0.93
$\|g_L\|^2$	0.06
$\|g_R\|^2$	0.13

Table 3.2: One-dimensional upper limits at 95 % confidence level for the anomalous Wtb couplings constrained by single top quark cross section measurements from the D0 collaboration.

3.6.3 Constraints with W boson helicity fractions

Due to the left-handed chirality of the electroweak interaction, W bosons coming from a top quark decay are produced in a favored helicity configuration. The W boson differential decay rate is parameterized as a function of the angle of the charged lepton coming from its leptonic decay [66], as follows:

$$\frac{1}{\Gamma}\frac{d\Gamma}{d\cos\theta^*} = \frac{3}{8}(1+\cos\theta_l^*)^2 F_R + \frac{3}{8}(1-\cos\theta_l^*)^2 F_L + \frac{3}{4}\sin^2\theta_l^* F_0 \qquad (3.6)$$

where θ^* is the angle between the charged lepton three-momentum in the W boson rest frame and the W boson three-momentum in the top quark rest frame and Γ the total decay rate. The fractions F_R, F_L and F_0 correspond to the three helicity states of the W boson (i.e. right-handed, left-handed and longitudinal helicities). These helicity fractions are independent of the top quark production process and can be therefore measured in strong (top quark pair) or electroweak (single top quark) events.

The Standard Model predictions at tree level for the helicity fractions are:

$$F_R = 0.000359, \quad F_L = 0.2971, \quad F_0 = 0.7025 \qquad (3.7)$$

assuming for the top quark, W boson and b-quark masses, $m_t = 175\ GeV$, $M_W = 80.4\ GeV$ and $m_b = 4.8\ GeV$, respectively [3]. These helicity fraction values show that the W bosons are predominantly produced in a left-handed or longitudinal helicity state, the right-handed state being strongly suppressed (the non-zero value obtained at tree level being due to a non null b-quark mass).

From the experimental side, the helicity fractions have been measured by the D0, CDF, ATLAS and CMS collaborations using $t\bar{t}$ events. With the event topology of single top quark production, the CMS collaboration has provided recently the first measurement of the W helicity fractions; the results combining 7 TeV and 8 TeV data in the muon+jets final state are [70]:

$$\begin{aligned} F_R &= 0.006 \pm 0.057\ (stat.)\ \pm 0.027\ (syst.), \\ F_L &= 0.293 \pm 0.069\ (stat.)\ \pm 0.030\ (syst.), \\ F_0 &= 0.713 \pm 0.114\ (stat.)\ \pm 0.023\ (syst.). \end{aligned} \qquad (3.8)$$

These results are shown in Figure 3-12(a) together with the comparison in Figure 3-12(b) of the measured right-handed helicity fraction to all measurements performed at the Tevatron and at the LHC in $t\bar{t}$ production.

The constraints on the tensor anomalous Wtb couplings imposed by the W helicity fractions measured in single top quark production are shown in Figure 3-13; these constraints are consistent with those determined by using only the single top quark cross section measurements (Table 3.2).

Harder constraints on the anomalous couplings can be extracted by combining various observables measured in top quark pair and single top quark productions. A first study has been carried out by the D0 collaboration through the combination of the W boson helicity fractions measured in $t\bar{t}$ production and single top quark cross section measurements [71]. Figure 3-14 shows the two-dimensional posterior probability density distributions given by the combination; the extracted limits are given in Table 3.3. Upper limits at the 95 % confidence level of 0.30, 0.05 and 0.12

[3] The NNLO calculation gives $F_R = 0.0017$, $F_L = 0.311$, $F_0 = 0.687$ with a smaller considered top quark mass $m_t = 172.8\ GeV$ [69].

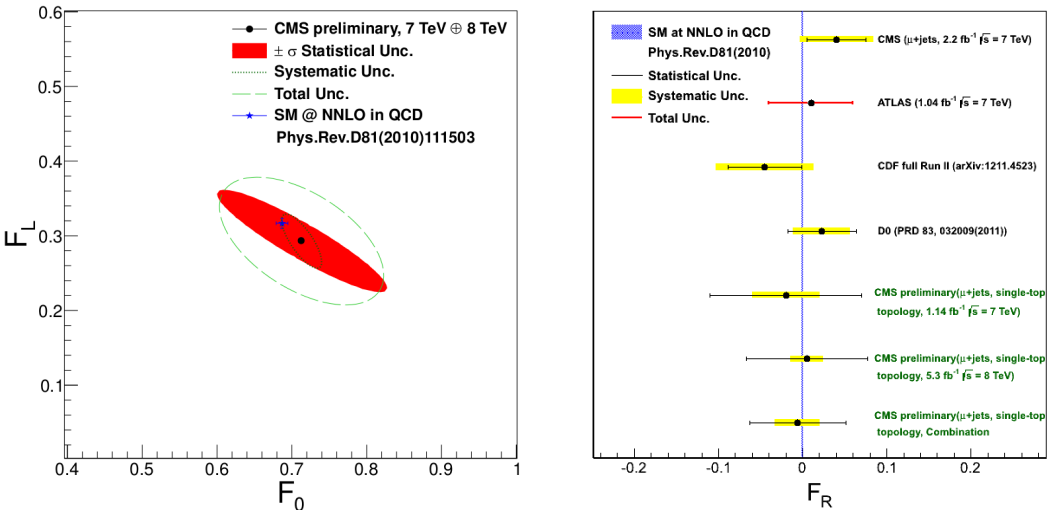

(a) (b)

Figure 3-12: (a) W boson helicity fractions F_0 and F_L measured by the CMS collaboration from single top quark events by combining data recorded at 7 TeV and 8 TeV center-of-mass energies, (b) Comparison of the helicity fraction F_R measured by CMS from single top quark events with all measurements carried out at the Tevatron and at the LHC from top quark pair events.

are thus obtained for the $|V_R|^2$, $|g_L|^2$ and $|g_R|^2$ coupling values, respectively. This combined extraction leads to stronger constraints than those derived only from the cross sections (Table 3.2).

Couplings	Upper limits
$\|V_R\|^2$	0.30
$\|g_L\|^2$	0.05
$\|g_R\|^2$	0.12

Table 3.3: One-dimensional upper limits at 95 % confidence level for the anomalous Wtb couplings constrained by the combination of the single top quark cross section and the W boson helicity fractions measured in $t\bar{t}$ production by the D0 collaboration.

3.6.4 Constraints with W boson polarization observables

The helicity basis allows to explore only three of the eight form factors which are functions of the four Wtb couplings; therefore additional polarization observables should be measured to fully constrain these couplings [72].

For the polarized top quarks produced via electroweak interaction, in addition to the W boson helicity fractions, it is worth defining and studying the normal and

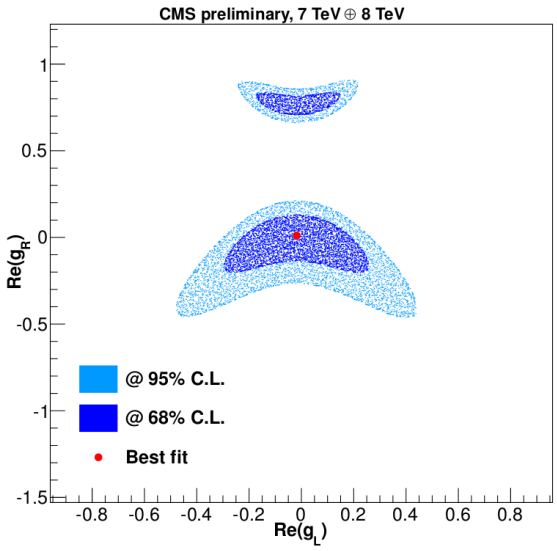

Figure 3-13: Constraints on the anomalous couplings g_L and g_R derived from the W boson helicity fractions measured by the CMS collaboration from single top quark events.

transverse fractions which characterize the W boson polarization along two spin directions orthogonal to its momentum [72]. The normal direction $\vec{N}$ is taken along the normal to the plane defined by the W boson momentum $\vec{q}$ in the top quark rest frame and the spin axis of the top quark $\vec{s_t}$: $\vec{N} = \vec{s_t} \times \vec{q}$. In single top quark t-channel production, the spin direction of the top quark is usually defined by the momentum of the spectator (light) quark in the top quark rest frame; the top quark polarization will be discussed in Section 3.6.5. The transverse direction $\vec{T}$ is defined as the axis orthogonal to the plane defined by the W boson momentum and the normal direction $\vec{N}$: $\vec{T} = \vec{q} \times \vec{N}$. These normal and transverse directions are shown in Figure 3-15(a).

As the helicity fractions, the normal and transverse polarization fractions can be measured from the angular distributions of the charged lepton coming from the W boson decay. These distributions have the same form than the angular distribution of the lepton in the helicity basis (Equation 3.6):

$$\frac{1}{\Gamma}\frac{d\Gamma}{d\cos\theta^{N,T}} = \frac{3}{8}(1+\cos\theta_l^{N,T})^2 F_+^{N,T} + \frac{3}{8}(1-\cos\theta_l^{N,T})^2 F_-^{N,T} + \frac{3}{4}\sin^2\theta_l^{N,T} F_0^{N,T} \quad (3.9)$$

where in that case $\theta^{N,T}$ are the angles between the charged lepton three-momentum in the W boson rest frame and the normal and transverse axes defined with respect to the top quark rest frame as explained above. The $F_{\pm,0}^N$ and $F_{\pm.0}^T$ factors define the W polarization fractions in the normal and transverse bases, respectively. The Standard Model predicts $F_-^T = 0.1718$, $F_+^T = 0.6794$, $F_0^T = 0.1487$, and $F_+^N = F_-^N = 0.4256$, $F_0^N = 0.1487$ at tree-level calculations [72]. However, in most processes, the top quarks are not produced with 100% degree of polarization along any axis, but with a certain degree of polarization P ($< 100\%$). Therefore, effective polarization frac-

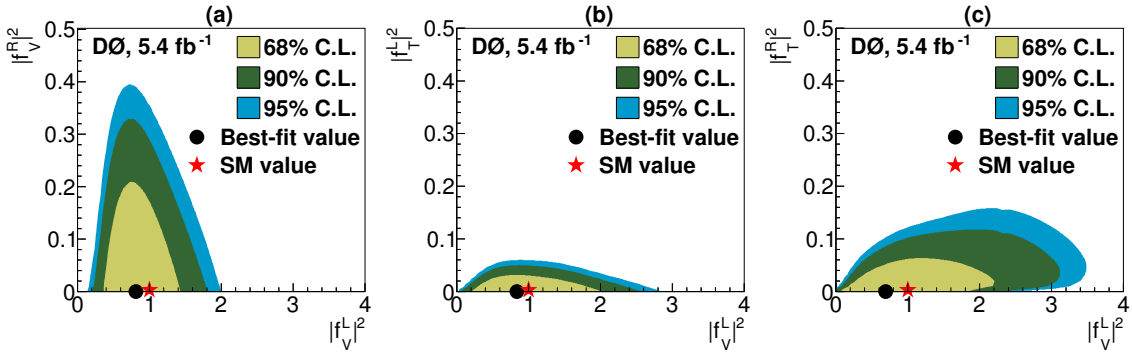

Figure 3-14: Two-dimensional posterior probability density distributions for the anomalous coupling configurations (V_L,V_R), (V_L,g_L), (V_L,g_R) extracted from the combination of the single top quark cross section measurements and the W boson helicity fractions measurements in $t\bar{t}$ production. The points represent the data and the red stars the Standard Model predictions.

tions are actually measured from the angular distributions expressed by Equation 3.9. These effective quantities depend on the degree of polarization according to:

$$\tilde{F}_+^{T,N} = \frac{1+P}{2} F_+^{T,N} + \frac{1-P}{2} F_-^{T,N} \tag{3.10}$$

$$\tilde{F}_-^{T,N} = \frac{1+P}{2} F_-^{T,N} + \frac{1-P}{2} F_+^{T,N} \tag{3.11}$$

while the fractions $F_0^{T,N}$ associated to the longitudinal polarization states are independent of P.

According to the Standard Model values, the angular distribution in the normal basis is expected to be symmetric since the $\tilde{F}_+^N$ and $\tilde{F}_-^N$ fractions are the same thanks to the equality $F_+^N = F_-^N$. However, in case of CP-violation, this symmetry could be broken. Indeed, as proposed in [72], the normal forward-backward asymmetry A_{FB}^N, which is defined by:

$$A_{FB}^N = \frac{N(\cos\theta^N > 0) - N(\cos\theta^N < 0)}{N(\cos\theta^N > 0) + N(\cos\theta^N < 0)} \tag{3.12}$$

has a very high sensitivity to CP-violation effects [4] through the relation:

$$A_{FB}^N = 0.64\ P\ \mathrm{Im}(g_R) \tag{3.13}$$

where $\mathrm{Im}(g_R)$ stands for the imaginary part of the right-handed tensor coupling g_R. This relation is valid for small g_R values and for $V_L = 1$, $V_R = g_L = 0$. The dependence of A_{FB}^N on the degree of top quark polarization P is introduced by the effective fractions.

The first measurement of this forward-backward asymmetry in the normal basis

[4] A non-zero imaginary part of g_R indicates CP-violation [72].

has been very recently reported by the ATLAS collaboration [73]. Figure 3-15(b) shows the measured asymmetry assuming a sliding of the top quark polarization P around the Standard Model value.

The measured value of the asymmetry is:

$$A_{FB}^{N} = 0.031 \pm 0.065(stat.)^{+0.029}_{-0.031}(syst.). \tag{3.14}$$

Taking this measurement together with the theoretical prediction of the top quark polarisation, the first experimental limits on Im(g_R) are determined to be [-0.20, 0.30] at 95% confidence level. Both the measurement and the limit are in good agreement with the Standard Model. This measurement could be added in the future in the combination discussed in the end of Section 3.6.3 in order to improve the constraints on the other coupling strengths of the Wtb vertex.

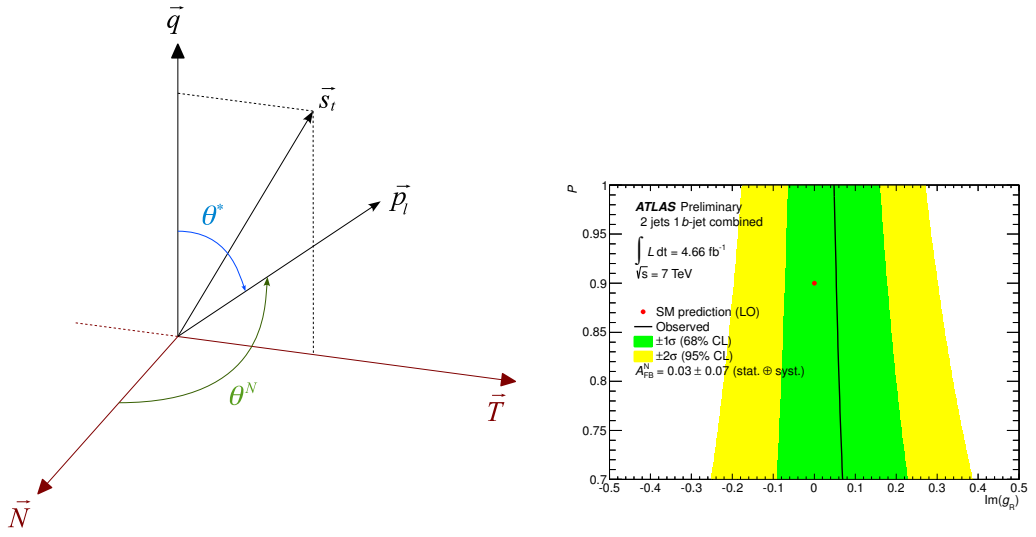

(a) (b)

Figure 3-15: (a) Definition of the normal and transverse W boson spin directions. The normal direction is defined by $\vec{N} = \vec{s_t} \times \vec{q}$ and the transverse direction by $\vec{T} = \vec{q} \times \vec{N}$ where $\vec{q}$ is the W boson three-momentum direction in the top quark rest frame, $\vec{s_t}$ the spin axis of the top quark and $\vec{p_l}$ the lepton three-momentum direction in the W boson rest frame. The θ^* angle of the charged lepton in the helicity basis is defined by the angle between $\vec{p_l}$ and $\vec{q}$ while the θ^N angle in the normal basis is defined by the angle between $\vec{p_l}$ and $\vec{N}$, (b) Constraints on Im(g_R) calculated from the normal forward-backward asymmetry A_{FB}^{N} measured by the ATLAS collaboration assuming a sliding on the top quark polarization P from 0.7 to 1.0 [73].

3.6.5 Top quark polarization

Top quarks produced by electroweak interaction are highly polarized contrary to the top quark pairs which are produced unpolarized due to the parity conservation in the

strong production within the Standard Model framework.

The top quark polarization can be measured from the angular distribution of any of its direct or indirect children; the differential decay rate for polarized top quarks is given by:

$$\frac{1}{\Gamma}\frac{d\Gamma}{d\cos\theta_X} = \frac{1}{2}(1 + \alpha_X P \cos\theta_X) \tag{3.15}$$

where θ_X is the angle between the three-momentum of the decay product X (called spin analyzer) in the top quark rest frame and the top quark spin direction (called spin basis). The constant α_X is the spin analyzing power associated to the spin analyzer X (it ranges between -1 and 1) and P the degree of top quark polarization along the chosen spin axis.

The value of the spin analyzing power α_X encodes the degree to which the spin analyzer X is correlated with the spin of the top quark. The spin analyzing powers, associated to different spin analyzers are summarized in Table 3.4. One can see that the charged lepton gives the maximal analyzing power ($\alpha_l = 1$ at tree level), the second interesting spin analyzer being the b-quark ($\alpha_b = -0.41$ at tree level). Only the charged lepton and b-quark spin analyzers will be therefore considered in the measurements reported in this thesis. In addition, they can be directly reconstructed from the recorded ATLAS data. The d-type quark, which has also a maximal correlation with the top quark spin ($\alpha = 1$ at tree level), is not considered in the analysis, since hadronically decayed W bosons lead to multijet final states, which are much more difficult to be separated from the QCD multijet backgrounds than the leptonic final states.

Spin analyzer	α (LO)	α (NLO)
W^+, b-quark	-0.41	-0.39
ν_l	-0.32	-0.33
u-type quark	-0.32	-0.31
$\bar{d}$-type quark	1	0.93
l^+	1	0.998

Table 3.4: Spin analyzing powers for the top quark decay products calculated at leading and next-to-leading orders [72]. u-type quark refers to u-quark and c-quark, while $\bar{d}$-type quark refers to $\bar{d}$-quark and $\bar{s}$-quark. One only needs to change the sign of α when flipping the particle to its antiparticle.

Different quantization axes for the top quark spin can be considered and the spin basis giving the largest expected degree of polarization P should be preferred for the measurements. It has been shown in [74, 75] that in single top quark t-channel production in pp collisions, the top quarks will have a large degree of polarization in the direction of the spectator quark or along the top quark direction of motion. The top quark spin axis could therefore be chosen either along the spectator quark momentum in the top quark rest frame (defining the so-called spectator basis) or along the

top quark momentum in the center-of-mass frame (which defines the helicity basis). The spectator basis being the easiest direction to reconstruct (the helicity basis needs indeed to reconstruct the center-of-mass frame instead of the top quark rest frame alone), the spectator basis will be therefore used for the polarization measurements presented in this document. Furthermore, the measured top quark polarizations could be more easily combined in the future with the other polarization results discussed in the previous sections (the normal and transverse W boson polarizations are indeed also defined with respect to the spectator basis). Within the Standard Model framework, the calculated degree of polarization in the spectator basis is 0.89 for t-channel single top quark production [76].

The direct observable which can be measured from the angular distribution given by Equation 3.15 is the product $\alpha \cdot P$ of the analyzing power associated to the spin analyzer, charged lepton or b-quark, by the degree of polarization of the top quarks in the spectator spin basis. This combined observable could be used to extract the degree of polarization P, assuming the Standard Model values for α_l and α_b, in order to constrain the couplings V_L, V_R, g_L and g_R, which parameterize the effective Wtb Lagrangian given by Equation 3.5. On the other hand, one can also use the combined observable $\alpha \cdot P$ measured with the two spin analyzers to derive the ratio r_{bl} :

$$r_{bl} = \frac{\alpha_b P}{\alpha_l P} = \frac{\alpha_b}{\alpha_l}. \tag{3.16}$$

As shown in Figure 3-16, adding the r_{bl} observable value in the combination of the measured single top quark cross sections and W boson helicity observables gives much stronger constraints on anomalous couplings.

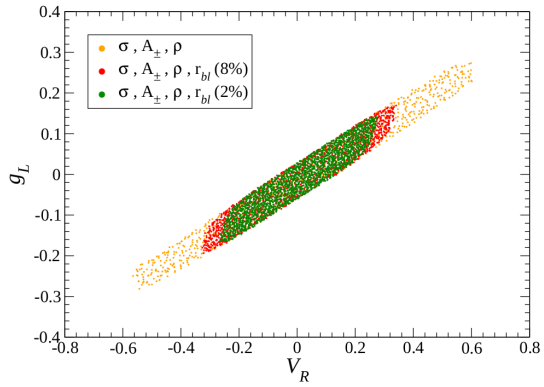

Figure 3-16: Projection on the (V_R, g_L) plane of the combined limits on Wtb couplings from single top quark cross section measurements and W boson helicity observables without (yellow dashed band) and with (red and green dashed bands) including the predicted value for r_{bl} [76]. The prediction for r_{bl} assumes an uncertainty of 8 % (red band) or 2 % (green band).

The analysis reported in this thesis focusses on the measurement of the top quark polarization in t-channel single top quark production. Wt associated production does not have a spin axis that allows highly polarized top quarks, and s-channel production

is not yet observed in pp collision by the experiments. The first measurements of the degree of polarization P and of the spin analyzing power ratio r_{bl} will be reported and discussed in Chapter 9. Various methods, based on unfolding and folding techniques coupled to an extraction of the polarization observable from the angular forward-backward asymmetry or from the fit of the deconvolved/convolved distributions, will be presented with their performances compared. It should be also mentioned that all the developed methods could be applied in the future to extract in parallel or simultaneously the top quark and W boson polarizations (as well as the production cross section) in order to maximally constrain the systematic uncertainties as well as to take into account the existing relations between these various observables [72].

3.7 Searches for new physics in single top quark production

Various scenarios of new physics can be searched for in single top quark production. These scenarios include the production of new particles such as massive W-like bosons (W'), excited quarks (b^*), charged Higgs bosons or charged composite top-pions. Other interesting properties, which can be studied in single top quark production, exist in the new couplings of the top quark to the known particles. Anomalous couplings (right-handed or tensor components) in the Wtb interaction can be investigated as discussed in the previous section. New couplings with flavor-changing neutral current (FCNC) may also be searched for. In the following, only the topics with recent progresses will be discussed.

3.7.1 Extra vector boson - W'

Many theories try to extend the Standard Model with a larger gauge symmetry group which can reduce to the Standard Model gauge at low energy. New gauge symmetry naturally introduces a new gauge boson that is usually called W'. The W' boson appears in phenomenological models involving extra space-time dimensions, such as Kaluza-Klein excitations of the Standard Model W boson [77] or from techni-colour models [78]. Other theories extend fundamental symmetries of the Standard Model and propose a massive right-handed counterpart to the W boson [79]. Nevertheless, to search directly for the new gauge boson W' in a model-independent way, one relies upon the use of an effective model [8, 9].

The Feynman diagram for the production and decay of a W' boson is shown in Figure 3-17. In its hadronic decay, the W' boson has the same final state than the Standard Model s-channel single top quark process (Figure 3-8(c)), namely a t-quark and a b-quark. One can therefore look for W' events within the s-channel signature and search for a large mass resonance.

A search for W' with hadronic decay has been recently performed at the LHC by the ATLAS collaboration under the center of mass energy of 8 TeV. A mass region between 0.5 and 3.0 TeV was covered; the new boson mass is excluded below

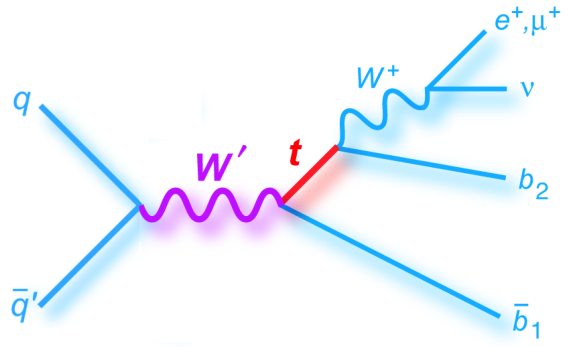

Figure 3-17: Feynman diagram for the production of W' boson and its hadronic decay into a t-quark and a b-quark. The leptonic decay of the final W boson is also represented.

1.74 TeV for a left-handed W' and 1.84 TeV for a right-handed W' at 95% confidence level [80].

3.7.2 New fermion - b^*-quark

A set of extra quarks is naturally required to solve problems on the radiative corrections generated dominantly by top quark loops which push the Higgs boson to have a mass of order 10^{19} GeV at the Planck scale. An excited b^*-quark is proposed in many theories such as Randall-Sundrum models [10, 11] and composite Higgs models [12, 13, 14], which focus on the coupling primarily between the excited b^*-quark and the third quark generation of the Standard Model. Therefore, the b^*-quark can be searched for through its decay into a W boson and a single top quark, which has a single top Wt-like final state as shown in Figure 3-18.

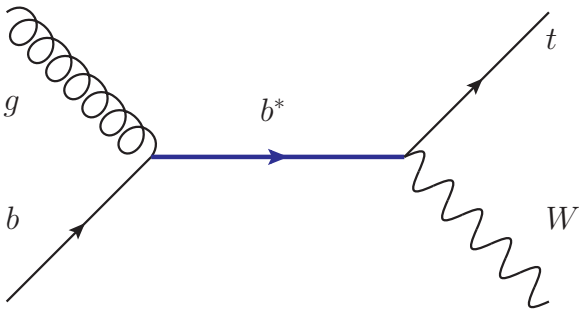

Figure 3-18: Feynman diagram for the production of an excited b^*-quark decaying into a W boson and a top quark.

A recent search for this process has been performed at the LHC by the ATLAS collaboration at the center of mass energy of 7 TeV [81]. The analysis excludes the b^*-quark with a mass below 870 GeV at the 95% confidence level.

3.7.3 New coupling - FCNC process

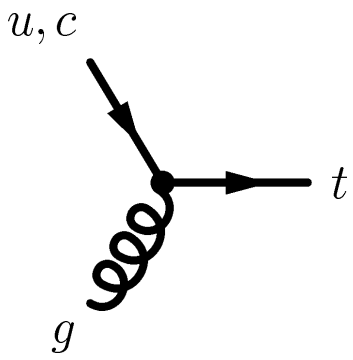

Figure 3-19: Feynman diagram for single top quark production via flavor-changing neutral current.

Apart from the Wtb vertex which is able to produce single top quark, flavor-changing neutral current (FCNC) is a possible and promising extra source of single top quark. FCNC processes are forbidden at tree level and are suppressed at higher orders due to the Glashow-Iliopoulos-Maiani (GIM) mechanism [82], but are predicted to reach a detectable level by several theories beyond the Standard Model such as the quark-singlet model (QS), the two-Higgs doublet model (2HDM), the flavour-conserving two-Higgs doublet model (FC 2HDM), the minimal supersymmetric model (MSSM), SUSY with R-parity violation and Topcolour-assisted Technicolour model (TC2) [83]. The branching ratios predicted by these various models for top quarks decaying to a quark and a photon or a Z boson or a gluon are listed in Table 3.5. The value for the coupling can be as high as 10^{-4} compared to the GIM suppressed Standard Model values which are around 10^{-13}.

Process	SM	QS	2HDM	FC 2HDM	MSSM	$\not{R}$ SUSY	TC2
$t \to u\gamma$	3.7×10^{-16}	7.5×10^{-9}	-	-	2×10^{-6}	1×10^{-6}	-
$t \to uZ$	8×10^{-17}	1.1×10^{-4}	-	-	2×10^{-6}	3×10^{-5}	-
$t \to ug$	3.7×10^{-14}	1.5×10^{-7}	-	-	8×10^{-5}	2×10^{-4}	-
$t \to c\gamma$	4.6×10^{-14}	7.5×10^{-9}	$\sim 10^{-6}$	$\sim 10^{-9}$	2×10^{-6}	1×10^{-6}	$\sim 10^{-6}$
$t \to cZ$	1×10^{-14}	1.1×10^{-4}	$\sim 10^{-7}$	$\sim 10^{-10}$	2×10^{-6}	3×10^{-5}	$\sim 10^{-4}$
$t \to cg$	4.6×10^{-12}	1.5×10^{-7}	$\sim 10^{-4}$	$\sim 10^{-8}$	8×10^{-5}	2×10^{-4}	$\sim 10^{-4}$

Table 3.5: Theoretical values for the branching ratios of FCNC top quark decays, predicted by the Standard Model, the quark-singlet model (QS), the two-Higgs doublet model (2HDM), the flavour-conserving two-Higgs doublet model (FC 2HDM), the minimal supersymmetric model (MSSM), SUSY with R-parity violation and Topcolour-assisted Technicolour model (TC2).

At the LHC, the FCNC production process $qg \to t$ (q labels u-quark or c-quark) has been searched for by the ATLAS collaboration in t-channel single top quark

final state [84] [5] (searches for $t \to qZ$ decay mode are performed in top quark pair production [85]). The corresponding Feynman diagram is shown in Figure 3-19. The obtained results, which are model-independent, constrain the coupling strengths κ_{ugt} and κ_{cgt} which enter in the general effective Lagrangian describing this process [86, 87, 67]:

$$\mathcal{L}_{eff} = g_s \sum_{q=u,c} \frac{\kappa_{qgt}}{\Lambda} T^a (f_q^L P_L + f_q^R P_R) q G^a_{\mu\nu} + h.c. \tag{3.17}$$

where κ_{ugt}, κ_{cgt} are dimensionless parameters that relate the strength of the new coupling to the strong coupling constant g_s. Λ is the new physics scale related to the mass cutoff scale above which the effective theory breaks down. This effective Lagrangian includes dimension-six operators with only tensor couplings.

The direct measurable of the ATLAS analysis is the overall cross section of the processes $ug \to t$ and $cg \to t$. The upper limit of this cross section is $\sigma_{gq\to t} \times \mathcal{B}(t \to Wb) < 3.9\ pb$. This cross section limit allows to make constraints on the coupling strengths $\frac{\kappa_{ugt}}{\Lambda}$, $\frac{\kappa_{cgt}}{\Lambda}$ as well as on the branching ratios of these two processes, as shown in Figures 3-20(a) and 3-20(b):

$$Br(t \to ug) = 5.7 \times 10^{-5} \tag{3.18}$$

$$Br(t \to cg) = 2.7 \times 10^{-4} \tag{3.19}$$

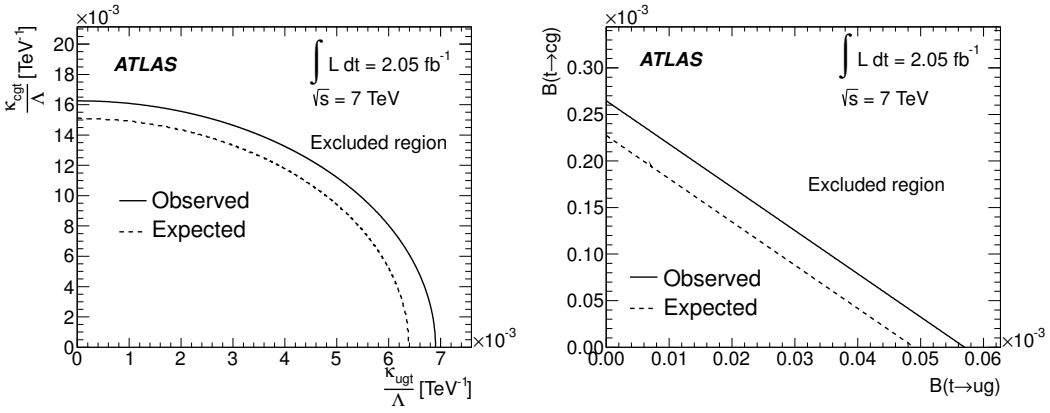

(a) (b)

Figure 3-20: (a) Upper limit on the coupling constants κ_{ugt}/Λ and κ_{cgt}/Λ, (b) Upper limit on the branching ratios for the $t \to ug$ and $t \to cg$ processes.

[5] In hadron colliders, the FCNC decay process $t \to qg$ cannot be separated from the overwhelming QCD multijet backgrounds.

Chapter 4

The ATLAS detector

This chapter leads a tour to the LHC and the ATLAS detector with its inside structures, which offers an access to deeper studies on particle physics, such as the Higgs mechanism, supersymmetry theory, extra dimensions based on string theory and dark matter. First of all, as a basic pre-introduction in experimental particle physics, Sections 4.1 will introduce the commonly used variables and parameters, such as luminosity and missing transverse energy, and the conventions defined for the units and the coordinates. Secondly, there comes the LHC introduction in Section 4.2, which introduces an overview of the LHC itself and the seven experiments operated on it. Then, the ATLAS detector is narrated in details firstly in Section 4.3 as a general idea of the whole ATLAS, followed by a series of detailed discussions on each subdetector. The magnetic system is introduced in Section 4.4, and inner detector in Section 4.5 followed by the calorimeters in Section 4.6, the muon spectrometer in Section 4.7, and the forward detectors in Section 4.8 as well as the trigger system in Section 4.9.

4.1 Basic definitions in high-energy experiments

In physics, the so-called natural units are commonly used, in which the physical units are based only on physical constants. In particle physics, the "natural units" generally adopts:

$$c = \hbar = k_B = 1 \tag{4.1}$$

where c is the speed of light, $\hbar$ the reduced Planck constant ($\hbar = h/2\pi$) and k_B the Boltzman constant. They are never explicitly written in equations. So, energy, momentum and mass share the same dimension, and the unit is given in electron volts eV [1], or more usually, GeV ($1\ GeV = 10^9\ eV$) and TeV ($1\ TeV = 10^{12}\ eV$), while length and time share the inversed dimension and the unit is given by eV^{-1}.

In accelerator physics, the luminosity (L) is one of the most important parameters. It is the measurement of the number of collisions produced every second in each square centimeter. Then, the integral of the luminosity over time derives the integrated luminosity. Usually, the integrated luminosity is reported with the unit of

[1] One Electronvolt (eV) is the amount of energy gained by a single electron moved across an electric potential difference of one volt, approximately equal to 1.6×10^{-19} Joule.

the inverse femtobarn (fb^{-1}) or inverse nanobarn (nb^{-1}), whose dimension is defined as the inverse of the cross section. In this case, we are able to calculate directly the number of the produced events for a given process by multiplying the integrated luminosity by its cross section.

Another important parameter to be introduced is the center-of-mass energy referring to the energy of the two incoming particles in the rest frame of the center-of-mass. Generally in the collision of two particles with an energy $E_{1,2}$ and a momentum $\vec{p}_{1,2}$, the total center-of-mass energy can be expressed in the Lorentz-invariant form as:

$$E_{center-of-mass} = \sqrt{(E_1 + E_2)^2 - (\vec{p}_1 + \vec{p}_2)^2} \tag{4.2}$$

which leads to $E_{center-of-mass} = 2E$ in the case of the LHC where $E = E_1 = E_2$ and $\vec{p}_1 + \vec{p}_2 = 0$. The LHC is designed with the center-of-mass energy of $14TeV$, which means each particle has an energy of $7TeV$.

The kinematic variables are relevant to the coordinate system that provide the position information, which will be introduced in the following. The cylindrical coordinate system is adopted by ATLAS as a result of the symmetry of the detector itself, which is a right-handed coordinate system with the x-axis pointing towards the center of the LHC tunnel, and the z-axis along the tunnel. From the Figure 4-1, which shows the whole coordinate system, it is easy to tell that the azimuthal angle ϕ ($\tan\phi = p_y/p_x$, where $p_{x,y}$ are the projections of momentum p on x-axis and y-axis) is measured in the x-y plane. ϕ increases from x-axis counterclockwise when looking at x-y plane from the positive z-axis. The polar angle θ is measured from the positive z-axis.

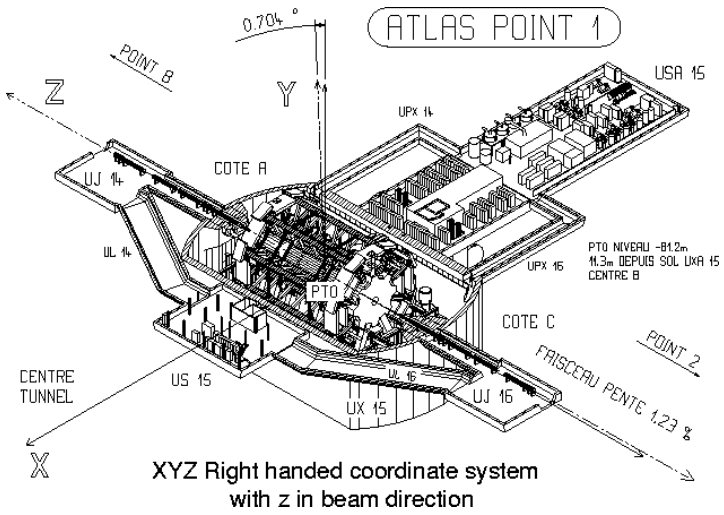

Figure 4-1: ATLAS coordinate system.

Regarding to the coordinate system in ATLAS, pseudorapidity is used, defined as $\eta = -ln(tan(\frac{\theta}{2}))$, which actually is derived from the rapidity $y = \frac{1}{2}ln[\frac{E+p_z}{E-p_z}]$ when the mass is negligible or the energy is high (the usual case of the LHC). Furthermore, the distance ΔR in the pseudorapidity-azimuthal angle space is defined as

$\Delta R = \sqrt{\Delta\eta^2 + \Delta\phi^2}$. The transverse impact parameter d_0 is defined as the transverse distance from the beam axis (z-axis) to the point of closest approach and its sign is determined by the reconstructed angular momentum of the track with respect to the beam axis.

More variables concerning energy and momentum are introduced in the following. The transverse momentum p_T and the transverse energy E_T, as well as the missing transverse energy E_T^{miss} and other transverse variables, are defined in the x-y plane in the same way of $X_T = X \cdot sin\theta$. The invariant mass is defined as, for example, $m_t = \sum_{i=e,\nu_e,b} P_i^\mu P_{i\mu}$, calculated for the invariant mass of top quark decaying into a b quark and a W boson that decays into an electron e and an electron neutrino ν_e, with their four momentum $P^\mu = (E, \vec{p})$.

4.2 The LHC

The Large Hadron Collider (LHC) is a proton-proton collider with a center-of-mass energy of 14 TeV [2], 27 km long, built in the previous LEP (Large Electron Positron Collider) collider tunnel by the European Organization for Nuclear Research (CERN) [3] from 1998 to 2008 for the researches on particle physics and other new physics.

Back to the early 1980s, the idea of the LHC had been already proposed, which is even earlier than the construction of LEP. In December 1994, the CERN Council finally approved the construction of the LHC. After years of efforts and the incident happened at first start in 2008 due to a faulty electrical connection in magnets, the LHC finally started to produce stable collisions at the center of mass energy of 900 GeV and 2.36 TeV in the end of 2009. Afterwards, the LHC successfully delivered 5.6 fb^{-1} data at the center of mass energy of 7 TeV in 2010 and 2011. Now, the LHC has 23.3 fb^{-1} data at the center of mass energy of 8 TeV in 2012 and started a long shutdown for more than two years, and is expected to run at 14 TeV in 2015.

At the LHC, there are two parallel proton beam lines circled in the collider tunnel, travelling around the circular ring path in opposite directions kept by 1232 dipole magnets and focused by the other 392 quadrupole magnets, colliding at four high luminosity intersection points.

4.2.1 The accelerator complex

Given the fact that it is impossible to produce such a high-energy proton beam with one simple acceleration, thus a set of accelerators was designed. The accelerator complex for the LHC is composed by a succession of machines, each of which accelerates particles to a higher energy than the previous one. In the view of this accelerator chain, the LHC is the last component, in which each proton particle beam are

[2]The LHC is also a Pb-Pb collider with a designed center-of-mass energy of 5.5 TeV.

[3]CERN originally from "Conseil Européen pour la Recherche Nucléaire", stands for "Organisation européenne pour la recherche nucléaire" now. It is is an international organization located in the northwest suburbs of Geneva whose purpose is to operate the world's largest particle physics laboratory.

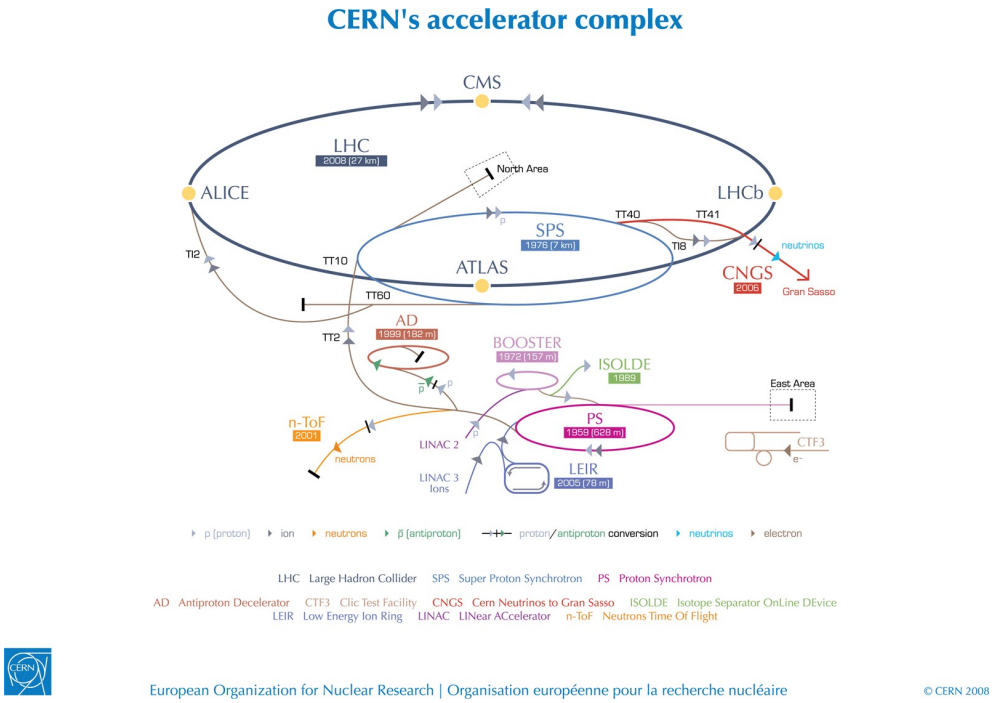

Figure 4-2: The accelerator complex at CERN

accelerated up to the energy of 4 TeV in 2012.

In Figure 4-2, the accelerator complex is described. In the beginning, protons are stripped from hydrogen atoms from a bottle of hydrogen gas. Right after this, they are sent into a linear accelerator (Linac2), which is the first accelerator in the chain, to make the protons reach the energy of 50 MeV, followed by the Proton Synchrotron Booster (PSB) that boosts the proton beam to 1.4 GeV. Protons are then injected to the Proton Synchotron (PS) to increase to the energy of 25 GeV, after which the Super Proton Synchotron (SPS) accelerate the proton beam to 450 GeV. The protons then are transferred to two beam lines travelling from different directions in the LHC ring. It takes around 20 minutes to reach the highest energy for collisions.

Besides the accelerators in this chain serving the experiments at the LHC, most of the other accelerators are designed for their own experiments at lower energy, such as the Antiproton Decelerator, the Online Isotope Mass Separator (ISOLDE) facility, and the neutron time-of-flight facility (nTOF).

In terms of the other particle operated in the LHC, the lead ion, comes from vaporized lead and enters a linear accelerator (Linac3) before being accelerated in the Low Energy Ion Ring (LEIR), followed by the same route as the protons.

4.2.2 The seven experiments

There are four high luminosity intersection points which stands for the four main experiments at the LHC. In fact, there are also three other experiments at the LHC, two of which were constructed years ago, while the third one is still under construction.

Starting with the two biggest experiments at the LHC, ATLAS (A Toroidal LHC

ApparatuS) [88] and CMS (Compact Muon Solenoid) [89] are the only two large general-purpose particle detectors at the LHC, designed with general purposes to investigate a large range of physics including the search for the origin of the mass, extra dimensions, supersymmetry and candidate particles for dark matter. They are independently designed and realized in order to be able to crosscheck the results on the same physics subjects. Briefly speaking, comparing to ATLAS, CMS is more compact (25 m long, 15 m in diameter), weighing about 12500 tons, with a stronger magnetic field of 4 T covering inner detector, electromagnetic and hadronic calorimeter. The ATLAS detector is introduced in details in Section 4.3.

Talking about the two medium-size experiments, ALICE (A Large Ion Collider experiment) [90] and LHCb (Large Hadron Collider beauty) [91] are designed for special physics purposes. ALICE aims at studies of heavy ion collisions from Pb-Pb nuclei collisions at a centre of mass energy of 2.76 TeV per nucleus. The heavy ion collisions could result in a high temperature and high energy density environment, which are expected to generate Quark-Gluon Plasma (QGP) that is believed to have existed soon after the Big Bang. The detector of ALICE is 26 m long, 16 m high and wide. It is designed with an asymmetric structure with a central barrel and a muon spectrometer in one forward direction instead of a symmetric two direction like in ATLAS and CMS. The LHCb is designed to study b hadrons to explain the matter-antimatter asymmetry of the universe. Additionally, LHCb detector can also measure some production cross-sections and electroweak physics in the forward region. From the site of detector size parameters, LHCb is even smaller than ALICE with 21 m in length, 10 m in height and 13 m in width. Similar to ALICE, LHCb is also designed in one forward region asymmetrically determined by its physics goals.

As mentioned at the beginning of this section, there are three more experiments, TOTEM (TOTal Elastic and diffractive cross section Measurement) [92], LHCf (Large Hadron Collider forward) [93] and MoEDAL (Monopole and Exotics Detector At the LHC) [94]. TOTEM and LHCf are designed for physics studies in the forward region at the LHC wherein the other experiments are not able to reach. TOTEM is able to detect particles very close to the beam pipe, and aims at measuring the total cross section, elastic scattering and diffraction dissociation of the collisions at the LHC. LHCf is designed to measure the number and the energy of neutral pions produced in the forward direction, and help to interpret and calibrate the cosmic ray background for the other detectors at the LHC. Apart from the six detectors mentioned above, a new detector called MoEDAL (Monopole and Exotics Detector At the LHC) [94] has been approved in May 2010 mainly for studies on new physics beyond the Standard Model. Its primary goal is to directly search for hypothetical particles, such the Magnetic Monopole and the Dyon. In the meanwhile it also targets on seeking other highly ionizing Stable Massive Particles, or pseudo-stable ones, with an array of plastic nuclear track detectors.

4.3 The ATLAS detector

The ATLAS (A Toroidal LHC ApparatuS) detector [88] is designed with general purposes. It is 46 m long, 25 m high and 25 m wide, installed 100 m underground close to the CERN main entrance. The subdetectors are designed symmetrically in the forward and backward direction. From the most inside to the most outside, the subdetectors are installed layer by layer including the inner detector, the electromagnetic calorimeter, the hadronic calorimeter and the muon spectrometer. The magnet system makes up the whole skeleton. The solenoid magnet system covers the inner detector with a magnetic field of $\sim 2\ T$, while the toroidal magnet system covers the muon spectrometer with a magnetic field of $\sim 0.5\ T$ in the barrel and $\sim 1.0\ T$ in the end-cap, leaving the calorimeters in the gap of the magnetic field.

An overview of the components in each subdetector is shown in Figure 4-3. Closest to the beam line, the inner detector consists of a pixel detector, a semiconductor tracker, and a transition radiation tracker. It provides precise measurements of the collision point (the primary vertex) and efficient tracking information of charged particles, causing as few energy loss as possible from them. Beyond the cover of the solenoid magnet, the electromagnetic calorimeter provides good energy measurements by stopping most of the electrons and photons with their energy deposited in the calorimeter cells in the form of electromagnetic showers. The hadronic calorimeter provides good energy measurements for hadrons by partially absorbing their energy in the nuclear reactions. In the most outside part, the muon spectrometer consists of four types of muon chambers that can provide either trigger information or tracking information with the help of the toroidal magnet system.

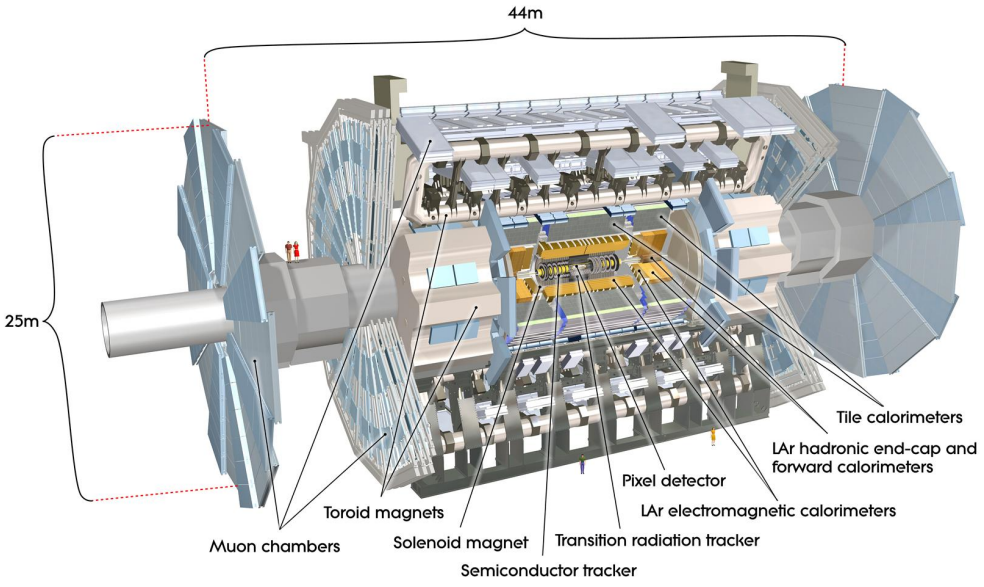

Figure 4-3: The overview of the ATLAS detector

4.4 Magnet system

The magnet system provides powerful magnetic fields to bend charged particles for momentum measurements by using a solenoid magnet system serving the inner detector and a toroidal magnet system serving the muon spectrometer in both the barrel and the end-cap. It extends 26 m in the length and 20 m in the diameter. NbTi/Cu/Aluminium are used for the magnetic superconductors.

The solenoid magnet, shown as a barrel around the beam in Figure 4-4, has a length of 5.3 m with a bore of 2.4 m, containing a total energy of 40 MJ and providing a central field of 2 T parallel to beam axis and a peak magnetic field of 2.6 T at the superconductor itself. The system can be cooled down to the operating temperature of 4.5 K by cold helium in one day and the coil can be charged and discharged in about 30 minutes. To minimize the energy deposit in dead materials before calorimeters, the solenoid magnet is designed as thin as possible without sacrifying the operational safety and reliability and shares the same vacuum vessel with the LAr electromagnetic calorimeter to be introduced later on. The solenoid magnet contributes around 0.66 radiation lengths.

The toroidal magnet system, designed in doughnut-shapes surrounding the beam outside of the solenoid as shown in Figure 4-4, consists of the barrel toroid and the end-cap toroid. It is 25.3 m in length, with inner and outer diameters of 9.4 m and 20.1 m, respectively, containing a total energy of 1.58 GJ. The light and open structure of the design is to minimize the multiple scattering effects that could degrade the muon identification performance and the momentum resolution. The barrel toroid consists of 8 large air-core toroids generating the magnetic field with the peak value at 3.9 T for the muon spectrometer covering the pseudorapidity range from 0 to 1.3. Two end-cap toroids are installed in both ends of the barrel toroid, providing a magnetic field with the peak value at 4.1 T covering the pseudorapidity range from 1.6 to 2.7.

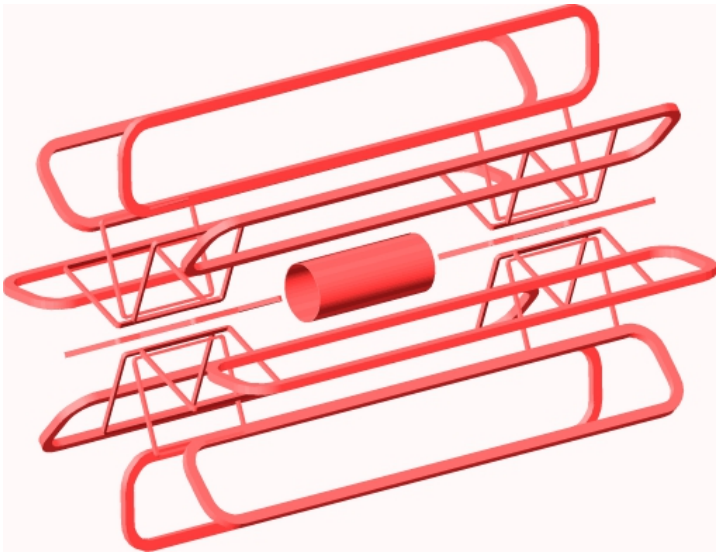

Figure 4-4: The overview of ATLAS magnet system skeleton removing all subdetectors

4.5 Inner detector

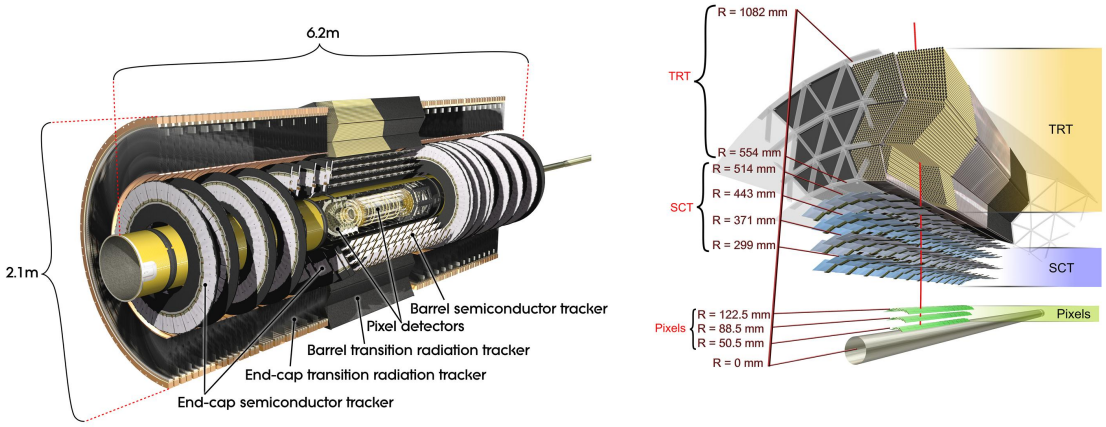

(a) (b)

Figure 4-5: (a) the ATLAS Inner Detector (ID) overview. (b) the ATLAS Inner Detector (ID) cross section view at barrel.

The ATLAS Inner Detector (ID) is designed for track reconstructions of charged particles and the measurements of vertices (primary and secondary) [4]. Being the first subdetector that particles pass through after collisions, it is installed as close as possible to the beam line. It is made of high-resolution sensors at the inner radii with continuous tracking elements at the outer radii all contained in a 2 T magnetic field provided by the central solenoid magnet system.

The layout of the inner detector is shown in Figure 4-5(a). It consists of high granularity semi-conductor pixel detector closest to the vertices, a semiconductor tracker (silicon microstrip detector), and a transition radiation straw tube tracker in the most outside part. The total number of precision layers is limited with respect to the dead materials they introduce and their expensive cost. Typically, three pixel layers and eight strip layers (four space points) are crossed by each track. Then a large number of tracking points (typically 36 per track) is provided by the straw tube tracker in the outer space, which provides continuous tracking information with much less materials per point and a lower cost. The inner detector extends with the radius of 1.15 m, the length of 7 m. Figure 4-6 gives an overview of the η-coverage of the subdetectors in the inner detector. The overall coverage extends to the edge of the end-cap semiconductor tracker where $|\eta| = 2.5$.

[4]The primary vertex refers to the collision point. The second vertex is usually due to long-life unstable particles that do not decay until flying for a while away from the primary vertex, such as B hadrons.

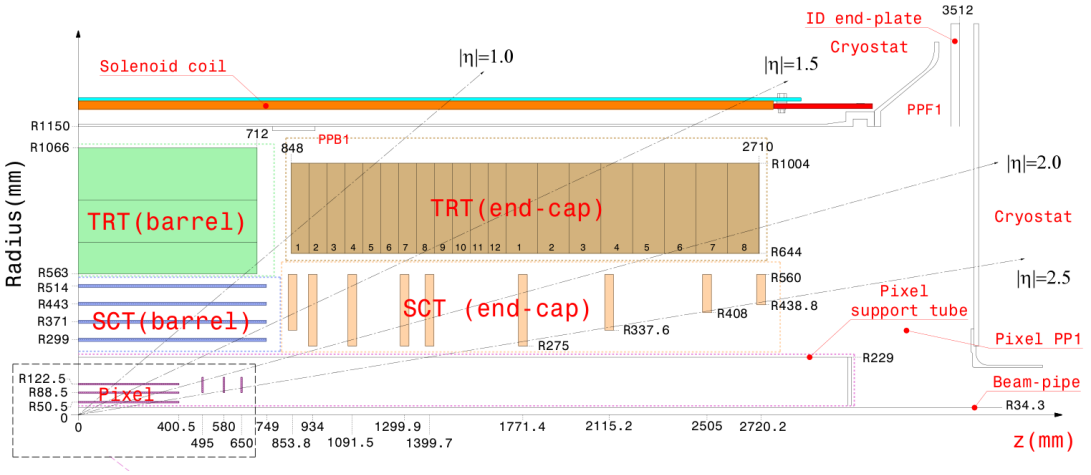

Figure 4-6: The η-coverage of inner subdetectors

4.5.1 Inner subdetectors

The Pixel Detector (PS) is designed for very precise measurements close to the interaction points. It is constructed in three layers of modules all with two-dimensional position measurements, as shown in Figure 4-5(b), providing three precision measurements over the full acceptance. A module is a rectangular active device approximately 6 cm by 2 cm with 46080 pixels, each 50 μm in azimuth by 400 μm along the beam. There are 1456 modules in barrel and 288 modules in end-caps, leading to over 80 million readout channels in total, which are about 50% of the total readout channels of the whole experiment.

The Semi-Conductor Tracker (SCT) is designed to provide eight precision measurements per track in the intermediate radial range, contributing to the measurement of momentum, impact parameter and vertex position. It has good pattern recognition thanks to the use of high granularity. The barrel SCT uses eight layers of silicon microstrip detectors to provide precision points in the $R\phi$ as well as z coordinates by using small angle stereo in each module.

The Transition Radiation Tracker (TRT) uses the straw detector, which is able to operate at the very high rates expected at the LHC thanks to their small diameters and the isolation of the sense wires within the individual gas volumes. In the straw tubes, Xenon gas is used to detect the transition-radiation photons created by electrons passing the radiator between the straws. It allows to enhance electron identification from π mesons as shown in Figure 4-7, where electrons tend to have more energy deposit than π mesons in TRT. It also provides a substantial discriminating power between electrons and other charged hadrons over a wide energy range (between 0.5 GeV and 100 GeV) via the detection of X-rays produced by transition radiation. TRT works with a non-flammable gas mixture of 70% Xe, 27% CO_2 and 3% O_2 at room temperature compared to the pixel detector and the semi-conductor tracker which work at $-25°C$.

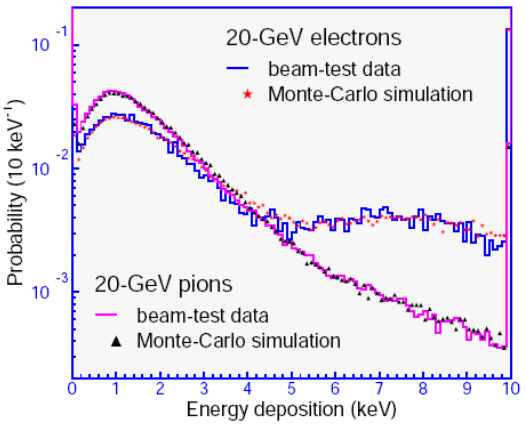

Figure 4-7: Energy deposit in TRT that enhances the separation between electrons and π mesons

4.5.2 Tracking and vertexing performance

Charged particle tracks with transverse momentum $p_T > 0.5\ GeV$ and $|\eta| < 2.5$ are reconstructed and measured in the inner detector with the solenoid field. The limitation on p_T is due to the dead materials in ID, which can wear out or deflect heavily the low p_T tracks, while the limitation on η coverage is only from the hardware geometry. To reconstruct tracks, one needs to start with seeds for tracking which are created from the pixel detector and the first layer of the semi-conductor tracker. Then seed tracks are extended out to the whole semi-conductor tracker and transition radiation tracker. After fitting, fake tracks are rejected and selected tracks are kept to be combined with either calorimeters or muon spectrometer later on.

The performance of the tracking is checked both from the kinematic resolutions such as p_T resolution and from the efficiencies of the reconstructed tracks. Here, as an example, the track efficiencies are studied with simulations [95]. On the left of Figure 4-8, the efficiencies as a function of $|\eta|$ are shown for reconstructing muons, pions and electrons with $p_T = 5\ GeV$. In addition to multiple-scattering shared by all three kinds of particles tested, pions are affected by hadronic interactions from the inner detector materials, while electrons suffer from even larger reconstruction inefficiencies due to the bremsstrahlung effect. The very low efficiencies in $1.5 < |\eta| < 2.5$ are fully correlated to the materials of the inner detector in this $|\eta|$ range. On the right of Figure 4-8, the efficiencies as a function of $|\eta|$ are shown for reconstructed pion tracks with p_T varying from 1 to 100 GeV. This efficiency curve can tell that the efficiency becomes larger and more uniform as a function of $|\eta|$ at higher energies.

Vertex recontruction is another important function of the inner detector. It needs to be fast and robust considering the large multiplicity of tracks at each bunch crossing (about 200 charged tracks under the designed luminosity). The tracks to be used in the vertex reconstruction usually need to fulfill some criteria on quality, such as $p_T > 1\ GeV$, $|d_0| < 0.25\ mm$, $|z_0| < 150\ mm$ and $\chi^2 < 0.5$ (from the track reconstruction) in order to select a track closer to the collision point with a momentum above the

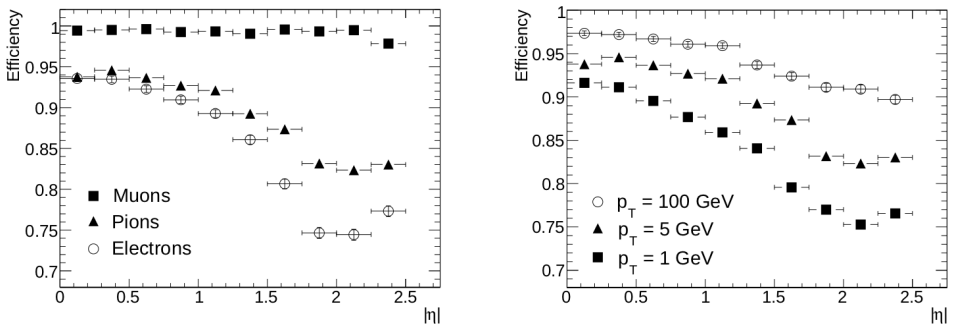

Figure 4-8: The track efficiencies of the inner detector. On the left, track reconstruction efficiencies as a function of $|\eta|$ for muons, pions and electrons with $p_T = 5\ GeV$. The inefficiencies for pions and electrons reflect the shape of the amount of material in the inner detector as a function of $|\eta|$. On the right, Track reconstruction efficiencies as a function of $|\eta|$ for pions with $p_T = 1$, 5 and 100 GeV.

safe threshold in tracking and a better reconstruction. The performance of vertexing is studied with simulations [96] and summarized in Table 4.1. The table shows the vertexing resolution in 3 dimensions (σ_x, σ_y, σ_z) and the average numbers of tracks for various simulated samples. Tracks are counted in three ways: "all" stands for the average number of all tracks; "good" stands for the average number of tracks that pass the quality cuts to be allowed as the fitting inputs; "fit" stands for the average number of tracks that are eventually used in the vertex fit. One can see that the precision of the vertex position depends mainly on the number of tracks successfully fitted. So the sample $H \to b\bar{b}$ with the largest track multiplicity used in the fit gives the best spacial resolution of vertexing.

Sample	Tracks (all/good/fit)	$\sigma_x(\mu m)$	$\sigma_y(\mu m)$	$\sigma_z(\mu m)$
Single min.bias	15.8/10.8/10.2	47	48	70
$H \to \gamma\gamma$ ($m_H = 100\ GeV$)	26.0/17.1/15.9	26	26	44
$H \to b\bar{b}$ ($m_H = 400\ GeV$)	60.2/43.3/35.8	10	11	24
$B \to J/\Psi K$	31.6/22.0/17.9	29	27	44
$B_S \to D_S\pi$	31.6/22.8/17.8	29	29	47

Table 4.1: Summary of primary vertex finding results on various simulated samples [96]. Tracks are counted in three ways: "all" stands for the average number of all tracks; "good" stands for the average number of tracks that pass the quality cuts to be allowed as the fitting inputs; "fit" stands for the average number of tracks that are eventually used in the vertex fit. The vertexing resolution is given in 3 dimensions (σ_x, σ_y, σ_z).

4.6 Calorimeters

Calorimeters are able to provide the measurement of the energy of charged and neutral particles, as well as the information of position and angle. When particles (like electrons or photons) enter calorimeters, they initiate showers which consume their energies. Calorimeters collect the energy deposit and count it as the whole or part of the energy of the particles. The ATLAS calorimetry consists of an electromagnetic (EM) calorimeter covering the pseudorapidity region $|\eta| < 3.2$, a hadronic barrel calorimeter covering $|\eta| < 1.7$, hadronic end-cap calorimeters covering $1.5 < |\eta| < 3.2$, and forward calorimeters covering $3.1 < |\eta| < 4.9$. The region $1.37 < |\eta| < 1.52$ is not used for precision physics measurements because of the large amount of dead materials situated in front of the EM calorimeter.

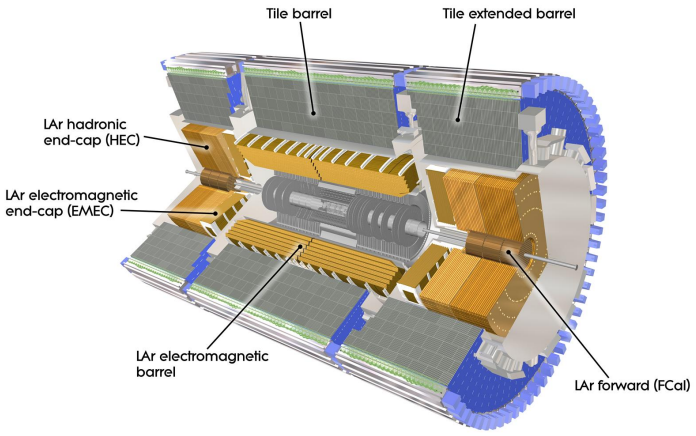

Figure 4-9: The ATLAS calorimeter

4.6.1 Electromagnetic calorimeter

The electromagnetic calorimeter adopts an accordion structure for both lead absorbers and electrodes shown in Figure 4-11(a) with the function of measuring the energy of the particles such as electrons and photons that have electromagnetic showers in the calorimeter. The structure is chosen to ensure azimuthal uniformity avoiding cracks. The gaps between electrodes and absorbers are filled with liquid Argon (LAr) due to its radiation hardness and reaction speed. The total thickness of the electromagnetic calorimeter is larger than 24 radiation lengths X_0 [5] in the barrel and larger than 26 X_0 in the end-caps. The number of radiation length X_0 as a function of $|\eta|$ are shown for electromagnetic calorimeter materials in Figure 4-10. Layer 2 (middle layer, defined below) contributes dominantly in central region and Layer 1 (front layer, defined below) contributes mainly in forward region.

[5]High energy electrons predominantly lose energy in matter by bremsstrahlung. The radiation length of a specific material correponds to the mean distance over which a high-energy electron loses all but $\frac{1}{e}$ of its energy by bremsstrahlung in this material.

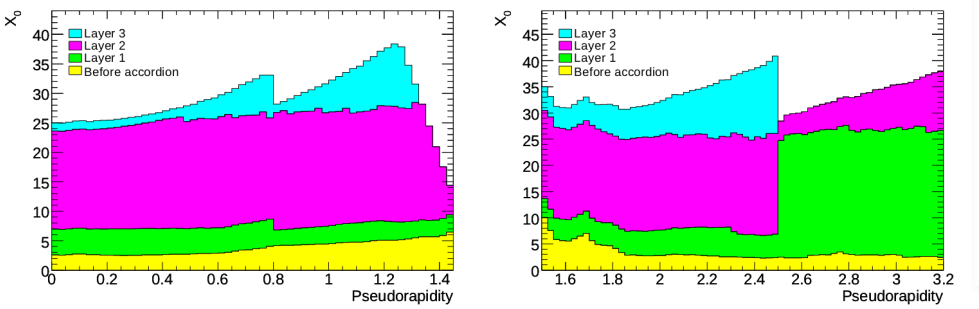

Figure 4-10: The amount of materials in front of the accordion electromagnetic calorimeter in the number of radiation length X_0 as a function of $|\eta|$ [95].

The electromagnetic calorimeter is designed with three sampling segmentations longitudinally as shown in Figure 4-11(b). Sampling 1 (front layer), with fine strip towers, of size $\Delta\eta \times \Delta\phi = 0.003 \times 0.100$, plays a role of presampler with a thickness of around 6 X_0, enhancing particle identification (γ/π^0 separation) and providing a precise position measurement in η. Sampling 2 (middle layer), with square towers, of size $\Delta\eta \times \Delta\phi = 0.025 \times 0.025$, collects main energy deposit with a thickness of around 24 X_0. Sampling 3 (back layer), with rectangle towers, of size $\Delta\eta \times \Delta\phi = 0.050 \times 0.025$, is used as trigger towers and helps to separate hadronic and electromagnetic showers. Additionally, a presampler is installed before the electromagnetic calorimeter along the way by which particles flying out, with the function of correcting for energy losses in the dead materials upstream of calorimeter. This is achieved by measuring the multiplicity of a particle shower that develops due to the interactions with the dead materials upstream.

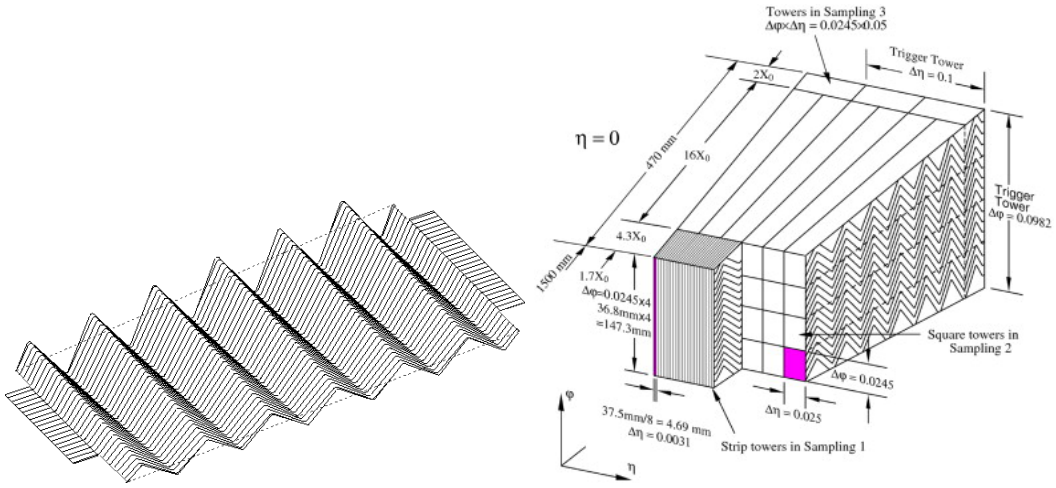

(a) (b)

Figure 4-11: (a) The accordion shape structure used in the ATLAS electromagnetic calorimeter, (b) the inner structure of the ATLAS electromagnetic calorimeter.

4.6.2 Hadronic calorimeters

Hadronic calorimeters includes the tile calorimeter, the liquid-Argon hadronic end-cap calorimeter (HEC) and the liquid-argon forward calorimeter (FCal) as shown in Figure 4-9. The tile calorimeter utilizes iron scintillating-tile technique in the barrel and in the extended barrel within the coverage of $|\eta| < 1.7$, while the hadronic end-cap calorimeter utilizes the liquid Argon technique in the hadronic end-cap calorimeter extending to $|\eta| < 3.2$ and the forward calorimeter also utilizes the liquid Argon at $3.1 < |\eta| < 4.9$. The hadronic end-cap calorimeter consists of two wheels in each end-cap cryostat: a front wheel (HEC1) and a rear wheel (HEC2), each wheel containing two longitudinal sections. Each forward calorimeter is split into three 45 cm deep modules: one electromagnetic module (FCal1) and two hadronic modules (FCal2 and FCal3). The hadronic end-cap calorimeter shares each of the end-cap cryostats with the electromagnetic end-cap (EMEC) and the forward calorimeter to avoid too many dead material.

Hadronic calorimeters cover the most largest range $|\eta| < 4.9$ of the ATLAS detector, and provide very good energy resolution of jets with the optimised thickness as well as good performance for missing transverse energy thanks to the large η-coverage.

4.6.3 Calorimeter performance

Exposed to test-beams, 4 out of 32 barrel and 3 out of 16 end-cap production modules of the electromagnetic calorimeter have been tested. Electrons and positrons of energies between 1 and 250 GeV from CERN SPS H8 and H6 beam lines have been used for the tests [97, 98, 99].

The uncertainty of the measured energy in the electromagnetic calorimeter is factorized as [99]:

$$\frac{\sigma(E)}{E} = \frac{a}{\sqrt{E(GeV)}} \oplus b \tag{4.3}$$

where a is the stochastic term and b is the constant term reflecting local non-uniformities in the response of the calorimeter. Various test bave been performed to extract the two parameters with different beam energy. As an example, the response uniformity at high energy as a function of η has been measured using an electron beam of 245 GeV for the barrel and of 119 GeV for the end-cap [97]. Figure 4-12 shows that non-uniformities of the response on the tested modules do not exceed 0.43% for the barrel modules and 0.62% for the end-cap modules. Therefore, the EM calorimeter performance on non-uniformity fulfills the original ATLAS goal of achieving a constant term of 0.7 % or smaller over the full calorimeter acceptance.

Many beam-tests as well as the simulation-tests were done for the tiles calorimeters in barrels, the hadronic end-cap calorimeter and the forward calorimeter [100, 101, 102, 103, 104, 105]. For example, the two forward calorimeters are tested with electron and pion beams with momenta from 10 to 200 GeV at the CERN SPS [104, 105], whose results are shown in Figure 4-13. The energy resolution depends on the technique used to correct the reconstructed energies from the electromagnetic scale to the hadronic scale. Two techniques were studied. The first one uses a linear combina-

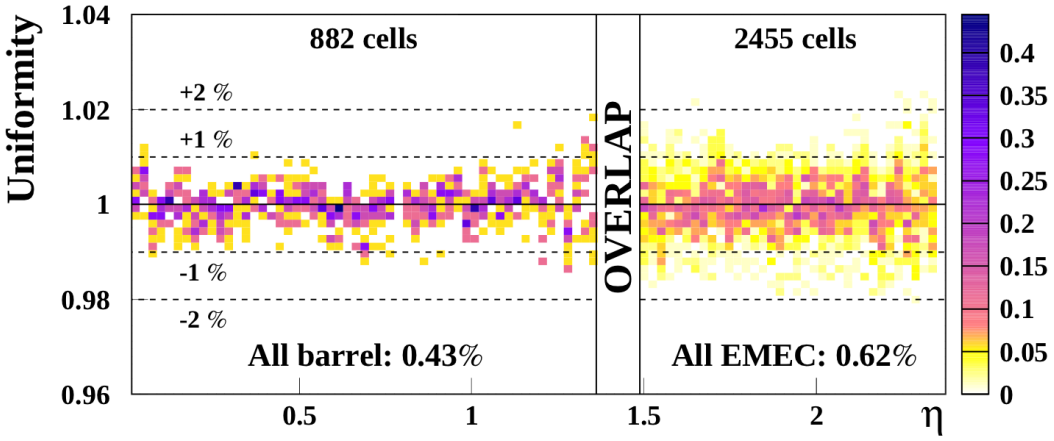

Figure 4-12: Distribution of the average energies measured in all cells of all tested modules as a function of the cell $|\eta|$, normalised to the mean energy measured in the modules. In the barrel, this mean energy was $\sim 245\ GeV$, while it was $\sim 120\ GeV$ in the electromagnetic end-cap. For each bin in η, the distribution is normalised to the number of middle cells in that bin (design value). This normalisation is only used to define the colour of each bin in the plot [95].

tion of the single weight (flat weights) for each module of the forward calorimeter as introduced in Section 4.6.2. The reconstructed energy with flat weights is calculated with:

$$E_{reco} = g_1 E_{FCAL1} + g_2 E_{FCAL2} + g_3 E_{FCAL3} \tag{4.4}$$

where $g_{1,2,3}$ are the fitted weights for the modules FCAL1, FCAL2 and FCAL3. The second technique uses radial weights. It sums up the weights of all instrumented cells according to the transverse distance from the beam impact point (taken from the tracking system) to each cell. Figure 4-13 shows the fractional energy resolution as a function of the beam energy obtained by the two techniques. Fitting to the general model for the energy resolution in Equation 4.3, one can extract the stochastic and constant terms of $(94.2 \pm 1.6)\ \%\sqrt{GeV}$ and (7.5 ± 0.4) with flat weights, respectively, while one can improve the stochastic term from 94 % to 70 % and the constant term from 7.5 % to 3.0 % with radial weights. The resolutions obtained with flat weights meet well the design specifications, which were expressed as stochastic and constant terms of 100% and 10% respectively for hadrons, and the resolutions obtained with radius weights are even better.

4.7 Muon spectrometer

The muon spectrometer is built in the most outer part of the detector, since muons can usually go through all calorimeter absorbers without being stopped. The spectrometer consists of four kinds of chambers: monitored drift-tube chambers, cathode strip chambers, resistive plate chambers and thin gap chambers, as shown in Figure 4-14.

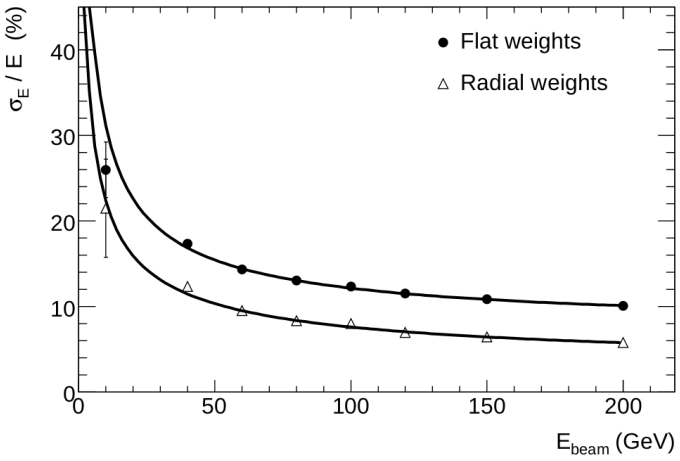

Figure 4-13: Fractional energy resolution obtained for pions, measured in all three modules of the forward calorimeter, as a function of the beam energy E_{beam} [104, 105]. The data are shown for two cell-weighting schemes and the curves correspond to the result of a fit to the data points using Equation 4.3.

4.7.1 Muon chambers

Monitored drift-tube chambers (MDT) are made of aluminium tubes of 30 mm diameter and 400 μm wall thickness, with a 50 μm diameter central W-Re wire. The tubes are filled with a non-flammable mixture of 93% Ar and 7% CO_2. Monitored drift-tube chambers cover the pseudorapidity range $|\eta| < 2.7$ (except in the innermost end-cap layer where their coverage is limited to $|\eta| < 2.0$). They provide precise spacial information and momentum measurements in both barrel and end-caps thanks to their small Lorentz angle, which makes themselves almost immune to magnetic fields. The maximum drifting time is around 700 ns.

Cathode strip chambers (CSC) are made of multiwire proportional chambers with cathode strip readouts and with a symmetric cell in which the anode-cathode spacing is equal to the anode wire pitch. The chambers are filled with a non-flammable mixture of 30% Ar, 50% CO_2 and 20% CF_4. They are able to provide precise two-dimensional coordinates of charged particles due to the fine segmented cathodes. Nevertheless, the spatial resolution of the CSCs is sensitive to the inclination of tracks and to the Lorentz angle. So, to minimise degradations of the resolution due to these effects, they are only installed in a tilted position in the end-caps before the toroidal magnets covering a forward region of $2 < |\eta| < 2.7$, such that tracks originating from the interaction point are normal to the chambers.

Resistive plate chambers (RPC) are made of chambers formed by two parallel resistive bakelite plates, separated by insulating gas, which is a mixture of 94.7% $C_2H_2F_4$, 5% Iso-C_4H_{10} and 0.3% SF_6. The chambers are installed in the barrel region of $|\eta| < 1.05$. They provide excellent time resolution of around 1 ns, which allows to be used as a fast trigger.

Thin gap chambers (TGC) are similar to multiwire proportional chambers with

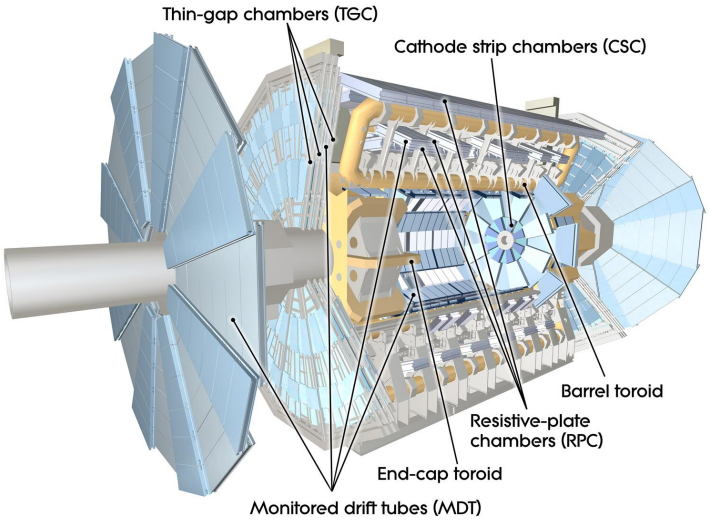

Figure 4-14: The ATLAS muon spectrometer

the difference that the anode wire pitch is larger than the anode-cathode distance. The chambers are installed in the end-cap between $1.05 < |\eta| < 2.4$. They provide a trigger function as well as the determination of the second azimuthal coordinate to complement the measurement of the monitored drift-tube chambers in the bending (radial) direction.

In summary, the tracking information is provided by monitored drift-tube chambers and cathode strip chambers, while the trigger information is provided by resistive plate chambers and thin gap chambers with the ability to identify the bunch crossing thanks to an excellent time resolution covering $|\eta| < 2.4$.

4.7.2 Muon spectrometer performance

The performance of the muon spectrometer can be quantified by the momentum resolution, the efficiency and the misidentification or fake rate. As an example, the expected transverse momentum resolution is discussed here as shown in Figure 4-15 [95].

On the left of Figure 4-15, the expected transverse momentum resolution as a function of $|\eta|$ is shown for muons with $p_T = 100\ GeV$ from both stand-alone and combined reconstructions (discussed in Section 5.2). In general, the resolution is around 3% except in the region of $1.1 < |\eta| < 1.7$ due to several effects described in the following. In region $1.1 < |\eta| < 1.3$, the degradation is due to the absence of the middle muon stations in the barrel/end-cap transition region for the initial data-taking. At larger values of $|\eta|$, the degradation is due to the combination of the low bending power of the magnetic field in the transition region between the barrel and end-cap toroids and of the large amount of material in the coils of the end-cap toroid in limited regions in ϕ. The contribution of the inner detector to the combined resolution is therefore more important in this η-region. In the barrel, the contribution of the inner detector remains significant, whereas it basically vanishes

for $|\eta| > 2.0$. This is due to the intrinsically worse momentum resolution in the inner detector because of the absence of any transition radiation tracker measurements in this η-region, of the solenoidal field non-uniformity, and of the shorter length of the tracks in the inner-detector magnetic volume.

On the right of Figure 4-15, the expected transverse momentum resolution as a function of ϕ is shown for muons with $p_T = 100\ GeV$ and $0.3 < |\eta| < 0.65$ from both stand-alone and combined reconstructions. The resolution is degraded at $\phi = 240°$ and $300°$, due to the additional material introduced by the feet which support the barrel part of the detector.

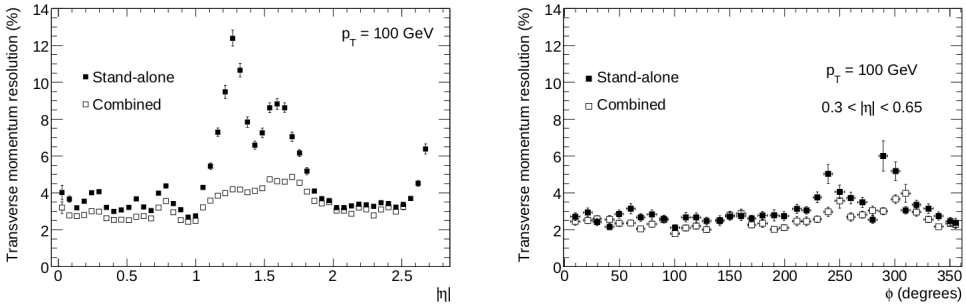

Figure 4-15: Expected transverse momentum resolutions. On the left, the expected transverse momentum resolution as a function of $|\eta|$ is shown for muons with $p_T = 100\ GeV$ from both stand-alone and combined reconstructions. On the right, the expected transverse momentum resolution as a function of ϕ is shown for muons with $p_T = 100\ GeV$ from both stand-alone and combined reconstructions.

4.8 Forward detectors

Complementary to the detectors in the barrel and end-caps presented above, there are three more detectors built for ATLAS to provide a good coverage in the very forward region.

Absolute Luminosity For ATLAS (ALFA) is a tracker system installed above and below the LHC beam axis at a distance of 240 m away from the interaction point at ATLAS as shown in Figure 4-16. It measures the trajectories of elastically scattered protons at very small angles in the limit of the Coulomb Nuclear Interference (CNI) region (around 3.5 μrad) with scintillating fibers to determine the absolute luminosity of the LHC to a precision of 3%.

LUminosity measurement using a Cherenkov Integrating Detector (LUCID) is designed for online instantaneous luminosity monitoring by detecting inelastic pp scattering in the forward direction, and is installed in each end-cap of ATLAS at a distance of approximately ± 17 m from the interaction point, as shown in Figure 4-17(a). It is based on Cherenkov Luminosity Counter with good time resolution to resolve individual beam crossings. In total twenty aluminium tubes are installed surrounding the beam-pipe and point toward the interaction point, providing a Cerenkov

threshold of 2.8 GeV for pions and 10MeV for electrons.

Zero-Degree Calorimeter (ZDC) is a calorimeter at the junction where the two beam pipes of the LHC become one, i.e. at 0° from the *pp* collisions as shown in Figure 4-17(b). It detects forward neutrons and photons with $|\eta| > 8.3$ in both *pp* and heavy-ion collisions. In *pp* collisions, ZDC is able to measure forward production cross sections for several types of particles at very high energies, which is useful for adjusting parameters for simulations and models. In heavy-ion collisions, ZDC plays a key role in determining the centrality of such collisions, which is strongly correlated to the number of very forward (spectator) neutrons.

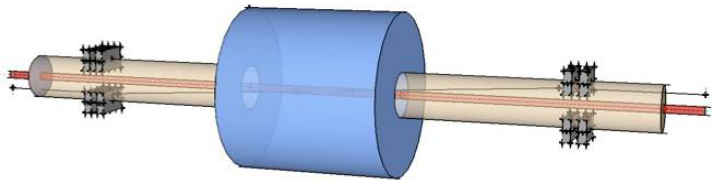

Figure 4-16: Absolute Luminosity For ATLAS (ALFA) installed about 240 m away from ATLAS in the tunnel.

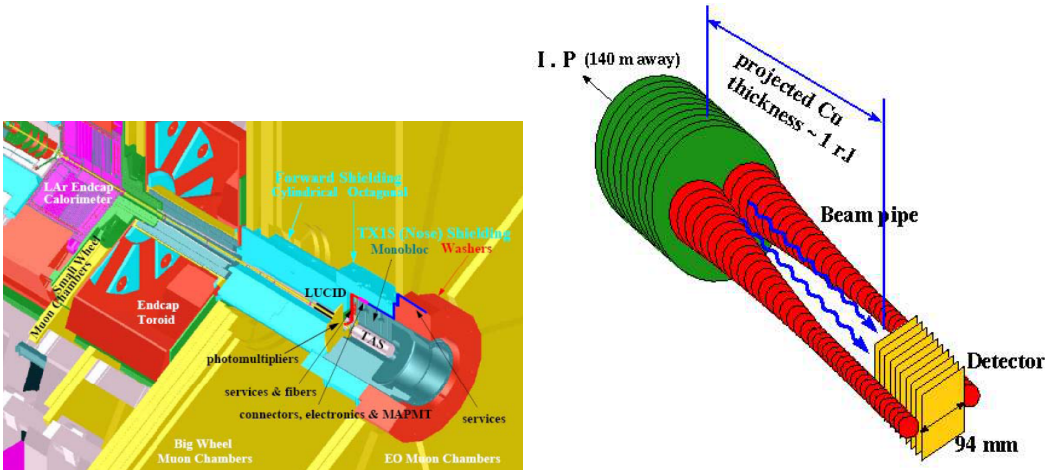

(a) (b)

Figure 4-17: (a) LUminosity measurement using a Cherenkov Integrating Detector (LUCID) at ATLAS, (b) Zero-Degree Calorimeter (ZDC) in the LHC tunnel.

4.9 The trigger system

4.9.1 The motivation for a trigger system

In general, the trigger system provides the ability to select and store on disks the collisions with potentially interesting events from a large amount of collisions that

take place in the collider. It is motivated by the fact that too many collisions are produced per second, while the physical limitations like recording rate and storage do not allow to store all the collisions and usually only a few of them are indeed interesting to physics analyses. At the LHC, the initial bunch-crossing rate is 40 MHz corresponding to one collision per 25 ns, while the output rate is limited at around 100 Hz considering the readout bandwidth and the permanent storage limitation as well as the speed at which the detector reads out with full granularity. This means only one event out of every 10^5 events will be selected, and most of them will be discarded. In this way, the readout system and the storage system can work normally with a reasonable data-taking rate controled by a stringent trigger system.

On the other hand, one cannot remove events only with respect to the physical limits mentioned above, since a wide variety of signatures are interesting according to the general purpose of the ATLAS detector on full physics potential exploration. The trigger system are required to be sensitive enough to keep all rare events demanded by all the physics searches.

The problem of constructing a trigger system then is to find the optimal trigger configuration yielding the lowest readout rate and the highest efficiency for the interesting events with respect to the physics goals. One should always be aware of that the triggered events are interesting (by definition), but not that the non-triggered events are not interesting. For this reason, one should also check by looking at a very small proportion of the events that are discarded by the trigger system.

4.9.2 The ATLAS tree-level trigger system

A tree-level trigger system is designed for ATLAS to reach a reasonable readout rate as well as an excellent efficiency allowing to keep as many as possible rare new physics processes, such as Higgs boson decays. The trigger system actually comprises several single top triggers which could be either independent or correlated. For example, top quark physics may requires triggers with the signatures of top quark final states, while SUSY physics may requires triggers with the signature of SUSY final states. Any trigger can make decision to store a certain event. So the events recorded are a full set of all interesting events defined by all physics analyses. Functionally, triggers are categorized into primary, supporting and monitoring or calibration triggers. Primary triggers select events for physics analyses while supporting triggers keep events supplementary to the physics analyses such as background estimations. Monitoring and calibration triggers mainly select events to monitor the machine status and make the corresponding calibrations.

The tree-level trigger is shown in Figure 4-18 with its three trigger levels: the level 1 trigger, the level 2 trigger and the event filter. Any event will pass through them consequently. The event can be passed to the next level trigger only if it passes the trigger in this level. The three-level triggers will be detailed in the following sections.

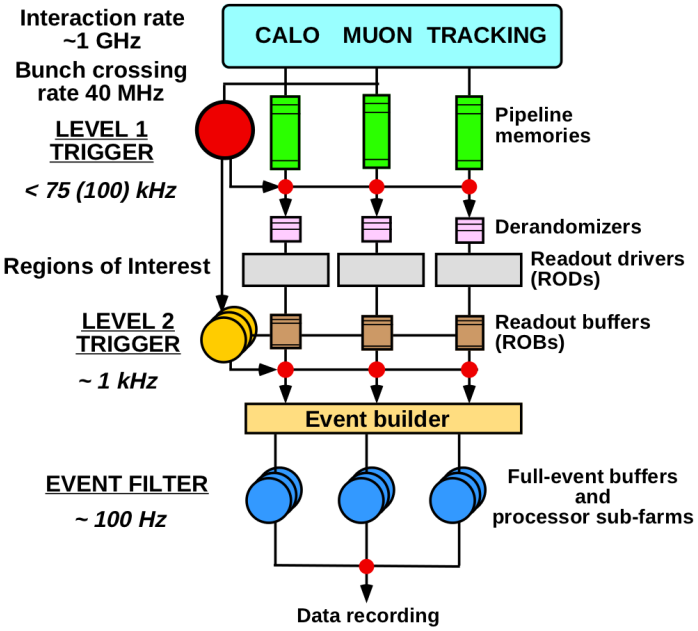

Figure 4-18: The ATLAS trigger system illustrated.

The level-1 trigger

As shown in Figure 4-18, the level-1 (LVL1) trigger is the first level of the trigger system that the data collected at a bunch crossing rate of 40 MHz should pass through. To be able to make decisions within an average time of 25 ns, only programmed hardware trigger in detector front-end (such as FPGA) is used in LVL1 considering the fast response. The LVL1 trigger is designed to reach a rejection factor of 99.8% leading to a reduced readout rate at a maximum value of 75 kHz (upgradable to 100 kHz).

Represented with a big red ball symbol in Figure 4-18, the LVL1 trigger reads in the information directly from both calorimeters and muon spectrometer with a reduced granularity. The calorimeters are used with $\Delta\eta \times \Delta\phi = 0.1 \times 0.1$ (trigger tower) in order to discover interesting objects like high-p_T electrons and γ, jets, τ-leptons decaying into hadrons, as well as large missing and total transverse energies. In the muon spectrometer, only resistive plate chambers (in the barrel) and thin gap chambers (in the end-caps) are used in order to discover objects like high-p_T muons. However, tracking information from the inner detector is not used, since no track can be reconstructed during such a short time in which the LVL1 trigger has to make decisions.

In the meanwhile of processing the detector information in the LVL1 trigger (the red ball), the data are buffered in the "pipeline memories" (shown in green), which can hold up to 100 bunch crossings considering that the maximum latency of the LVL1 trigger is 2.5 μs. Once the decision is made by the LVL1 trigger, the pipeline will be informed to keep or not the event, and the event that passes the LVL1 trigger will get into the queue in Read-Out Buffers (ROBs, shown in dark yellow) to wait for

the request of the next level trigger.

Another function of the LVL1 trigger is to define Regions of Interest (RoIs), which describes the geometrical regions of the identified possible trigger objects within the event in the detector η-ϕ plane, and these RoIs will be used as seeds in the next level trigger.

The level-2 trigger

The level-2 (LVL2) trigger, a part of High-Level Trigger (HLT), is realized by software running on computing farms. The LVL2 trigger (light yellow layered balls shown in Figure 4-18) requests events buffered in Read-Out Buffers (shown in dar yellow) with the guide from RoIs generated by the LVL1 trigger which acts like a map providing informations on where LVL2 should look for potential objects in the plane of η-ϕ. With the help of the RoI map, the LVL2 trigger usually only needs to access a few percent of the full event data. In the end, the LVL2 trigger reduces the rate to around 1 kHz with a rejection power of around 30 thanks to the utilization of higher thresholds on kinematic cuts and the consideration of full granularity.

All the subdetectors are used at this stage including tracking information leading to an average processing time of 50 ms per event. After the decision made by the LVL2 trigger, the data with full detector information will be passed to Event Builder which will prepare the inputs for the next level trigger.

The event filter

As the other part of High-Level Trigger, the Event Filter (EF), is also realized by software and employs "offline" algorithms and methods with the latest calibration and alignment information. The aim is to reduce the LVL2 trigger rate by around 10 in order to write the data at a rate of 100 MB/s (100 Hz with around 1 MB per event). The EF trigger firstly confirms the results of the LVL2 trigger decision and subsequently uses the results of the LVL2 trigger to seed its own analyses. The rejection power of the EF trigger comes from higher thresholds on kinematic cuts and refined algorithms.

4.9.3 The trigger chains and streams

ATLAS triggers are organized in terms of chains. One trigger chain includes all trigger configurations spanning each trigger level: LVL1, LVL2 and EF. So, mentioning a trigger is actually referring to a trigger chain most of the case. For instance, a muon trigger refers to a muon trigger chain including three muon triggers in hardware implemented in the LVL1 trigger from the muon spectormeter, in software implemented in the LVL2 trigger with a refined reconstruction in object level as well as in software implemented by the EF trigger with a better refined reconstruction in event level.

A stream is defined as a collection of several trigger chains. The event that passed one or more than one trigger chain will be written into the corresponding streams which the fired trigger chains belong to. There are mainly four primary streams

for physics analyses: Egamma stream including photon and electron triggers, Muons stream including muon triggers, JetTauEtmiss stream including tau-lepton and E_T^{miss} triggers and MinBias stream including minimum-bias and random triggers. These streams are not fully independent. They usually have some overlaps between each other (less than 5%), which wastes some disk spaces, and also needs to be taken into account in physics analyses. For instance, an event that passes a muon trigger and fires in the same time E_T^{miss} trigger will be recorded by both the Muons and the JetTauEtmiss streams and will be written into disk twice.

Apart from the object triggers such as electron triggers, muon triggers that are used in the physics analyses to be introduced in the corresponding sections in Chapter 5, the non-physical triggers, Random triggers and Minimum-bias triggers are presented here. These two triggers are configured with the purpose to select an unbiased set of all possible collisions events that take place in the collider. As indicated by the name, the Random triggers select events randomly without any event properties taken into account. So there is not any requirement at the LVL2 or EF level trigger. Only at the LVL1 trigger, there is a configuration on the rate at which events are stored. The Random triggers could be used to monitor the changes in the environment as well as the cosmic backgrounds. The Minimum-bias triggers are based on the outputs from the detectors, for instance, the minimum-bias trigger scintillators. They can provide large events statistics for initial physics studies at luminosities of $10^{31}\ cm^{-2}s^{-1}$ or less.

Chapter 5

Physics object reconstruction

Physics objects reconstructed from the detector response are the basic elements in the final states of any interesting process. This chapter will introduce the reconstructed physics objects needed by the analysis of single top quark t-channel events, which have a final state constituted of an isolated lepton (electron or muon), jets with a large transverse momentum and a large missing transverse momentum that stands for the undetected neutrino. These various objects will be discussed with their reconstructions and corresponding efficiencies as well as their energy or momentum scales in the first four sections of this chapter. The luminosity measurement and the data quality monitoring will be presented in the two last sections.

5.1 Electrons

From the information provided by the tracking systems and the electromagnetic calorimeter, one can reconstruct electrons with a high efficiency and a high jet rejection rate [106]. This is done in three steps: triggering, reconstruction and identification.

5.1.1 Trigger

At the first trigger level (LVL1), electrons with a high transverse momentum are triggered by the calorimeter using a trigger tower defined by a cluster with a reduced granularity of the cells. The second trigger level (LVL2) implements fast calorimeter and tracking reconstruction algorithms with the cluster seed located by the most energetic cell in the second electromagnetic layer. The last trigger level (EF) implements full offline reconstruction algorithms at the event level.

Figures 5-1(a) and 5-1(b) show the trigger efficiencies obtained from studies performed with full simulations [107] as a function of the electron transverse energy and pseudorapidity, respectively. The trigger chain used here is "e20_loose" that requires an electron with approximately a transverse momentum $p_T > 20\ GeV$ and a loose identification at LVL1 and LVL2. The trigger efficiency plateau starts after the p_T threshold of 20 GeV and becomes stable at around 25 GeV (Figure 5-1(a)) whatever

the trigger level, the stable trigger efficiency being around 98 %. For all three trigger levels, low efficiencies are observed (Figure 5-1(b)) in the pseudorapidity transition region of the electromagnetic calorimeter at $1.37 < |\eta| < 1.52$ [1], where services are installed between the barrel and the end-caps.

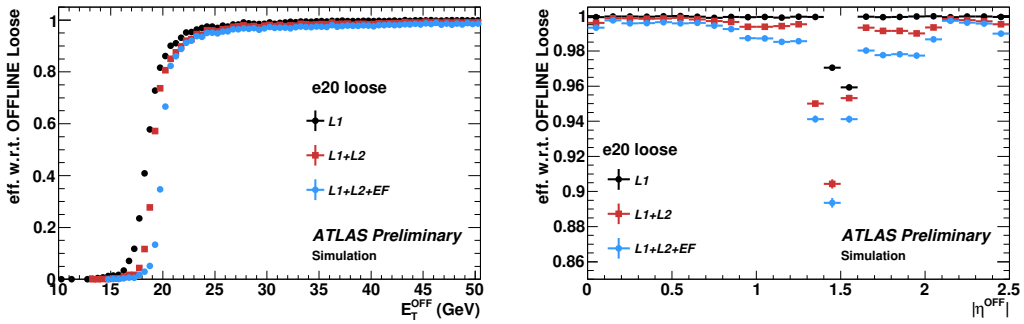

(a) (b)

Figure 5-1: Trigger efficiencies at the three levels for the e20_loose trigger chain as a function of the electron (a) transverse energy and (b) pseudorapidity.

5.1.2 Reconstruction

Both electromagnetic calorimeter and trackers allow an optimal reconstruction of the electron within the full momentum and pseudorapidity ranges under any luminosity. In the calorimeter, a set of seed clusters with energy above 2.5 GeV and size of $\eta \times \phi = 3 \times 5$ in middle layer cell units are created by a sliding window algorithm. On the other hand, charged tracks are reconstructed by the trackers in the pseudorapidity domain $|\eta| < 2.5$. All these tracks are processed to match the seed clusters created in the calorimeter. If any one or more tracks are matched, then one electron is defined. In the matching procedure, the extrapolation of the tracks from the last measured point is passed to the second calorimeter layer with the consideration of Bremsstrahlung losses. Then the impact point on the calorimeter is compared with the corresponding position of the seed cluster. If the difference is below a certain threshold, the track and the cluster are considered matched. When more than one tracks are matched with the same seed cluster, the one with the smallest difference $\Delta R = \sqrt{(\Delta\eta^2 + \Delta\phi^2)}$ between its impact point on the calorimeter and the seed cluster is selected. Apart from that, tracks with silicon hits have priority over tracks without silicon hits, since the latter tracks more likely belong to electrons originating from photon conversions. In the end, the electron four-momentum is provided with the track information from the best track matched to the original seed cluster, and the

[1] In ATLAS, the services are installed at the same z-position from the inner to the outer calorimeter layer. In the electromagnetic calorimeter, the performances are thus degraded by the service installation in the region of $1.37 < |\eta| < 1.52$, while in the tile calorimeter, the performances are degraded in the region at around $|\eta| = 1$.

energy is calculated from a weighted average between the cluster energy and the track momentum. The cluster energy is calculated from the four following contributions: the estimated energy deposit in the material in front of the calorimeter, the measured energy deposit in the cluster, the estimated external energy deposit outside the cluster (lateral leakage) and the estimated energy deposit beyond the calorimeter.

5.1.3 Identification

After trigger and reconstruction, some of the selected candidates might come from fake electrons such as jets from hadrons or electron pairs due to photon conversions. The identification consists in a series of simple cuts using calorimeter, tracking and combined variables applied in order to reduce contamination from fake electrons. With different sets of cuts, three types of electrons are defined, loose, medium and tight, the latters being subsets of the previous ones. The definition of the variables used by the identification cuts can be found in Table 5.1.

The identification of **Loose electrons** utilizes variables associated to hadronic leakage and to the middle layer of the electromagnetic calorimeter, which give a powerful rejection against hadrons faking electrons. Concerning the shower depth, two variables are defined based on the hadronic leakage: (i) the ratio R_{had1} of the transverse energy E_T in the first layer of the hadronic calorimeter to the one in the electromagnetic cluster over the pseudorapidity range $|\eta| < 0.8$ and $|\eta| > 1.37$ and (ii) the ratio R_{had} of E_T in the hadronic calorimeter to the one in the electromagnetic cluster over the pseudorapidity range $0.8 < |\eta| < 1.37$. Regarding the shower width, two variables are defined based on the middle layer of the electromagnetic calorimeter: (i) the ratio R_η of the energy in 3×7 cells over the energy in 7×7 cells centered at the electron cluster position and (ii) the lateral shower width $\omega_{\eta 2}$ defined by $\sqrt{(\Sigma E_i \eta_i^2)/(\Sigma E_i) - ((\Sigma E_i \eta_i)/(\Sigma E_i))^2}$, where E_i is the energy and η_i the pseudorapidity of cell i, the sums being calculated within a window of 3×5 cells.

The distributions of the shower depth and width, given by the simulations [107], are presented in Figures 5-2(a) and 5-2(b) for different types of electrons (isolated and non-isolated electrons, hadrons and background electrons). The considerable long tail on the R_{had1} distribution (Figure 5-2(a)) for hadron faking electrons indicates that hadrons have larger chances to deposit more energies in the hadronic calorimeter, which is quite different from isolated electrons. The distributions of the lateral shower width $\omega_{\eta 2}$ (Figure 5-2(b)) shows that hadrons have larger showers than isolated electrons in the middle layers of the calorimeter.

The identification of **Medium electrons** utilizes variables associated to the strip layer (front layer) of the calorimeter and to the trackers, which are devoted to suppress the electrons originating from photon conversion (background electrons). Concerning the shower properties, two variables are defined based on the strip layer of the calorimeter: (i) the shower width ω_{stot} defined by $\sqrt{(\Sigma E_i (i - i_{max})^2)(\Sigma E_i)}$, where i runs over all strips in a window $\Delta\eta \times \Delta\phi \approx 0.0625 \times 0.2$ (corresponding typically to 20 strips in η) and i_{max} the index of the highest-energy strip; (ii) the ratio E_{ratio} of the energy difference between the largest and second largest energy deposits in the cluster over the sum of these energies. Concerning the tracking quality, three variables are

Type	Name	Description
Loose selection		
Acceptance	$\|\eta\| < 2.47$	
Hadronic leakage	R_{had1}	Ratio of E_T in the first layer of the hadronic calorimeter to E_T of the EM cluster (used over the range $\|\eta\| < 0.8$ and $\|\eta\| > 1.37$)
	R_{had}	Ratio of E_T in the hadronic calorimeter to E_T of the EM cluster (used over the range $0.8 < \|\eta\| < 1.37$)
Middle layer of EM calorimeter	R_η	Ratio of the energy in 3×7 cells over the energy in 7×7 cells centred at the electron cluster position
	$\omega_{\eta 2}$	Lateral shower width, $\sqrt{(\Sigma E_i \eta_i^2)/(\Sigma E_i) - ((\Sigma E_i \eta_i)/(\Sigma E_i))^2}$, where E_i is the energy and η_i the pseudorapidity of cell i and the sum is calculated within a window of 3×5 cells
Medium selection (includes loose)		
Strip layer of EM calorimeter	ω_{stot}	Shower width, $\sqrt{(\Sigma E_i (i - i_{max})^2)(\Sigma E_i)}$, where i runs over all strips in a window of $\Delta\eta \times \Delta\phi \approx 0.0625 \times 0.2$, corresponding typically to 20 strips in η, and i_{max} is the index of the highest-energy strip
	E_{ratio}	Ratio of the energy difference between the largest and second largest energy deposits in the cluster over the sum of these energies
Track quality	n_{pixel}	Number of hits in the pixel detector (≥ 1)
	n_{Si}	Number of total hits in the pixel and SCT detectors (≥ 7)
	d_0	Transverse impact parameter ($\|d_0\| < 5\ mm$)
Track-cluster matching	$\Delta\eta$	$\Delta\eta$ between the cluster position in the strip layer and the extrapolated track ($\|\Delta\eta\| < 0.01$)
Tight selection (includes medium)		
Track cluster matching	$\Delta\phi$	$\Delta\phi$ between the cluster position in the strip layer and the extrapolated track ($\|\Delta\phi\| < 0.02$)
	E/p	Ratio of the cluster energy to the track momentum
	$\Delta\eta$	Tighter $\Delta\eta$ requirements ($\|\Delta\eta\| < 0.005$)
Track quality	d_0	Tighter transverse impact parameter requirement ($\|d_0\| < 1\ mm$)
TRT	n_{TRT}	Total number of hits in the TRT
	f_{HT}	Ratio of the number of high-threshold hits to the total number of hits in the TRT
Conversions	n_{BL}	Number of hits in the b-layer (≥ 1)
		Veto electron candidates matched to reconstructed photon conversions

Table 5.1: Definition of the variables used for the electron indentification cuts [106].

used: (i) the number n_{pixel} of hits in the pixel detector (the selection $n_{pixel} \geq 1$ is required), (ii) the total number n_{Si} of hits in the pixel and SCT detectors ($n_{Si} \geq 7$) and (iii) the transverse impact parameter of the track d_0 (selection cut $|d_0| < 5\ mm$). Furthmore, a criterion on the track-cluster matching variable $\Delta\eta$ between the cluster position in the strip layer and the extrapolated track is applied ($|\Delta\eta| < 0.01$).

Figures 5-3(a) and 5-3(b) show the simulated distributions of some of the calorime-

ter and tracking variables used for the identification of medium electrons. In Figure 5-3(a), the total shower width ω_{stot} in the strip layer of the electromagnetic calorimeter shows that background electrons from photon conversion have fatter showers than isolated electrons. In Figure 5-3(b), the distribution of the energy difference ratio E_{ratio} shows that background electrons from photon conversion and hadron faking electrons do not have an energy deposit peak as significant as isolated electrons. In Figure 5-4(a), the number n_{pixel} of hits in the pixel detector is totally different between background electrons from photon conversion and all other electrons, because the conversion from a photon to electrons seldom leaves any traces in the first few layers of the pixel detector. In Figure 5-4(b), the distribution of the transverse impact parameter d_0 is very wide and off the peak at 0 for background electrons from photon conversion compared to other electrons, since these electrons are usually generated away from the primary vertex.

The identification of **Tight electrons** utilizes additional combined information from track-cluster matching as well as the TRT hits and a photon conversion veto, which enhance the rejection against electrons from hadrons and photon conversions. Some of the criteria used in the definition of medium electrons are also tightened. With more information from track-cluster matching, two variables are defined: (i) the azimuthal difference $\Delta\phi$ between the cluster position in the strip layer and the extrapolated track (electron candidates with $|\Delta\phi| < 0.02$ are selected) and (ii) the ratio E/p of the cluster energy to the track momentum. A tighter requirement on the $\Delta\eta$ track-cluster variable is also considered ($|\Delta\eta| < 0.005$) in combination with a tighter transverse impact parameter selection ($|d_0| < 1\ mm$) applied in order to improve the track quality. Concerning the TRT sub-system response, two variables are defined: (i) the total number n_{TRT} of TRT hits and (ii) the ratio f_{HT} of the number of high-threshold TRT hits to the total number of TRT hits. Additionally, a selection is applied on the number n_{BL} of hits in the b-layer ($n_{BL} \geq 1$) and a veto to the electron candidates matched to reconstructed photon conversions is required.

The simulated distributions of two of the variables allowing to suppress electrons from hadrons and photon conversions are shown in Figures 5-5(a) and 5-5(b). In Figure 5-5(a), the ratio E/p of the cluster energy over the track momentum peaks exactly at 1 for isolated electrons thanks to their negligible masses, but peaks below 1 for hadrons since they deposit only a fraction of their energy in the hadronic calorimeter. In Figure 5-5(b), the fraction f_{HT} of high-threshold TRT hits offers a big enhancement on the rejection against hadrons due to the fact that hadrons radiate much less in TRT than electrons.

5.1.4 Energy scale

The electron energy measured from the clusters cannot be used directly. It needs to be calibrated with the real data and corrected for energy losses due to dead materials or cluster leackages. Therefore, a so-called *electron energy scale* needs to be applied to the measured raw energies. This scale factor is derived from test-beam data and is improved thanks to the analysis of the 2010 data [107]. Energy calibration from test-beam takes advantage of the well-controled particles with respect to their precise

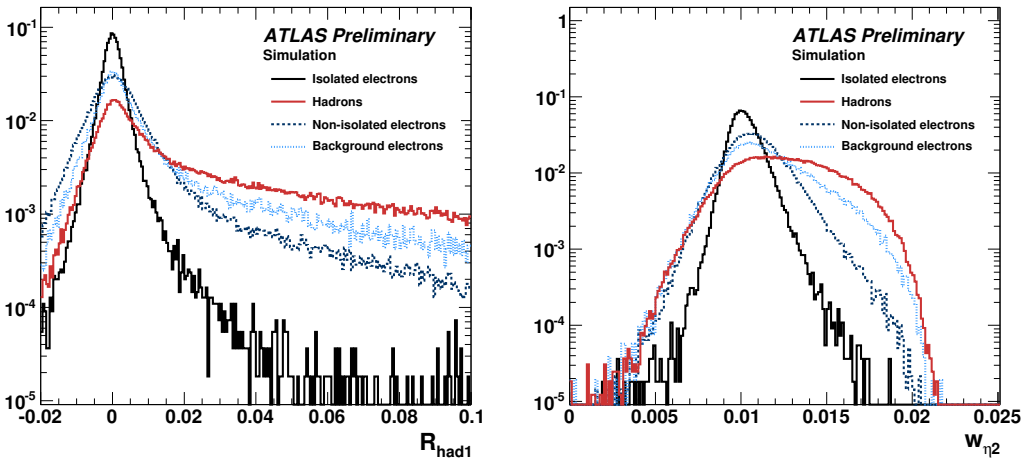

(a) (b)

Figure 5-2: Simulated distributions of variables used to select loose electrons (a) first layer hadronic leakage R_{had1} and (b) middle layer lateral shower width $\omega_{\eta 2}$.

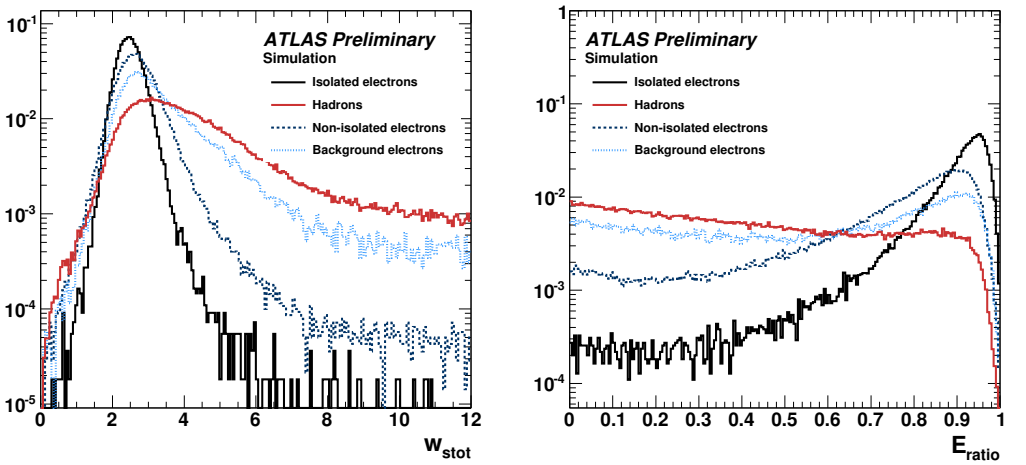

(a) (b)

Figure 5-3: Simulated distributions of the calorimetric variables used to select medium electrons (a) strip layer total shower width ω_{stot} and (b) energy difference ratio E_{ratio}.

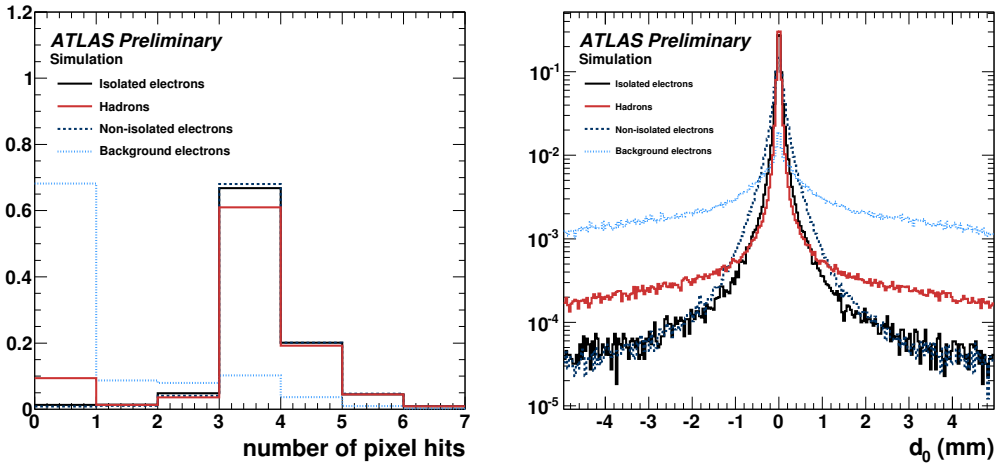

(a) (b)

Figure 5-4: Simulated distributions of tracking variables used to select medium electrons (a) number of pixel hits n_{pixel} and (b) transverse impact parameter d_0.

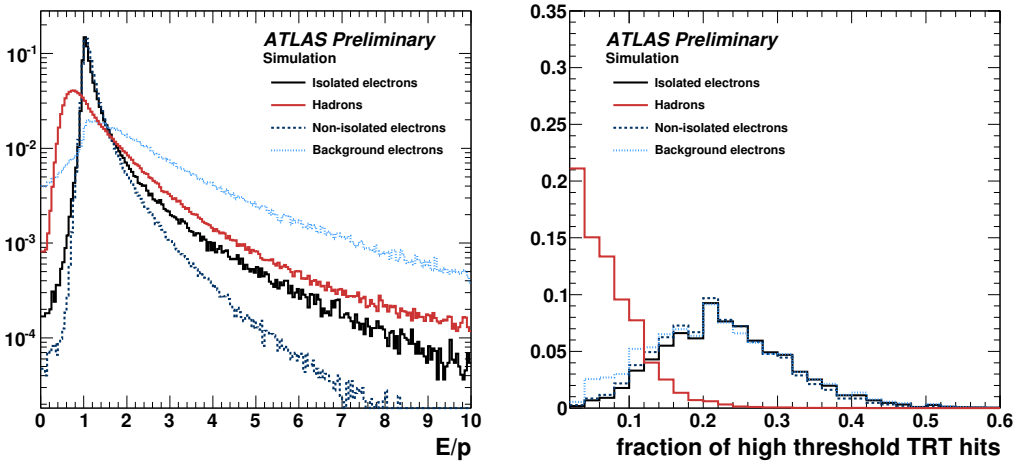

(a) (b)

Figure 5-5: Simulated distributions of variables used to select tight electrons (a) ratio of the cluster energy to the track momentum E/p and (b) fraction of high threshold TRT hits f_{HT}.

positions and energies, but it cannot provide the real effects from the dead materials in front of the electromagnetic calorimeter, or the biases caused by the real environment (temperature, voltage fluctuations, pileup effects, ...) in the ATLAS cavern. Instead, energy calibrations with real data via in-situ methods consider everything under the real operating situation and provide precise measurements, once we have a good calibration reference. $Z \to ee$ and $J/\psi \to ee$ events selected from real collisions data are used as electron energy scale reference in the baseline calibration thanks to the well-measured Z and W boson masses [106]. An alternative method is based on the study of the ratio of the calorimeter energy to the track momentum E/p [106]. This method takes advantage of the larger statistics of the $W \to e\mu$ event samples, but it depends on the knowledge of the momentum scale from the trackers.

Energy calibration from $Z \to ee$ events

This method utilizes a likelihood fit performed on the distribution of the reconstructed Z boson mass to extract the energy scale factors [108]. The electron energy measured in a given kinematic region i, $E_i^{measured}$, is written as a function of the real energy, E^{true}, as follows:

$$E_i^{measured} = E^{true}(1 + \alpha_i) \tag{5.1}$$

where the energy scale factor α_i represents the residual miscalibration in region i. The Z boson invariant mass, $M_{i,j}^{measured}$, calculated from the energies measured for the two electrons in a given region (i, j) is thus given as a function of the true invariant mass, M^{true}, by:

$$M_{i,j}^{measured} = M^{true}(1 + \frac{\alpha_i + \alpha_j}{2}) = M^{true}(1 + \frac{\beta_{i,j}}{2}) \tag{5.2}$$

$$\text{with } \beta_{i,j} = \alpha_i + \alpha_j. \tag{5.3}$$

The probability density function of the real Z boson mass follows a relativistic Breit-Wigner distribution:

$$BW(M) \sim \frac{M^2}{(M^2 - M_Z^2)^2 + \Gamma_Z^2 M^4 / M_Z^2} \tag{5.4}$$

where M_Z and Γ_Z are the Z boson mass and width. In proton-proton collisions, the parton distribution functions are strongly peaked at small x-values, and the production of low-mass systems is thus favored. Therefore the Z boson mass spectrum is no more a symmetrical relativistic Breit-Wigner distribution, and is convolved with the incoming flux provided by the parton distribution functions [109]:

$$\mathcal{L}(M) = 1/M^{\beta} \tag{5.5}$$

where the parton luminosity factor β is assumed to be a constant; it is determined from the fit of the Z boson mass distribution obtained for events generated with Pythia. As it can be seen in Figure 5-6, this effect makes the lower mass tail taller

than the case of ignoring the incoming flux.

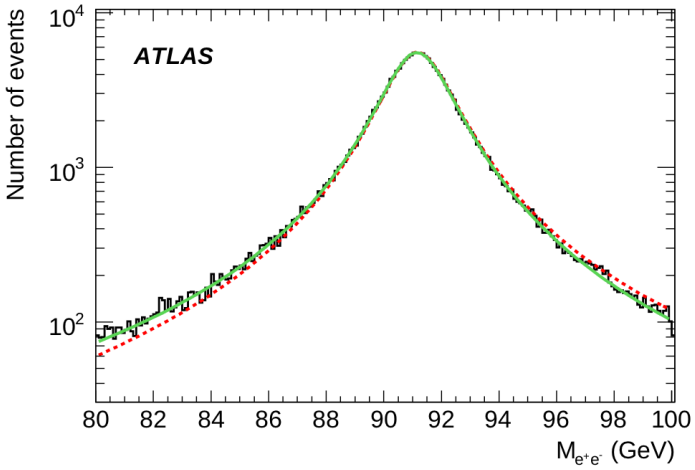

Figure 5-6: Z boson mass distribution extracted from PYTHIA events fitted by a Breit-Wigner distribution with (green solid line) and without (red dashed line) the parton luminosity factor β of Equation 5.5 giving a χ^2/N_{DOF} value of 1.09 and 3.96, respectively [109].

To introduce the finite resolution of the electromagnetic calorimeter, a Gaussian term is convolved with the Breit-Wigner distribution as follows:

$$L(M,\sigma_M) = \int_{-\infty}^{+\infty} BW(M-u)\mathcal{L}(M-u)\frac{e^{-u^2/2\sigma_M^2}}{\sqrt{2\pi}\sigma_M}du \tag{5.6}$$

$$\text{with } \frac{\sigma_M}{M} = \frac{1}{2}\sqrt{(\frac{\sigma_{E_1}}{E_1})^2 + (\frac{\sigma_{E_2}}{E_2})^2} \tag{5.7}$$

where the resolution σ_M of the measured invariant mass is derived from the energy resolutions σ_{E_1} and σ_{E_2} associated to the two electron energies E_1 and E_2. Therefore the likelihood function is constructed by summing over the number of measured Z boson events N:

$$-\ln L_{total} = \sum_{k=1}^{N} -\ln L(\frac{M_k}{1+\beta_{i,j}/2}, \sigma_M). \tag{5.8}$$

By fitting the asymmetric Breit-Wigner distribution, the total energy scale factor $\beta_{i,j}$ can be extracted. By implementing a least squares method detailed in [108], α_i can then be determined from $\beta_{i,j}$. The results on the electron energy scale factor α can be found in Figure 5-7(a); they are cross checked, as shown in Figure 5-7(b), using the same method applied to datasets of $J/\psi \to ee$ events.

The total uncertainties coming from detector materials, electronic readouts and backgrounds are shown in Figures 5-8(a) and 5-8(b) as a function of the electron transverse energy E_T for two pseudorapidity regions. In the central region, the overall

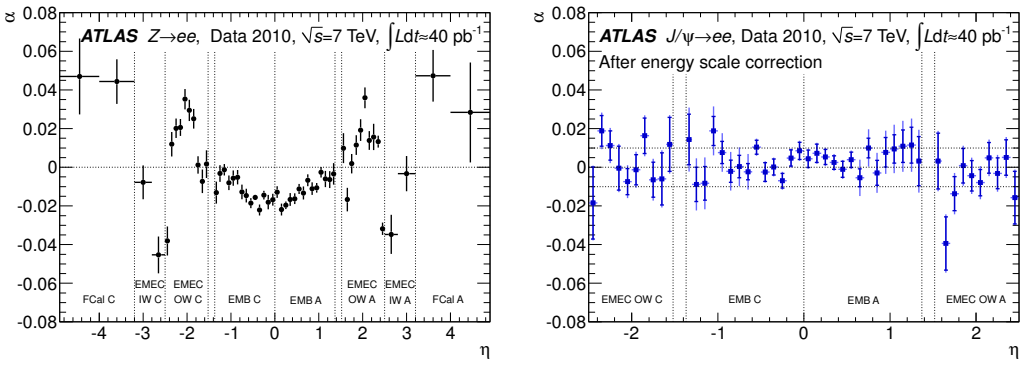

(a) (b)

Figure 5-7: (a) Energy scale factor α as a function of the pseudorapidity of the electron cluster derived from fits to $Z \rightarrow ee$ data; the uncertainties stand for statistical error, (b) Energy scale factor α as a function of the pseudorapidity of the electron cluster derived from fits to $J/\psi \rightarrow ee$ data; the inner error bars show statistical uncertainties, while the outer error bars include all systematic uncertainties. The results of the J/ψ analysis are derived after calibration with the energy scale factors extracted from the $Z \rightarrow ee$ datasets [106].

uncertainty varies from 0.3% to 1.6% with the smallest uncertainties (typically below 0.4%) around $E_T = 40\ GeV$.

The alternative calibration method based on the E/p distributions measured in $W \rightarrow e\nu$ event samples, gives, within its larger systematic uncertainties, results that agree with the baseline calibration using the $Z \rightarrow ee$ mass distributions. Furthermore, the azimuthal (ϕ) uniformity of the calorimeter response is studied and a non-uniformity of less than 1% is found. Finally, the linearity of the calorimeter energy response is checked and variations of about 0.1% and 0.8% are found in the central and forward pseudorapidity regions, respectively.

5.1.5 Energy resolution

The calorimeter energy resolution is usually parameterized by:

$$\frac{\sigma_E}{E} = \frac{a}{\sqrt{E}} \oplus \frac{b}{E} \oplus c \tag{5.9}$$

where a corresponds to shower intrinsic fluctuations (stochastic term or sampling term), b to noise fluctuations like electronic or pedestal (noise term), and c to shower leackage representing the quality of the energy response uniformity of the calorimeter (constant term). Basically, all these parameters are pseudorapidity-dependent. With the limited statistics of the 2010 data, only the constant term is determined from $Z \rightarrow ee$ data events, leaving the sampling and noise terms determined from Monte Carlo simulations [106].

According to the energy resolution formulation given by Equation 5.9, both sam-

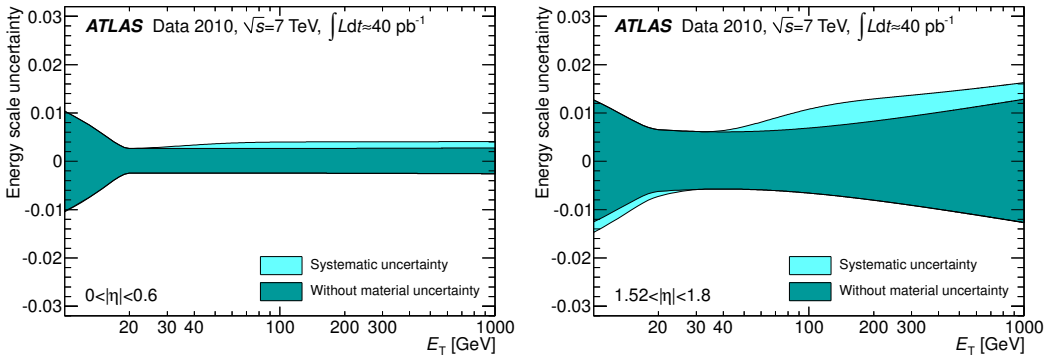

(a) (b)

Figure 5-8: Total systematic uncertainty on the electron energy scale α as a function of the electron transverse energy (a) in the central pseudorapidity region $|\eta| < 0.6$ and (b) in the forward pseudorapidity region $1.52 < |\eta| < 1.8$.

pling and noise terms dominate in the low energy region while they contribute to a lesser extent when the energy increases. Figure 5-9 presents the distribution of the dielectron invariant mass from $J/\psi \to ee$ data and simulated events. The good agreement obtained between data and simulation shows that the sampling and noise terms extracted from the Monte Carlo simulation describe well the energy resolution in the low energy domain covered by the J/ψ resonance. Therefore we can extrapolate them into the high energy region to further extract the constant term c. The constant term depends strongly on the real situation like the materials in front of the calorimeter and the energy leakage, which differs from one particle to another. The $Z \to ee$ mass distribution reconstructed from the 2010 data is used to extract this constant term.

From Equation 5.7, one can write down the measured mass uncertainties for data and Monte Carlo events:

$$(\frac{\sigma_M}{M})_{data} = \frac{1}{2}\sqrt{(\frac{\sigma_{E_1}}{E_1})^2_{data} + (\frac{\sigma_{E_2}}{E_2})^2_{data}} \tag{5.10}$$

$$(\frac{\sigma_M}{M})_{MC} = \frac{1}{2}\sqrt{(\frac{\sigma_{E_1}}{E_1})_{MC})^2 + (\frac{\sigma_{E_2}}{E_2})^2_{MC}}. \tag{5.11}$$

Subtracting the two equations above, one gets:

$$(\frac{\sigma_M}{M})^2_{data} - (\frac{\sigma_M}{M})^2_{MC} = \frac{1}{4}((\frac{\sigma_{E_1}}{E_1})^2_{data} - (\frac{\sigma_{E_1}}{E_1})^2_{MC} + (\frac{\sigma_{E_2}}{E_2})^2_{data} - (\frac{\sigma_{E_2}}{E_2})^2_{MC}). \tag{5.12}$$

Given the fact that the a and b resolution terms extracted from the Monte Carlo simulations are also valid for data, one obtains:

$$(\frac{\sigma_E}{E})^2_{data} = (\frac{a}{\sqrt{E}})^2_{MC} + (\frac{b}{E})^2_{MC} + c^2_{data} \tag{5.13}$$

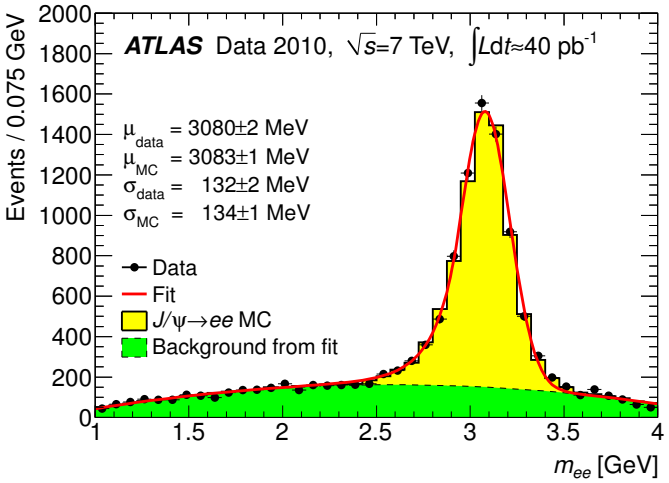

Figure 5-9: Reconstructed dielectron invariant mass distribution for $J/\psi \to ee$ events after applying the baseline energy calibration. The data are compared to the sum of the Monte Carlo signal (light filled histogram) and background contributions (darker filled histogram) modelled by a Chebyshev polynomial. The mean value and the Gaussian width of the fitted Crystal Ball function are given for both data and MC [106].

$$(\frac{\sigma_E}{E})^2_{MC} = (\frac{a}{\sqrt{E}})^2_{MC} + (\frac{b}{E})^2_{MC} + c^2_{MC}. \tag{5.14}$$

One can then derive:

$$(\frac{\sigma_M}{M})^2_{data} - (\frac{\sigma_M}{M})^2_{MC} = \frac{1}{4}(c^2_{data} - c^2_{MC} + c^2_{data} - c^2_{MC}) \tag{5.15}$$

$$c_{data} = \sqrt{2((\frac{\sigma_M}{M})^2_{data} - (\frac{\sigma_M}{M})^2_{MC}) + c^2_{MC}} \tag{5.16}$$

where the constant term in data c_{data} can be extracted from the measured Z mass uncertainties by fitting both the data and Monte Carlo Z mass distributions with a convolution of a Breit-Wigner function with a Crystal Ball function, as shown in Figures 5-10(a) and 5-10(b). The value of the constant term in the simulations is about 0.5%. The results for c_{data} are $1.2\% \pm 0.1\%(stat)^{+0.5\%}_{-0.6\%}(syst)$ for $|\eta| < 1.37$ and $1.8\% \pm 0.4\%(stat) \pm 0.4\%(syst)$ for $1.52 < |\eta| < 2.47$ [106].

5.1.6 Efficiency

Once the electrons are triggered, reconstructed, identified and finally selected by isolation cuts, the number of candidate events containing electrons given by the simulation usually differs from the number of candidate events in the data due to our non-perfect knowledge of the detector. The simulated events need thus to be corrected by scale factors derived from the data/simulation ratios including contributions from the efficiencies from trigger, reconstruction, identification and isolation. This decomposition of the efficiencies is very important: it indeed allows to utilize data-driven methods

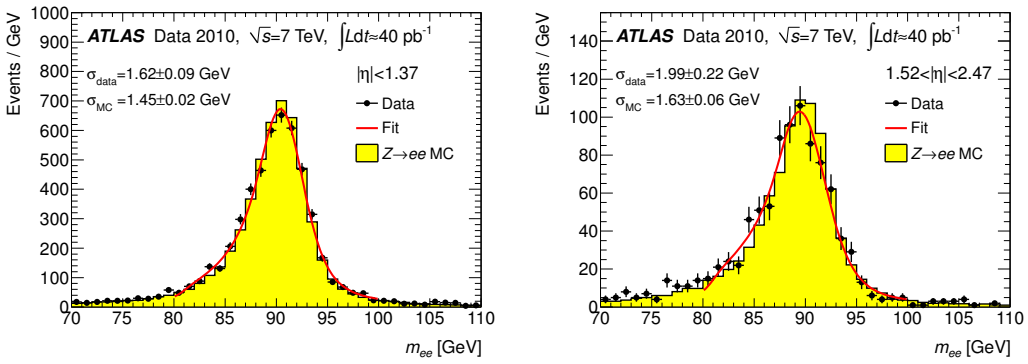

(a) (b)

Figure 5-10: Reconstructed dielectron invariant mass distributions for $Z \to ee$ events after applying the baseline calibration (a) in the central region $|\eta| < 1.37$ and (b) in the forward region $1.52 < |\eta| < 2.47$. The Gaussian width of the Crystal Ball function is given for both data and Monte Carlo simulation [106].

such as the tag-and-probe method to measure them, and limits the reliance on simulations. The simulation is corrected by the ratios of the efficiencies measured from data over the ones predicted by Monte Carlo simulations as a function of the electron kinematics (typically E_T and η). The tag-and-probe method "tags" electrons by selection cuts and "probes" by loosened cuts in order to provide a clean and unbiased sample of electrons, to which any selection cut can be applied for the extraction of the corresponding efficiency.

To measure the identification efficiency through the tag-and-probe method, three sets of events are selected: $Z \to ee$ events tagged by a well-identified electron, $W \to e\nu$ events tagged by a high missing transverse momentum and $J/\psi \to ee$ events tagged by a well-identified electron (mainly for electrons with E_T less than 20 GeV). The measured efficiencies (for the high E_T region) from $Z \to ee$ and $W \to e\nu$ samples are compatible. The efficiencies measured from $Z \to ee$ events with medium and tight electron identification cuts are compared with the Monte Carlo predictions in Figures 5-11(a) and 5-11(b) as a function of the electron transverse energy and in Figures 5-12(a) and 5-12(b) as a function of the pseudorapidity. The overall efficiency with the medium cuts is $94.7\% \pm 0.4\%(stat) \pm 1.5\%(syst)$ in the data and 96.3% in the simulation leading to a data/MC scale factor of $0.984 \pm 0.004 \pm 0.015$. For the tight cuts, the overall efficiency is $80.7\% \pm 0.5\%(stat) \pm 1.5\%(syst)$ in the data and 78.5% in the simulation giving a scale factor of $1.028 \pm 0.006 \pm 0.016$. A good agreement between the data and simulation efficiencies is found. The non-uniformity as a function of the pseudorapidity seen for the tight identification efficiency is due to the fact that the tight identification cuts rely on tracking information which is quite sensitive to the interactions of the electrons in the inner detector material which features an η-dependence.

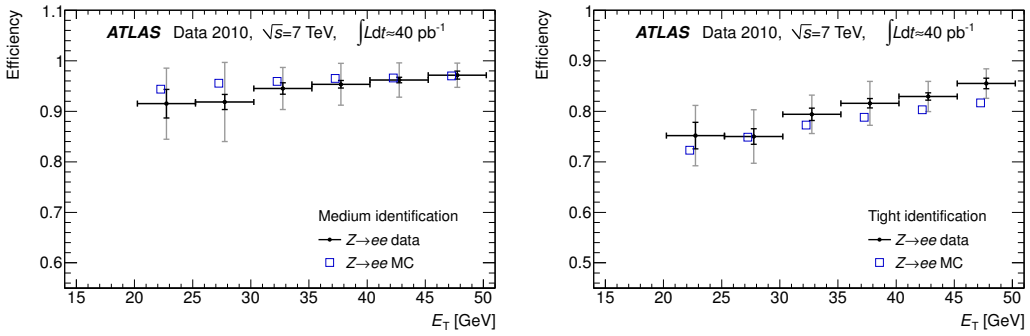

(a) (b)

Figure 5-11: Efficiencies measured and predicted from $Z \to ee$ events for (a) medium and (b) tight electron identifications as a function of the transverse energy E_T over the pseudorapidity range $|\eta| < 2.47$ excluding the transition region $1.37 < |\eta| < 1.52$. The inner error bars show the statistcal uncertainties, while the outer error bars give the total uncertainties including systematic uncertainties mainly coming from the background subtraction [106].

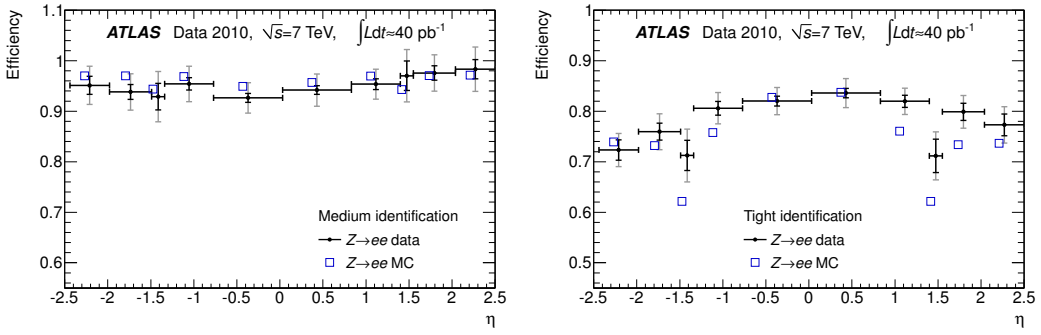

(a) (b)

Figure 5-12: Efficiencies measured and predicted from $Z \to ee$ events for (a) medium and (b) tight electron identifications as a function of the pseudorapidity η over the transverse energy domain $20 < E_T < 50\ GeV$. The inner error bars show the statistcal uncertainties, while the outer error bars give the total uncertainties including systematic uncertainties mainly coming from the background subtraction [106].

5.2 Muons

Muons are able to pass through almost all detector parts, including the inner detector (ID) where muons leave curved trails, the electromagnetic and hadronic calorimeters where they leave very limited energy deposits, and the muon spectrometer (MS) where they leave segmented trails in the separated muon chambers.

With the information from the inner detector, the calorimeters and the muon spectrometer, one can define four types of muons according to the reconstruction method [110]:

- **Stand-alone muon**: The muon track is only reconstructed in the muon spectrometer. The direction of flight and the impact parameter of the muon at the interaction point are determined by extrapolating the spectrometer track back to the beam line taking into account the energy loss of the muon in the calorimeters.
- **Combined muon**: The track reconstruction is performed independently in the inner detector and in the muon spectrometer; a track is then formed from the combination of a spectrometer track with an inner one.
- **Segment tagged muon**: A track in the inner detector is identified as a muon if this track extrapolated to the muon spectrometer is associated with straight track segments in the precision muon chambers.
- **Calorimeter tagged muon**: A track in the inner detector is identified as a muon if the associated energy deposits in the calorimeters are compatible with the hypothesis of a minimum ionizing particle.

Except Stand-alone muons covering the pseudorapidity range $|\eta| < 2.7$, any other muons cover the domain $|\eta| < 2.5$ due to the utilization of the inner detector in the reconstruction. Combined muons have the highest purity candidates. The efficiency of Combined muons is mainly limited by the independent reconstruction in the muon spectrometer which has a small acceptance hole at $|\eta| \sim 0$ due to the service space and has only one layer of chambers installed in the transition region $|\eta| \sim 1.2$. Segment tagged muons are reconstructed mainly in order to identify muons with very low transverse momenta ($p_T \lesssim 5\ GeV$), since the deflection of these low energy muons in the muon spectrometer is too large to let them cross more than two layers of muon chambers (minimum requirements of a Stand-alone muon). Segment tagged muons have therefore a higher efficiency than Combined muons due to the extra acceptance to the low energies. The Calorimeter tagged muons are designed to cover the acceptance gap of the muon spectrometer at $|\eta| \sim 0$ where services of the inner detector and the calorimeters are installed.

5.2.1 Reconstruction

In the early phase of the LHC operation, ATLAS uses two algorithm chains with different pattern recognition strategies to reconstruct Combined and Segment tagged muons:

- **Chain 1 (Staco)**: This reconstruction algorithm utilizes a statistical combination of the independent measurements in both the inner detector and the muon spectrometer by means of their covariance matrices. For example, given two tracks with parameters represented by the vectors $\vec{P_1}$ and $\vec{P_2}$ and with corresponding covariance matrices C_1 and C_2, the tracks are combined by calculating the vector of track parameters $\vec{P}$ with its covariance matrix C as follows:

$$C^{-1} \cdot \vec{P} = C_1^{-1} \cdot \vec{P_1} + C_2^{-1} \cdot \vec{P_2} \quad with \quad C = (C_1^{-1} + C_2^{-1})^{-1} \tag{5.17}$$

  With the two weights from the covariance matrices, the Combined track is defined as an "average" of the inner and spectrometer tracks. The inner track dominates the measurement up to transverse momenta $p_T \sim 80\ GeV$ in the barrel and $p_T \sim 20\ GeV$ in the end-caps. For higher p_T up to $\sim 100\ GeV$, the inner and spectrometer tracks have similar weights, while the spectrometer track dominates at $p_T \gtrsim 100\ GeV$.

- **Chain 2 (MuId)**: This algorithm performs a combined track fit to all muon hits in the inner detector and in the muon spectrometer with the MUONBOX and the iPatRec packages [111]. The fit procedure includes the recovery of missing or wrongly assigned spectrometer hits, most frequently arising from missing or low quality information in the transverse projection.

When a muon is reconstructed as both a Combined and Segment tagged muon, only the Combined muon is used in the analysis.

5.2.2 Reconstruction efficiency

Muons are predominantly produced in weak decays of hadrons with transverse momenta p_T up to 30 GeV, while the higher transverse momentum region is dominated by muons decaying from W and Z bosons. Therefore, the muon reconstruction efficiency is determined (using the tag-and-probe method) with $J/\psi \to \mu\mu$ events [112] in the low p_T region and with $Z \to \mu\mu$ events [113] in the high p_T region. In the following, only the high p_T muon efficiency determination will be presented.

The full reconstruction efficiency for a Combined or a Segment tagged muon can be decomposed into the reconstruction efficiency in the inner detector, the reconstruction efficiency in the muon spectrometer and the matching efficiency between the inner and spectrometer measurements. These individual efficiencies can be measured separately using the tag-and-probe method. Considering high p_T muons decaying from Z bosons, events containing two oppositely charged isolated tracks with a dimuon invariant mass near the Z boson mass are selected. One of the tracks must be a Combined muon ("tag" muon) and the second track ("probe") must be a Stand-alone muon if the inner detector efficiency is to be measured or an inner track if the combined spectrometer and matching efficiency is to be measured. The inner detector reconstruction efficiency is defined as the fraction of Stand-alone muon probes which can be associated to an inner track. The spectrometer and matching efficiency is the

fraction of inner muon probes which can be associated to a Combined or a Segment tagged muon.

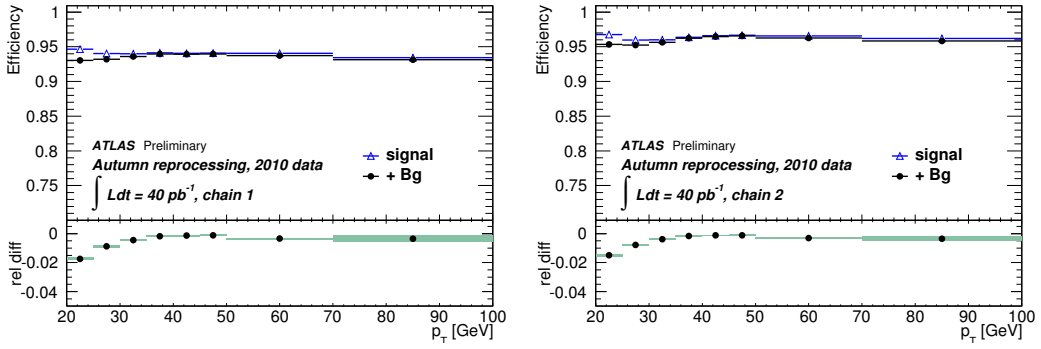

(a) (b)

Figure 5-13: Combined muon efficiencies for the two reconstruction algorithms obtained as a function of p_T from Monte Carlo simulated events using inner detector probes. The triangles stand for the efficiencies determined from Monte Carlo $Z \to \mu\mu$ event samples, while the black dots show the efficiencies obtained with the tag-and-probe method when taking into account in addition all simulated backgrounds [113]. (a) efficiencies for chain 1 and (b) efficiencies for chain 2.

To fully select the "tag" and "probe" muons from data or Monte Carlo simulations, stringent data quality cuts, detailed in [113], are required and a matching procedure is applied to the "probe". A match between an inner track probe and a muon is considered successful if they have the same measured charge and are close in $\eta - \phi$ space ($\Delta R \leqslant 0.01$) whereas a match between a Stand-alone muon probe and an inner track is considered successful if $\Delta R \leqslant 0.05$. Before presenting the efficiency results, one more thing needs to be considered. The backgrounds, $Z \to \tau\tau$, $W \to \mu\nu$, $W \to \tau\nu$, $b\bar{b}$, $c\bar{c}$ and $t\bar{t}$, actually represent a very small amount of contamination, since the simulation studies show that, for both reconstruction chains, 99.3% of the selected events with an inner track "probe" contain $Z \to \mu\mu$ decays, and 99.9% of the selected events with a Stand-alone muon "probe" contain $Z \to \mu\mu$ decays. Figures 5-13(a) and 5-13(b) show that the effect of the background contamination on the muon reconstruction efficiency is negligible for the transverse momenta $p_T \gtrsim 30\ GeV$ (it is less than 1%).

The inner detector reconstruction efficiency is shown in Figure 5-14 as a function of the muon pseudorapidity. A small η-dependence is obtained and the average efficiency is 99.1±0.1 %. The lower efficiencies at $\eta \sim 0$ and $|\eta| \sim 1$ are respectively due to dead regions without any TRT radiation and a small transition area in the inner detector. The results are independent of the choice of the algorithm chain for the Stand-alone muon. Additional studies [95] show that the inner detector efficiency is independent of ϕ and p_T.

The Combined muon reconstruction efficiency is shown in Figure 5-15 as a function of the transverse momentum and of the pseudorapidity. The mean value of the η-dependent scale factor curve is 98.9 ± 0.3 % for chain 1 and 99.5 ± 0.2 % for

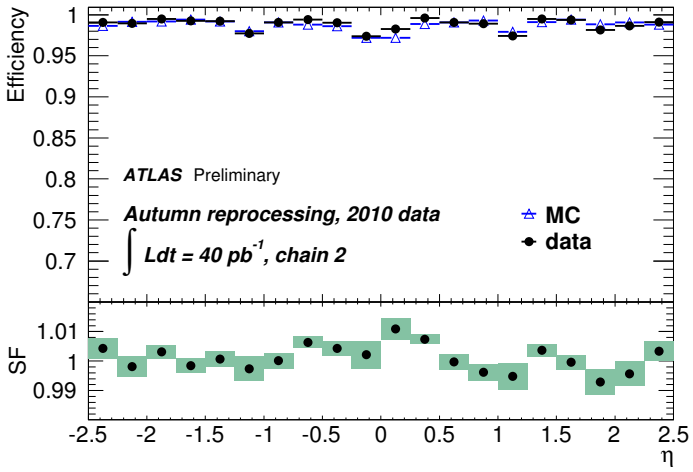

Figure 5-14: Measured inner detector muon reconstruction efficiency for chain 2 (MuId) as a function of the pseudorapidity. The scale factors (data/simulation corrections) are shown in the bottom part; they are consistent with unity within the uncertainties which are less than 1% [113].

chain 2 (statistical errors only). The largest deviation from unity (∼0.94) in the overall efficiency scale factor of chain 1 is found in the transition region, since the accuracy of the magnetic field map in this region is quite limited leading to a small mismeasurement of the Stand-alone muon momentum.

To cover the detector regions where the muon spectrometer is partially installed ($\eta \sim 0$ and $|\eta| \sim 1.2$), Segment tagged muons are used in addition to Combined muons. One obtains an enhanced reconstruction efficiency of Combined + Segment tagged muons compared with the efficiency for only Combined muons as shown in Figure 5-16. The overall reconstruction efficiencies with Combined + Segment tagged muons are 97.0 ± 0.1 % and 98.0 ± 0.1 % for chains 1 and 2, respectively. Furthermore, the data and Monte Carlo agreement is even better when Segment tagged muons are additionally used together with Combined muons, since scale factors of 1.003 ± 0.002 for chain 1 and 1.001 ± 0.002 for chain 2 are found [113].

5.2.3 Momentum resolution

The muon momentum resolution is affected by the amount of dead materials that the muon traverses, the spatial resolution of the individual track points, and the precision of the internal alignment of the inner detector and of the muon spectrometer. The momentum resolution provided by the muon spectrometer is usually modeled as:

$$\frac{\sigma(p)}{p} = \frac{p_0^{MS}}{p_T} \oplus p_1^{MS} \oplus p_2^{MS} \cdot p_T \tag{5.18}$$

where $\frac{p_0^{MS}}{p_T}$ is related to the energy loss in the calorimeter material, p_1^{MS} to multiple scattering and $p_2^{MS} \cdot p_T$ to the intrinsic resolution. Similarly, the momentum resolution

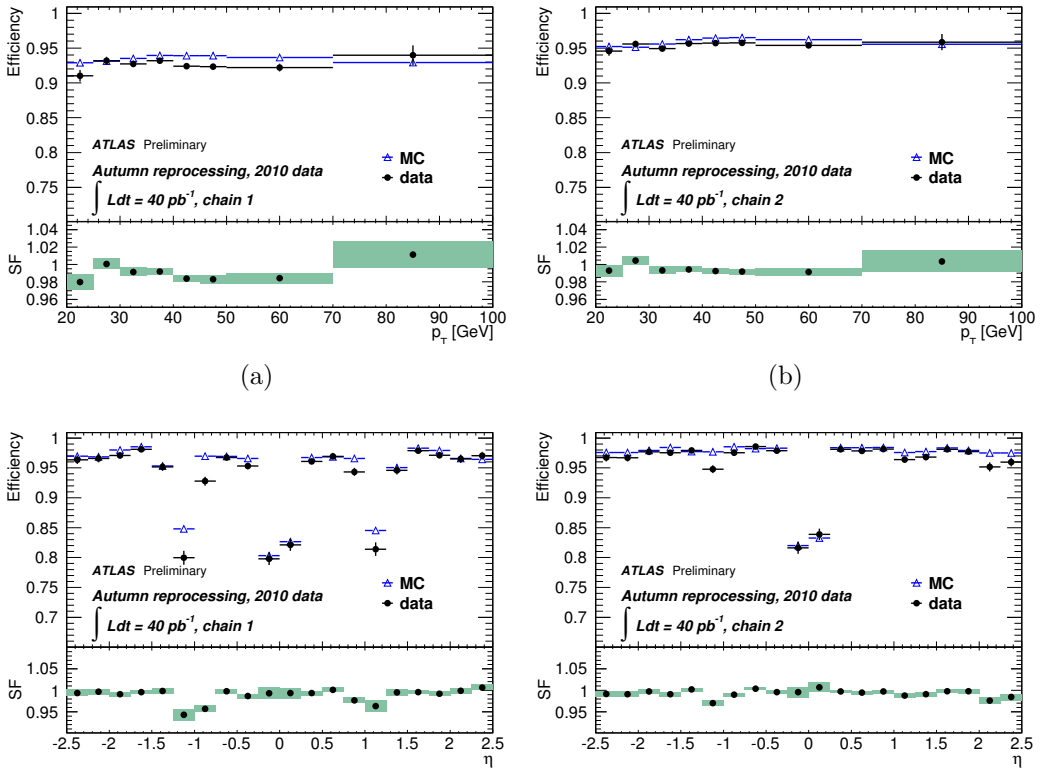

Figure 5-15: Reconstruction efficiencies for Combined muons obtained for the two reconstruction chains from data without background correction (dots) and from Monte Carlo simulations including backgrounds (open triangles) [113]. The corresponding scale factors are shown in the lower part of each figure. (a) Chain 1 efficiency as a function of p_T, (b) chain 2 efficiency as a function of p_T, (c) chain 1 efficiency as a function of η and (d) chain 2 efficiency as a function of η.

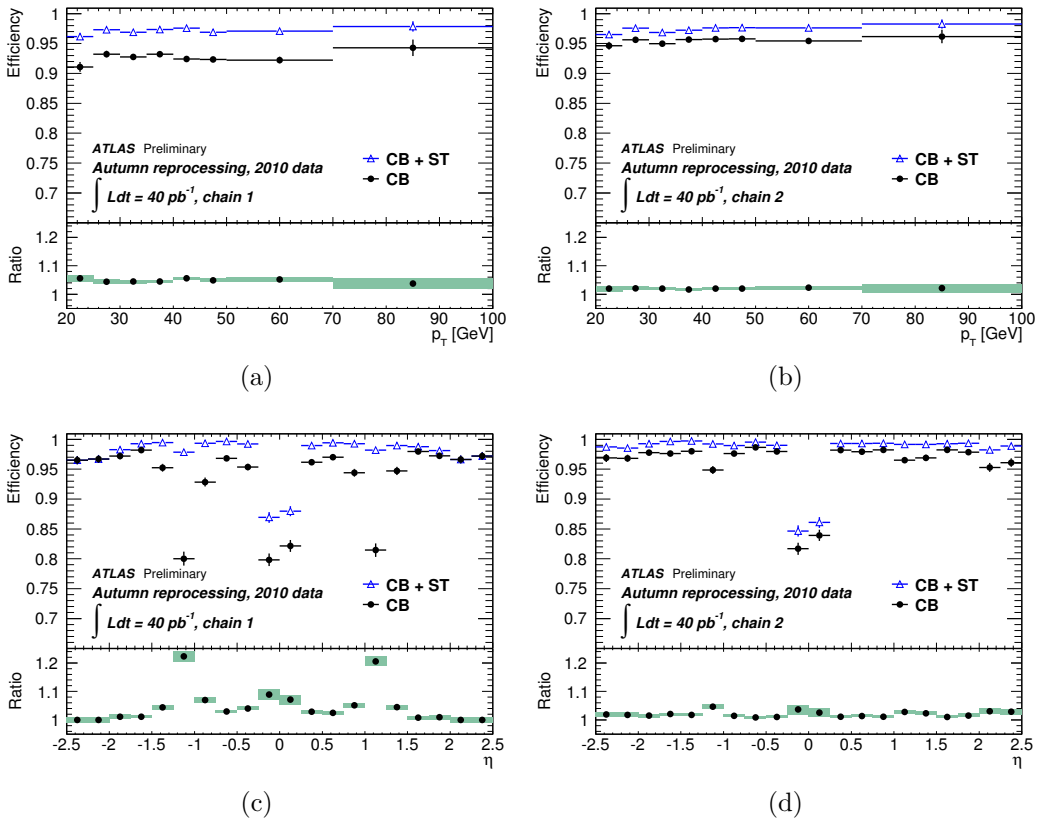

Figure 5-16: Reconstruction efficiencies for Combined + Segment tagged muons (open triangles) compared to those for Combined muons only (dots) [113]. The corresponding scale factors are shown in the lower part of each figure. (a) Chain 1 efficiency as a function of p_T, (b) chain 2 efficiency as a function of p_T, (c) chain 1 efficiency as a function of η and (d) chain 2 efficiency as a function of η.

provided by the inner detector can be modeled with respect to the multiple scattering (p_1^{ID}) and the intrinsic resolution (p_2^{ID}):

$$\frac{\sigma(p)}{p} = p_1^{ID} \oplus p_2^{ID} \cdot p_T \tag{5.19}$$

This parameterization is only valid for $|\eta| < 1.9$ which corresponds to the TRT pseudorapidity range. For $|\eta| > 1.9$, a modeling dependent on the muon polar angle θ is considered for the momentum resolution:

$$\frac{\sigma(p)}{p} = p_1^{ID} \oplus p_2^{ID} \cdot p_T \cdot \frac{1}{\tan^2\theta}. \tag{5.20}$$

Because the measurement of the transverse momentum in the inner detector is derived from the curvature dependent on the track length in the active material, which is dramatically reduced outside of TRT, the p_T resolution will get worse when muons go beyond the TRT coverage.

The momentum resolution is parameterized as a function of the muon pseudorapidity. Considering the geometry of the inner detector which constrains the performance of Combined muons, the η parameterization covers the four following regions: (i) Barrel: $0 < |\eta| < 1.05$, (ii) Transition region: $1.05 < |\eta| < 1.7$, (iii) End-caps: $1.7 < |\eta| < 2.0$ and (iv) CSC (no TRT): $2.0 < |\eta| < 2.5$.

The 7 TeV data recorded in 2010 with the integrated luminosity of 40 pb^{-1} is used to extract the muon momentum resolution [114] and a global fit to the transverse momenta measured in the data by the Monte Carlo smeared distributions allows to extract simultaneously the momentum resolutions of the inner detector and of the muon spectrometer. The muon spectrometer p_T given by the Monte Carlo simulations is randomly varied according to:

$$p'_T(MS) = p_T(MS)(1 + \Delta(MS)) \tag{5.21}$$

with

$$\Delta(MS) = \xi\Delta p_1^{MS} + \xi\Delta p_2^{MS} p_T \tag{5.22}$$

where ξ is a random number following a normal distribution with $\mu = 0$ and $\sigma = 1$. For the inner detector, the Monte Carlo muon p_T is varied as follows:

$$p'_T(ID) = p_T(ID)(1 + \Delta(ID)) \tag{5.23}$$

where

$$\Delta(ID) = \xi\Delta p_1^{ID} + \xi\Delta p_2^{ID} p_T \quad (|\eta| < 1.9) \tag{5.24}$$

$$\Delta(ID) = \xi\Delta p_1^{ID} + \xi\Delta p_2^{ID} p_T / \tan^2\theta \quad (|\eta| > 1.9). \tag{5.25}$$

Additional knowledge is added into the fit to constrain the interesting parameters which are Δp_1^{ID}, Δp_1^{MS} and Δp_2^{MS}. The parameter Δp_1^{ID}, which represents the correction to the inner detector multiple scattering term, is constrained to the expected value of zero with the uncertainty on the inner material budget which has been investigated by K_s^0 mass studies [115], J/ψ width studies [116] and the resolution on

the transverse impact parameter for low p_T inner tracks [117]. The parameter Δp_0^{MS}, which is the correction to the calorimetric energy loss term, is not taken into account since the contribution to the momentum resolution from this energy loss is negligible in the momentum range of 20 GeV to 100 GeV [118]. The parameter Δp_1^{MS}, which corresponds to the correction to the spectrometer multiple scattering term, is set free without any constrain. The parameter Δp_2^{MS}, which is the correction to the intrinsic resolution term, is constrained by the spectrometer misalignment determined from studies performed on the 2009 and 2010 data [114].

By a χ^2 minimization including all the terms and constrains discussed above, the various corrections are extracted and transformed into the corresponding parameters of the momentum resolution model. The muon spectrometer momentum resolutions obtained as a function of p_T are shown in Figure 5-17 separately for the four considered η regions. Significant disagreements between the data resolutions and the uncorrected parameters obtained from the simulation are observed whereas the agreement is very good when the data are compared with the cosmic results.

A correction function is built up with respect to the measured momentum resolution. This correction is applied to the Monte Carlo samples without the consideration of the correlation between the inner and spectrometer resolutions, since the large amount of calorimeter material between the two systems make them decorrelated. The new corrected muon p_T is given by:

$$p'_T(CB) = p_T(CB) \cdot (1 + \frac{\frac{\Delta(MS)}{\sigma^2(MS)} + \frac{\Delta(ID)}{\sigma^2(ID)}}{\frac{1}{\sigma^2(MS)} + \frac{1}{\sigma^2(ID)}}) \tag{5.26}$$

where $\Delta(MS, ID)$ is the overall correction to the simulated spectrometer or inner muon p_T, while $\sigma(MS, ID)$ are the resolutions extracted from the global fit. With these corrections, the reconstructed dimuon invariant mass in the Z mass range gives a good agreement between data and simulation as shown in Figures 5-18(a), 5-18(b) and 5-19. The measured muon momentum resolutions are summarized in Table 5.2 through the values of the parameters entering in the resolution models expressed by Equations 5.18 and 5.19 extracted in the different $|\eta|$ regions.

5.3 Jets

Jets originate from quarks, which produce showers due to the gluon radiations and the hadronization described in Section 3.2 as well as to the interactions with the active materials in the calorimeters.

5.3.1 Reconstruction

Jets are defined as groups of topologically-related energy deposits in the calorimeters [95], most of which are associated with tracks of charged particles measured in the inner detector. To reconstruct a jet, the first step consists of defining topological clusters from the calorimeters; a finding algorithm using these topological clusters as

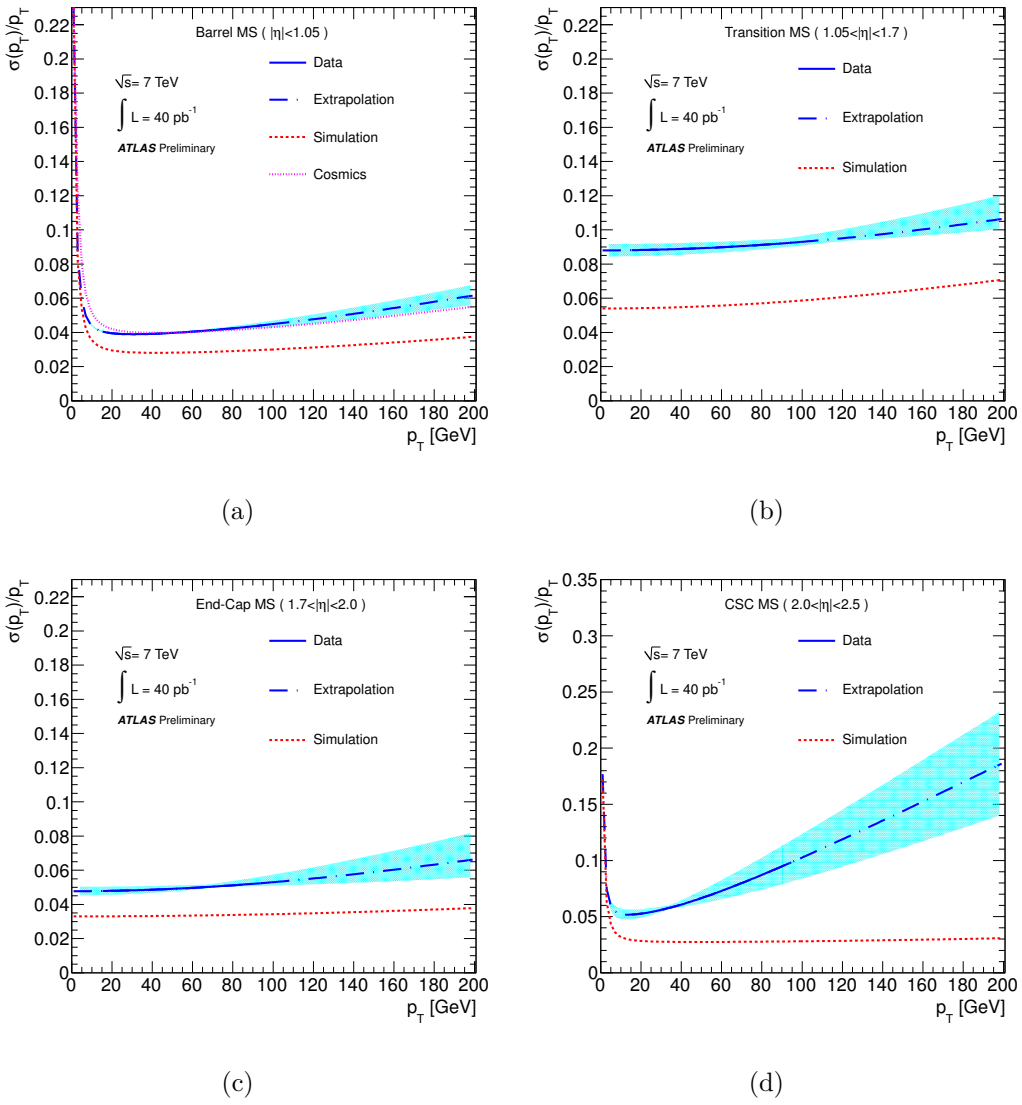

Figure 5-17: Muon spectrometer resolution curves obtained from the fitted parameter values in collision data and simulation as a function of the muon p_T for the different η regions of the detector [114]. The solid blue lines show determinations based on data and are continued as dashed lines for the extrapolation to the high p_T domains not accessible. The shaded bands represent the sum in quadrature of the statistical and systematic uncertainties. (a) Barrel muon spectrometer ($|\eta| < 1.05$), (b) Transition muon spectrometer ($1.05 < |\eta| < 1.7$), (c) End-cap muon spectrometer ($1.7 < |\eta| < 2.0$) and (d) CSC muon spectrometer ($2.0 < |\eta| < 2.5$). For the case of the barrel region, a comparison with the curves obtained from cosmic ray data is overlaid for comparison.

η region	p_0^{MS} (TeV)	p_1^{MS} (%)	p_2^{MS} (GeV^{-1})	p_1^{ID} (%)	p_2^{ID} (TeV^{-1})
Barrel	0.23 ± 0.01	3.75 ± 0.10	0.24 ± 0.04	1.60 ± 0.32	0.49 ± 0.04
Transition	0	8.80 ± 0.46	0.30 ± 0.16	2.60 ± 0.54	0.95 ± 0.10
End-caps	0	4.77 ± 0.35	0.23 ± 0.12	3.40 ± 0.58	1.39 ± 0.05
CSC/no TRT	0.17 ± 0.02	4.87 ± 0.65	0.90 ± 0.25	4.10 ± 0.50	0.140 ± 0.004

Table 5.2: Values of the muon momentum resolution parameters as defined in Equations 5.18 and 5.19 for the spectrometer and the inner detector. The parameter values are given for the four pseudorapidity regions: (a) Barrel muon spectrometer ($|\eta| < 1.05$), (b) Transition muon spectrometer ($1.05 < |\eta| < 1.7$), (c) End-cap muon spectrometer ($1.7 < |\eta| < 2.0$) and (d) CSC muon spectrometer ($2.0 < |\eta| < 2.5$). The measurements are obtained by adding the correction parameters in quadrature to the uncorrected momentum resolution given by the simulation [114].

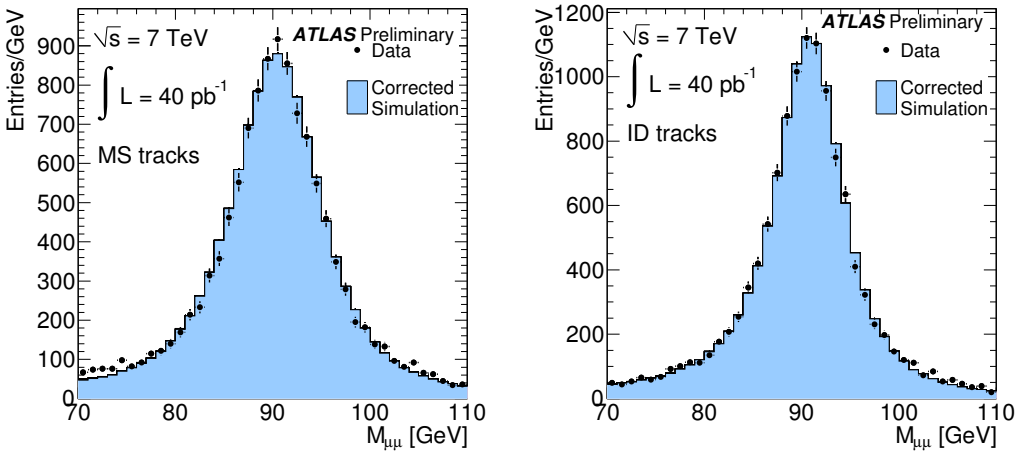

(a) (b)

Figure 5-18: Measured dimuon invariant mass in the Z boson mass range compared to the Monte Carlo simulations after correction of the simulated momentum resolution according to Equation 5.26. (a) muons from spectrometer tracks and (b) muons from inner detector tracks.

inputs is then executed in a second step.

Jets are made of one or more topological clusters (topoclusters) [119], which are actually groups of calorimeter cells neighboring to each other in the three-dimensional space. A topocluster is formed from a seed cell whose signal-to-noise ratio (the energy deposited in the calorimeter cell over the standard deviation of the energy distribution measured in random events) is above a threshold of 4. Then this initial topocluster grows by merging the neighboring cells once their signal-to-noise ratios are larger than 2. In this newly formed topocluster, the cell with the local maximum energy deposit will be set as a seed and the topocluster formation procedure will be implemented

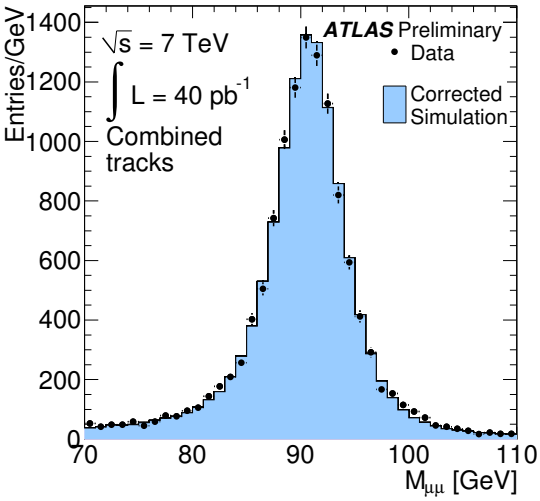

Figure 5-19: Measured dimuon invariant mass in the Z boson mass range for Combined muons compared to the Monte Carlo simulations after correction of the simulated momentum resolution according to Equation 5.26.

iteratively. The topocluster will be splitted into smaller topoclusters in each iteration. The iteration will stop when the local maximum energy deposit in this iteration is the same as the one in the previous step. In the end, the topocluster is fixed and its energy is computed as the sum of the energy of all the included cells. The four momentum of the topocluster is calculated with its energy and the direction reconstructed in the calorimeters, assuming that the mass is zero.

In the jet-finding stage, the topoclusters will be used as inputs to a certain finding algorithm, which will group and merge the topoclusters into jets. The jets used in the analysis presented in this thesis are reconstructed by the anti-k_t algorithm [120] using the FastJet software [121, 122]. In this algorithm, the distance d_{ij} between two topoclusters i and j, and the distance d_{iB} between the topocluster i and the beam B are defined as follows:

$$d_{ij} = \min(k_{ti}^{-2}, k_{tj}^{-2}) \frac{\Delta_{ij}^2}{R^2} \tag{5.27}$$

$$d_{iB} = k_{ti}^{-2} \tag{5.28}$$

where $\Delta_{ij}^2 = (y_i - y_j)^2 - (\phi_i - \phi_j)^2$, and k_{ti}, y_i and ϕ_i are the transverse momentum, the rapidity and the azimuthal angle of the topocluster i, respectively. The parameter R defines the radius of the finding algorithm, which is set to 0.4 in our case. For all the topoclusters, the distances d_{ij} and d_{iB} are calculated and the smallest distance d_{min} will be found. If $d_{min} = d_{ij}$, which means that the two topoclusters i and j are too close to each other, these two neighboring objects will be merged into one compound topocluster which will be inputed into the next iteration. If $d_{min} = d_{iB}$, the topocluster i (it could be a compound topocluster) is then defined as a jet. This procedure will be iterated until no more jets can be found.

5.3.2 Energy scale

Jets are first reconstructed at the electromagnetic scale. At this stage, the energy scale is corrected by using the invariant mass of $Z \to ee$ events as discussed in the previous section for the electron energy scale. The goal of the jet energy scale calibration is to correct the energy to the hadronic scale. The hadronic jet energy scale is on the average restored using data-derived corrections and calibration constants extracted from Monte Carlo simulations through comparisons to the truth jet information. The jet energy scale calibration is then validated with in-situ techniques. The points one needs to consider for the hadronic energy scale are the following: by design the hadronic calorimeter measures partially the energy; a fraction of the energy is lost in inactive regions of the detector; the particles pass by the calorimeter but some of their energy leak out in the hadronic calorimeter; the energy difference between the truth jet and the reconstructed jet due to different jet reconstruction; there are signal losses in calorimeter clustering and jet reconstruction.

ATLAS uses a simple calibration scheme which applies jet-by-jet corrections as a function of the jet energy and pseudorapidity at the electromagnetic scale. This calibration scheme is made of the following steps [123]: the average additional energy due to pileup is subtracted from the energy measured in the calorimeters using correction constants extracted from an in-situ measurement; the position of the jet is corrected such that the jet direction points towards the primary vertex of the interaction instead of the geometrical centre of the ATLAS detector; the jet energy and position as reconstructed in the calorimeters are corrected using constants derived from the comparison of the kinematics of reconstructed jets and the corresponding truth jets in Monte Carlo samples.

Figure 5-20 shows the average jet energy scale correction as a function of the calibrated jet transverse momentum in three pseudorapidity intervals [123]. In general, the jet energy scale corrections are larger in the central region than in the forward ones. Concerning the uncertainty estimations, several sources are taken into account: the calibration procedure brings slight deviations in the closure test done with Monte Carlo simulations; the calorimeter response is tested with the energy deposit from single particles that constitute jets, taking into account additional material in the inner detector and overall additional dead material; the different modelling of the hard subprocess and soft processes is tested in the Monte Carlo generators. The jet energy scale uncertainty in the central region reaches 2% to 4% for $p_T < 60\ GeV$, and it is between 2% and 2.5% for $60\ GeV \leq p_T < 800\ GeV$. For high p_T jets above $800\ GeV$, the uncertainty rises from 2.5% to 4% since the particles constituting the jet can have a momentum beyond $400\ GeV$ leading to larger uncertainties in the calorimeter response. In the end-caps, the uncertainty amounts to up to 7% and 3%, respectively, for $p_T < 60\ GeV$ and $p_T > 60\ GeV$, where the central uncertainty is taken as a baseline and the uncertainty due to the relative calibration is added. In the forward region, a 13% uncertainty is estimated for $p_T < 60\ GeV$, with the dominant contribution from the modelling of the soft physics in the forward region.

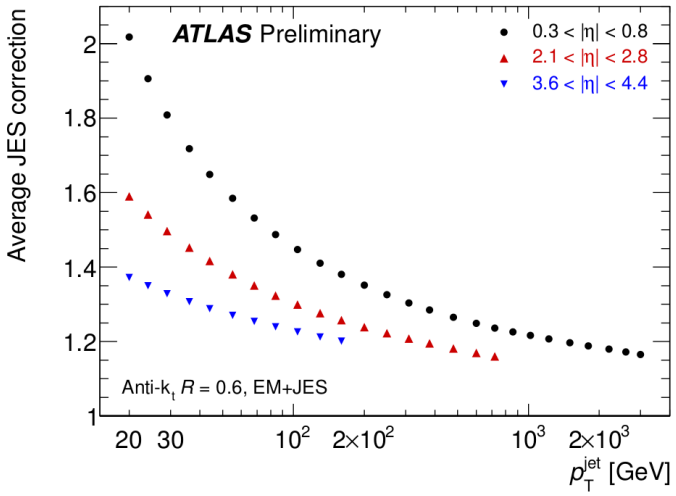

Figure 5-20: Average jet energy scale correction as a function of the calibrated jet transverse momentum for three representative η-intervals. The correction is only shown over the accessible kinematic range, i.e. values for jets above the kinematic limit are not shown [123].

5.4 Missing transverse momentum

The reconstruction of the missing transverse momentum, E_T^{miss}, follows the momentum conservation in the transverse plane. It is calculated by the opposite of the sum of all the transverse momenta. Taking into account all significant energy deposits in the calorimeters and the muons reconstructed in the muon spectrometer, the calculation of the missing transverse momentum E_T^{miss} consists of:

$$E_{x,y}^{miss} = E_{x,y}^{miss,calo} + E_{x,y}^{miss,\mu} \tag{5.29}$$

$$E_T^{miss} = \sqrt{(E_x^{miss})^2 + (E_y^{miss})^2}. \tag{5.30}$$

The calibration of E_T^{miss} is done with all reconstructed physics objects to which the calorimeter cells are associated. All of the calorimeter cells are associated with a reconstructed and identified high-p_T parent object in a chosen order: electrons, photons, hadronically decaying τ-leptons, jets and muons. Concerning the cells not associated to any recontructed physics objects, they are taken into account by $E_T^{miss,cellout}$. Therefore the calculation of E_T^{miss} can be written as:

$$E_{x,y}^{miss} = E_{x,y}^{miss,e} + E_{x,y}^{miss,\gamma} + E_{x,y}^{miss,\tau} + E_{x,y}^{miss,jets} + E_{x,y}^{miss,softjets} + E_{x,y}^{miss,calo,\mu} + E_{x,y}^{miss,CellOut}. \tag{5.31}$$

To determine the absolute E_T^{miss} scale, one implements a fit to the distribution of the transverse mass m_T of the lepton-E_T^{miss} system by using $W \to l\nu$ events. Another method using the interdependence of the neutrino and lepton momenta in $W \to l\nu$ is also implemented for the E_T^{miss} scale. Only the first method will be discussed here.

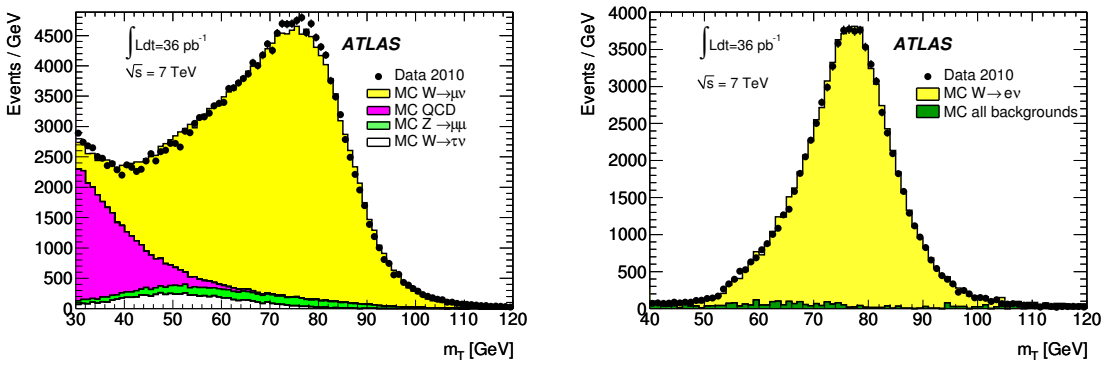

(a) (b)

Figure 5-21: Distributions of the transverse mass m_T of the lepton-E_T^{miss} system for data and Monte Carlo events. The $W \to l\nu$ Monte Carlo signal template is obtained using the E_T^{miss} after smearing with the scale and resolution parameters obtained from the fit [124]. (a) Distribution for the muon channel and (b) distribution for the electron channel.

The transverse mass m_T of the lepton + neutrino is reconstructed as follows:

$$m_T = \sqrt{2p_T^l E_T^{miss}(1 - cos\phi)} \tag{5.32}$$

where ϕ is the azimuthal angle between the lepton and E_T^{miss}. The template of the distribution of m_T is generated by convoluting the transverse mass distribution described above with a Gaussian function:

$$E_T^{miss,smeared} = \alpha E_{x,y}^{miss} \cdot Gauss(0, k \cdot \sqrt{\Sigma E_T}) \tag{5.33}$$

where the parameters α and k are the E_T^{miss} scale and the resolution respectively. Then the smeared distribution of m_T is used to fit the data in order to extract α and k. As shown in Figure 5-21, the distributions of m_T are drawn with the data and the fitted templates in good agreement [124]. The fitted values for the E_T^{miss} scale and the resolution are listed in Table 5.3. The E_T^{miss} scale $\alpha - 1$ is around 5% for muon events (both data and Monte Carlo simulation), while it is compatible with 0 for electron events (both data and simulation). The E_T^{miss} resolution is always around 0.50 for both muon and electron events (both data and MC).

The systematic uncertainties for the measured E_T^{miss} depend on the uncertainties coming from each terms in Equation 5.31, which are different from one analysis to another considering their different final states. In fact, these uncertainties concerning the terms of the physics objects such as $E_{x,y}^{miss,e}$ and $E_{x,y}^{miss,jets}$, will be automatically propagated to the final measurements in each analysis by the calculation in Equation 5.31. So the only terms of which one should evaluate the uncertainties explicitly are $E_{x,y}^{miss,CellOut}$ and $E_{x,y}^{miss,softjets}$. The overall uncertainty from $E_{x,y}^{miss,CellOut}$ on the scale is 13% after considering the effects from the dead materials in the detector as well as the different shower models. The overall uncertainty from $E_{x,y}^{miss,softjets}$

on the scale is evaluated to be about 10% after considering the same effects as in $E_{x,y}^{miss,CellOut}$ [124].

Channel	$\alpha - 1$ (%)	k
$W \to \mu\nu$ data	5.1 ± 0.8	0.52 ± 0.01
$W \to \mu\nu$ MC	5.5 ± 0.8	0.50 ± 0.01
$W \to e\nu$ data	-0.8 ± 1.6	0.49 ± 0.01
$W \to e\nu$ MC	1.8 ± 1.7	0.50 ± 0.01

Table 5.3: Results of the fit of the m_T distribution in $W \to l\nu$ events [124]. The second and third columns show the values obtained for the scale $\alpha - 1$ and resolution k parameters. The errors are statistical and take into account background subtraction uncertainties and correlations.

5.5 Luminosity measurement

The Luminosity quantifies the amount of collisions (data) delivered by the LHC or recorded by the ATLAS acquisition system. The luminosity appears in all physics measurements, since the number of events associated to any physics process is equal to $N = L \times \sigma \times \epsilon$, where L is the integrated luminosity, σ the cross section and ϵ the selection efficiency. The uncertainty of the luminosity will thus be propagated into any physics measurements or searches.

In the LHC beam, the protons are grouped into bunches, and the interaction between two protons (the event) takes place in a bunch crossing (a collision). In previous low luminosity colliders, there were a few interactions among many bunch crossings, but in the LHC, which is a high luminosity collider, there can be as many as 30 to 40 interactions in each bunch crossing. Regardless the problems caused by multiple interactions per bunch crossing, the luminosity can benefit from the increase of the number of interactions in one bunch crossing as well as the number of bunches in each LHC "fill". The LHC operates with "fills" which contain a fixed number of bunches. One "fill" can last several hours for collisions. From Table 5.4, one can explain the significantly increased luminosity from 2010 to 2011: with a shorter bunch spacing and a longer fill, one can have more bunches per fill (from 348 to 1331); with larger bunch proton densities (bunch population from 0.9 to 1.2), the interactions in each bunch crossing increase. In the end, the total delivered luminosity is 48 pb^{-1} for 2010 and $5.6 fb^{-1}$ for 2011.

At the interact point, the luminosity is measured with the equation:

$$L = \frac{\mu_{vis} n_b f_r}{\sigma_{vis}} \tag{5.34}$$

where $\sigma_{vis} = \epsilon \sigma_{inelastic}$ is the total inelastic cross section multiplied by the efficiency ϵ of a particular detector and algorithm, and similarly for the observed interaction rate per bunch crossing $\mu_{vis} = \epsilon\mu$. n_b is the bunch number and f_r is the revolution

Parameter	2010	2011
Maximum number of bunch pairs per fill	348	1331
Minimum bunch spacing (ns)	150	50
Typical bunch population (10^{11} protons)	0.9	1.2
Peak luminosity (10^{33} cm^{-2} $s-1$)	0.2	3.6
Maximum inelastic interactions per crossing	~ 5	~ 20
Total integrated luminosity delivered	48 pb^{-1}	5.6 fb^{-1}

Table 5.4: Some LHC parameters for pp colissions at $\sqrt{s} = 7\ TeV$ in 2010 and 2011 [125]. Comparisons of the parameters between 2010 and 2011 give the reasons of the significantly increased luminosity in 2011.

frequency. n_b and f_r are taken from the LHC, while μ_{vis} can be measured by several detectors discussed soon. Therefore, the calibration of the luminosity scale is equivalent to the determination of the visible cross section σ_{vis}.

To measure μ_{vis}, counting algorithms are developed with the corresponding detectors. The inner detector is used for the determination of the primary vertices in pp collisions. The Beam Conditions Monitor (BCM) that consists of four small diamond sensors, are located at $|\eta| = 4.2$ close to the beam, whose four sensors give counting results independently. The LUCID detector discussed in Section 4.8 covers $5.6 < |\eta| < 6.0$ and provides 30 counting channels.

To determine the visible cross section σ_{vis}, the information from the beam line luminosity is needed. It is performed by beam-separation scans at the collision point, known as "van der Meer" (vdM) scans. During these scans, the absolute luminosity can be inferred from direct measurements of the beam parameters [126, 127]:

$$L = \frac{n_b f_r n_1 n_2}{2\pi \Sigma_x \Sigma_y} \tag{5.35}$$

where $\Sigma_{x,y}$ are the horizontal and vertical convolved beam widths which can be measured directly from the separated two beams in "van der Meer" scans. With the bunch population $n_1 n_2$ from external measurements, one can determine σ_{vis} as follows:

$$\sigma_{vis} = \mu_{vis}^{MAX} \frac{2\pi \Sigma_x \Sigma_y}{n_1 n_2} \tag{5.36}$$

where μ_{vis}^{MAX} is the visible interaction rate per bunch crossing observed at the peak of the scan curve as measured by that particular algorithm.

Considering all the uncertainties propagated from the calibration of σ_{vis}, one can determine the luminosity and its overall uncertainty. At the center of mass energy of 7 TeV, a luminosity uncertainty of $\Delta L/L = \pm 3.4\%$ is obtained for the 48 pb^{-1} of data delivered to ATLAS in 2010, and an uncertainty of $\Delta L/L = \pm 1.8\%$ is obtained for the 5.6 fb^{-1} delivered in 2011. In this thesis, the full data recorded by ATLAS in 2011 are used.

5.6 Data quality

During the data taking, the environment and the status of the detector must be monitored on a regular basis and the Data Quality (DQ) has to be evaluated. This quality monitoring can help the analyzers to avoid badly recorded data in particular due to the high-voltage failure and hardware trips, and also can give a chance to access the badly recorded data which could be possibly recovered afterwards.

The data is monitored online and offline to give a full state of the detector and data taking environment, which are summarized and recorded in a general file "Good Run List". The good run list file contains the flags for the data quality, which reflect the overall status of the ATLAS detector and its subdetectors. They act as traffic lights, with the defined colors (from bad to good): black (sub-detector off), grey (undefined), red (bad data), yellow (use with caution, experts should decide), and green (data good). The flags are assigned for every subsystem per luminosity block (LB), which is a basic time unit of data taking. The boundaries of each luminosity block is controled by the Center Trigger Processor (CTP), and in general, the duration is around one minute for each of them. For each luminosity block, the corresponding information is recorded such as the prescale [2] changes due to the trigger configuration changes, the integrated luminosity, and the detector status as well as conditions within the same luminosity block. Figure 5-22 shows the proportions of events with overall data quality "good" in each subdetectors for 2011. In general, all detectors show excellent performance, except the electromagnetic calorimeter whose proportion of "good" qualified data is 96.9% due to six dead front-end boards (FEB) used for the electronic readout in the barrel of the electromagnetic calorimeter in 2011.

ATLAS p-p run: March-October 2011

Inner Tracker			Calorimeters		Muon Spectrometer				Magnets	
Pixel	SCT	TRT	LAr	Tile	MDT	RPC	CSC	TGC	Solenoid	Toroid
99.8	99.6	99.2	96.9	99.2	99.4	98.8	99.4	99.1	99.8	99.3

All good for physics: 89.9%

Luminosity weighted relative detector uptime and good quality data delivery during 2011 stable beams in pp collisions at √s=7 TeV between March 13th and October 30th (in %) - corresponding to 5.2 fb^{-1} of recorded data. This data quality status refers to the data after the summer reprocessing campaign.

Figure 5-22: Data quality status for each subdetector system during the 2011 stable beams in pp collisions at $\sqrt{s} = 7\ TeV$ between March 13^{th} and October 30^{th}.

[2] Trigger selects 1 event out of N events, then the prescale is N, which is usually larger than one.

Chapter 6

Simulations and data

The measurement discussed in this document uses single top quark t-channel events with leptonically decayed W bosons, characterized by a final state "l+jets". In Section 6.1, simulations are discussed first with considerations on the phenomenology, the event topology and the Monte Carlo generator for the t-channel events as well as the expected Standard Model backgrounds including other single top quark channels, top quark pair, W/Z+jets, diboson and QCD multijet processes, followed by a brief description of the simulation of pileup events. Finally, the recorded ATLAS data used by this measurement are described in Section 6.2.

6.1 Event topology and simulations

Events produced by a certain physics process are characterized by their final state topology in the detector. One can pay efforts to make sequential cuts or construct a discriminator[1] according to the specific signal topology to suppress as much background events as possible while keeping as much signal events as possible. However, background events can partially survive the selection cuts due to their same final state or similar final states that are misidentified like signal events. These background events need to be studied and estimated precisely in order to get a trustable final measurement.

The purpose of simulations is double: they allow first to study the performances of the detector response and of the reconstruction algorithms; secondly they allow to decompose the data into signal and background components in order to be able to propagate the uncertainties associated to each component to the final measurements. For each component that comes from a given physics process, one can simulate events with a dedicated or general event generator which applies Monte Carlo techniques to the corresponding physics model. This physics model should be connected to parton

[1] A discriminator is a variable calculated from one or more kinematic variables that characterize the signal from the backgrounds, such as the neural network discriminator (NN), or the boosted decision tree discriminator (BDT). Usually, the purpose is to have a more discriminating power from many variables to separate the signal from backgrounds, when it cannot be achieved by a single variable.

distribution functions, discussed in Section 3.2.2, since hadrons are initially colliding. After simulation of the hard physics process, the parton shower and the hadronization processes should be connected; they are respectively due to the gluon emission and evolution of the quarks discussed in Section 3.2. In the final step, one needs to pass the generated events to the detector simulations to mimic the interactions between the generated particles and the detector materials, followed by the digitization step, which allows to convert all the detector hits into electronic signals similarly to what one gets from the ATLAS electronics with real collisions. In the digitization step, one can also introduce multiple interactions and pileup effects to each physics event. At this stage, the simulations are complete and can therefore be used in the analysis.

6.1.1 Single top quark t-channel

As introduced in Section 3.5.2, single top quark t-channel events are produced by W-gluon fusion, which leads to an event topology of one charged lepton, one neutrino, one light quark and two b-quarks, as shown in Figure 6-1. Such an event topology with a charged lepton corresponds to the leptonic decay of the W boson coming from the top quark. This leptonic t-channel event will eventually evolve into a final state constituted of one isolated lepton with a high transverse momentum, a high missing transverse momentum due to the neutrino, one light jet, one b-jet in the central pseudorapidity region of the detector and one b-jet in the forward region. This signature, called "l+jets", is more recognizable from background topologies than the one resulting from a hadronic decay of the W boson, because the latter will lead to five jets in the final state which could hardly be separated from top quark pair production ($t\bar{t}$) as well as from QCD multijet events. The event selections, presented in Section 8.2, which will be performed to find signal events and to suppress background contamination, will consist in topological requirements based on the "l+jets" final state and in additional kinematic cuts to take into account the specific parton kinematics expected for t-channel production.

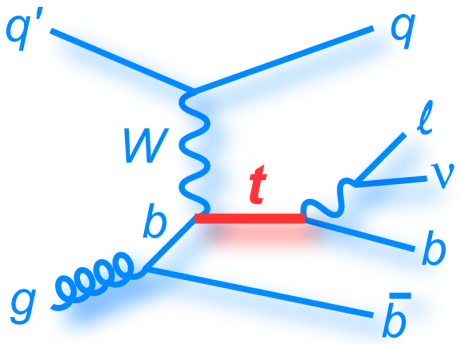

Figure 6-1: Feynman diagram ($2 \rightarrow 3$ process) for single top quark t-channel production and leptonic decay.

The analyzed events will be artificially divided into two categories, the electron channel and the muon channel, because they have different reconstructions and per-

formances leading to different calibrations and corrections. These two categories of events being orthognal, "one and only one" lepton is required which could be either an electron or a muon coming from the W boson decay. The tau lepton final state does not lead to a dedicated channel since it will decay either hadronically to several jets which will not be selected, or leptonically to an electron or a muon which could be naturally selected into the two channels defined above. The leptonic tau decay contributes to almost 10% of the selected events; tau events are simulated with dedicated samples.

The lepton is required to be isolated which means that it should have few tracks and a low electromagnetic calorimeter activity around it. This isolation requirement allows to select lepton decaying from a W boson and not from a heavy jet (i.e. a jet formed from a heavy c or b-quark), since in the latter case the lepton would be produced within a shower full of tracks and energy deposits making it non-isolated. Furthermore, the lepton flies out with a high transverse momentum whose distribution peaks around $30 - 40\ GeV$; the W boson indeed passes around half of its energy to the lepton momentum which actually cannot be lower than half of the W boson mass. The same amount of energy will be passed to the neutrino, which leads to the requirement of a high measured missing transverse momentum.

There are three jets in the t-channel final state: a forward light jet called spectator due to the forwardly scattered light quark, a central b-jet due to the b-quark decaying from the top quark and a forward soft b-jet due to the gluon splitting in the initial state. The light and b-jets can be separated by a so-called b-tagging algorithm, which makes use of the long life-time of B hadrons, recognizing a b-jet as a b-tagged jet and a light jet as an untagged jet in most of the cases. The scattered forward light jet has a transverse momentum distribution p_T peaked at around $30 - 40\ GeV$. The central b-tagged jet decaying from the massive top quark has a hard p_T distribution peaked at around $60\ GeV$ and flies out centrally. To suppress backgrounds with soft jets, a high-p_T threshold, between 20 and 30 GeV, is required for each jet, and additionally, the b-tagged jet is required to have a central pseudorapidity ($|\eta| < 2.5$). The forward soft b-jet produced in t-channel events has a p_T distribution peaked below $10\ GeV$, which does not pass the usual high-p_T threshold used in the analysis. Furthermore, it usually flies forwardly out of the acceptance of the b-tagging algorithms which are based on vertexing information from the inner tracker which has a limited pseudorapidity acceptance ($|\eta| < 2.5$). Therefore, for the measurements presented in this thesis, one requires to have exactly two jets in the events; nevertheless, events with three jets could be used in the future to define control regions in order to add in particular more constraints on the $t\bar{t}$ background events.

In summary, the t-channel event selection requires exactly one isolated high-p_T lepton, a high missing transverse momentum and exactly two high-p_T jets one of them being b-tagged and the other one untagged.

At the center of mass energy of 7 TeV, the theoretical t-channel cross section is 64.6 pb [52] (it gives 21.03 pb for the W boson leptonic decay, the branching ratio for each lepton flavor being 0.108 as discussed in Section 3.3). The simulated events are generated with the AcerMC multi-leg leading order (LO) generator [128] using the MRST LO** [129] parton distribution functions (PDFs), which correspond to a

modified set with more next-to-leading order compatibility when leading order matrix elements are connected. This process is produced by merging the two subprocesses presented in Section 3.5.1: $q+g \to q'+t+b$ $(2 \to 3)$ and $q+b \to q'+t$ $(2 \to 2)$. In the latter an additional b-quark distribution function is introduced in the proton. The matching and overlapping problems between the two subprocesses in the AcerMC generator are handled by an automated procedure, called ACOT algorithm, described in [130], which basic idea is to sum up the $2 \to 2$ diagram at the order of $\alpha_s^{(0)}$ and the $2 \to 3$ diagram at the order of $\alpha_s^{(1)}$ with the "subtraction term" at the order of $\alpha_s^{(1)}$, where α_s stands for the QCD coupling constant. Consequently, this subtraction procedure introduces negative event weights. The parton shower connected to the AcerMC generator is realized by Pythia [36].

6.1.2 Single top quark backgrounds

The other two single top quark processes, Wt associated production and s-channel, are backgrounds to the t-channel process due to the fact that both of them have a signature similar to the signal one and therefore pass the event selection. The Wt process, shown in Figure 6-2(b), produces a single top quark associated with a W boson. After top quark decay, there will be two W bosons, each of them being able to decay leptonically or hadronically. In particular, when one of the two W bosons decays leptonically and the other one hadronically, the Wt process leads to a "l+jets" final state. Concerning s-channel, as shown in Figure 6-2(c), the top quark is associated with a b-quark that will evolve into a jet and the final state will also be "l+jets".

At the center of mass energy of 7 TeV, the Wt events are produced with a cross section of 15.7 pb [53], while the s-channel events are produced with a cross section of 4.63 pb [54]. They are irreducible backgrounds due to the real top quark produced in the processes but they are actually minor backgrounds to t-channel events, considering their smaller cross sections. Wt and s-channel events are generated with the PowHeg next-to-leading order (NLO) generator [131] using CT10 [132] as PDFs. This generator overcomes the problem of negatively weighted events found in the generator MC@NLO used in the previous analyses. The parton shower and hadronization are realized by Pythia.

6.1.3 Top quark pair background

The production process of top quark pairs ($t\bar{t}$), as shown in Figure 6-2(a), leads to two W bosons and two b-quarks. Considering the decay modes of the W boson introduced in Section 3.3, $t\bar{t}$ events could have the following final states: "6jets" when both W bosons decay hadronically (branching ratio of 0.46), "l+4jets" when one of the two W bosons decays leptonically (branching ratio of 0.44) and "2l+2jets" when both W bosons decay leptonically (branching ratio of 0.10). The $t\bar{t}$ events with a fully hadronic decay can hardly pass the event selection due to their high jet multiplicities, while the events with a semileptonic or a dileptonic decay can contribute significantly to the backgrounds of the single top quark analyses when some jets are missing in the

semileptonic decay from the reconstruction step or one of the two leptons is missing in the dileptonic decay.

The $t\bar{t}$ production rate is almost three times the single top quark production rate, the production cross section of top quark pairs being $166.8^{16.5}_{17.8}\ pb$ at $\sqrt{s} = 7\ TeV$ [133]. This process is therefore a large background to single top quark events due to its real top quarks and its large cross section. The simulated $t\bar{t}$ events are generated with the POWHEG NLO generator [131] using CT10 [132] as PDFs. The parton shower is realized by PYTHIA.

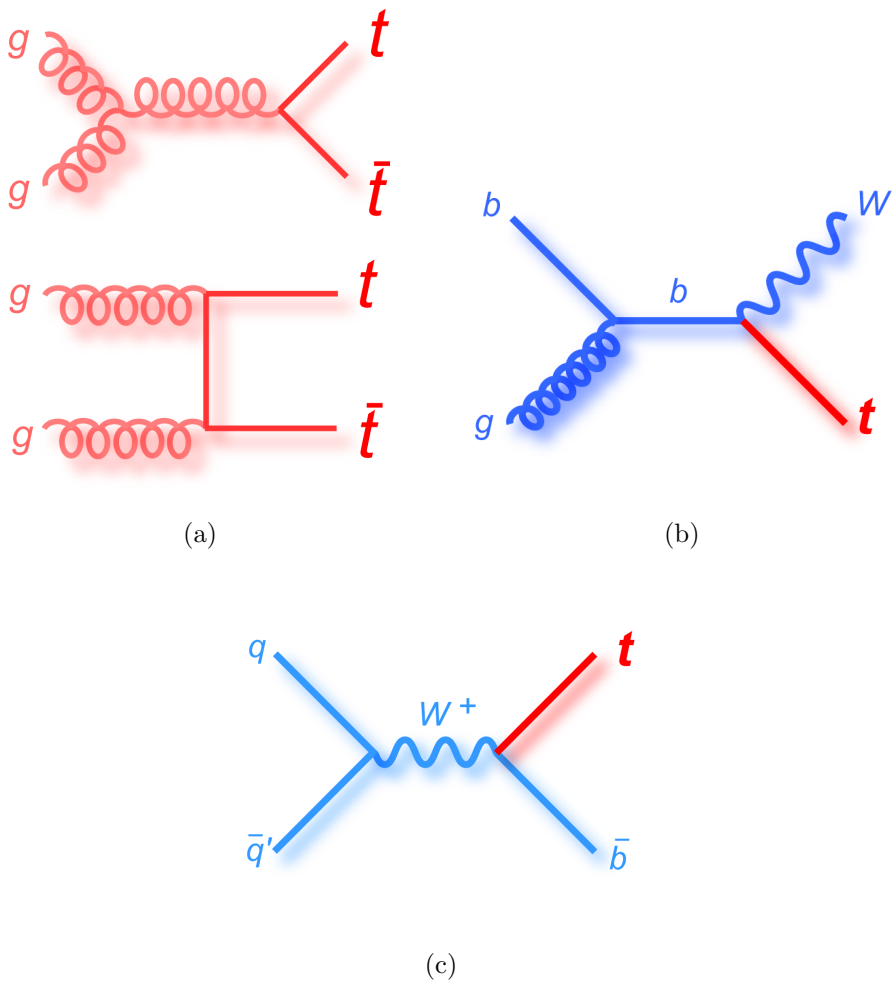

Figure 6-2: Feynman diagrams for top quark production processes (a) top quark pair production, (b) Wt associated production and (c) single top quark s-channel production.

6.1.4 W+jets backgrounds

$W+jets$ processes produce events with a real W boson that could decay (leptonically) into a charged lepton and a neutrino, leading to a final state "l+jets". These events have almost the same transverse momentum p_T distributions than the signal events

after the high-p_T requirements applied. The only difference exists in the distribution of the reconstructed top quark mass, the distribution of the corresponding invariant mass for the $W + jets$ events being peaked at lower values than for events containing a real top quark.

The $W + jets$ events are categorized into $W + heavy\,jets$ ($Wb\bar{b}+ jets$, $Wc\bar{c}+ jets$, $Wc+ jets$) events due to some of the jets coming from a heavy flavor quark (i.e. from a c or a b-quark), otherwise the events are categorized into $W + light\ jets$ events. The $W + heavy\ jets$ events are more similar to the signal ones due to their higher probability of having finally b-tagged jets. They are therefore expected to be the dominant background process after event selections.

If only considering the leptonic decay, the $W + light\,jets$ events are produced with a cross section of around 10480 pb at the center of mass energy of 7 TeV while the $W + heavy\,jets$ events are produced with a cross section of around 1879 pb. $W + jets$ events are generated with the ALPGEN LO generator [134] using CTEQ6L1 [135] as PDFs. Samples of $W + light\,jets$ and $W + heavy\,flavor\,jets$ are produced separately due to the badly-known fractions of $W + jets$ events containing heavy flavor jets. These flavor fractions will be corrected in the analysis using data-driven procedures as well as the overall $W + jets$ normalization 8.5. The parton shower interfaced to the event generator is HERWIG.

6.1.5 Z+jets and diboson backgrounds

Z+jets processes produce events with a Z boson that could decay into a lepton pair leading to a final state "l+jets" when one of the leptons is missing after the reconstruction step. The diboson processes, such as WW, WZ, ZZ, produce two vector bosons and one of them could decay leptonically and the other one hadronically leading to a "l+jets" final state. At the center of mass energy of 7 TeV, Z+jets events are produced with a cross section of around 1072 pb which is less than one tenth of the $W + jets$ production cross section, while diboson events are produced with a rather smaller cross section of around 24 pb. Considering the possibility of missing a lepton in the reconstruction (around 20% are not reconstructed as discussed in Section 5.1.6) and their relatively small cross sections, these two processes are minor backgrounds of t-channel events. $Z + jets$ events are generated with the ALPGEN LO generator [134] using CTEQ6L1 [135] as PDFs. Diboson processes are produced with the HERWIG generator [37]. In both cases, the parton shower interfaced to the event generator is HERWIG.

6.1.6 QCD multijet backgrounds

QCD multijet events are produced with several jets in the final state and one of them could be misidentified as an electron or a muon, leading to a final state "l+jets". In the case of a jet misidentified as an electron, the jet gives an electromagnetic shower with measured properties quite close to the one expected for an electron, such as a narrow shower width or a low leakage in the hadron calorimeter. In the case of a jet misidentified as a muon, the corresponding hadron that evolves into the jet could

leptonically decay into a muon which is actually non-isolated but which could pass the isolation criteria. Depending on the isolation criteria, the efficiency of selecting non-isolated muons is about 10% to 30% which is much less than the efficiency of selecting real isolated muons (ususally above 80%).

At the center of mass energy of 7 TeV, QCD multijet events are produced with a huge cross section up to 10^8 pb. Considering its overwhelming production rate and the sizeable misidentification probability, this background could be a non-negligible contribution to the selected events, usually 5% to 10%. QCD multijet background events are generated with the PYTHIA generator [36]. Events are produced from the dominant dijet process and are filtered with a jet transverse energy threshold $E_T > 17$ GeV. Actually, the QCD background is usually estimated from the data due to its large theoretical cross section uncertainty. In the electron channel, the simulated QCD events are used to model the kinematics thanks to its larger statistics compared to the data, the normalization being derived from the data. For the muon channel, both the kinematic modeling and the normalization are extracted from the data (in that case, data samples with loosened selection criteria are considered and their statistics is sufficient to achieve a reliable modeling of the kinematics). The parton shower connected to the PYTHIA dijet generator is realized by HERWIG.

6.1.7 Monte Carlo samples

The simulated samples for the various physics processes are listed in Table 6.1 for the top-quark processes and in Table 6.2 for processes without any top quark. In the generated top quark samples, a top quark mass of 172.5 GeV is assumed.

Concerning the generator systematic uncertainties, dedicated samples are produced. For t-channel, samples produced by the generator PROTOS interfaced to PYTHIA [76] with the Standard Model configuration are compared with the default samples produced with ACERMC interfaced to PYTHIA to estimate the generator uncertainty. Additional samples produced by PROTOS with non-standard parameterizations are used to study the interplay between anomalous Wtb couplings and polarization observables (to be discussed in Chapter 7). For the $t\bar{t}$ process, samples generated by MC@NLO interfaced to HERWIG are compared with the samples generated by POWHEG also interfaced to HERWIG in order to estimate the generator uncertainty. Samples generated by ACERMC interfaced to PYTHIA, tuned with more and less radiations, are used to estimate the ISR/FSR (initial/final state radiation) uncertainties for all top quark processes.

From above, only the generators simulating the physics processes and the parton shower are introduced. In fact, there are two additional steps in the ATLAS simulation framework [136] to provide fully simulated events: (i) the simulation of the detector, which considers the effects of particle interactions with the detector materials (ii) the digitization procedure, which converts the energies deposited in the sensitive regions of the detector into voltage and current signals that mimic the real data that would be taken from the detector electronics.

The simulation of the detector geometry, of the particle interactions with detector materials and of the electronic responses are realized by GEANT4 [137, 138] which

Process	σ (pb^{-1})	Generator	MC statistics
t-channel(e+jets)	6.94	AcerMC+Pythia	1000k
t-channel(μ+jets)	6.83	AcerMC+Pythia	1000k
t-channel(τ+jets)	7.26	AcerMC+Pythia	1000k
s-channel($e/\mu/\tau$+jets)	1.508	PowHeg+Pythia	200k
Wt inclusive	15.74	PowHeg+Pythia	200k
$t\bar{t}$ not fully hadronic	90.57	PowHeg+Pythia	2000k

Table 6.1: Cross sections and generator information for top quark involved processes. The cross sections are from approximate next-to-next-to-leading-order calculations [52, 53, 54, 133]. MC statistics stand for the numbers of generated events.

is a generic toolkit for detector simulations.

The fully simulated events are then submitted to the physics object recontruction algorithms described in Chapter 5 and to the event selection presented in Chapter 8 to search for and reconstruct the interesting events.

6.1.8 Pileup simulations

Besides the various simulation ingredients discussed previously, one important effect that cannot be ignored in the simulation, especially in high luminosity hadron collisions, is the contribution of pileup events. In order to simulate these effects, the ATLAS framework takes the approach of overlaying additional simulated interactions onto a given physics event under the same detector geometry during the last digitization stage of the full simulation chain described in the previous section.

There are mainly two types of pileup effects considered and they are independently simulated and overlaid onto the physics events: the in-time and out-of-time pileups. The in-time pileup interactions mainly come from minimum bias and cavern background events. Minimum bias event is a generic term refering to events which are selected with a "loose" trigger that accepts a large fraction of the overall inelastic cross section. They are usually events with a very soft kinematics. Cavern background events include mainly thermalised slow neutrons, long-lived K^0 mesons and low-energy photons escaping from the calorimeters, the forward beam and the shielding elements. The out-of-time pileup effects come from the fact that the time-window for data acquisition is significantly longer than a single bunch crossing and usually covers several bunch crossings. For example, the Monitored Drift Tubes require an overall integration time window from -36 to +32 bunch crossings around the simulated signal event due to the 400-1200 ns drift time.

6.2 Data

The datasets used in the measurement correspond to the proton-proton collisions delivered by the LHC in 2011 at the center of mass energy $\sqrt{s} = 7\ TeV$. Figure 6-

Process	σ (pb^{-1})	K-factor	Generator	MC statistics
$Z \to ll + 0\,partons$	668	1.25	ALPGEN+HERWIG	24000k
$Z \to ll + 1\,partons$	134	1.25	ALPGEN+HERWIG	6000k
$Z \to ll + 2\,partons$	41	1.25	ALPGEN+HERWIG	5000k
$Z \to ll + 3\,partons$	11	1.25	ALPGEN+HERWIG	1600k
$Z \to ll + 4\,partons$	2.9	1.25	ALPGEN+HERWIG	440k
$Z \to ll + 5\,partons$	0.8	1.25	ALPGEN+HERWIG	145k
$W \to l\nu + 0\,parton$	6920	1.2	ALPGEN+HERWIG	17000k
$W \to l\nu + 1\,partons$	1300	1.2	ALPGEN+HERWIG	12000k
$W \to l\nu + 2\,partons$	380	1.2	ALPGEN+HERWIG	11000k
$W \to l\nu + 3\,partons$	100	1.2	ALPGEN+HERWIG	3000k
$W \to l\nu + 4\,partons$	26	1.2	ALPGEN+HERWIG	1700k
$W \to l\nu + 5\,partons$	7	1.2	ALPGEN+HERWIG	900k
$W \to l\nu + b\bar{b} + 0\,parton$	47	1.2	ALPGEN+HERWIG	475k
$W \to l\nu + b\bar{b} + 1\,partons$	36	1.2	ALPGEN+HERWIG	360k
$W \to l\nu + b\bar{b} + 2\,partons$	17	1.2	ALPGEN+HERWIG	175k
$W \to l\nu + b\bar{b} + 3\,partons$	7	1.2	ALPGEN+HERWIG	70k
$W \to l\nu + c\bar{c} + 0\,parton$	128	1.2	ALPGEN+HERWIG	1275k
$W \to l\nu + c\bar{c} + 1\,partons$	105	1.2	ALPGEN+HERWIG	1050k
$W \to l\nu + c\bar{c} + 2\,partons$	52	1.2	ALPGEN+HERWIG	525k
$W \to l\nu + c\bar{c} + 3\,partons$	17	1.2	ALPGEN+HERWIG	170k
$W \to l\nu + c + 0\,parton$	644	1.52	ALPGEN+HERWIG	6500k
$W \to l\nu + c + 1\,partons$	205	1.52	ALPGEN+HERWIG	2070k
$W \to l\nu + c + 2\,partons$	51	1.52	ALPGEN+HERWIG	520k
$W \to l\nu + c + 3\,partons$	11	1.52	ALPGEN+HERWIG	115k
$W \to l\nu + c + 4\,partons$	3	1.52	ALPGEN+HERWIG	30k
WW	11.5	1.48	HERWIG	250k
WZ	3.46	1.60	HERWIG	250k
ZZ	0.97	1.30	HERWIG	250k

Table 6.2: Cross sections and generator information for vector boson production processes. The K-factors give the corrections needed to go from leading order calculation to next-to-leading order calculation. MC statistics stand for the numbers of generated events.

3(a) shows the integrated luminosity as a function of the time (in day unit): a total integrated luminosity of 5.61 fb^{-1} was delivered by the LHC for physics (i.e. with stable beam conditions) and a total integrated luminosity of 5.25 fb^{-1} was recorded by the ATLAS apparatus. The delivered luminosity is measured with the beam parameters determined during the "van der Meer" scans and the recorded luminosity is determined from counting rates measured by the luminosity detectors presented in Section 5.5. The recorded luminosity is usually lower than the delivered one due to a slight inefficiency of the luminosity detectors (around 6% on the overall). The instan-

taneous peak luminosity delivered to ATLAS is shown in Figure 6-3(b) as a function of time. At the end of the data-taking year, the instantaneous peak luminosity reached $3.65 \times 10^{33}\ cm^{-2}s^{-1}$.

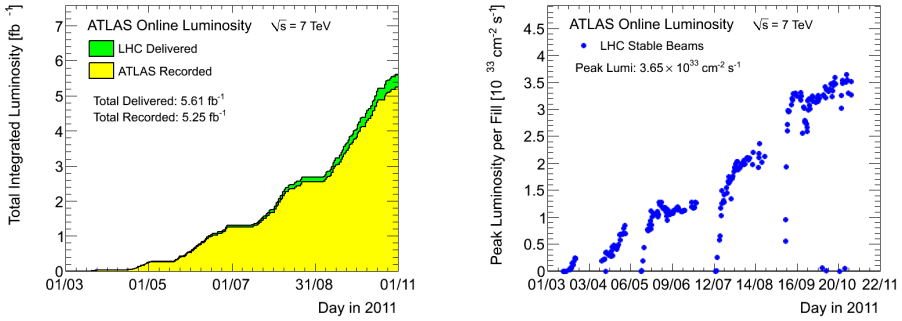

(a) (b)

Figure 6-3: Integrated luminosity (a) and peak luminosity (b) in the 2011 LHC runs.

With this high instantaneous luminosity, the average number of interactions per bunch crossing is usually much larger than 1 as discussed in Section 5.5. Figure 6-4 shows the distribution of the number of interactions per bunch crossing during the 2011 data-taking runs. The number of interactions per bunch crossing is calculated from the instantaneous luminosity by $\mu = L \times \sigma_{inel}/(n_b \times f_r)$ (derived from Equation 5.34) where L is the instantaneous luminosity, σ_{inel} the inelastic cross section taken as 71.5 mb, n_b the number of colliding bunches and f_r the LHC revolution frequency. The average number of interactions per bunch crossing $< \mu >$ is determined from the mean of the Poisson distribution of the number of interactions per bunch crossing. During the technical stop occuring in September 2011, one of the beam parameters, β^*, was changed to achieve a higher luminosity. β^* is defined as the distance between the collision point and the point where the beam width is twice the one at the collision point. The smaller β^* is, the stronger the squeezing power one imposes to the beams is, and the higher density of protons in the two incoming bunches is, which leads to a higher instantaneous luminosity. The blue curve in Figure 6-4 is the distribution of μ using $\beta^* = 1.5\ m$ before the technical stop, while the red curve is the distribution of μ using $\beta^* = 1.0\ m$ after this technical stop. After upgrading the β^* parameter, the average number of interactions per bunch crossing reaches 11.6, almost doubling its previous value. This allowed to increase the instantaneous luminosity from around $2 \times 10^{33}\ cm^{-2}s^{-1}$ in August to around $3.6 \times 10^{33}\ cm^{-2}s^{-1}$ in September as shown in Figure 6-3(b).

To take into account the different beam parameters and the different triggers, which were regularly adjusted to the collision rates, as well as the different detector conditions, the data recorded in 2011 are naturally divided into several periods, labelled by B, D, E, F, G, H, I, J, K, L, M. Table 6.3 summarizes the data recorded by ATLAS with the integrated luminosities corresponding to each data-taking period. The total integrated luminosity used in the analysis is $4656 \pm 84\ pb^{-1}$ [139] after applying the data quality filtering discussed in Section 5.6 through the rejection of

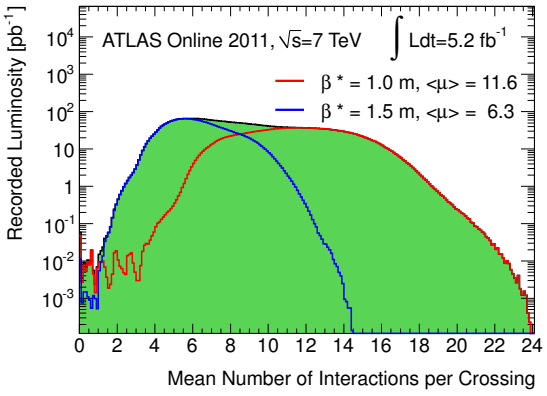

Figure 6-4: Average number of interactions per bunch crossing for the 2011 data-taking runs. The blue curve shows the average number of interactions per bunch crossing with $\beta^* = 1.5$ before the technical stop occuring in September 2011 and the red curve the distribution with $\beta^* = 1.0$ obtained after the technical stop.

badly recorded and reconstructed events.

Period	Integrated luminosity (pb^{-1})	Run numbers
$B - D$	176 ± 3	$177986 - 180481$
$E - H$	938 ± 17	$180614 - 184169$
I	333 ± 6	$185353 - 186493$
J	224 ± 4	$186516 - 186755$
K	583 ± 11	$186873 - 187815$
$L - M$	2402 ± 43	$188902 - 191933$

Table 6.3: 2011 data periods with their integrated luminosities. Only luminosity blocks with good data quality are included in the calculation of the integrated luminosities.

Chapter 7

Simulations with PROTOS

This chapter presents the leading order PROTOS generator, which allows to modify the values of the coupling strengths V_L, V_R, g_L and g_R entering in the effective Lagrangian of the Wtb vertex expressed by Equation 3.5. Simulated samples of t-channel single top quark events with various configurations can be produced in order to understand the relations between anomalous couplings in the top quark production and decay vertices and the corresponding degree of polarization of the top quark and spin analyzing powers of its decay products. Moreover, these samples could be used in the future to validate the methods developed to measure the polarization values (for the time-being, a simple re-weighting method is implemented for the validation samples in the analysis presented in the next chapters).

The observables for the top quark polarization are reintroduced first in Section 7.1. The validation of the PROTOS generator is presented in Section 7.2. Then the configurations used in PROTOS to generate different values of the top quark polarization and the corresponding simulated samples are presented in Section 7.3. Finally, additional studies on W boson polarization observables are reported in Section 7.4.

7.1 Top quark polarization

The top quark polarization can be measured from angular observables that follow the distribution as introduced in Section 3.6.5:

$$\frac{1}{\Gamma}\frac{d\Gamma}{d\cos\theta_{l,b}} = \frac{1}{2}(1 + \alpha_{l,b}P\cos\theta_{l,b}) \tag{7.1}$$

where $\theta_{l,b}$ is the angle between the momentum of the spin analyzer, lepton or b-quark in our analysis, and the spectator quark momentum, all boosted in the top quark rest frame. The spectator quark momentum is chosen as spin axis for the top quark and defines the so-called spectator spin basis. The observable directly measurable is the product $\alpha_{l,b} \cdot P$ combining the degree of polarization of the top quark and the spin analyzing power of the lepton or of the b-quark.

7.2 Generator validation

The PROTOS generator is first validated against commonly used leading order t-channel generators, in particular against AcerMC which is the reference generator used in the analysis (generator described in Section 6.1.1). PROTOS simulations configured by using the Standard Model parameters are produced, and the obtained kinematic distributions are then compared to the ones given by AcerMC.

The PROTOS generator is configured as follows: The center of mass energy is set to 7 TeV. The parton distribution function set is MRSTMCal-MC-20651, chosen from LHAPDF [140]. The factorisation scales are set with $Q^2 = -p_W^2$ for the light quark where p_W is the momentum of the W boson, and $Q^2 = p_{\bar{b}}^2 + m_b^2$ for the gluon where $p_{\bar{b}}$ is the momentum of the $\bar{b}$-quark and m_b the b-quark mass. Only the t-channel $t\bar{b}q$ process (i.e. $2 \rightarrow 3$ process discussed in Section 3.5.1) is used, and no cuts are applied on the phase space at the parton level. According to the predictions of the Standard Model, V_L is set to 1, while V_R, g_L and g_R are set to 0. In the following, only distributions corresponding to the electron flavor (from the W boson decay) are shown, since simulations with the other flavors (muon and tau) lead to similar distributions.

The generated events are compared to AcerMC at the parton level. For both PROTOS and AcerMC events, the distributions of the transverse momentum and of the pseudorapidity associated to the spectator and top quarks are shown in Figure 7-1. The distributions of the same kinematic variables corresponding to the decay products of the top quark (W boson, b-quark, charged lepton and neutrino) are shown in Figures 7-2 and 7-3. The angular distributions corresponding to the top quark polarization in the spectator basis are presented in Figure 7-4. The angular distribution with the lepton taken as spin analyzer is plotted on the left while the angular distribution for the b-quark spin analyzer is shown on the right. From the various presented distributions, an overall quite good agreement is obtained between the generated PROTOS and AcerMC events, validating the PROTOS generator at the parton level.

7.3 PROTOS samples

7.3.1 Anomalous coupling configuration

To produce samples with different top quark polarizations, one can change in PROTOS the values of the vector and tensor coupling strengths V_L, V_R, g_L and g_R; the PROTOS code is indeed configured in such a way that the real and imaginary parts of any coupling component can be modified separately.

The angular distributions obtained at parton level for the lepton spin analyzer in the spectator basis are shown in Figure 7-5 for various simple configurations for the real and imaginary parts of the four couplings. The four upper plots (a), (b), (c), (d) show the distributions generated by setting only the real parts of g_L, g_R, V_R, V_L to 1, respectively. The three bottom plots (e), (f), (g) show the distributions obtained

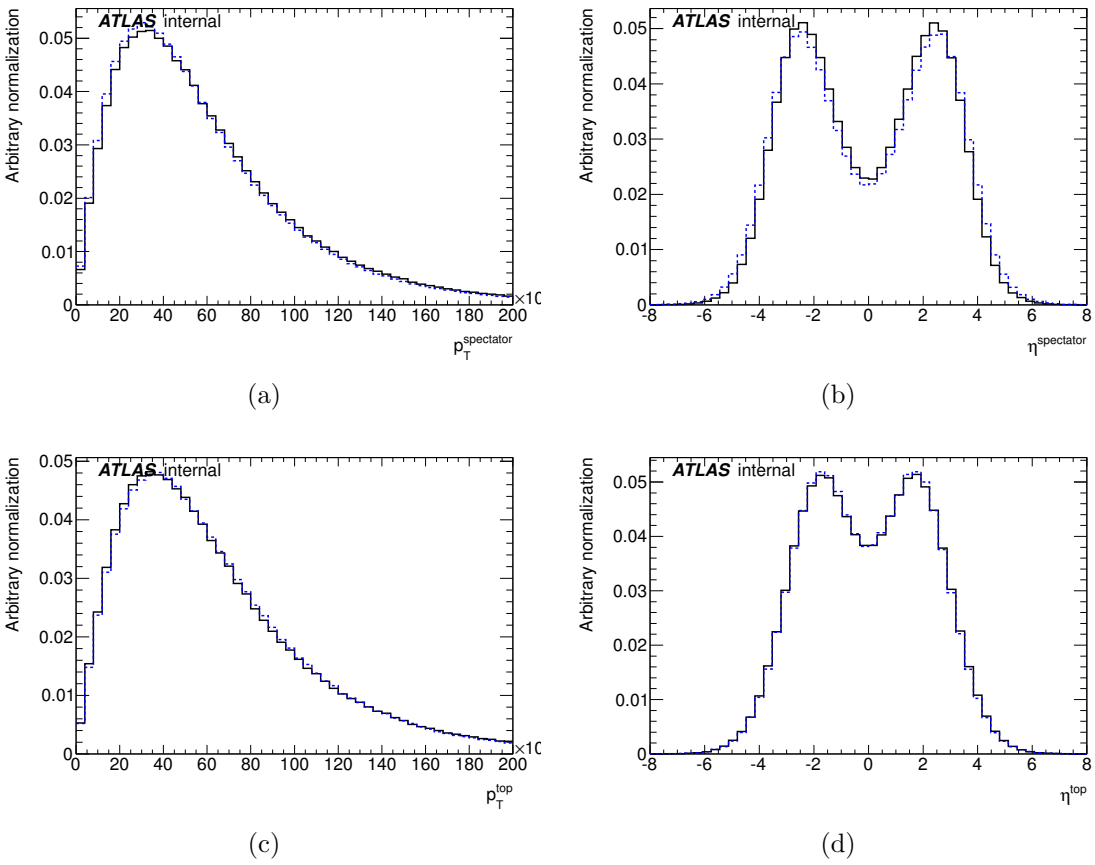

Figure 7-1: Comparison of the kinematic distributions for AcerMC (solid lines) and PROTOS (dashed lines) events in the electron channel (a) spectator quark transverse momentum, (b) spectator quark pseudorapidity, (c) top quark transverse momentum and (d) top quark pseudorapidity. The PROTOS generator is configured using the Standard Model values for the Wtb couplings.

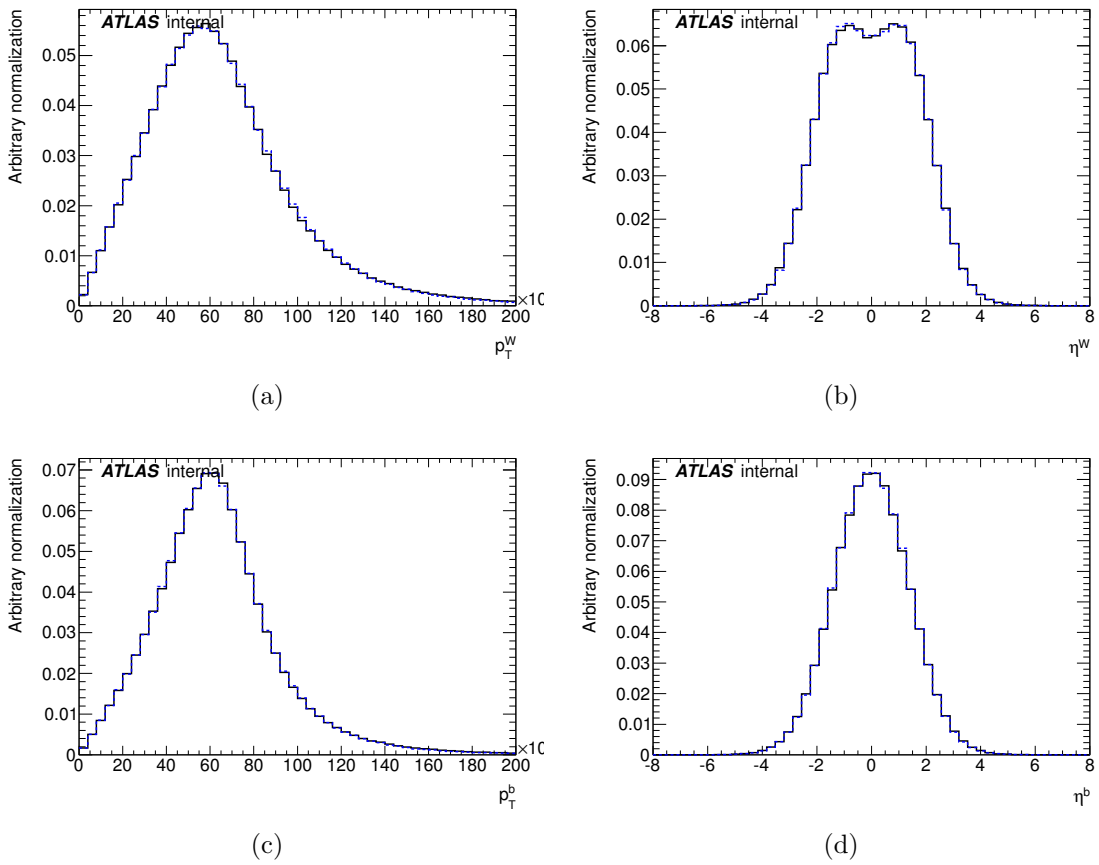

Figure 7-2: Comparison of the kinematic distributions of the top quark decay products for AcerMC (solid lines) and PROTOS (dashed lines) events in the electron channel (a) W boson transverse momentum, (b) W boson pseudorapidity, (c) b-quark transverse momentum and (d) b-quark pseudorapidity. The PROTOS generator is configured using the Standard Model values for the Wtb couplings.

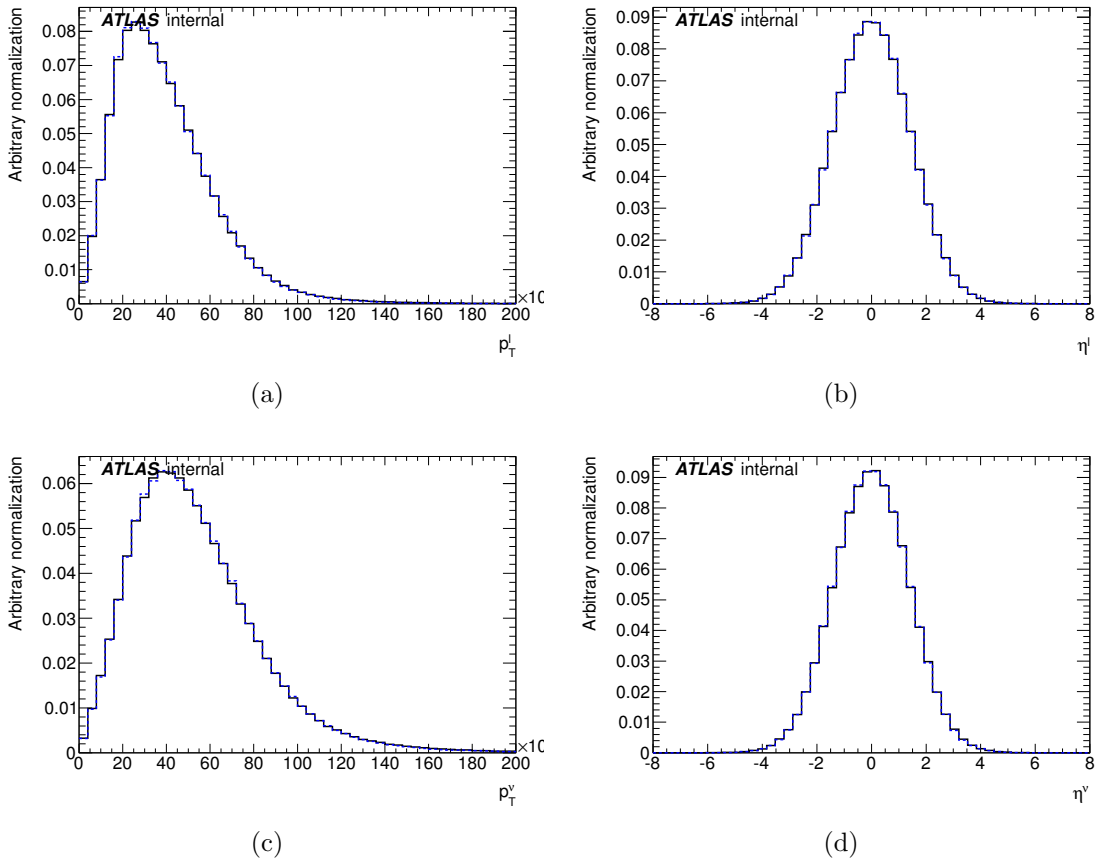

Figure 7-3: Comparison of the kinematic distributions of the W boson decay products for AcerMC (solid lines) and PROTOS (dashed lines) events in the electron channel (a) lepton transverse momentum, (b) lepton pseudorapidity, (c) neutrino transverse momentum and (d) neutrino pseudorapidity. The PROTOS generator is configured using the Standard Model values for the Wtb couplings.

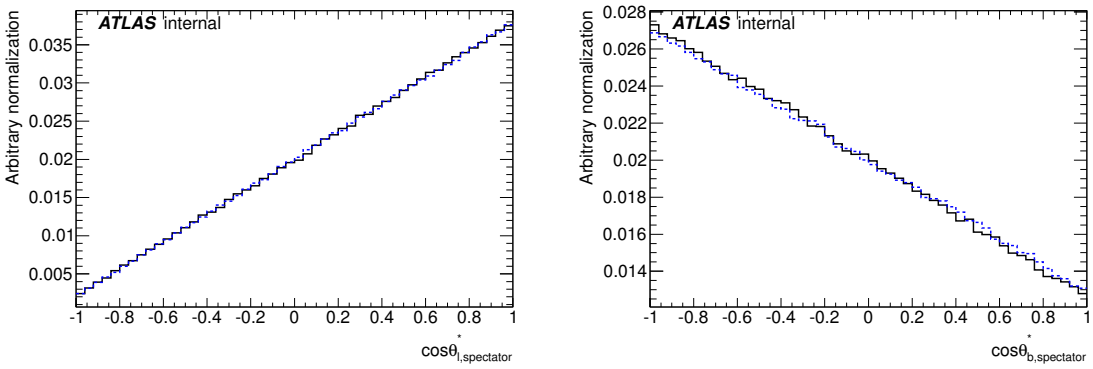

(a) (b)

Figure 7-4: Comparison between the angular distributions calculated in the spectator basis for AcerMC (solid lines) and PROTOS (dashed lines) events in the electron channel (a) lepton spin analyzer and (b) b-quark spin analyzer. The spectator basis is defined along the spectator quark momentum. The spin analyzer and the spin basis are both boosted to the top quark rest frame. The PROTOS generator is configured using the Standard Model values for the Wtb couplings.

by setting only the imaginary parts of g_L, g_R, V_R to 1, respectively. Setting to 1 only the real parts of g_L, g_R, V_R lead to the same distributions than setting to 1 only the imaginary parts of the same couplings; the slopes of the distributions being exactly the same, generating samples with different top quark degrees of polarization can therefore be done by changing only the value of the real parts of the anomalous couplings. Non-zero imaginary parts in the couplings introduce CP-violation which could only be observed from the measurement of other polarization observables (in particular via the normal W boson polarization discussed in Chapter 3).

From plots (d) ($V_L = 1$) to (c) ($V_R = 1$) in Figure 7-5, the top quark polarization (actually $\alpha_l \cdot P$) extracted from the distribution slope is changed from 0.92 to -0.91 due to the introduction of a right-handed vector coupling instead of the Standard Model left-handed one. From plots (a) ($g_L = 1$) to (b) ($g_R = 1$), the top quark polarization is changed from 0.89 to -0.77 with the introduction of the right-handed tensor coupling instead of the left-handed one. When looking at the number of generated events, the introduction of tensor couplings (plots (a), (b)) produces event samples with lower statistics than the use of vector couplings (plots (d), (c)). Therefore, in order to produce samples with a high output statistics for top quark polarization studies, only the vector couplings (real parts) are set to non-zero values in the input PROTOS configuration.

Table 7.1 shows the various configurations on V_L and V_R constrained by $|V_L|^2 + |V_R|^2 = 1$ for the production of samples with different polarization values. These samples are used to study the top quark degree of polarization and the spin analyzing power in correlation with modifications of the production and/or decay vertex. They will also allow to test in the future the polarization measurement methods through linearity checks involving the full changes in the parton kinematics due to different

input polarizations (the alternative re-weighting method is based on the kinematics of the Standard Model parameterization).

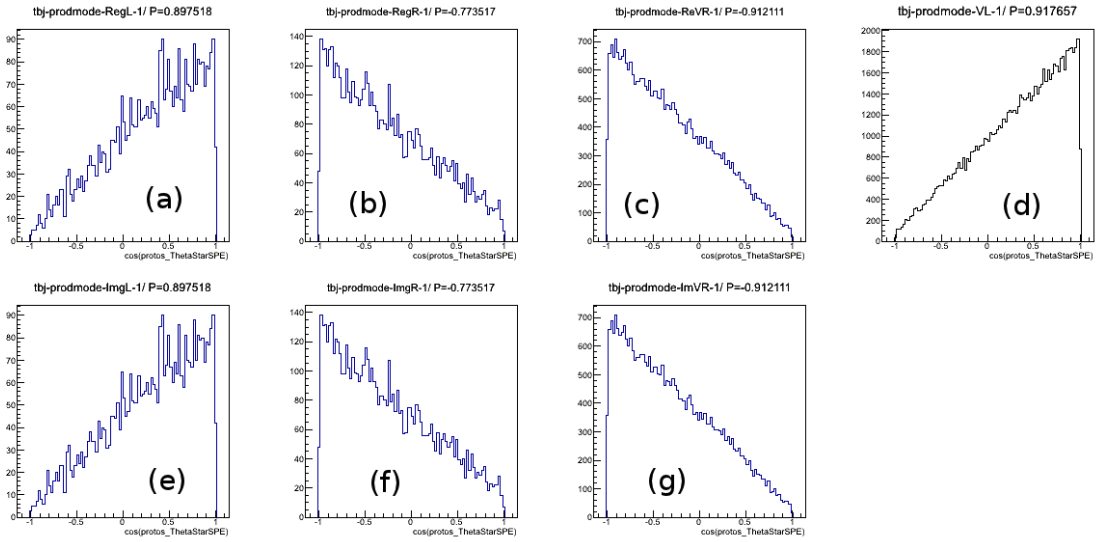

(a)

Figure 7-5: Angular distributions of the lepton spin analyzer in the spectator basis calculated at the parton level using different coupling configurations in the production Wtb vertex The four upper plots (a), (b), (c), (d) show the distributions obtained by setting to 1 only the real parts of g_L, g_R, V_R, V_L, respectively. The three bottom plots (e), (f), (g) show the distributions calculated by setting to 1 only the imaginary parts of g_L, g_R, V_R, respectively. These distributions are generated from top quark production; consistent distributions are found for anti-top quarks.

7.3.2 Vertex configuration

In single top quark production, a Wtb vertex exists in both the production and decay vertices, as shown in Figure 7-6. Anomalous couplings can therefore be set either to the production or to the decay vertex or to both of them. These different cases can result in different angular distributions with different values of the extracted observable $\alpha \cdot P$. With the purpose of decomposing the impacts on the degree of polarization P and on the spin analyzer α, a set of tests is implemented by modifying in the PROTOS configuration the production and decay vertices independently with the coupling parameterizations previously listed in Table 7.1. This allows to verify that the production vertex only affects the degree of top quark polarization P and the decay vertex only the spin analyzer α. Table 7.2 reports the results obtained for the different vertex and anomalous coupling configurations set to generated the PROTOS event samples. The first three columns represent the label and corresponding coupling values (V_L and V_R) of the configurations, as listed in Table 7.1. The two next columns correspond to the ratios of the lepton and b-quark spin analyzing powers, $r_{bl} = \frac{\alpha_b P}{\alpha_l P} = \frac{\alpha_b}{\alpha_l}$, and to the products $\alpha_l \cdot P$ of the lepton spin analyzing power and

Label	V_L	V_R
SM	1.000	0.00
VR05	0.999	0.05
VR10	0.995	0.10
VR15	0.989	0.15
VR20	0.980	0.20
VR25	0.968	0.25
VR30	0.954	0.30
VR35	0.937	0.35
VR40	0.916	0.40
VR45	0.893	0.45
VR50	0.866	0.50

Table 7.1: Configurations of coupling strengths in the PROTOS generator for top quark polarization studies. Only vector couplings are configured leaving the tensor couplings to 0 and only the real parts of V_L and V_R are configured leaving all imaginary parts to 0.

the degree of top quark polarization. The three parts of the table contain the lists of values corresponding to the three possible configurations for the vertices: anomalous couplings set to the production vertex, to the decay vertex and to both of them, respectively. To check which modified vertex affects α and/or P, one can refer to the changes on the spin analyzing power ratio α_{bl} and on the polarization product $\alpha_l \cdot P$ as discussed below.

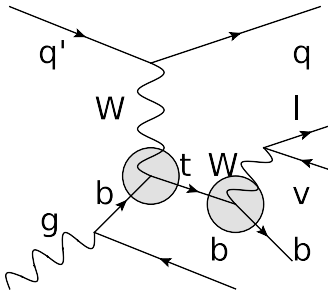

Figure 7-6: Feynman diagram for single top quark t-channel production and leptonic decay. The two Wtb vertices are spotted by the grey circles.

When only the production vertex is modified ("Anomalous production vertex" part of Table 7.2), one can see that the r_{bl} ratio does not change when different configurations on V_L, V_R are implemented (the slight changes which are due to statistical fluctuations are negligible). One can also verify that the production vertex does not affect α but only P, by looking at the varied values obtained for $\alpha_l \cdot P$.

If only the decay vertex is modified ("Anomalous decay vertex" part in Table 7.2), the values of r_{bl} are changed as expected since only the decay vertex can have an

impact on the spin analyzing power α (the different $\alpha_l \cdot P$ values are actually caused by the single variation on α).

The comparison between the values of $\alpha_l \cdot P$ obtained when only the decay vertex is modified and the values resulting from the simultaneous modification of the two vertices ("Anomalous production vertex and decay vertex" part in Table 7.2) shows that larger changes are found in the latter case since the anomalous couplings are introduced to the production vertex additionally. When anomalous couplings are introduced to both production and decay vertices, the polarization ratio r_{bl} and product $\alpha_l \cdot P$ are varying, since both α and P are independently modified.

7.3.3 Generated samples

According to the configurations proposed in Section 7.3.1, PROTOS samples are generated with anomalous couplings set in both production and decay vertices. The specific configurations chosen from Table 7.1 are: $V_L = 1.000$ and $V_R = 0.00$ (SM), $V_L = 0.968$ and $V_R = 0.25$ (VR25), $V_L = 0.866$ and $V_R = 0.50$ (VR50), $V_L = 0.000$ and $V_R = 1.00$ (VR100). The first configuration corresponds to the Standard Model parameterization. The kinematic and angular distributions at the parton level associated to the samples of events generated using these different coupling configurations are shown in Figures 7-7 to 7-10 in order to compare them.

The distributions of the transverse momentum and of the pseudorapidity of the spectator and top quarks are shown in Figure 7-7. These distributions do not differ from each other whatever the implemented couplings (Standard Model or anomalous configurations), the coupling modifications only impacting the top quark decay products as shown below.

In Figures 7-8 and 7-9, are shown the distributions of the transverse momentum and of the pseudorapidity of the top quark decay products, on-shell W boson, b-quark, charged lepton and neutrino. The kinematics of the W boson and of the b-quark generated with anomalous couplings almost do not deviate from the Standard Model ones, except that the transverse momentum distribution p_T of the W boson becomes a little harder and correspondingly the p_T distribution of the b-quark becomes a little softer in the configuration with $V_L = 0.866$ and $V_R = 0.50$ (VR50). The kinematics of the charged lepton and neutrino with the configurations $V_L = 0.968$, $V_R = 0.25$ (VR25) and $V_L = 0.866$, $V_R = 0.50$ (VR50) deviate from the Standard Model case more than their W boson parent. The extreme case with $V_L = 0.000$ and $V_R = 1.00$ (VR100) produces completely different kinematics for the charged lepton and the neutrino. In summary, higher the right-handed coupling V_R is, harder the p_T distribution of the charged lepton is, and correspondingly, softer the p_T distribution of the neutrino is.

In Figure 7-10, the angular distributions are shown for the lepton and b-quark spin analyzers in the spectator basis. The polarization changes as expected when an increasing right-handed vector coupling V_R is introduced.

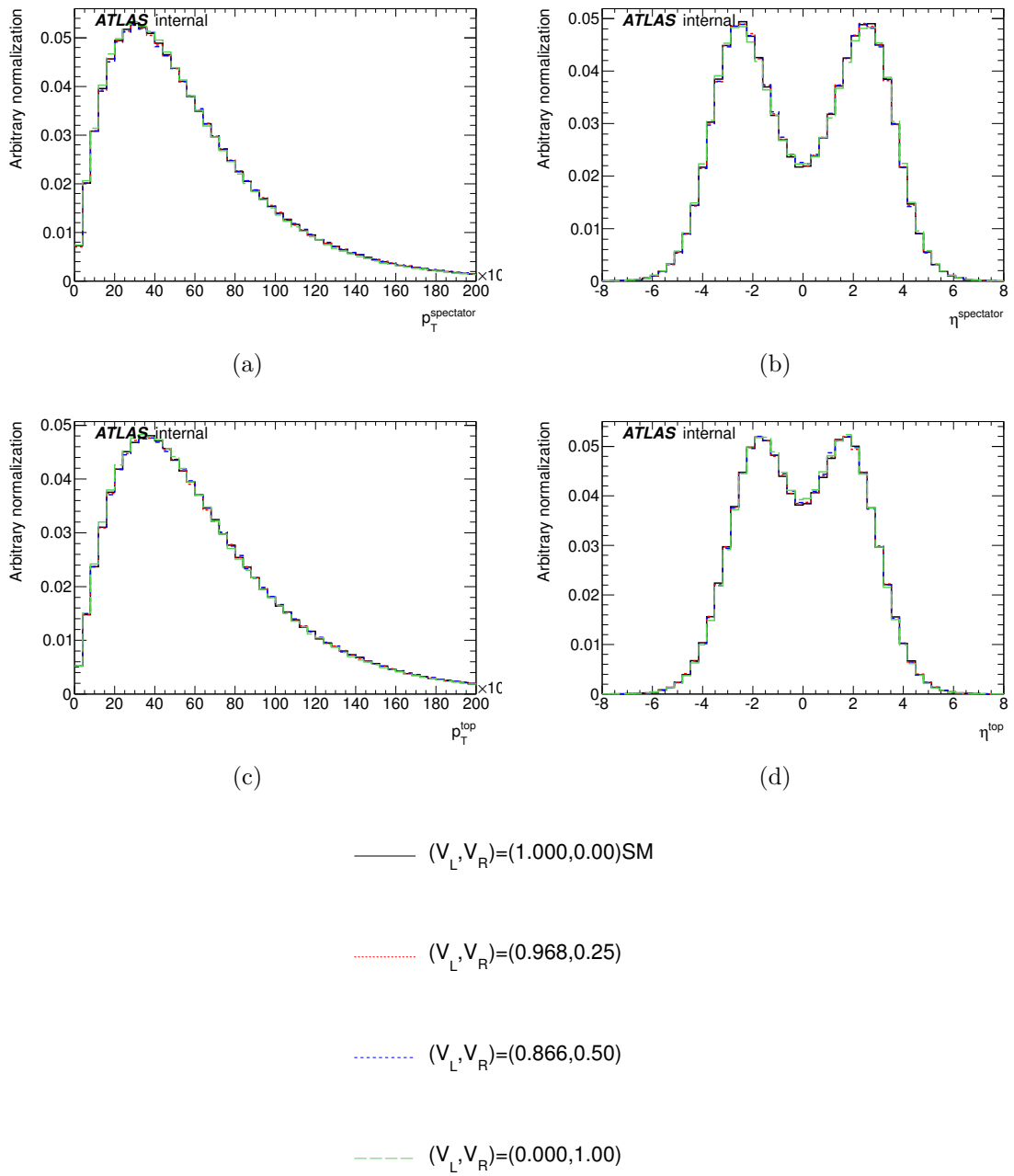

Figure 7-7: Comparison of the parton-level kinematic distributions for PROTOS events produced with the Standard Model (black solid lines) and anomalous (colored dashed lines) couplings configured in both production and decay vertices (a) spectator quark transverse momentum, (b) spectator quark pseudorapidity, (c) top quark transverse momentum and (d) top quark pseudorapidity. The color code with the corresponding anomalous configurations are given in the legend. The distributions are shown for the electron channel.

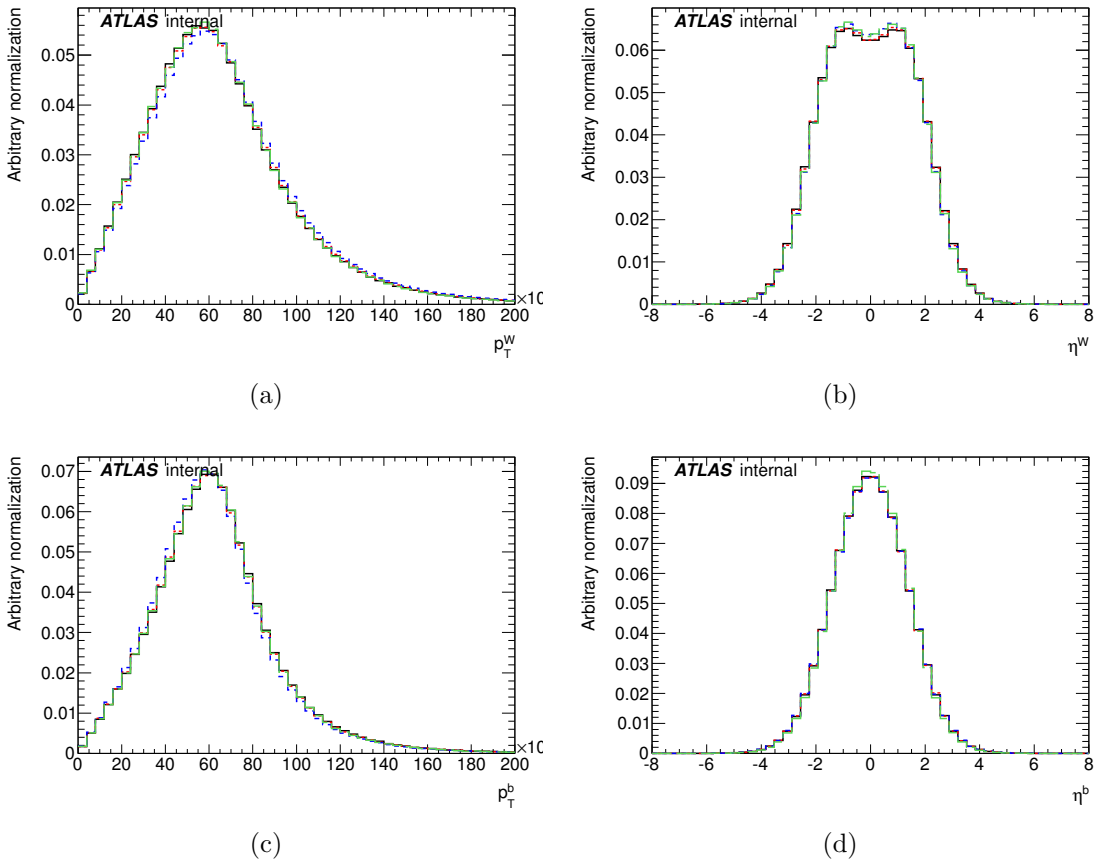

Figure 7-8: Comparison of the parton-level kinematic distributions of the top quark decay products for PROTOS events produced with the Standard Model (black solid lines) and anomalous (colored dashed lines) couplings configured in both production and decay vertices. (a) W boson transverse momentum, (b) W boson pseudorapidity, (c) b-quark transverse momentum and (d) b-quark pseudorapidity. The color code and the corresponding anomalous configurations are the same than in Figure 7-8. The distributions are shown for the electron channel.

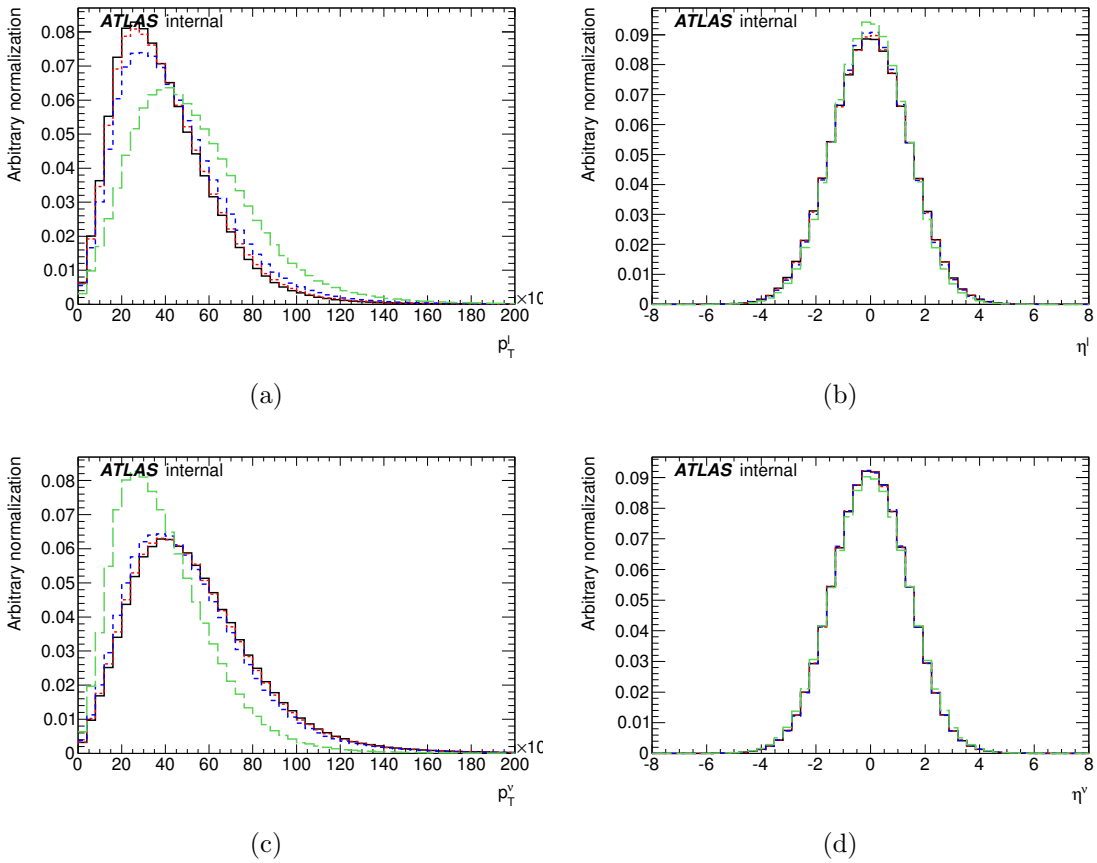

Figure 7-9: Comparison of the parton-level kinematic distributions of the W boson decay products for PROTOS events produced with the Standard Model (black solid lines) and anomalous (colored dashed lines) couplings configured in both production and decay vertices. (a) lepton transverse momentum, (b) lepton pseudorapidity, (c) neutrino transverse momentum and (d) neutrino pseudorapidity. The color code and the corresponding anomalous configurations are the same than in Figure 7-8. The distributions are shown for the electron channel.

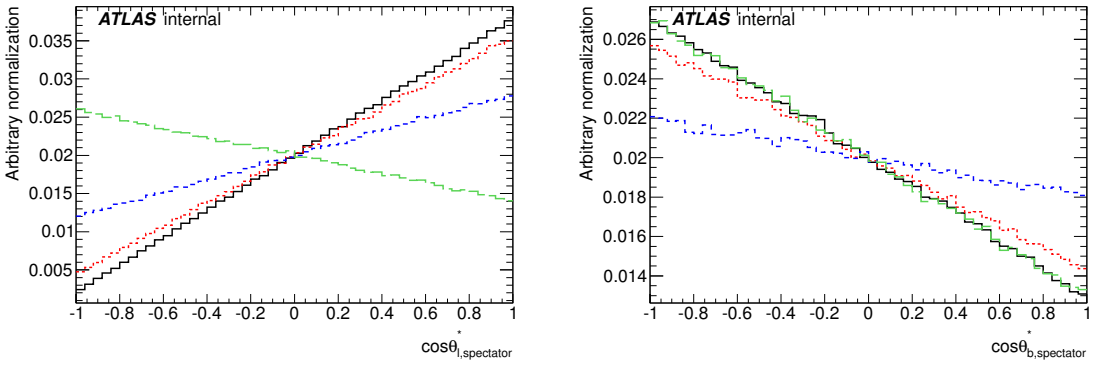

(a) (b)

Figure 7-10: Comparison of the parton-level angular distributions in the spectator basis for PROTOS events produced with the Standard Model (black solid lines) and anomalous (colored dashed lines) couplings configured in both production and decay vertices. (a) lepton spin analyzer and (b) b-quark spin analyzer. The color code and the corresponding anomalous configurations are the same than in Figure 7-8. The distributions are shown for the electron channel.

7.3.4 Energy configuration

This section presents the expected top quark polarization as a function of the center of mass energy up to the LHC designed energy of 14 TeV. Samples are generated by the PROTOS generator configured with the Standard Model couplings at the center of mass energies of 7 TeV, 8 TeV and 14 TeV. The kinematic distributions associated to the partons are shown in Appendix A.1. As expected, harder transverse momenta and wider pseudorapidities are observed when the center of mass energy increases. Figure 7-11 shows the angular distributions calculated for the lepton spin analyzer in the spectator basis. These angular distributions have slopes which are independent on the center of mass energy, illustrating that the Standard Model V_L coupling strength does not have an energy-dependency.

7.4 W boson polarization

The various W boson polarization observables which can be measured in single top quark production are introduced in Section 3.6.4. From the angular distributions of the charged lepton reconstructed in the helicity, normal and transverse bases, one can extract three sets of helicity/polarization fractions which also can be used to probe the Wtb vertex.

This section reports the studies performed in order to understand the impact on the parton-level angular distributions related to the W boson polarization of the introduction of anomalous couplings in the production and decay vertices.

The PROTOS samples generated with the anomalous configurations described in Section 7.3.1 have right-handed couplings V_R and can be used to study the W

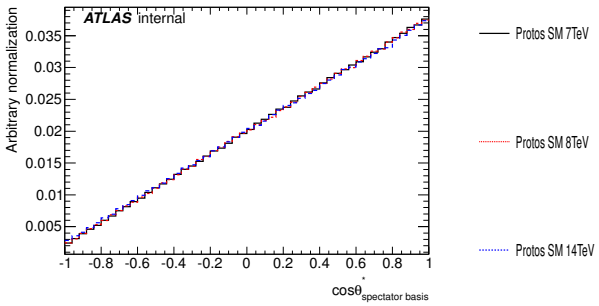

(a)

Figure 7-11: Angular distributions of the lepton spin analyzer in the spectator basis for PROTOS events generated with the Standard Model Wtb couplings at $\sqrt{s}$ = 7 TeV (black solid line), 8 TeV (red dashed line) and 14 TeV (blue dashed line). The distributions are shown for the electron channel.

polarization for the three cases: anomalous couplings only in the production or in the decay vertex and anomalous couplings in both of them. The studied configurations which are only based on real vector couplings assume therefore no CP-violation since it can only be introduced via non-zero imaginary parts. Only the W boson helicity and transverse polarization will be thus discussed in this section because a discussion about normal polarization would require imaginary contributions in the anomalous couplings.

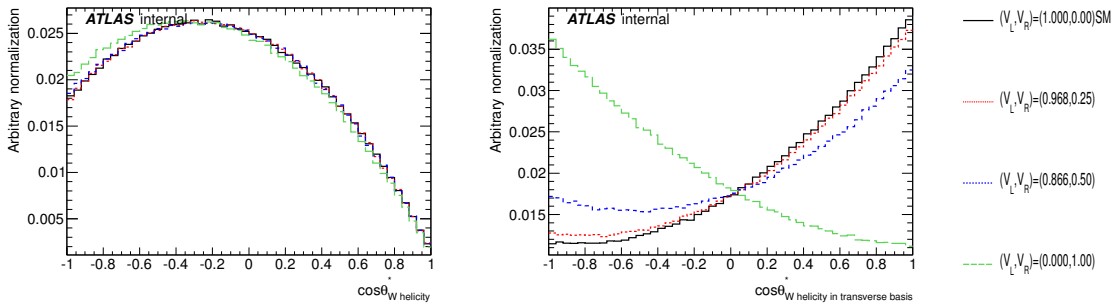

(a) (b)

Figure 7-12: Comparison of the parton-level angular distributions of the lepton (a) in the helicity basis and (b) in the transverse basis for events produced with PROTOS. The anomalous couplings are set only to the production vertex. The different line styles stand for the configurations given in the legend: black line for the Standard Model configuration and colored lines for anomalous configurations. The distributions are shown for the electron channel.

Figure 7-12 shows the angular distributions of the lepton in the helicity and transverse bases when anomalous couplings exist only in the production vertex. The four plotted curves stand for four different combinations of the V_L and V_R anomalous couplings. The three colored distributions with anomalous couplings are compared with

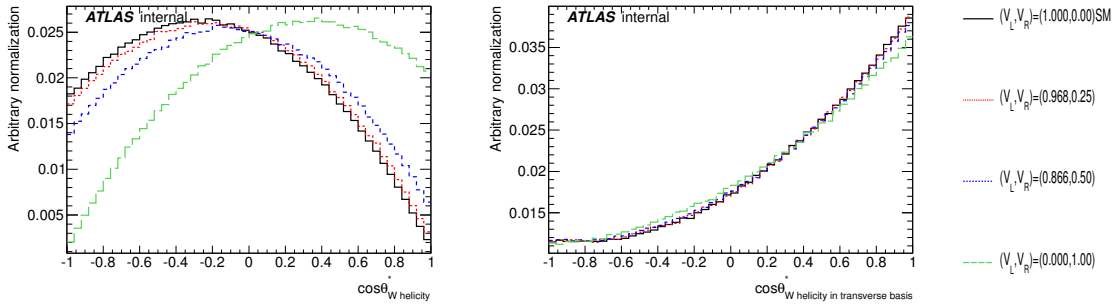

(a) (b)

Figure 7-13: Comparison of the parton-level angular distributions of the lepton (a) in the helicity basis and (b) in the transverse basis for events produced with PROTOS. The anomalous couplings are set only to the decay vertex. The different line styles stand for the configurations given in the legend: black line for the Standard Model configuration and colored lines for anomalous configurations. The distributions are shown for the electron channel.

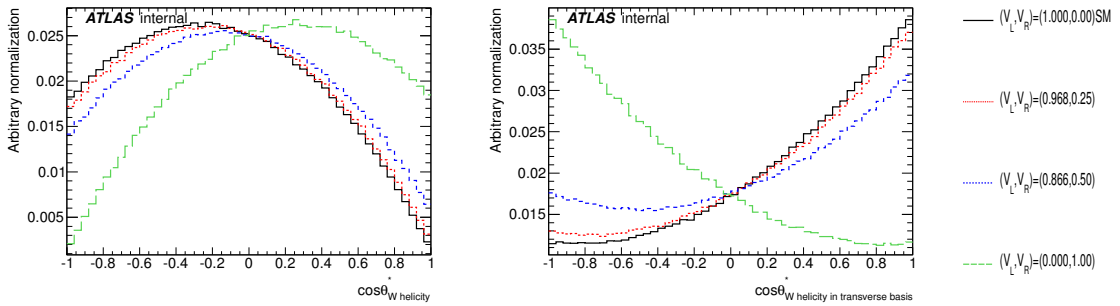

(a) (b)

Figure 7-14: Comparison of the parton-level angular distributions of the lepton (a) in the helicity basis and (b) in the transverse basis for events produced with PROTOS. The anomalous couplings are set to both production and decay vertices. The different line styles stand for the configurations given in the legend: black line for the Standard Model configuration and colored lines for anomalous configurations. The distributions are shown for the electron channel.

the black curve representing the Standard Model expectation. As one can see in Figure 7-12(a), the angular distributions in the helicity basis generated with anomalous couplings in the production vertex do not deviate from the one produced with the Standard Model couplings, while in Figure 7-12(b), the distributions in the transverse basis deviate from the Standard Model case. One can draw the conclusion that the W boson helicity fractions are immune to anomalous couplings in the production vertex whereas the W boson transverse polarization fractions are sensitive to an anomalous production vertex. The helicity fractions are indeed not expected to be dependent on the top quark polarization contrary to the transverse fractions, since the transverse spin axis is defined with respect to the top quark spin axis taken along the spectator momentum in the top quark rest frame.

Figure 7-13 shows the angular distributions of the lepton in the helicity and transverse bases in the alternative case of anomalous couplings only in the decay vertex. As one can see in Figure 7-13(a), the angular distributions in the helicity basis produced with anomalous couplings in the decay vertex deviate from the one produced within the Standard Model, while in Figure 7-13(b), the distributions in the transverse basis do not deviate from the Standard Model case. The W boson helicity fractions are therefore sensitive to anomalous couplings in the decay vertex while the transverse polarization fractions are immune to an anomalous decay vertex.

From the above discussion, one can then predict that the angular distributions in the helicity and transverse bases will both deviate from the Standard Model distributions when an anomalous configuration is set in both production and decay vertices. This is confirmed by the distributions presented in Figure 7-14.

SetName	V_L	V_R	r_{bl}	$\alpha_l \cdot P$
Anomalous production vertex				
SM	1.000	0.00	-0.401	0.888
VR05	0.999	0.05	-0.401	0.889
VR10	0.995	0.10	-0.401	0.881
VR15	0.989	0.15	-0.401	0.865
VR20	0.980	0.20	-0.401	0.839
VR25	0.968	0.25	-0.401	0.804
VR30	0.954	0.30	-0.401	0.760
VR35	0.937	0.35	-0.401	0.706
VR40	0.916	0.40	-0.401	0.642
VR45	0.893	0.45	-0.402	0.568
VR50	0.866	0.50	-0.402	0.484
Anomalous decay vertex				
SM	1.000	0.00	-0.401	0.888
VR05	0.999	0.05	-0.400	0.886
VR10	0.995	0.10	-0.398	0.882
VR15	0.989	0.15	-0.392	0.875
VR20	0.980	0.20	-0.384	0.864
VR25	0.968	0.25	-0.372	0.850
VR30	0.954	0.30	-0.356	0.834
VR35	0.937	0.35	-0.338	0.814
VR40	0.916	0.40	-0.314	0.791
VR45	0.893	0.45	-0.285	0.765
VR50	0.866	0.50	-0.250	0.735
Anomalous production vertex and decay vertex				
SM	1.000	0.00	-0.401	0.888
VR05	0.999	0.05	-0.400	0.887
VR10	0.995	0.10	-0.398	0.875
VR15	0.989	0.15	-0.392	0.852
VR20	0.980	0.20	-0.384	0.816
VR25	0.968	0.25	-0.372	0.770
VR30	0.954	0.30	-0.357	0.714
VR35	0.937	0.35	-0.338	0.647
VR40	0.916	0.40	-0.315	0.572
VR45	0.893	0.45	-0.287	0.489
VR50	0.866	0.50	-0.253	0.401

Table 7.2: Comparison of the spin analyzing powers and of the top quark degrees of polarization when different vertex and anomalous coupling configurations are set in generated PROTOS events. The first column is the name of the configuration. The second and third columns record the values of the V_L and V_R couplings. The third and fourth columns give the ratios of the lepton and b-quark spin analyzing powers, r_{bl}, and the degree of top quark polarization combined to the lepton spin analyzing power, $\alpha_l \cdot P$. The part "Anomalous production vertex" corresponds to anomalous couplings set only to the production vertex, "Anomalous decay vertex" to anomalous couplings only set to the decay vertex and "Anomalous production vertex and decay vertex" to anomalous couplings set to both vertices.

Chapter 8

Event selection

This chapter introduces how the signal events are selected and how the contributions of the background events are estimated either from Monte Carlo simulations or from data using data-driven methods. First of all, the physics objects are defined in Section 8.1 based on the general object reconstructions discussed in Chapter 5. With the defined objects, Section 8.2 describes the event selection based on the single top quark signature discussed in Chapter 6, the reconstruction of the top quark from the selected events being detailed in Section 8.3. The two data-driven background estimations are then presented. The QCD multijet background is estimated with different treatments for the electron and muon channels as discussed in Section 8.4; the estimation of the overall and flavor normalizations of the $W + jets$ background is described in Section 8.5. Then, the data and expected yields after the event selection are given in Section 8.6. Finally, kinematic distributions are shown in Section 8.7 with the comparison between data and expectation in order to check the simulation modeling and normalization in both signal and control regions.

8.1 Object selections

The physics object reconstruction and identification procedures presented in Chapter 5 are designed for general purposes. Additional specific selection cuts have to be applied to discriminate events with a single top t-channel signature from the expected backgrounds as discussed in Section 6.1.1. This section presents the specific cuts applied on the physics objects involved in the final state of t-channel events.

The selected electrons are required to match the objects triggering the "Egamma" stream introduced in Section 4.9.3: their distance ΔR with respect to the calorimeter seed firing the trigger has to be less than 0.15. The specific trigger chains are EF_e20_medium, EF_e22_medium and EF_e22vh_medium1 [141] for the periods B-H, I-K and L-M introduced in Section 6.2, respectively. These trigger chains correspond to a threshold of $20-22\ GeV$ on the transverse energy of the trigger object measured at the electromagnetic scale. The electron transverse energy E_T is determined by combining the pseudorapidity η measured by the tracks in the inner detector and the cluster energy measured in the electromagnetic calorimeter, $E_T = E_{cluster}/cosh(\eta_{track})$,

and the requirement is $E_T > 25\ GeV$. The η acceptance is defined by the limitations of the tracker and calorimeter, i.e. $|\eta| < 2.47$ and $1.37 < |\eta| < 1.52$ (the transition region between the calorimeter barrel and end-caps is removed). The quality requirements are "Tight++" (an enhanced version of the "Tight" quality introduced in Section 5.1), which include stringent selection cuts on calorimeter, tracking and combined variables in order to provide a good separation between isolated electrons and jets. The isolation cuts help to suppress further the QCD faked electrons. With cone sizes of $\Delta R = 0.2$ and $\Delta R = 0.3$ used for calorimeter and track isolation, respectively, the isolation cuts are chosen at the efficiency point of 90% for both. In case of double counting with jets, a final overlap removal step allows to reject electrons with $\Delta R(e, jet) < 0.4$. This last cut is applied after the main electron-jet overlap removal which will be discussed below.

The selected muons are required to match the objects triggering the "Muons" stream introduced in Section 4.9.3: as for electrons, their distance ΔR with respect to the trigger object has to be less than 0.15. The specific trigger chains are EF_mu18 and EF_mu18_medium [141] for the periods B-I and J-M, respectively. These trigger chains correspond to a threshold of 18 GeV on the transverse momentum of the trigger object. The Combined muons reconstructed as defined in Section 5.2 are used: they are determined by combining the tracks indenpendently reconstructed in the inner detector and in the muon spectrometer. The transverse momentum is required to be $p_T > 25\ GeV$. The pseudorapidity acceptance is $|\eta| < 2.5$, within the limit of the inner detector. The isolation requirements are $E_T^{0.2} < 4\ GeV$ and $p_T^{0.3} < 2.5\ GeV$, where $E_T^{0.2}$ is the sum of the transverse energy within a cone of radius $\Delta R = 0.2$ around the muon, and $p_T^{0.3}$ is sum of the transverse momentum of the inner detector tracks within a cone of radius $\Delta R = 0.3$ around the muon. Finally, to suppress muons from hadron decays, any muon with $\Delta R(\mu, jet) < 0.4$ is removed where the jets are selected after the electron-jet overlap removal which will be discussed in the following.

Jets are reconstructed by the Anti-k_t algorithm with a radius parameter $R = 0.4$ and are calibrated to the hadronic scale using simulation-based p_T and η dependent correction factors as discussed in Section 5.3.2. Many reconstructed jets (*bad* jets) come from out-of-time pileups, noisy cells in the calorimeter, LHC beam-gas interactions, cosmic-ray induced showers and so on. Events with any *bad* jets above the p_T threshold of 20 GeV are rejected. For each jet, the transverse momentum p_T is required to be larger than 30 GeV. The pseudorapidity acceptance is defined by $|\eta| < 4.5$ which corresponds to the limitation of the calorimeters. In addition, the jets are required to have $p_T > 35\ GeV$ in the region $2.75 < |\eta| < 3.75$ to remove a temporary mismodeling in that pseudorapidity region. Additionally, in-time pileup jets are suppressed by requiring $|JVF| > 0.75$ where the jet vertex fraction JVF is defined as the sum of the transverse momentum of all matched-tracks from a given vertex divided by the total jet-matched track p_T. To avoid double counting with selected electrons, an overlap removal is finally performed by removing the jet when it is the closest one to the electron within a distance $\Delta R(e,\ jet)$ less than 0.2.

The b-tagging algorithm mentioned in Section 6.1.1 constructs a variable which allows to identify whether the jet comes from a b-quark, by examining the characteristic long life time (i.e. long flight path) of b-flavored hadrons and their decay vertex (sec-

ondary vertex) that is usually away from the primary vertex (collision point). There are several b-tagging algorithms that can be used, such as IP3D, JetFitter, JetFitterCOMBNN [142]. The IP3D tagger uses the combination of the impact parameter in the longitudinal and transverse projections with a likelihood ratio technique to distinghuish b-jets from light jets. JetFitter uses a Kalman filter to find the position of the b-vertex and c-vertex on a common line to calculate an approximate flight path for the flavored hadrons; with a likelihood using the flight length significance of the vertices and additional variables such as the invariant mass of tracks associated with a vertex, the discrimination between b, c and light jets could be achieved. The tagger JetFitterCOMBNN uses an artificial neural network to combine JetFitter and IP3D outputs in addition to the variables describing the topology of the hadron decay chain. In this analysis, the tagger JetFitterCOMBNNc is used, which is a JetFitterCOMBNN tagger enhanced with a more efficient c-jet rejection. With this b-tagger, the selection of the b-jets is performed at the working point corresponding to a b-tagging efficiency of 55% estimated with $t\bar{t}$ simulated events, a rejection factor of 200 for light quark jets and 20 for c-quark jets. b-tagged jets are also selected using a reduced pseudorapidity acceptance $|\eta| < 2.5$.

8.2 Event selections

Selection of single top quark events is a two-step procedure. A first set of preselection cuts picks out events with a t-channel like topology as described in Section 6.1.1 and a series of cuts is applied in a second step to further discriminate the t-channel events from background contamination. In addition, specific selections are used to define, from the preselected datasets, control event samples allowing to determine background contributions with data-driven methods.

8.2.1 Event preselection

Generic event preselection criteria are applied in the first step of the analysis. The single electron and muon triggers, which depend on the data taking period as listed in Section 8.1, are considered to select separately the electron and muon channels. The data quality requirements are then applied by filtering the events belonging to the good runs and to the good blocks of luminosity as detailed in Section 5.6. Events containing jets with a bad reconstruction quality as well as events with noise bursts from the electromagnetic calorimeter are also rejected. In addition, to suppress remaining pileup events, one requires that at least one primary vertex is reconstructed from at least five tracks.

To select events with a single top quark t-channel signature, one requires exactly one isolated lepton (electron or muon), exactly two jets and a missing transverse momentum $E_T^{miss} > 30\ GeV$. To further reduce contribution of the QCD multijet background, one requires $m_T^W > 30\ GeV$ where m_T^W is the W boson transverse mass which is calculated according to:

$$m_T^W = \sqrt{2p_T^l E_T^{miss}(1 - \cos\Delta\phi(l, E_T^{miss}))} \tag{8.1}$$

where $\Delta\phi(l, E_T^{miss})$ is the azimuthal angle difference between the charged lepton momentum p_T^l and the missing transverse momentum. Finally, triangular cuts are applied to remove the mismodeling in the low lepton p_T region (mainly for muons), which has a sizeable impact in the region where the QCD multijet contribution is significant:

$$p_T^l > \left[40 \pm \left(\frac{40}{\pi - 1}\right)(\Delta\phi(l, jet1) \mp \pi)\right] \, GeV \tag{8.2}$$

where $\Delta\phi(l, jet1)$ is the azimuthal angle difference between the lepton momentum and the leading jet momentum.

These event preselections without any b-tagging requirements define the PRETAG event samples while the subsets with exactly one central b-tagged jet among the selected jets define the TAG event samples. This central requirement for the b-tagged jet is due to the tagging algorithms which make use of secondary vertices reconstructed from the information given by the tracking systems that extend only up to $|\eta| = 2.5$.

8.2.2 Signal event selection

For purifying candidate events with a t-channel signature, an additional set of cuts needs to be applied on the TAG samples. Two alternative sets of cuts are used for the studies of single top quark t-channel production. They were both originally optimized for cross section measurements derived from cut-based analyses.

A first series of soft cuts [143], labelled SELECTION-1, is considered to generate the signal event samples:

- $140\ GeV < m(l\nu b) < 187\ GeV$, where $m(l\nu b)$ is the invariant mass reconstructed from the lepton, the neutrino and the b-tagged jet. This quantity is an estimator of the top quark mass for signal events. The procedure used to calculate the unmeasured neutrino kinematics will be detailed in the next section;

- $|\eta(light\ jet)| > 1.7$, where $\eta(light\ jet)$ is the pseudorapidity of the non b-tagged (light, forward, spectator) jet;

- $|\Delta\eta(bjet, W)| < 1.0$, where $\Delta\eta(bjet, W)$ is the difference in pseudorapidity between the b-tagged jet and the reconstructed W boson.

The second set of cuts [144], labelled SELECTION-2, implements harder selection criteria in general:

- $150\ GeV < m(l\nu b) < 190\ GeV$, where $m(l\nu b)$ is the invariant mass presented above;

- $H_T > 210\ GeV$, where H_T is the scalar sum of the transverse momenta of all objects including the missing transverse momentum E_T^{miss};
- $|\eta(light\,jet)| > 2.0$, where $\eta(light\,jet)$ is the pseudorapidity of the non b-tagged jet;
- $|\Delta\eta(bjet, light\,jet)| > 1.0$, where $\Delta\eta(bjet, light\,jet)$ is the difference in pseudorapidity between the b-tagged and non b-tagged jets.

SELECTION-2 is the default set of cuts used in the analysis, while SELECTION-1 is always studied in parallel with SELECTION-2 to cross check the expected results with a lower signal-over-background ratio and a higher statistics in the selected signal event samples.

8.2.3 Event selections for background estimates

To estimate background contributions, such as QCD multijet and W+jets events, with data-driven methods, specific PRETAG and TAG samples are produced either by loosening some cuts to get background enriched control regions or by adding cuts to generate control samples orthogonal to the signal ones.

To estimate the QCD multijet background in the electron channel using the jet-electron model, one produces control event samples by removing the E_T^{miss} cut. To estimate the QCD multijet background in the muon channel with the matrix method, one makes loose samples by removing the isolation cuts when selecting the muon candidates. The jet-electron model and the matrix method are discussed in Section 8.4.

To extract the W+jets background normalization and flavor correction factors, one produces PRETAG and TAG background enriched control samples by adding a mass veto on the invariant mass $m(l\nu b)$: the mass window used in the SELECTION-2 set of cuts is reverted, i.e. one requires $m(l\nu b) < 150\ GeV$ or $m(l\nu b) > 190\ GeV$. The procedure used to extract the W+jets corrections is presented in Section 8.5.

To constrain the two main background contributions, which are $t\bar{t}$ and W+jets processes, an additional control region is defined by requiring the TAG events to have a high invariant mass $m(l\nu b)$ ($m(l\nu b) > 250\ GeV$). This control sample is used in the likelihood fit performed in the folding method to be discussed in Section 9.6.

8.3 Top quark reconstruction

The top quark can be reconstructed from its decay products, namely the b-quark and W boson. The b-quark evolves into a heavy-flavored jet in the detector which is reconstructed and eventually identified as a b-tagged jet by an appropriate algorithm and with a given efficiency (usually chosen at around 50%). The W boson can also be reconstructed from its decay products, which are a charged lepton and a neutrino in our case. The lepton is reconstructed from the inner detector and the electromagnetic calorimeter (electron) or the spectrometer (muon) information. The neutrino cannot

be detected; its transverse momentum is assumed to be the measured missing transverse momentum E_T^{miss} whereas its unknown longitudinal momentum component is determined by using the W boson mass constraint.

Using the four-momentum conservation law and constraining to the W boson pole-mass value ($m(W) = 80.42\ GeV$ [4]) the invariant mass calculated by combining the lepton and neutrino kinematics, one derives the following quadratic equation which gives the neutrino longitudinal momentum p_z:

$$p_z^2(\nu) - 2 \cdot \frac{\mu \cdot p_z(l)}{E^2(l) - p_z^2(l)} \cdot p_z(\nu) + \frac{E(l)^2 \cdot E_T^{miss\,2} - \mu^2}{E^2(l) - p_z^2(l)} = 0 \tag{8.3}$$

$$\text{with} \quad \mu = \alpha + E_T^{miss} \cdot \beta \quad , \tag{8.4}$$

$$\alpha = \frac{m(W)^2 - m(l)^2}{2} \quad , \tag{8.5}$$

$$\text{and} \quad \beta = p_x(l) \cdot \cos\phi(E_T^{miss}) + p_y(l) \cdot \sin\phi(E_T^{miss}) \quad . \tag{8.6}$$

where $p_{x,y}(l)$ are the transverse momentum components of the lepton, $E(l)$ its energy and $\phi(E_T^{miss})$ the azimuthal angle associated to the missing transverse momentum. To solve this equation, one has first to calculate the determinant Δ which is proportional to $m(W)^2 - m_T(W)^2$ where $m_T(W)$ is the W boson transverse mass calculated according to Equation 8.1. Two real solutions are obtained when Δ is positive and in that case the smallest p_z value is chosen. In more than 30% of the events, the calculated determinant is negative because the transverse mass reconstructed for the W boson is larger than its pole-mass. This case happens when the missing transverse momentum is mis-measured from the calorimeter cells or when additional physics processes contribute to the missing transverse momentum (extra neutrinos from B-hadron and τ decays, extra p_T contributions from ISR/FSR, ...). To save those events with complex solutions, the measured E_T^{miss} is modified in such a way that the transverse mass matches the pole-mass (i.e. Δ is re-scaled to 0) although keeping unchanged its azimuthal angle $\phi(E_T^{miss})$. The value of the re-scaled missing transverse momentum, $E_T^{miss'}$, is thus obtained by solving the new quadratic equation:

$$\left(\beta^2 - (E^2(l) - p_z^2(l))\right) \cdot E_T^{miss'\,2} + 2 \cdot \alpha \cdot \beta \cdot E_T^{miss'} + \alpha^2 = 0 \tag{8.7}$$

This equation leads to two real solutions (its determinant is always positive) and therefore to two solutions for the longitudinal momentum of the neutrino; the smallest p_z value is also chosen in that case. With this procedure, the top quarks can be reconstructed for all events (i.e. the reconstruction efficiency is 100%).

8.4 QCD multijet background estimation

The QCD multijet production proceeds via the strong interaction and is overwhelming with a cross section up to 10^8 pb in proton-proton collisions at 7 TeV. The selection cuts are tight enough to remove most of the QCD multijet events but instrumentally

some of them are misidentified as a "l+jets" final state and therefore can pass the final event selection step. These events are nevertheless only a small fraction of the whole QCD multijet production but the fraction is multiplied by a huge cross section ending up in a significant background contribution in the signal event samples.

The various sources of QCD multijet events seen as fake lepton events are the following: semi-leptonic decay of a b-jet, decay-in-flight of a $\pi^{\pm}$ or a K meson, reconstruction of a π^0 as an electron, and reconstruction of a direct photon or a photon conversion as an electron. In the electron channel, the QCD multijet events can fake an electron in the various ways listed above while in the muon channel, the dominant source of fake muons comes from the semi-leptonic decay of a heavy flavor jet.

In the electron channel, electrons faking jets are usually modeled from data or Monte Carlo events using the anti-electron or the jet-electron model. The QCD multijet normalization is then determined by fitting to the data the distribution of an appropriate observable in a QCD-enriched control region. In the anti-electron model, faked electrons are generated by inverting the isolation cuts whereas jets acting like electrons are used in the jet-electron model.

For the muon channel, one utilizes the matrix method which is a very reliable approach when fake muons originate from a single source. The matrix method is able to provide both the overall normalization and the shape modeling of the observables.

8.4.1 Electron channel

The jet-electron model [145] is used to mimic faked-electron events coming from QCD multijet production. Events from Monte Carlo simulated samples containing only real jets (actually filtered dijet events generated with Pythia - see Section 6.1.6) with exactly one of them faking an electron candidate are selected. This faked jet should have the same transverse momentum threshold and the same pseudorapidity coverage than a signal electron and in addition 80% to 95% of its energy deposited in the electromagnetic calorimeter. Additionally, it is required that at least four tracks are found in the jet in order to reduce the amount of converted photons. The cut at 0.75 is also applied on the jet vertex fraction to avoid pileup contributions. Finally, a positive or negative charge, randomly chosen, is assigned to the jet-electron (a charge symmetry is assumed in faking electrons).

Using the jet-electron model to get template distributions for the QCD multijet background, one obtains its overall normalization through a binned likelihood fit to the data. The likelihood fit is performed on the distribution measured for the missing transverse momentum. The parameters of the fit are, besides the QCD multijet normalization, the scale factors associated to the top quark processes and to the W+jets production, while the Z+jets and diboson background contributions are fixed to their predicted cross sections. For all processes, the Monte Carlo distribution shapes are used in the fit. The QCD multijet normalization is determined in the low E_T^{miss} region ($E_T^{miss} < 30GeV$) where QCD multijet events are expected to be dominant. The likelihood fit is performed after having applied all the preselection requirements listed in Section 8.2.1 but leaving out the E_T^{miss} cut. The QCD multijet contribution is then extrapolated in the signal region $E_T^{miss} > 30\ GeV$ from the

normalization factor given by the fit.

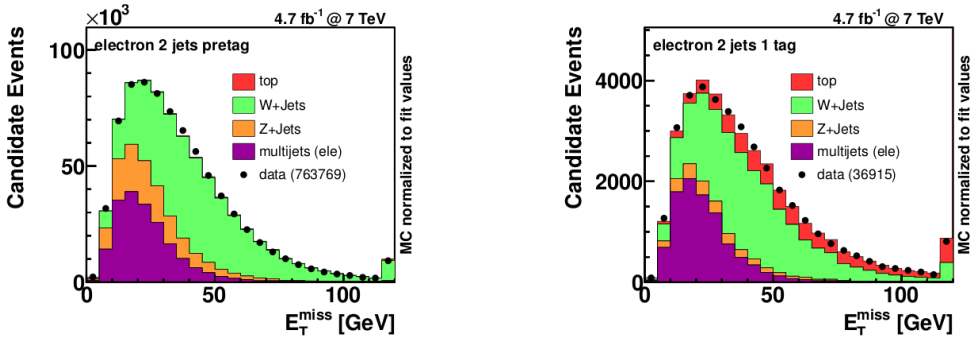

Figure 8-1: Distributions of the missing transverse momentum for the PRETAG (left) and TAG (right) samples with the QCD multijet normalizations estimated by the likelihood fit to the data and the jet-electron shape modeling.

	PRETAG sample		TAG sample	
	QCD events	QCD fractions	QCD events	QCD fractions
Central electrons	9014 ± 4507	5.1%	664 ± 332	6.0%
Forward electrons	10491 ± 5246	12.2%	426 ± 213	11.5%

Table 8.1: QCD multijet contributions estimated by the likelihood fit to the data and the jet-electron model for events with a central ($|\eta| < 1.37$) and a forward ($1.52 < |\eta| < 2.47$) electron.

Figure 8-1 shows the distributions of the missing transverse momentum for the PRETAG and TAG samples with the templates given by the jet-electron model for the QCD multijet background and the templates from Monte Carlo simulations for the other components. The QCD multijet contribution is normalized to the rate estimated from the fit and the other ones are all normalized to their theoretical predictions. The good agreement between the data and the expected distributions shows that the QCD multijet background contribution is well modeled by the jet-electron model.

The estimated numbers and fractions of events are listed in Table 8.1 for the PRETAG and TAG samples. These estimates are provided separately for events with a central ($|\eta| < 1.37$) and a forward ($1.52 < |\eta| < 2.47$) electron according to the geometry of the electromagnetic calorimeter. The fraction of QCD multijet events over the total number of events is 5.1% in the central region and 12.2% in the forward region for the PRETAG sample and 6.0% in the central region and 11.5% in the forward region for the TAG sample. The rejection of QCD multijet events is therefore better in the barrel than in the end-caps of the electromagnetic calorimeter.

For the final signal samples, the QCD multijet event rates are derived from the TAG values given in Table 8.1 by additionally applying the efficiency corrections corresponding to the SELECTION-1 and SELECTION-2 sets of cuts, which are used in the event yields reported in Section 8.6.2.

A common systematic uncertainty of 50% on the extracted QCD multijet rates is evaluated from pileup studies, cross checks using less sensitive variables for the binned likelihood fit and comparison with an alternative estimation procedure (matrix method).

8.4.2 Muon channel

The matrix method was first developed for the analyses of the $D0$ experiment [146]. This method utilizes the different identification-related efficiencies between real and fake leptons to estimate the fraction of fake lepton events in the analyzed data samples. To implement this method, one needs to define two types of events: a "tight" sample which is the one used for the measurements and a "loose" sample which is a mother set of the "tight" one obtained by removing the isolation cuts in the selection of the lepton. By combining the numbers of events and the efficiencies associated to the two types of events and lepton candidates, one can write down:

$$\begin{aligned} N^{loose} &= N^{loose}_{real} + N^{loose}_{fake} \\ N^{tight} &= \epsilon_{real} N^{loose}_{real} + \epsilon_{fake} N^{loose}_{fake} \end{aligned} \tag{8.8}$$

where N^{loose} and N^{tight} are the numbers of events in the loose and tight samples while the real efficiency ϵ_{real} and the fake efficiency ϵ_{fake} are defined as the probability to identify a real lepton and a fake lepton as an isolated tight lepton, respectively. These efficiencies can be obtained from dedicated control samples enriched in either real lepton events (containing mainly W and Z bosons decaying leptonically) or fake lepton events (mainly QCD multijet events). The two unknown ingredients in Equation 8.8 are N^{tight}_{real} and N^{tight}_{fake} which are the number of real lepton events and the number of fake lepton events passing the tight selection requirements, respectively. By solving the two equations, one get the QCD multijet event rate:

$$N^{tight}_{fake} = \frac{\epsilon_{fake}}{\epsilon_{real} - \epsilon_{fake}} (N^{loose} \epsilon_{real} - N^{tight}). \tag{8.9}$$

To get a good precision on the fake rate estimated with this method, there are several points which need to be satisfied. First, the real and fake efficiencies should be sufficiently different from each other. When the efficiencies have similar values, the two components will not be distinguishable from each other: the fake or real lepton rates could go freely with the other one compromising to keep their sum invariant. Secondly, both efficiencies should be as independent of the event topology as possible: they should be determined in two separate control regions before being applied to the signal events. Finally, a parameterization on the detector geometry as well as on the physics kinematics should be considered to give a better description of the efficiencies. The tight cut used here is the muon isolation requirement described in Section 8.1.

The real efficiencies ϵ_{real} are simply derived directly from Monte Carlo simulated samples of physics processes producing prompt isolated muons and from events satisfying all the signal event preselection criteria. The estimated real efficiencies are

around 95% for the PRETAG and TAG samples as listed in Table 8.2. The efficiencies measured from the data with $Z \to \mu\mu$ events agree with the ones derived from the simulation within 1%.

PRETAG	TAG
0.961±0.003	0.944±0.014

Table 8.2: Muon real efficiencies estimated from Monte Carlo simulated events of physics processes producing prompt isolated muons before (PRETAG) and after (TAG) applying the b-tagging requirement. Uncertainties are statistical only. These efficiencies are extracted with the preselection cuts only applied.

The fake efficiencies ϵ_{fake} are measured from the data using only muons with a high significance of the transverse impact parameter (d_0) relative to the primary vertex and from the preselected events enriched in multijet by requiring a low W boson transverse mass ($m_{\mathrm{T}}(W) < 20$ GeV). An additional inverted triangular cut is also applied to further enrich this control region in multijet events ($E_T^{miss}+m_T^W < 60$ GeV). This measurement assumes that the multijet background in the muon+jets channel is dominated by the leptonic decayed heavy flavor jets, which produce muons featured by a large impact parameter with respect to the primary vertex. The loose-to-tight muon efficiencies obtained from data and simulations are displayed in Figures 8-2 as a function of the threshold on the d_0 significance. These efficiency curves can be fitted with the equation:

$$f(x) = ae^{-bx^2} + cx + d \tag{8.10}$$

where x stands for the threshold on the d_0 significance and a, b, c, d are free parameters of the fit. The asymptote constant d is considered as the fake efficiency [147]. Figure 8-2(a) shows that the efficiencies calculated with simulated events including real and fake lepton events (solid dots) and the efficiencies calculated with only simulated QCD multijet events (blue squares) converge in the high d_0^{sign} region; this validates the method of extraction of the fake efficiency from events with a high d_0 significance.

The estimated fake efficiencies ϵ_{fake} with the parameterization on the muon pseudorapidity $|\eta|$ are reported in Table 8.3. In general, the fake efficiency values fluctuate between 7% to 16%. These values are very different from the real efficiencies listed in Table 8.2.

To calculate the contribution of the multijet background in the various analyzed control and signal datasets, each event of the corresponding "loose" data samples is re-weighted according to the quality (loose or tight) of the selected lepton by using the following formula:

$$w_{tight} = \epsilon_{fake}\frac{\epsilon_{real} - 1}{\epsilon_{real} - \epsilon_{fake}} \quad and \quad w_{loose} = \frac{\epsilon_{fake}\ \epsilon_{real}}{\epsilon_{real} - \epsilon_{fake}}. \tag{8.11}$$

Table 8.4 summarizes the estimated QCD multijet contributions. In the PRETAG sample, the QCD multijet fraction is 1.3% while it is 3.4% in the TAG sample. For the final signal samples, the QCD multijet rates are also directly determined by reweight-

Muon $\|\eta\|$	PRETAG	TAG
0.0-0.5	0.096±0.001	0.074±0.003
0.5-1.1	0.112±0.002	0.082±0.003
1.1-1.4	0.135±0.002	0.103±0.005
1.4-2.0	0.138±0.002	0.110±0.003
2.0-2.5	0.157±0.004	0.122±0.007

Table 8.3: Muon fake efficiencies estimated for the multijet enriched samples before (PRETAG) and after (TAG) applying the b-tagging requirement. Uncertainties are statistical only. These efficiencies are extracted with the preselection cuts only applied.

ing the "loose" data samples selected with the SELECTION-1 and SELECTION-2 cuts. The obtained event yields are listed in Section 8.6.2.

Comparison of the multijet event fractions estimated with alternative procedures to extract the efficiencies and to define the multijet enriched control region leads to significant differences and a systematic uncertainty of 50% is assigned to the estimates of the multijet background for all event samples.

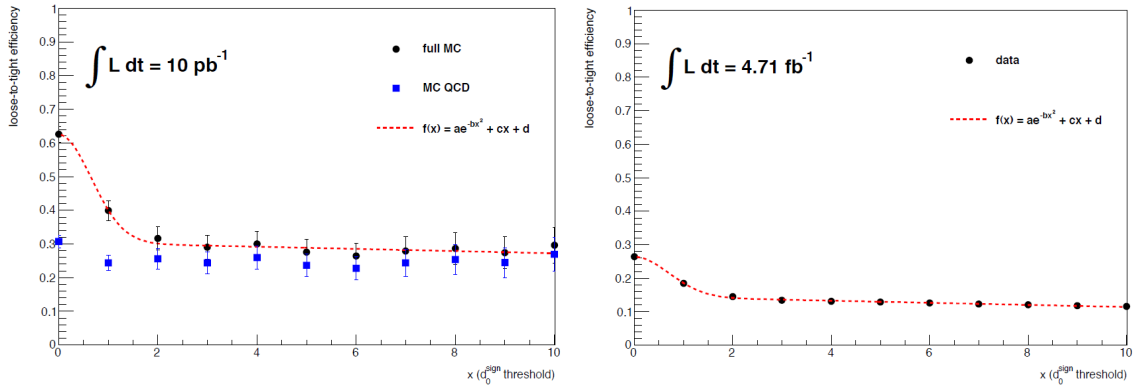

(a) (b)

Figure 8-2: Efficiencies as a function of the threshold on the d_0 significance for (a) simulations and (b) data. On the left, the solid dots represent the efficiencies calculated with simulated events including real and fake lepton events while the blue squares represent the efficiencies calculated with only simulated QCD multijet events. The red dashed lines show the fit with Equation 8.10. The fake efficiency is extracted from the fit of the efficiency curve obtained from the data.

8.5 $W + jets$ background estimation

$W + jets$ events are an irreducible background to single top quark events due to their real leptonic decayed W bosons. For the $W + jets$ processes, one usually uses

	PRETAG sample		TAG sample	
	QCD events	QCD fractions	QCD events	QCD fractions
Muons	4182 ± 2091	1.3%	550 ± 275	3.4%

Table 8.4: QCD multijet contributions estimated with the matrix method for the muon channel.

the Monte Carlo simulations to model the distribution shapes while data-driven scale factors are applied to correct the theoretical cross sections. The correction factors are decomposed into two parts: the overall normalization factor for a global correction of all $W+jets$ processes and a set of flavor K-factors that corrects the flavor composition of the simulated samples, K_{light} for $W + light\ jets$, $K_{bb} = K_{cc}$ for $W + b\bar{b}$ and $W + c\bar{c}$ and K_c for $W + c$. As the ratio between $W + b\bar{b}$ and $W + c\bar{c}$ is well known, one uses the same K-factor for both of them.

A simple counting method is used to determine the overall normalization correction; it is defined as the ratio of the number of W+jets events in the data ($N_{W+jets,data}$) over the number of W+jets events in the simulation ($N_{W+jets,MC}$) and is calculated as follows:

$$K_{tot} = \frac{N_{W+jets,data}}{N_{W+jets,MC}} = \frac{N_{data} - N_{top} - N_{electroweak} - N_{QCD}}{N_{W+jets,MC}} \tag{8.12}$$

where N_{data} is the total number of events in the data, N_{top} the number of all top quark events given by the simulations, $N_{electroweak}$ the number of events predicted by the simulations for the other electroweak processes and N_{QCD} the number of QCD multijet events determined with the data-driven methods. The number of $W + jets$ events in the data is simply obtained by subtracting to the data the expected numbers of events for all non W+jets processes.

The PRETAG samples generated with an additional mass veto ($m_t < 150\ GeV$ or $m_t > 190\ GeV$), as explained in Section 8.2.3, are used to extract the overall normalization corrections. These control samples are highly enriched with $W + jets$ events (85%) with a signal contamination estimated at around 1%.

The flavor correction factors $K_{b\bar{b}}$, K_c and K_{light} are extracted by considering the TAG samples in addition to the PRETAG ones, both including the additional mass veto. The procedure used in this analysis also needs PRETAG and TAG events selected by requiring only one jet in addition to the usual 2-jets samples. These extra samples which are essentially composed of W+jets events allow to strongly constrain the extraction of the flavor correction factors.

The flavor composition of the simulated W+jets events is expressed by the following relation:

$$N_{W+jets,MC} = K_{b\bar{b}} \left(N_{b\bar{b},MC} + N_{c\bar{c},MC} \right) + K_c N_{c,MC} + K_{light} N_{light,MC} \tag{8.13}$$

where the K-factors are defined as the ratios between the flavor fractions in the data

and those in the Monte Carlo simulations:

$$K_{b\bar{b},c\bar{c},c,light} = \frac{F_{b\bar{b},c\bar{c},c,light,data}}{F_{b\bar{b},c\bar{c},c,light,MC}}. \tag{8.14}$$

In Equation 8.13, $K_{c\bar{c}}$ is replaced by $K_{b\bar{b}}$ since we assume that $F_{c\bar{c}} = k_{c\bar{c}tob\bar{b},MC} F_{b\bar{b}}$ where $k_{c\bar{c}tob\bar{b},MC}$ is the ratio between the $c\bar{c}$ and $b\bar{b}$ fractions taken from the Monte Carlo simulations. The fractions $F_{b\bar{b}}$, F_c and F_{light} add up to unity leading to the following sum rule which relates the three unknown flavor fractions to be measured from the data:

$$\left(1 + k_{c\bar{c}tob\bar{b},MC}\right) F_{b\bar{b}} + F_c + F_{light} = 1. \tag{8.15}$$

The flavor correction factors are extracted with a χ^2 minimization procedure which involves the PRETAG and TAG samples associated with one or two jets. The minimization is performed on the differences between the observed ($N_{W+jets,data}$) and expected ($K_{tot} * N_{W+jets,MC}$) numbers of W+jets events in the samples, the expectations including the normalization correction (Equation 8.12) and the flavor K-factors (Equation 8.13).

The procedure described above is used to estimate the flavor corrections for events with two jets. The corrections for the other jet multiplicites, in particular for the 1-jet event samples, are derived by renormalizing the 2-jets K-factors according to:

$$K_{b\bar{b},c,light,1} = \frac{K_{b\bar{b},c,light,2}}{F_{b\bar{b},MC,1} K_{b\bar{b},2} + k_{c\bar{c}tob\bar{b},MC,1} F_{b\bar{b},MC,1} K_{b\bar{b},2} + F_{c,MC,1} K_{c,2} + F_{light,MC,1} K_{light,2}} \tag{8.16}$$

where $F_{b\bar{b},MC,1}$, $F_{c,MC,1}$, $F_{light,MC,1}$ are the flavor fractions and $k_{c\bar{c}tob\bar{b},MC,1}$ the ratio between the $c\bar{c}$ and $b\bar{b}$ fractions given by the Monte Carlo simulations of the 1-jet event samples.

The estimated correction factors are summarized in Table 8.5 for the electron and and muon channels as well as for the combination of the two channels. In this table, the individual flavor K-factors and the overall normalization factor K_{tot} are listed as well as the final corrections calculated by $K_{tot} * K_{flavor}$.

Channel	K_{tot}	K_{bb}	K_c	K_{light}	$K_{tot} * K_{bb}$	$K_{tot} * K_c$	$K_{tot} * K_{light}$
Electron	0.992	1.135	1.426	0.886	1.126	1.415	0.879
Muon	1.031	1.425	1.213	0.893	1.469	1.251	0.921
Combined	1.014	1.307	1.301	0.890	1.326	1.320	0.903

Table 8.5: Estimated overall and flavor corrections factors for $W+jets$ for the electron and muon channels and for the combined electron+muon channel.

The impact of the various sources of systematic uncertainties on the calculated overall normalizations and flavor corrections is estimated using a statistical frequentist method based on the generation of a large number of correlated pseudo-experiments.

The systematic uncertainties which are taken into account and the pseudo-experiment generation procedure will be discussed in Section 9.7.

The total relative systematic and statistical uncertainties on the final correction factors $K_{tot}{}^{*}K_{b\bar{b}}$, $K_{tot}{}^{*}K_{c}$ and $K_{tot}{}^{*}K_{light}$, derived from the analysis of the output distributions of the pseudo-experiments, are reported in Table 8.6. The uncertainties are listed for the electron and muon channels separately and for the combination of the two channels. In general, the total uncertainty is around 25% for the correction factors on the $Wbb(cc)$ process, around 21% for the Wc process, and around 14% for the $W + light$ process.

To have a deeper look into the uncertainties, the breakdown of the relative contributions to the statistical and systematic uncertainties on the final correction factors $K_{tot}{}^{*}K_{b\bar{b}}$, $K_{tot}{}^{*}K_{c}$ and $K_{tot}{}^{*}K_{light}$ are reported in Table 8.7 for the combination of the electron and muon channels. The jet energy scale uncertainty strongly affects all the K-factors, since it affects the rates of all $W + jets$ processes by 10% to 20%. The b-tagging scale factor uncertainty affects the K-factor on Wbb process largely due to its two jets originating from b-quarks, while the c-tagging scale factor uncertainty affects the K-factor on Wc process largely due to its jet originating from a c-quark.

These K-factors and their uncertainties will enter into the measurements of the top quark polarization with the unfolding method. They will not be used for the measurements performed with the folding method, since, in that case, the W+jets normalization correction factors are directly included in the fit to the data distributions, via the constraint from the control region containing only high invariant mass events ($m(l\nu b) > 250\ GeV$) introduced in Section 8.2.3. The unfolding and folding methods will be discussed in Chapter 9.

Channel	$K_{tot}{}^{*}K_{b\bar{b}}$ (%)	$K_{tot}{}^{*}K_{c}$ (%)	$K_{tot}{}^{*}K_{light}$ (%)
Electron	34.8 (9.5)	23.0 (7.7)	15.3 (1.4)
Muon	21.9 (6.1)	21.4 (7.9)	12.7 (1.2)
Combined	25.5 (5.1)	20.9 (5.6)	13.6 (0.9)

Table 8.6: Total relative uncertainties (statistical+systematics) on the final correction factors $K_{tot}{}^{*}K_{flavor}$ estimated for the $W_{b\bar{b}}$, W_c and W+light jets processes for the electron and muon channels as well as for the combined electron+muon channel. The total statistical errors are quoted in parentheses.

8.6 Event yields

8.6.1 Preselection

The event yields obtained with the preselections described in Section 8.2.1 for the PRETAG and TAG samples are given in Tables 8.8 and 8.9 for the electron and muon channels, respectively. The expectations for the top quark, Z+jets and diboson processes are estimated from the Monte Carlo simulations as discussed in Section 6.1,

Systematic	$Wb\bar{b}$ (%)		Wc (%)		W+light jets (%)	
Data statistics	+3.9	-3.9	+4.0	-4.0	+0.6	-0.6
Simulation statistics	+3.4	-3.4	+3.9	-3.9	+0.7	-0.7
Luminosity	+3.3	-3.3	+1.8	-1.8	+0.2	-0.2
top background normalization	+14.5	-14.5	+9.0	-9.0	+0.2	-0.2
Z+jets, diboson normalization	+0.3	-0.3	+3.9	-3.9	+3.7	-3.7
Multijet normalization	+8.2	-8.2	+1.0	-1.0	+1.6	-1.6
E_T^{miss}	+0.6	-0.5	+0.2	-1.1	+0.3	-0.3
Lepton reconstruction	+5.7	-5.2	+0.0	-0.0	+2.2	-2.0
Lepton energy resolution	+0.3	-0.2	+0.2	-0.5	+0.0	-0.0
Lepton energy scale	+1.4	-0.9	+0.3	-0.3	+0.5	-0.4
Jet reconstruction	+0.1	-0.1	+0.0	-0.0	+0.0	-0.0
Jet energy resolution	+3.7	-3.6	+1.0	-0.9	+3.7	-3.5
Jet energy scale	+9.3	-4.0	+10.6	-17.9	+10.3	-13.3
Jet vertex fraction	+2.7	-3.0	+0.2	-0.2	+0.7	-0.6
b-tagging factor	+14.9	-11.8	+5.0	-6.4	+1.0	-1.3
c-tagging factor	+4.1	-3.6	+7.0	-5.7	+2.5	-3.0
mis-tagging factor	+1.0	-1.0	+1.0	-1.1	+0.5	-0.5
ISR/FSR	+5.7	-5.7	+3.9	-3.9	+0.1	-0.1
t-channel generator	+1.0	-1.0	+1.9	-2.0	+0.4	-0.4
$t\bar{t}$ generator	+1.4	-1.5	+0.7	-0.7	+0.1	-0.1
W+jets shape variation	+0.8	-0.8	+0.9	-0.9	+0.9	-0.8
Total statistics	+5.1	-5.1	+5.6	-5.6	+0.9	-0.9
Total systematic	+26.6	-23.3	+17.6	-22.8	+12.2	-14.9
Total	+27.1	-23.9	+18.4	-23.5	+12.3	-15.0

Table 8.7: Breakdown of the relative uncertainties on the final correction factors $K_{tot}{}^{*}K_{flavor}$ estimated for the $W_{b\bar{b}}$, W_c and W+light jets processes for the combination of the electron and muon channels. The included sources of systematic uncertainties will be discussed in Section 9.7. The uncertainties are quoted in per cent.

while the ones for the W+jets and QCD multijet contributions are estimated with the data-driven methods presented in the previous sections. The uncertainties of all expected yields are given by the theoretical uncertainties except for the QCD multijet events to which one associates a 50% uncertainty as mentioned in Section 8.4.

In the PRETAG samples, the largest background comes from the $W + light\ jet$ process due to its large cross section and to exactly the same final state "l+jets" as the signal before any b-tagging requirements. The $W + heavy\ jets$ processes are the second largest backgrounds. All $W + jets$ processes take up 80% to 90% of the total event yields. The contributions from the $Z + jets$, diboson and QCD multijet processes are also copious before the b-tagging selection. At this stage, the signal-over-background ratio, calculated from the expectations, is around 0.01.

After b-tagging (TAG samples), the $W+light\ jets$ process is no more the dominant

background, 99% of the events being cut away by the requirement of one b-tagged jet in the final state. Instead, $W + heavy\ jets$ processes and other top quark processes turn out to be dominant taking up 70% of the whole event yield due to the existence of real b-jets in their final states. At this stage, the signal-over-background ratio reaches 0.1.

Process	PRETAG	TAG
t-channel	3386±339	1703±170
$t\bar{t}$,Wt,s-channel	9965±997	4743±474
W+light jets	134406±40322	1339±402
W+heavy flavor	73835±36918	5237±2619
Z+jets,diboson	20651±12391	317±190
Multijet	19505±9752	1090±545
Total expectation	261747±100717	14429±4400
Data	260193	14738

Table 8.8: Expected and observed event yields for the electron channel in the PRETAG and TAG control samples. The uncertainties correspond to the theoretical uncertainties except the QCD multijet background to which a 50% uncertainty is associated.

Process	PRETAG	TAG
t-channel	4089±409	2053±205
$t\bar{t}$,Wt,s-channel	11755 ±1176	5573±557
W+light jets	187630±56289	1926±578
W+heavy flavor	97380±48690	7689±3845
Z+jets,diboson	14441±8664	333±200
Multijet	4182±2091	550±275
Total expectation	319478±117319	18124±5660
Data	316944	17966

Table 8.9: Expected and observed event yields for the muon channel in the PRETAG and TAG control samples. The uncertainties correspond to the theoretical uncertainties except the QCD multijet background to which a 50% uncertainty is associated.

8.6.2 Signal selection

Based on the preselected samples, one applies the final t-channel cuts introduced in Section 8.2.2 to purify the selected samples in order to reach a higher signal-over-background ratio. The event yields obtained for the SELECTION-1 and SELECTION-2 samples are listed in Tables 8.10 and 8.11, respectively. The uncertainties are all from theoretical uncertainties except for the QCD multijet background where the data-driven uncertainty of 50% is associated. Both SELECTION-1 and SELECTION-2

cuts manage to reduce the W + *heavy jets* and background top quark events below 50% of the total event yield (compared to 70% in the TAG samples) although they are still the dominant backgrounds. The SELECTION-1 soft set of cuts gives a signal-over-background ratio of 0.60 whereas a higher S/B value, close to 1, is found for the harder SELECTION-2 cuts.

Process	e-channel	μ-channel
t-channel	394±39	459±46
$t\bar{t}$,Wt,s-channel	257±26	300±30
W+light jets	72±22	123±37
W+heavy flavor	240±120	298±149
Z+jets,diboson	15±9	14±8
Multijet	41±20	27±14
Total expectation	1018±236	1221±284
Data	1097	1186
S/B	0.63±0.21	0.60±0.20

Table 8.10: Expected and observed event yields for the electron and muon channels after applying the soft SELECTION-1 set of cuts. The uncertainties correspond to the theoretical ones except for the QCD multijet background to which a 50% uncertainty is associated. The signal-over-background ratios (S/B) derived from the expected yields are also given.

Process	e-channel	μ-channel
t-channel	262±26	318±32
$t\bar{t}$,Wt,s-channel	131±13	160±16
W+light jets	15±4	23±7
W+heavy flavor	107±53	138±69
Z+jets,diboson	5±3	5±3
Multijet	17±8	6±3
Total expectation	537±109	650±130
Data	576	691
S/B	0.95±0.30	0.96±0.30

Table 8.11: Expected and observed event yields for the electron and muon channels after applying the tight SELECTION-2 set of cuts. The uncertainties correspond to the theoretical ones except for the QCD multijet background to which a 50% uncertainty is associated. The signal-over-background ratios (S/B) derived from the expected yields are also given.

8.7 Kinematic distributions

In this section, the kinematic distributions of the PRETAG, TAG and t-channel selection samples are presented. The data are compared with the expectations for the signal and backgrounds. The total absolute statistical errors from the expectations added to the 50% uncertainty on the QCD multijet contribution are shown in the shadowed bands drawn on top of the stacked histograms. Additionally, to make the comparison easier, the ratio of the data over the expectations is shown in the bottom part of each figure.

8.7.1 PRETAG distributions

The distributions of the transverse momentum and of the pseudorapidity of the physics objects (lepton, leading and sub-leading jets) as obtained in the PRETAG samples are shown in Appendix B.1 for both electron and muon channels. On the whole, these basic kinematic distributions show a good agreement between data and simulations.

The distributions of the missing transverse energy and of the W boson transverse mass are shown in Figure 8-3 for both electron and muon channels. The transverse mass distributions are peaked close to the W boson mass with the main contributions from the $W + jets$ processes. The QCD multijet events are enriched in the low mass region which is cut off by the preselection. For these two types of distributions, the simulations also agree well with the data.

8.7.2 TAG distributions

The distributions of the transverse momentum and of the pseudorapidity of the physics objects (lepton, b-tagged and light jets) as obtained in the TAG samples are shown in Appendix B.2 for both electron and muon channels. On the overall, these basic kinematic distributions show a good agreement between data and simulations. The distributions of the variables used to define the SELECTION-1 and SELECTION-2 series of cuts are also shown in Appendix B.2. A global good agreement between the data and the simulations is found for all these distributions.

The distributions of the missing transverse momentum and of the W boson transverse mass are shown in Figure 8-4 for both electron and muon channels. The transverse mass distributions are peaked close to the W boson mass with the main contributions coming from the $W + heavy\ jets$ and top quark pair events as well as from single top t-channel events. The simulations agree well with the data for these distributions.

8.7.3 Signal distributions

For t-channel selection samples, the kinematic distributions for the physics objects are shown in Appendix B.3 for both the SELECTION-1 and SELECTION-2 samples and for both electron and muon channels. The statistics is quite low after these final

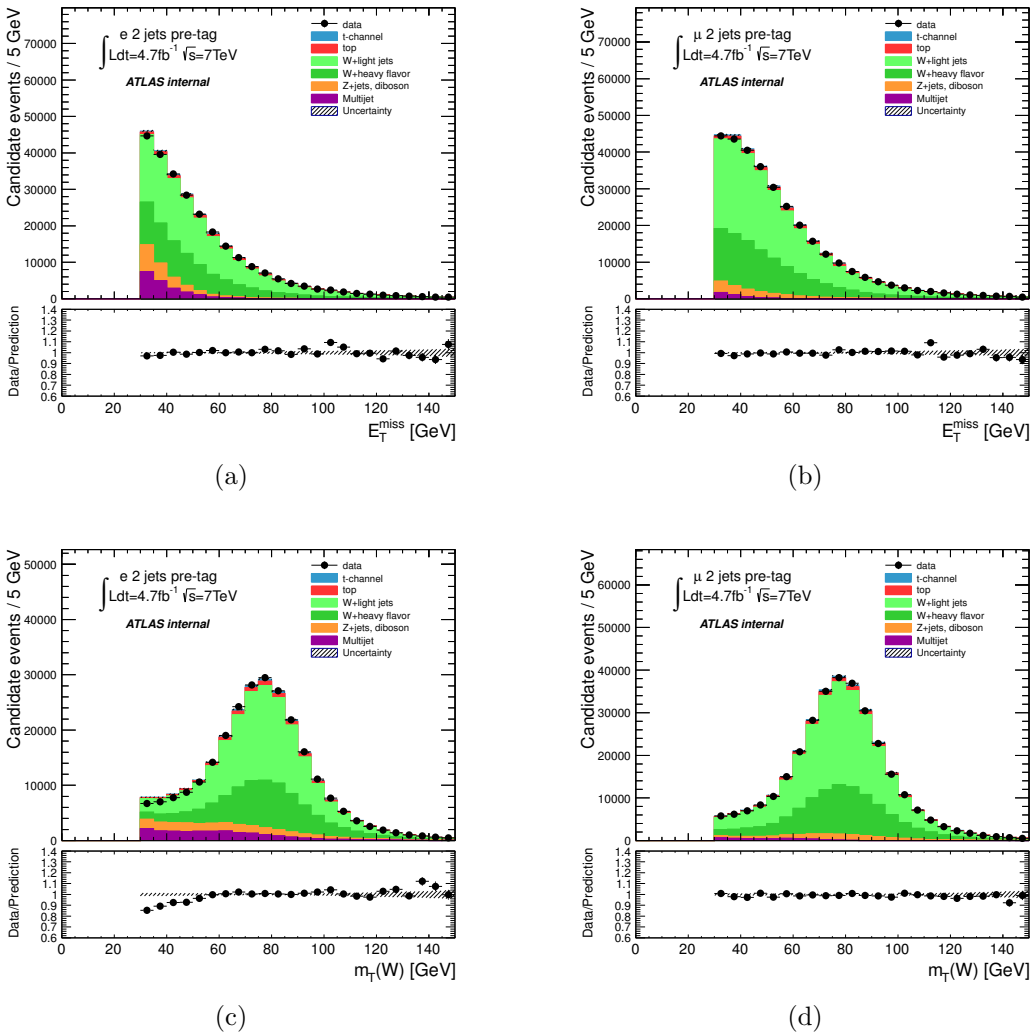

Figure 8-3: Missing transverse momentum and W boson transverse mass distributions for the PRETAG sample (a) missing transverse momentum for the electron channel, (b) missing transverse momentum for the muon channel, (c) W boson transverse mass for the electron channel and (d) W boson transverse mass for the muon channel.

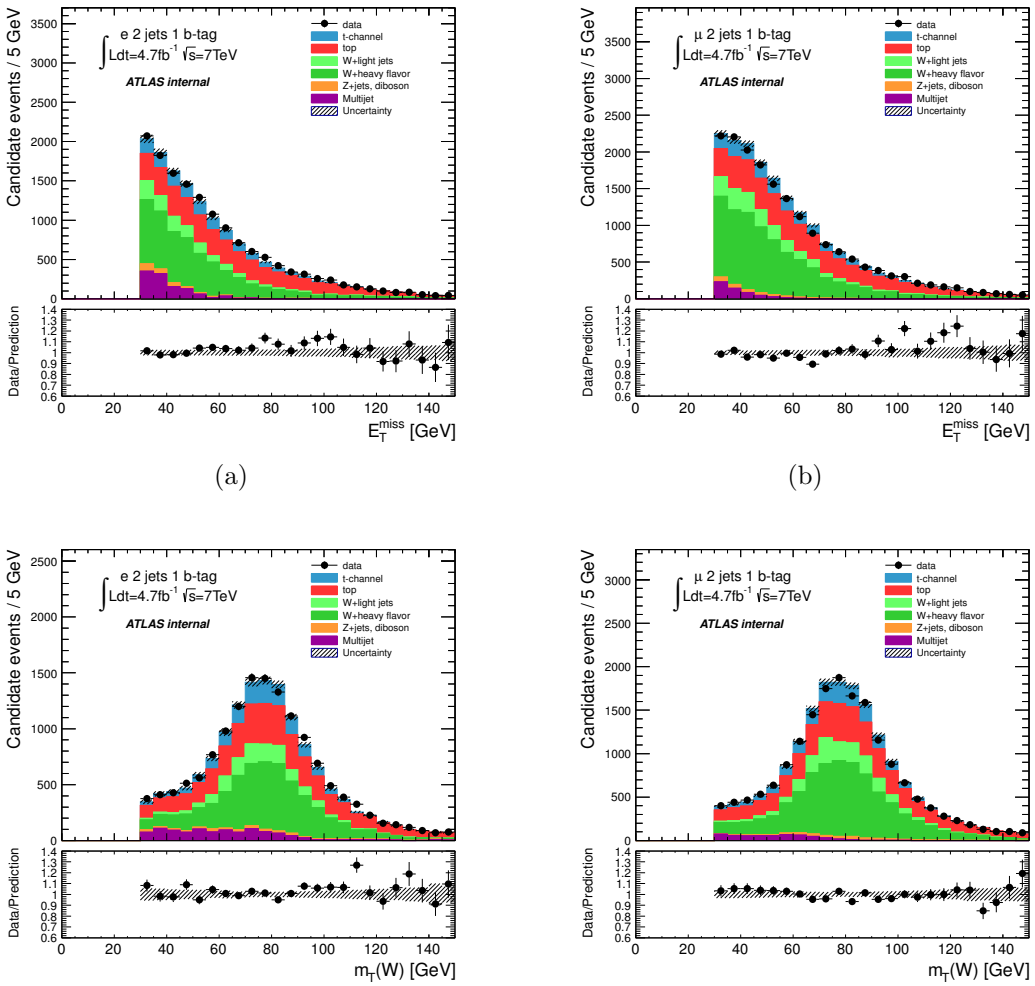

Figure 8-4: Missing transverse momentum and W boson transverse mass distributions in the TAG sample (a) missing transverse momentum for the electron channel, (b) missing transverse momentum for the muon channel, (c) W boson transverse mass for the electron channel and (d) W boson transverse mass for the muon channel.

cuts. Nevertheless, a good modeling of the measured kinematic distributions is on the overall seen within the statistical errors

The distributions of the missing transverse momentum and of the W boson transverse mass are shown in Figures 8-5 and 8-6 for the SELECTION-1 and SELECTION-2 samples respectively and for both electron and muon channels. The transverse mass distributions are peaked close to the W boson mass with the main contributions from the t-channel events as well as from the $W + heavy\ jets$ and $t\bar{t}$ events. The simulation modelings agree well with the data for these distributions.

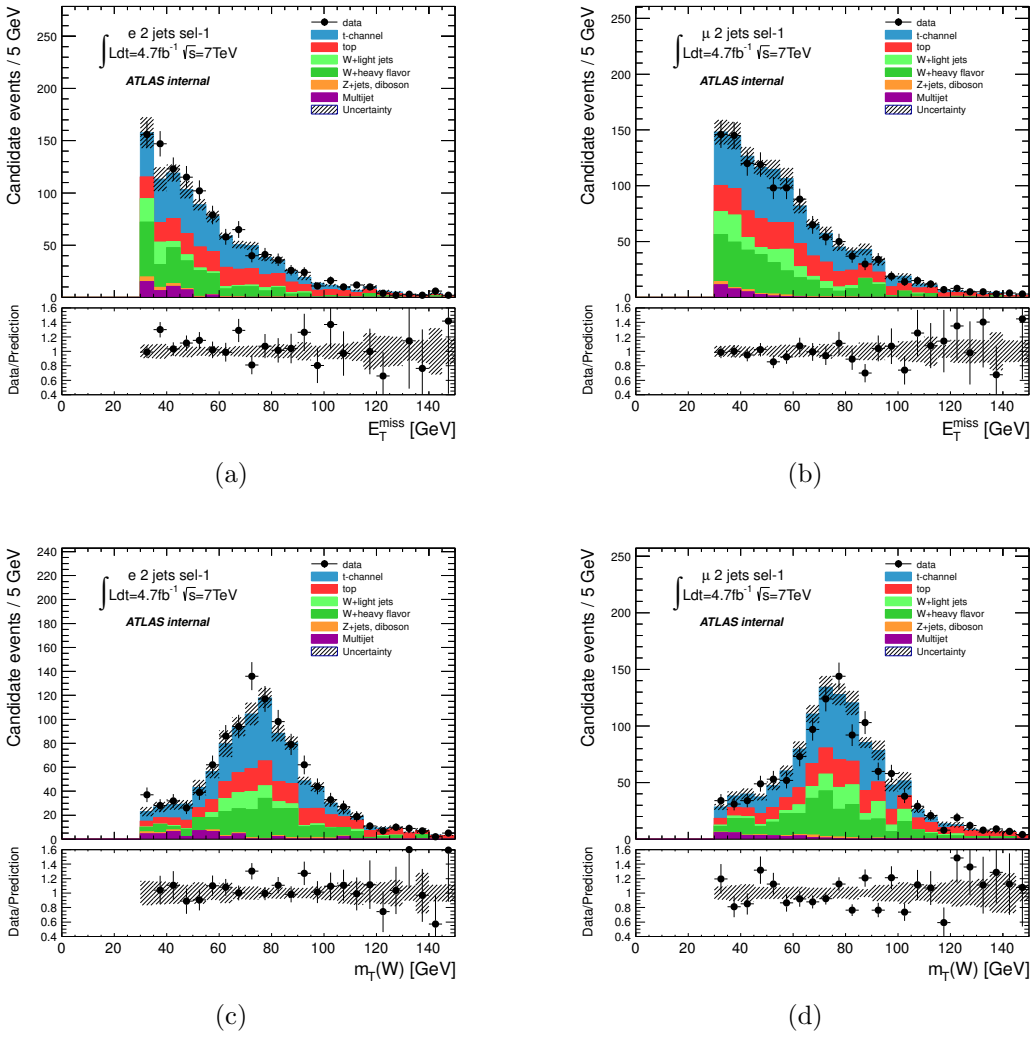

Figure 8-5: Missing transverse momentum and W boson transverse mass distributions for the SELECTION-1 sample (a) missing transverse momentum for the electron channel, (b) missing transverse momentum for the muon channel, (c) W boson transverse mass for the electron channel and (d) W boson transverse mass for the muon channel.

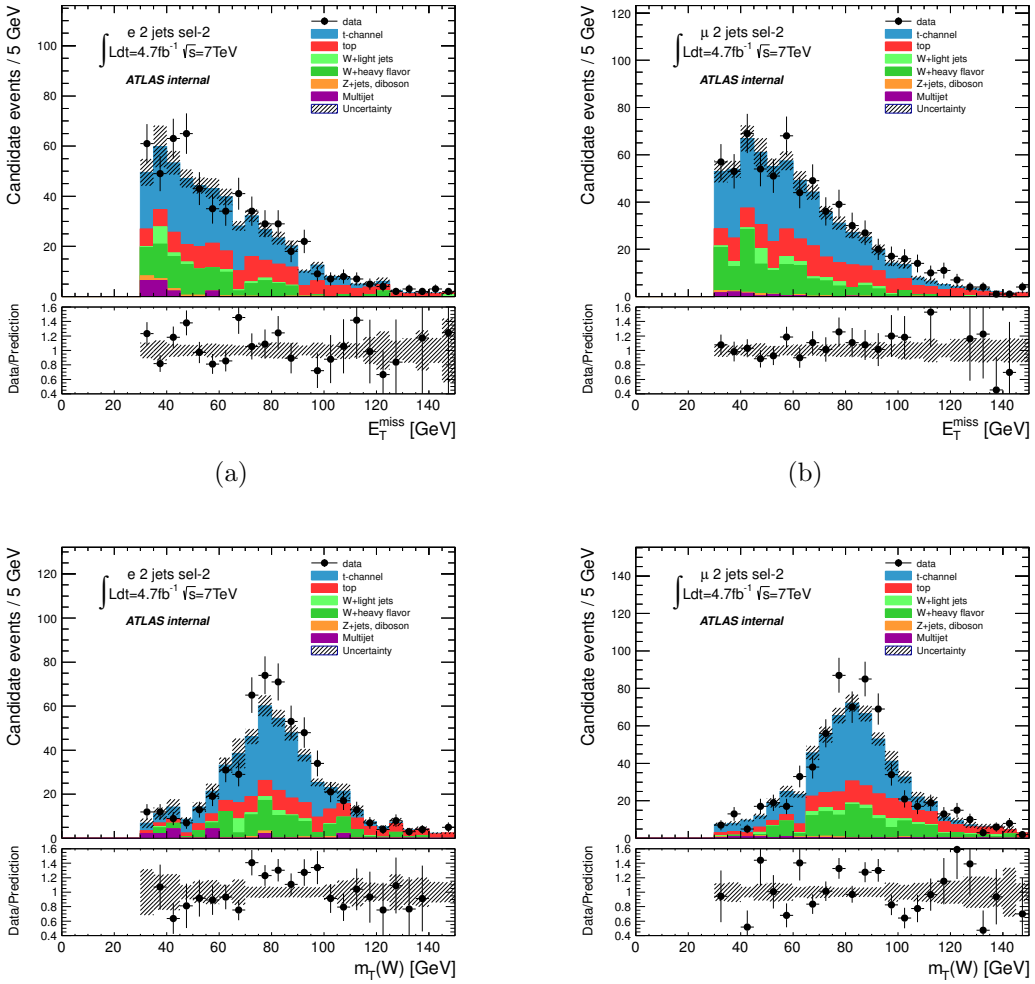

Figure 8-6: Missing transverse momentum and W boson transverse mass distributions for the SELECTION-2 sample (a) missing transverse momentum for the electron channel, (b) missing transverse momentum for the muon channel, (c) W boson transverse mass for the electron channel and (d) W boson transverse mass for the muon channel.

Chapter 9

Top quark polarization measurement

Top quarks produced by electroweak interaction are highly polarized and their degree of polarization can be measured through the angular distributions of their decay products with respect to the chosen spin quantization axis. The differential decay rate of the top quark is given by the following equation as introduced in Section 3.6.5:

$$\frac{1}{\Gamma}\frac{\mathrm{d}\Gamma}{\mathrm{d}\cos\theta_X} = \frac{1}{2}(1 + \alpha_X P \cos\theta_X) \tag{9.1}$$

where θ_X is the angle between the three-momentum of the decay product X (called spin analyzer) in the top quark rest frame and the top quark spin axis (called spin basis), α_X is the spin analyzing power of object X, and P stands for the degree of polarization of the top quark. Object X can be any of the decay products of the top quark: the b-quark or W boson as well as the charged lepton or neutrino coming from the leptonic decay of the W boson. The corresponding analyzing powers α are given in Table 3.4. Only the angular distributions obtained from the charged lepton and the b-quark will be considered in this analysis since they are the only final state objects that can be directly detected and reconstructed. The considered spin basis is the spectator basis which defines the top quark spin axis along the spectator (light) jet momentum in the top quark rest frame.

The direct measurement from the angular distribution is the product $\alpha \cdot P$. One can extract this combined observable either by fitting the shape of the angular distribution or by counting the numbers of events in the forward and backward regions. The latter is called forward-backward asymmetry and is directly related to the product $\alpha \cdot P$ as follows:

$$A_{FB} = \frac{N(\cos\theta > 0) - N(\cos\theta < 0)}{N(\cos\theta > 0) + N(\cos\theta < 0)} = \frac{1}{2}\alpha P \tag{9.2}$$

where the forward-backward asymmetry A_{FB} is defined by the difference in numbers of events between the forward ($\cos\theta > 0$) and backward ($\cos\theta < 0$) angular regions normalized to the total number of events.

In this chapter, the angular distributions obtained at the parton and reconstruc-

tion levels are presented in Section 9.1 and Section 9.2, respectively, followed, in Section 9.3, by a discussion about the differences between the parton-level and reconstructed distributions in terms of migration and efficiency effects. The migration matrices and efficiencies are presented in Section 9.4; they are applied in the extraction of the top quark polarization using the unfolding and folding methods discussed in Section 9.5 and Section 9.6, respectively. To consider the uncertainties on the measurements, the various sources of systematic uncertainties and their realization are described in Section 9.7. The polarization values with their uncertainties extracted from both the expected and data distributions using the different methods are presented and discussed in Section 9.8. Finally, the conclusion, given in Section 9.9, reports the final polarization measurement.

9.1 Angular distributions at parton level

At the parton level, the angular distributions are simply straight lines with a slope that depends on the choice of the spin analyzer (lepton or b-quark in our case) and on the choice of the spin basis (spectator basis in our case), according to Equation 9.1. The parton-level angular distributions for t-channel events generated by AcerMC are shown in Figure 9-1 for the charged lepton and the b-quark analyzers. The top quark and anti-top quark events are combined in both cases. The corresponding values of the product $\alpha \cdot P$ are extracted by a simple χ^2 fit: for the charged lepton, the extracted value is 0.895 while it is -0.361 for the b-quark. As the same degree of polarization P is expected for both analyzers, the difference in slope of the two distributions only reflects the difference of the spin analyzing powers (α_l=1 and α_b=-0.41 at tree level).

The degrees of polarization obtained from the fit to the angular distributions produced by AcerMC are summarized in Table 9.1. Taking into account that particles and anti-particles have spin analyzing powers with opposite signs, degrees of polarization with opposite signs are found for top quark and anti-top quark productions. In addition, a slightly larger value (by around 5%) for the $\alpha \cdot P$ product is obtained for top quark production with respect to anti-top quark production: for the lepton spin analyzer, $\alpha \cdot P$ is 0.912 for top quark and 0.862 for anti-top quark, whereas for the b-quark spin analyzer, $\alpha \cdot P$ is -0.368 for top quark and -0.349 for anti-top quark. The spin analyzing power being naturally the same for top and anti-top quark decays into a given product, the absolute value of the degree of polarization is therefore slightly greater in top quark production than in anti-top quark production.

The reason why top and anti-top quark productions have slightly different degrees of polarization can be explained by the contents in valence quarks (uud) of the two colliding protons and by the properties of the Wtb interaction. From the calculation reported in [74], single top quarks are produced with a spin direction which is maximally correlated (aligned) with the momentum of the initial or final d-type quark involved in the hard process (a much less correlation is expected with the u-type quark). In fact, these correlations between the top quark spin and the directions of initial/final u/d-quark momemtum can be also inferred by crossing symmetry from decay to production, regarding the values of the spin analyzing powers given in Ta-

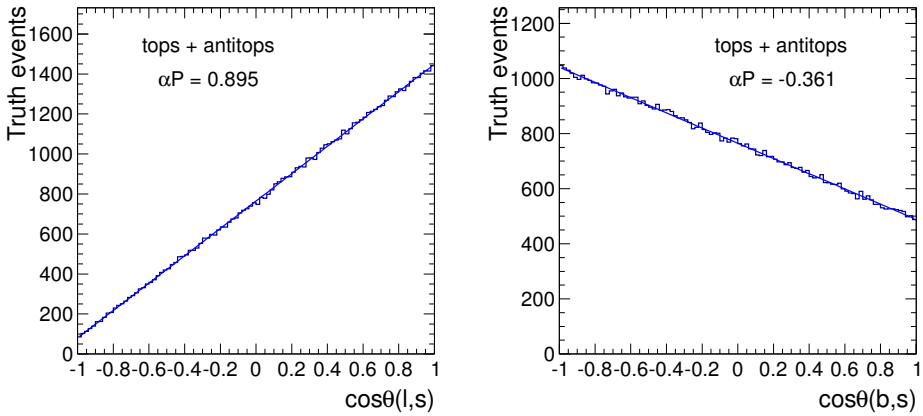

(a) (b)

Figure 9-1: Angular distributions in the spectator basis at parton level (a) for the charged lepton and (b) for the b-quark spin analyzers. The spectator basis is defined by the spectator quark momentum in the top quark rest frame. The distributions include both top quark and anti-top quark decays and are derived from event samples produced with the AcerMC generator. They are fitted using Equation 9.1 and the extracted slopes $\alpha \cdot P$ are given in the plots.

ble 3.4. Different fractions of the production cross section, given in Table 9.2, are calculated for top and anti-top quark productions as a function of the type of the initial quark. For top quark production, the largest fractional cross section is obtained for an incoming u-quark (74%), which becomes a spectator d-quark in the final state. For anti-top quark production, the largest fractional cross section is no more associated to an incoming u-quark (20%) but to the d-quark (56%) which leads to a spectator u-quark in the final state. Top quarks are therefore mainly produced with a spin preferentially aligned along the momentum of the spectator quark since it is in most of the cases a d-type quark whereas anti-top quarks are mainly produced with a spin along the momentum of the incoming quark which is the most likely a d-type quark in that case. Thus, using the spectator quark as the spin axis, top quarks have a maximal polarization, since the spectator quark has more chances to be a d-type quark, while anti-top quarks have a degraded polarization since the spectator quark has less chances to be a d-type quark in this case. However, the degradation is not strong, since the spectator quark has almost the same direction of the momentum as the initial quark after slight deflection.

Considering the small difference between top quark and anti-top quark polarizations and a larger statistics when using all events together, the polarization will be measured from the combination of the top quark and anti-top quark events.

Spin analyzer	Spectator basis		
	t-quark	$\bar{t}$-quark	t+$\bar{t}$-quarks
charged lepton	0.912	0.862	0.895
b-quark	-0.368	-0.349	-0.361

Table 9.1: Degrees of polarization multiplied by the spin analyzing powers, $\alpha \cdot P$, for the charged lepton and b-quark spin analyzers. They are extracted from the angular distributions calculated in the spectator basis for top quark and anti-top quark productions with the AcerMC event generator.

Initial quark	Fractional σ (t)	Fractional σ $(\bar{t})$
u	74%	20%
d	12%	56%
s	8%	13%
c	6%	11%

Table 9.2: Fractional cross sections for single top and anti-top quark t-channel productions in proton-proton collisions at the center of mass energy of 14 TeV. These fractions are decomposed according to the flavor of the valence quark of the initial state [148].

9.2 Angular distributions at reconstruction level

The angular distributions calculated from the reconstructed objects are strongly distorded due to the detection response and to the object and event reconstructions and selections one made to collect the signal events as well as to suppress background contaminations.

At the reconstruction level, the angular distributions are determined from the charged lepton and b-tagged jet four-momenta boosted in the top quark rest frame. The spectator basis is defined by the direction of the untagged (light) jet whose four momentum is also boosted in the top quark rest frame. The procedure used to reconstruct the top quark kinematics is discussed in Section 8.3.

The angular distributions obtained for the Tag preselection event samples are shown in Figure 9-2 for the electron and muon channels. The angular distributions obtained after the final t-channel selections applied are displayed in Figures 9-3 and 9-4 for the Selection-1 and Selection-2 sets of cuts, respectively. On the overall, the expected angular distributions agree with the ones from the data. In the electron channel, a sizeable discrepancy is nevertheless found close to $\cos\theta = 0$ for the lepton analyzer and for both Selection-1 and Selection-2 samples. This is not completely understood and could be due to the multijet modelling as well as the statistical fluctations. The discrepancy could possibly be covered by the uncertainties when considering all systematic sources. The agreement will be considered acceptable in the following. In both electron and muon channels, shown in Figure 9-3(c)

and 9-3(d), SELECTION-1 destroys the angular structure near $\cos\theta = -1$ of the b-quark analyzer due to the introduction of the cut on the pseudorapidity difference $\Delta\eta(bjet, W)$.

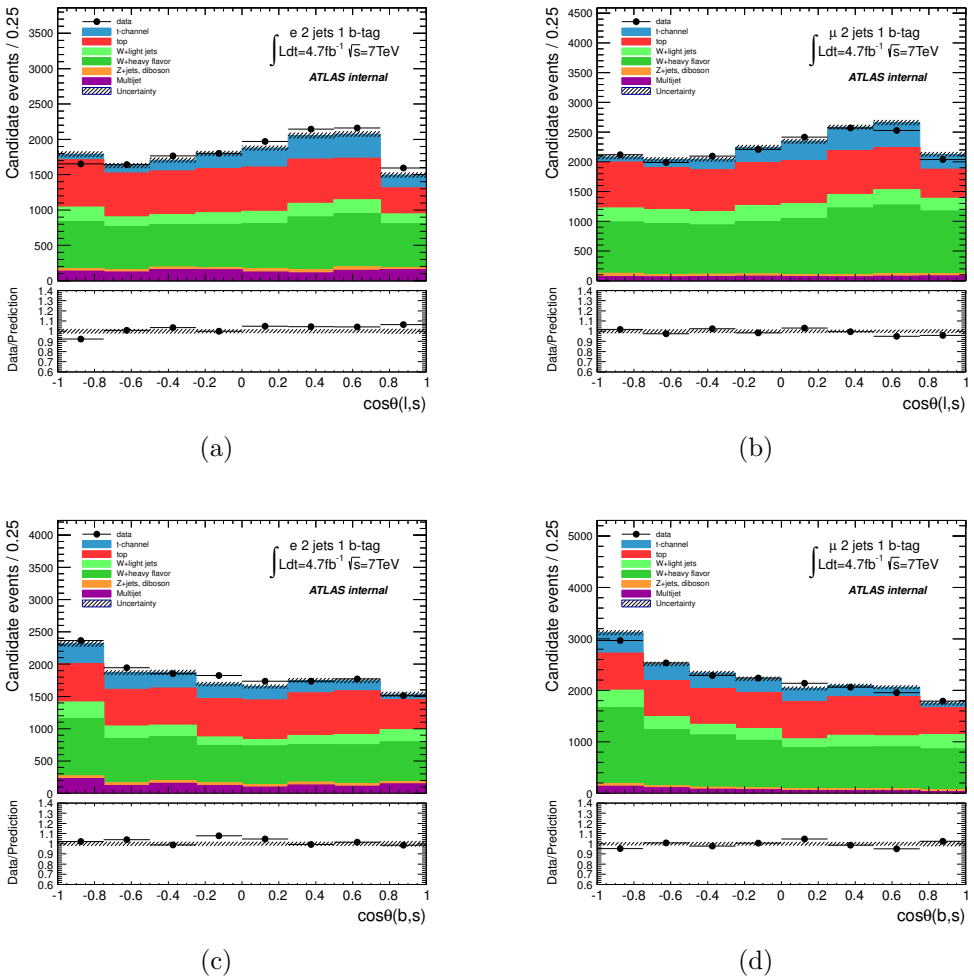

Figure 9-2: Angular distributions reconstructed in the spectator basis for the TAG event samples (a) angular observable for the lepton analyzer in the electron channel, (b) angular observable for the lepton analyzer in the muon channel, (c) angular observable for the b-quark jet analyzer in the electron channel and (d) angular observable for the b-quark jet analyzer in the muon channel.

When comparing the angular distributions at parton and reconstruction levels, one can see that the distributions reconstructed from the data are not simple straight lines any more due to the distorsion effects coming from the detector response, the recontruction algorithms and selection biases as well as to the contamination of background events not completely removed by the final event selections.

In Figures 9-2 to 9-4, one can see that the angular distributions expected for the background contributions are much more flat than those associated to the signal events. No correlations are indeed expected for the various background processes

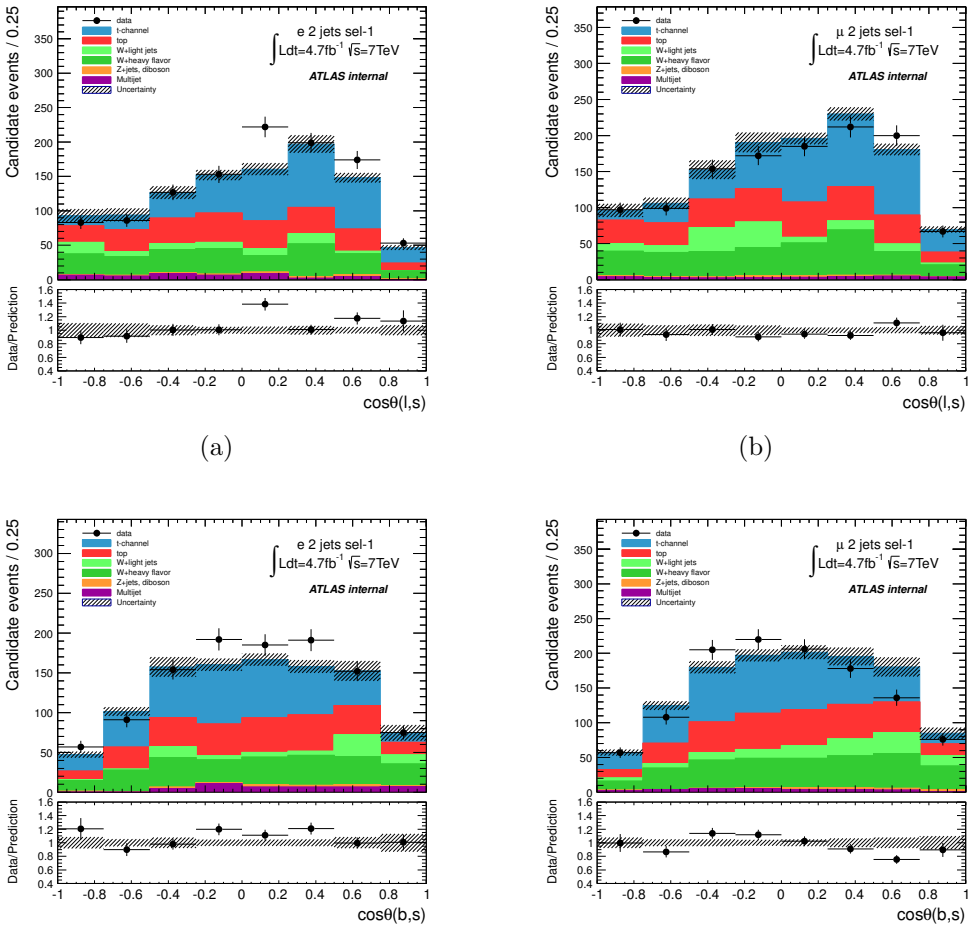

Figure 9-3: Angular distributions reconstructed in the spectator basis for the event samples selected with the SELECTION-1 cuts (a) angular observable for the lepton analyzer in the electron channel, (b) angular observable for the lepton analyzer in the muon channel, (c) angular observable for the b-quark jet analyzer in the electron channel and (d) angular observable for the b-quark jet analyzer in the muon channel.

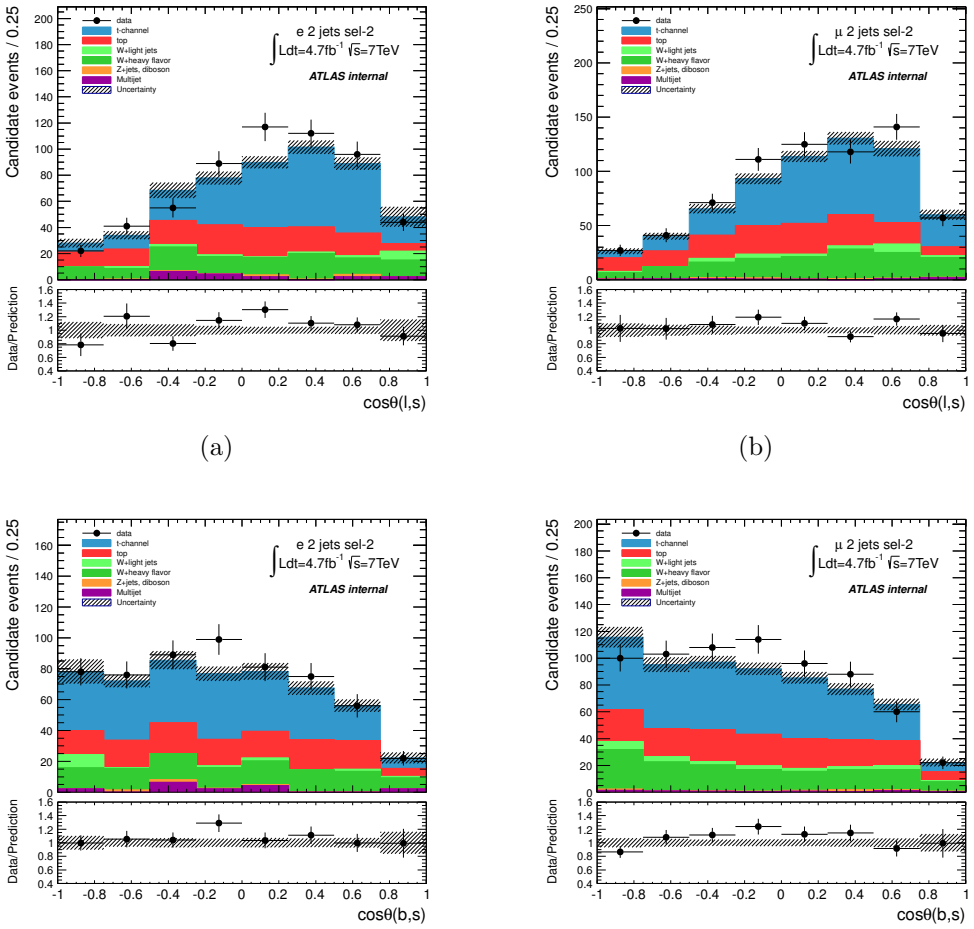

Figure 9-4: Angular distributions reconstructed in the spectator basis for the event samples selected with the SELECTION-2 cuts (a) angular observable for the lepton analyzer in the electron channel, (b) angular observable for the lepton analyzer in the muon channel, (c) angular observable for the b-quark jet analyzer in the electron channel and (d) angular observable for the b-quark jet analyzer in the muon channel.

between the charged lepton or the b-tagged jet and the chosen reference axis whatever the presence or not of a real top quark in the hard process.

The top quark polarization will be extracted from the data distributions remaining after the subtraction of all background contributions (Monte Carlo or data-driven template distributions). The resulting signal distributions are strongly modified with respect to their shape at parton level, and corrections, which will be discussed in the following sections, should be applied to recover the parton-level information from the finally reconstructed distributions.

The angular distributions obtained for the signal after subtracting from the data all the (Monte Carlo and data-driven) background contributions are shown in Figure 9-5 and 9-6 for the SELECTION-1 and SELECTION-2 events, respectively. They are compared to the expected signal distributions from only t-channel. On the overall, the expectations agree well with the data, except some spikes that are seen especially in the SELECTION-1 distributions. The SELECTION-1 angular distributions for the b-quark analyzer are strongly distorted for $\cos\theta$ close to -1 due to the cut introduced on $\Delta\eta(bjet, W)$, while these distributions in the SELECTION-2 sample are better reconstructed when compared to the angular distributions at the parton level.

9.3 Corrections on reconstructed distributions

Produced from the hard process, the leptons and quarks will evolve by themselves (bremsstrahlung for electrons, parton shower and hadronization for quarks) and interact with the detector materials and will end up with much complicated particles and objects which are then reconstructed. Neutrinos are not detectable and their three-momentum is derived from other reconstructed physics objects as described in Section 5.4. In the end, any physics objects are observed and reconstructed with a deflected three-momentum which will change the value of the polarization angle resulting in a distorted final distribution due to the "migration" of the events from one angular bin to another one. Additionally, the intrinsic detector resolution on the measured momentum and energy also changes the values of the reconstructed angular observables, contributing to the "migration" effects.

Apart from the "migration" effects, one also considers the "efficiency" effects coming from the selection cuts one applies to the objects and events to discriminate the signal contribution from background contaminations. These cuts may have different impacts in different regions of the angular distributions. For example, due to the isolation requirements and the overlap removal procedures described in Section 8.1, events with small relative angles between the lepton and the spectator jet are strongly suppressed leading to a significant loss of efficiency (and therefore rate) in the high-value region ($\cos\theta$ close to 1) of the angular distribution of the lepton in the spectator basis. Due to these sizeable variations of the selection efficiency as a function of the angular observable, the reconstructed angular distribution is significantly modified with respect to the parton-level one.

From above, one factorizes the distortions after the reconstruction into "migration" and "efficiency" effects. Two solutions can be explored to deal properly with

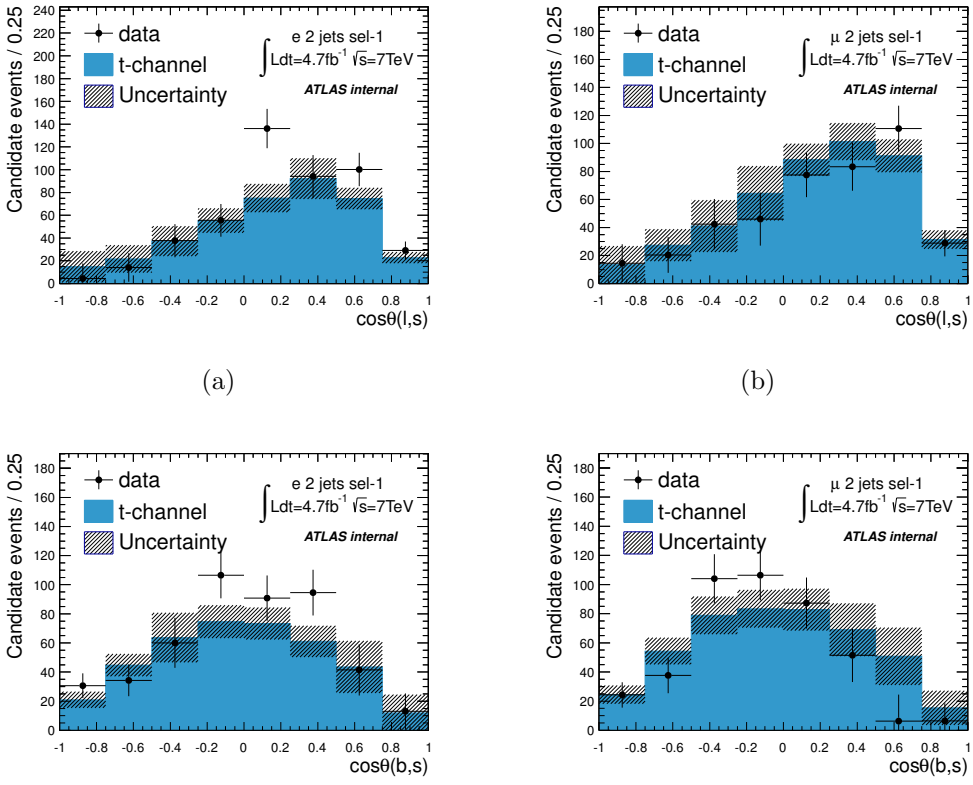

(a) (b)

(c) (d)

Figure 9-5: Angular distributions reconstructed in the spectator basis for the events selected with the SELECTION-1 cuts obtained by subtracting all background contributions from the data. They are compared to the angular distributions expected for the t-channel signal process: (a) angular observable for the lepton analyzer in the electron channel, (b) angular observable for the lepton analyzer in the muon channel, (c) angular observable for the b-quark jet analyzer in the electron channel and (d) angular observable for the b-quark jet analyzer in the muon channel. The shadowed bands represent the total statistical errors from the expectations (signal and backgrounds) added to the 50% uncertainty on the QCD multijet contribution.

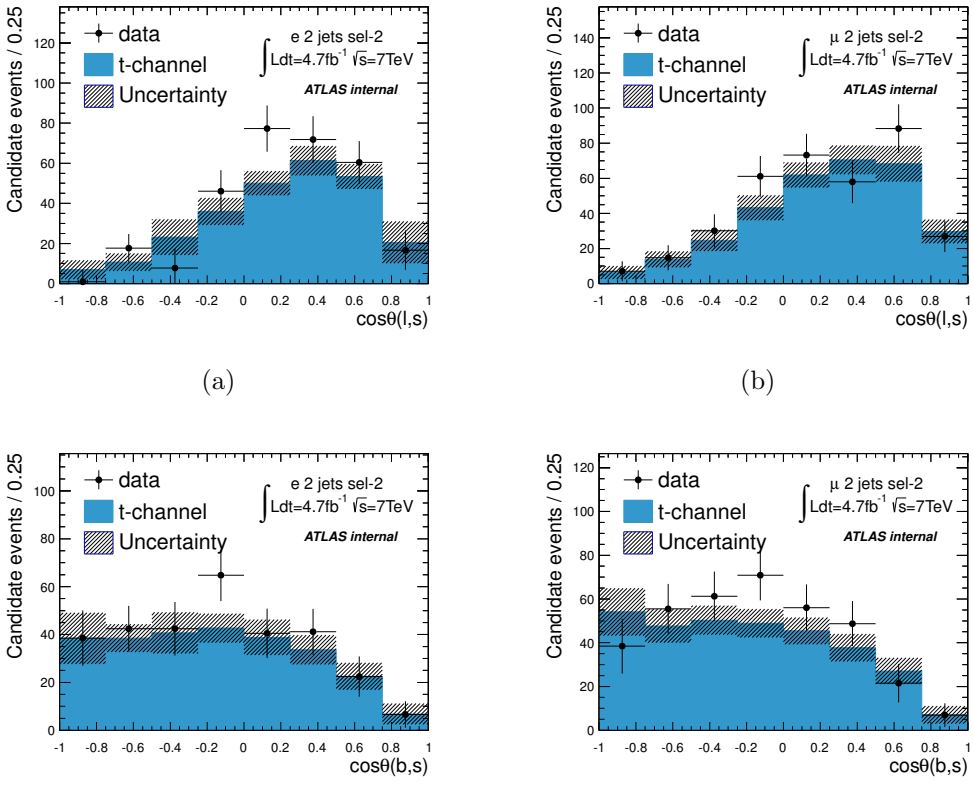

Figure 9-6: Angular distributions reconstructed in the spectator basis for the events selected with the SELECTION-2 cuts obtained by subtracting all background contributions from the data, They are compared to the angular distributions expected for the t-channel signal process: (a) angular observable for the lepton analyzer in the electron channel, (b) angular observable for the lepton analyzer in the muon channel, (c) angular observable for the b-quark jet analyzer in the electron channel and (d) angular observable for the b-quark jet analyzer in the muon channel. The shadowed bands represent the total statistical errors from the expectations (signal and backgrounds) added to the 50% uncertainty on the QCD multijet contribution.

these distortion effects: the associated corrections could be applied either to the reconstructed angular distributions or to the parton-level (theoretical) angular distributions.

To take into account the resolution and efficiency effects, one could indeed deconvolve them from the reconstructed distribution after having subtracted the background contributions from the data in order to recover the parton-level distribution from which the polarization is extracted. Unfolding methods are proposed to realize this deconvolving procedure.

Another technique to take into account the migration and efficiency effects is to convolve them into the parton-level distribution expected for the signal events in order to build the reconstructed distribution. The reconstructed distribution is then added to the background template distributions before being fitted to the data in order to extract the polarization. A folding method is used to realize this convolving procedure.

Both unfolding and folding methods use the same migration matrix and the same efficiency corrections to deal with the two types of distortion effects separately. What is different in unfolding methods is that one needs to invert the resolution matrix. Before going into the details of the two methods, the constructions of the migration matrix and of the efficiency corrections are discussed in the next sections.

Additionally, to check if the methods are able to give an unbiased and linear response for the measurement of the top quark polarization, validation studies are carried out using dedicated simulation samples. These specific simulations are based on the t-channel AcerMC samples which are reweighted event-by-event in order to artificially shift the original degree of polarization (actually $\alpha \cdot P$) by factors of $\pm 5\%$ and $\pm 10\%$. These event weights are calculated from the ratio between the angular distributions (given by Equation 9.1) associated to the nominal (Standard Model) and modified polarization values. They are calculated from the parton-level (true) angular distributions and applied to the reconstructed events.

The goal of these linearity tests is to show that the considered analysis procedures are able to provide an accurate measurement of the top quark polarization observable, whatever its real level of deviation around the value predicted by the Standard Model.

9.4 Migration and efficiency corrections

9.4.1 Migration matrix

The migration matrix is built from simulated events after the final selections, using the correspondence between the true angular information ($\cos\theta_{parton}$) and the reconstructed one ($\cos\theta_{reco}$). Each matrix element represents the probability that a given event migrates from its original angular bin at parton level to another one at the reconstruction level.

In the unfolding method, the reconstructed angular distribution is thus multiplied by the inverted migration matrix in order to derive the parton-level distribution. Conversely, in the folding method, the theoretical angular distribution is multiplied

by the non-inverted migration matrix in order to get the reconstructed distribution.

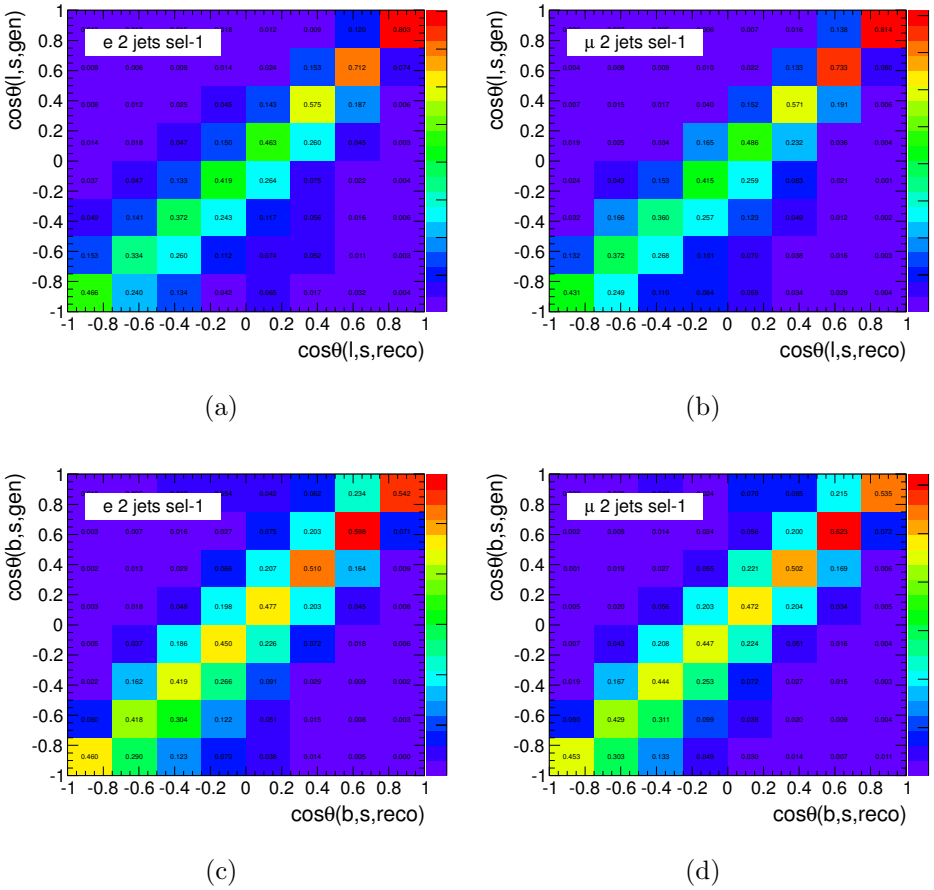

(a) (b)

(c) (d)

Figure 9-7: Migration matrices $R(\cos\theta_{reco}, \cos\theta_{parton})$ calculated with the AcerMC generator in the spectator basis for events selected with the Selection-1 cuts (a) charged lepton in the electron channel, (b) charged lepton in the muon channel, (c) b-quark jet in the electron channel and (d) b-quark jet in the muon channel. The migration matrices are defined using eight angular bins.

Figure 9-7 and Figure 9-8 show the migration matrices $R(\cos\theta_{reco}, \cos\theta_{parton})$ constructed with the events simulated with AcerMC and selected by the Selection-1 and Selection-2 criteria for both electron and muon channels. The resolution matrices are presented in the form of probability matrices by normalizing to unity the integral of the distribution of the reconstructed angle associated to each bin of the parton-level distribution (i.e. the matrices are normalized line-by-line). The two upper plots in each figure show the migration matrices for the lepton analyzer, while the bottom ones correspond to the b-quark jet analyzer. From the diagonal elements, which give the probabilities that the events stay in the same bin from parton to reconstruction levels instead of migrating, one can see that the migration effect is less severe when using the lepton spin analyzer than when using the b-quark jet analyzer. This is due to the better reconstruction of both the direction and energy of the leptons.

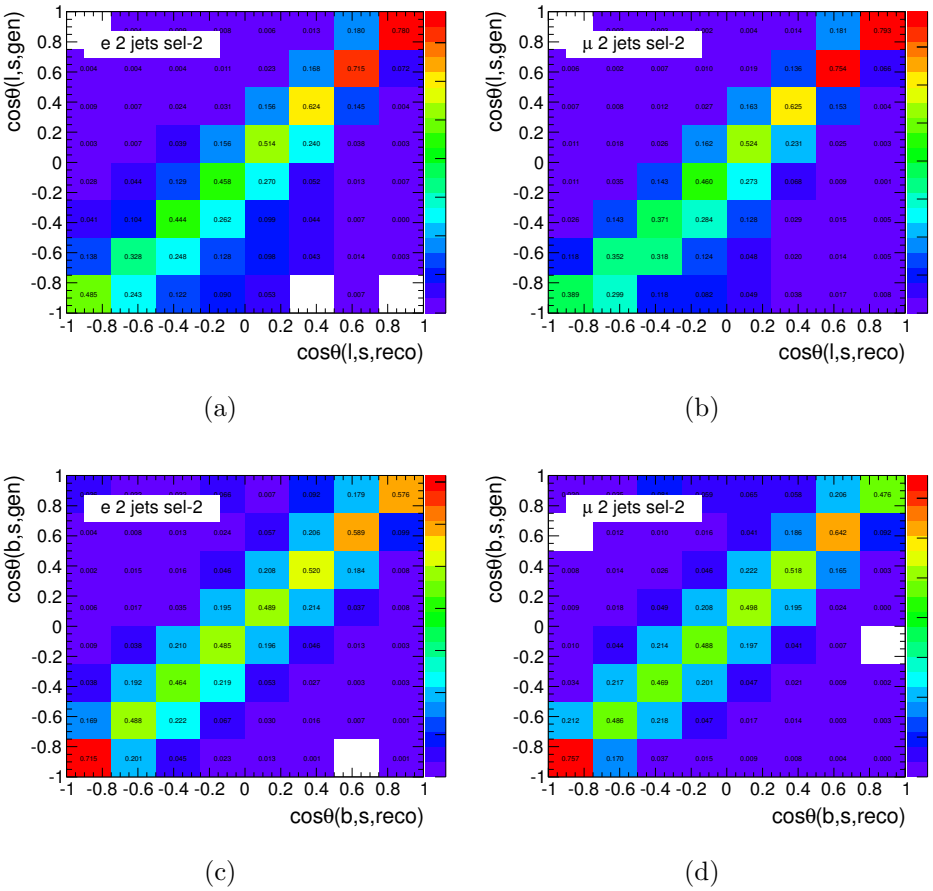

Figure 9-8: Migration matrices $R(\cos\theta_{reco}, \cos\theta_{parton})$ calculated with the AcerMC generator in the spectator basis for events selected with the Selection-2 cuts (a) charged lepton in the electron channel, (b) charged lepton in the muon channel, (c) b-quark jet in the electron channel and (d) b-quark jet in the muon channel. The migration matrices are defined using eight angular bins.

9.4.2 Efficiencies

The efficiency corrections are derived from the simulated events by calculating, for each bin in the true angular distribution, the ratio between the number of reconstructed and selected events and the number of generated events: $\epsilon = N_{reco}/N_{parton}$. Figures 9-9 and 9-10 present the efficiency curves calculated with AcerMC for the lepton and the b-quark jet spin analyzers, respectively. The efficiencies are given for both Selection-1 and Selection-2 events and for both electron and muon channels. As expected, the efficiencies from the harder set of cuts (Selection-2) are lower than the ones obtained from the softer cuts (Selection-1). In all cases, the efficiencies close to $\cos\theta = 1$ ($\theta \sim 0$) are degraded mainly due to the object overlap removals and isolation requirements as mentioned previously.

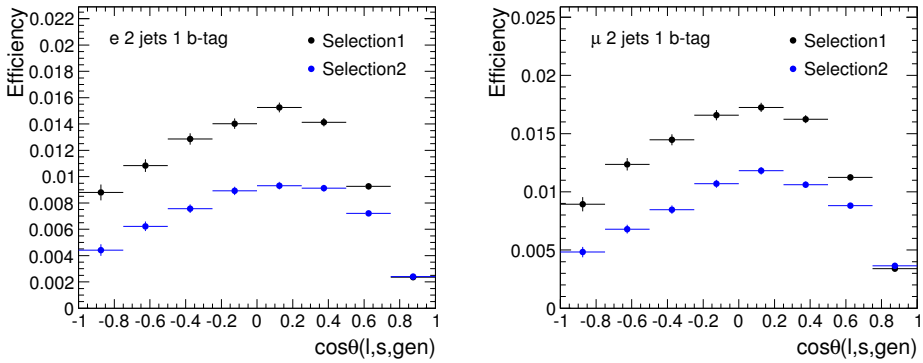

(a) (b)

Figure 9-9: Efficiency curves, $\epsilon(\cos\theta_{parton})$=$N_{reco}/N_{parton}$, calculated with the AcerMC generator as a function of the parton-level angle of the charged lepton in the spectator basis for the (a) electron and (b) muon channels. The events are selected with the Selection-1 (black points) and Selection-2 (blue points) cuts. The efficiency curves are defined using eight angular bins.

9.5 Unfolding methods

The unfolding method deconvolves the reconstructed angular distribution from the distortion effects in order to recover the parton-level distribution. The reconstructed angular distribution for the signal is obtained by subtracting all the background contributions from the data. The inverted migration matrix is then applied to the signal distribution which is finally corrected bin-by-bin using the selection efficiencies.

One problem in unfolding methods is the matrix inversion. If the migration matrix has too large off-diagonal elements, the inversion could lead to very large fluctuations and even non-physical values. Too large off-diagonal elements may be caused by too bad detector performances or by too many bins being used in the migration matrix. Figure 9-11 illustrates a typical case of large fluctuations in the unfolded distribution

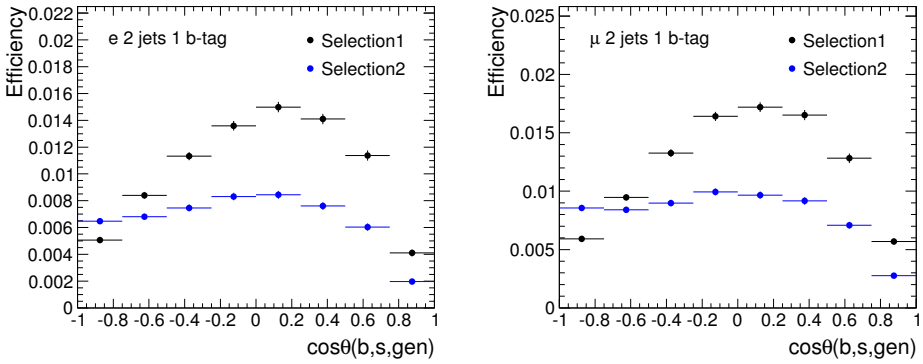

(a) (b)

Figure 9-10: Efficiency curves, $\epsilon(\cos\theta_{parton})=N_{reco}/N_{parton}$, calculated with the AcerMC generator as a function of the parton-level angle of the b-quark jet in the spectator basis for the (a) electron and (b) muon channels. The events are selected with the Selection-1 (black points) and Selection-2 (blue points) cuts. The efficiency curves are defined using eight angular bins.

resulting from the matrix inversion: plot (a) gives the real distribution, plot (b) the observed (solid line) and expected (dashed line) reconstructed distributions and plot (c) the unfolded distribution with a migration matrix defined with too many bins.

To avoid large fluctuations caused by the inversion of the migration matrix, one can either use a reduced number of bins or special regularization techniques. One solution is an ordinary unfolding by inverting the migration matrix normally from angular distributions reconstructed with only two bins and the other one is an iterative unfolding utilizing the Bayesian regularization procedure which can be used whatever the number of bins. With the ordinary unfolding method, the top quark polarization is therefore only derived from the forward-backward asymmetry (corresponding to a 2-bin scheme), while it is derived either from the forward-backward asymmetry or from the fit to the angular distribution shape when using the iterative unfolding method.

9.5.1 Ordinary unfolding

For ordinary unfolding, angular distributions reconstructed with only two bins are used. This leads to a direct measurement from the forward-backward asymmetry A_{FB} of the top quark polarization product $\alpha \cdot P$, according to Equation 9.2. With this two-bin scheme, the migration matrix does not have large off-diagonal elements (all below 10%) and the simple matrix inversion does not cause any big fluctuations in the final distribution.

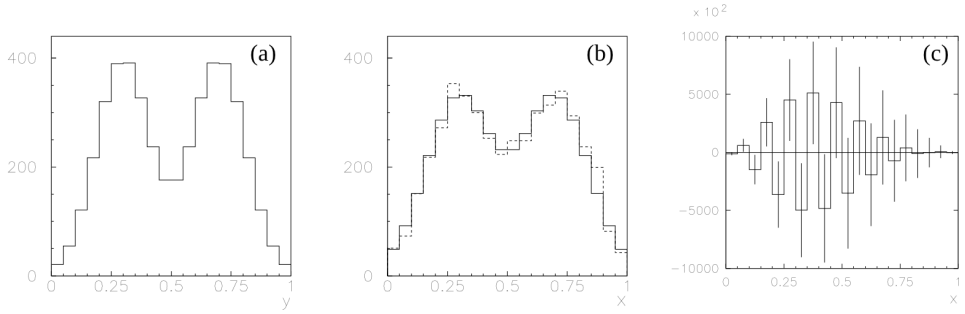

Figure 9-11: Typical case of unfolding result with a bad migration matrix inversion due to too many bins (a) true distribution, (b) observed (solid line) and expected (dashed line) reconstructed distributions and (c) unfolded distribution through inversion of the migration matrix.

Linearity check

The ordinary unfolding procedure, as well as the two other analysis methods which will described in the next sections, is validated using the nominal AcerMC t-channel samples and the derived re-weighted samples corresponding to polarization values shifted by factors $\pm 5\%$ and $\pm 10\%$, described in the end of Section 9.3. The validation test consists in comparing for each type of simulated events the polarization value extracted from the unfolded reconstructed distribution to the (true) value directly extracted from the parton-level distribution. Only signal events without any background contributions are considered and the migration matrices and efficiencies calculated from the baseline AcerMC samples, as described previously, are used to unfold the reconstructed distributions whatever the configuration of the tested sample. Moreover, the migration matrices and efficiencies are determined with the same number of bins as used to define the reconstructed angular distributions. All validation tests are performed with combination of the electron and muon channels.

The polarization observables, $\alpha \cdot P$, extracted from the unfolded reconstructed forward-backward asymmetry is shown in Figure 9-12 as a function of the values extracted from the parton-level asymmetry for the two spin analyzers (charged lepton and b-quark jet) and for the two sets of selections (Selection-1 and Selection-2 events). These response curves are fitted with a linear function $(\alpha \cdot P)_{response} = k(\alpha \cdot P)_{input} + c$, where k represents the linearity parameter while c represents the bias. An accurate response of the method is found when k is close to 1 (linear response) and c close to 0 (no bias). As we can see in Figure 9-12, where the fitted lines (solid lines) are compared to the benchmark response ($k = 1$ and $c = 0$ - red dashed lines), a very good linearity without any important bias is obtained for both selection sets and both spin analyzers. The numerical results of the linearity check are summarized in Table 9.3; the linearity parameters k are all close to 1 and the bias values c all close to 0 within 7% at the maximum. In conclusion, there is no significant non-linearity and bias in the response of the ordinary unfolding method applied to angular distributions reconstucted with two bins.

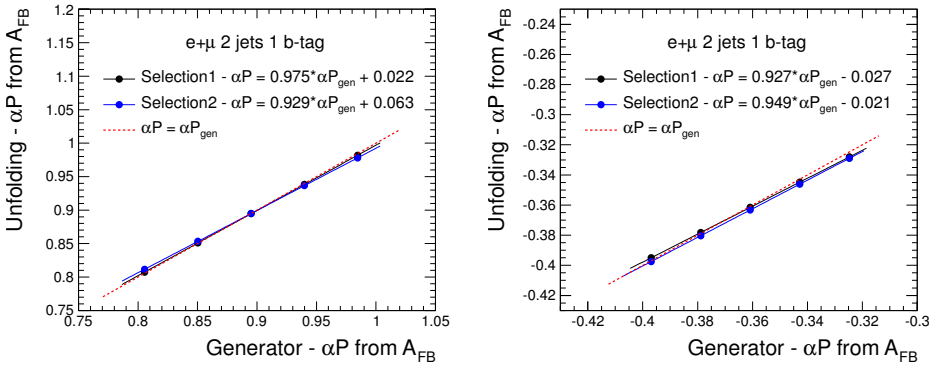

(a) (b)

Figure 9-12: Values of the polarization observable, $\alpha \cdot P$, extracted with the ordinary unfolding method as a function of the parton-level values for (a) the lepton and (b) the b-quark jet spin analyzers. The original and re-weighted AcerMC samples are used and selected with the Selection-1 (black points) and Selection-2 (blue points) sets of cuts. From the left to the right, the five points are derived from the samples with the value of $\alpha \cdot P$ shifted by -10%, -5%, 0%, $+5\%$ and $+10\%$. The unfolded and parton-level polarization values are both extracted from the forward-backward asymmetry; the reconstructed angular distributions are defined with only 2 bins and the parton-level distributions with 100 bins. The solid lines represent the linearity fits with the function $(\alpha \cdot P)_{response} = k(\alpha \cdot P)_{input} + c$ and the red dashed lines show the ideal case $(\alpha \cdot P)_{response}$=$(\alpha \cdot P)_{input}$.

Spin analyzer	Selection-1		Selection-2	
	k	c	k	c
lepton	0.975	0.022	0.929	0.063
b-quark jet	0.927	-0.027	0.949	-0.021

Table 9.3: Results of the linearity fit of the response curves shown in Figure 9-12 with the function $(\alpha \cdot P)_{response} = k(\alpha \cdot P)_{input} + c$. The response curves are extracted from the ordinary unfolding of the angular distributions reconstructed with 2 bins for the lepton and b-quark jet spin analyzers and for the Selection-1 and Selection-2 events. The polarization values, $\alpha \cdot P$, are extracted from the unfolded forward-asymmetry asymmetries.

Pull distributions

In order to check that the statistical errors are properly propagated in the ordinary unfolding procedure, pull distributions are built from simulated events. The pull for the measurable X is defined as:

$$pull = \frac{X^{measured} - X^{true}}{\sigma(X^{measured})} \tag{9.3}$$

where $X^{measured}$ and X^{true} are the measured and true values of X, respectively, and $\sigma(X^{measured})$ the error of the measured X. X^{true} is known from the simulations, and $X^{measured}$ is derived from the pseudo-experiments considering only statistical fluctuations. The statistical error is properly propagated if the pull follows a standard normal distribution ($\mu = 0$ and $\sigma = 1$). The pull distributions for the unfolded forward-backward asymmetries are shown in Figure 9-13 for the lepton and b-quark jet analyzers, respectively. For both analyzers, the pull distributions agree well with standard normal distributions, leading to the conclusion that the statistical error is properly propagated in the ordinary unfolding method.

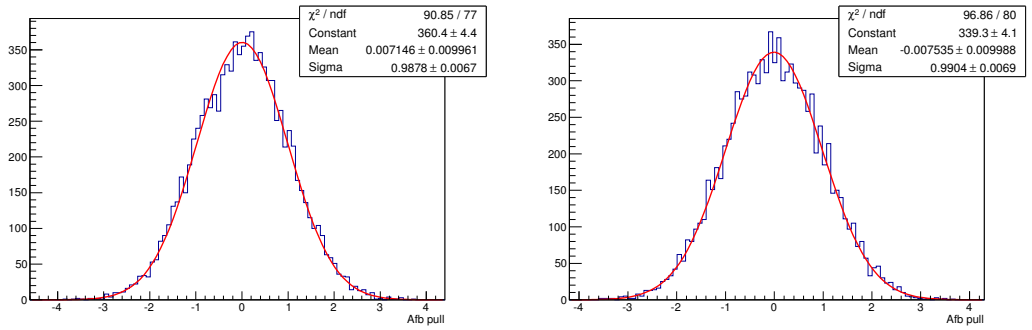

(a) (b)

Figure 9-13: Pull distributions of the forward-backward asymmetries unfolded with a simple matrix inversion for (a) the lepton and (b) the b-quark jet spin analyzers.

9.5.2 Iterative unfolding

The iterative unfolding method with a Bayesian regularization is introduced to solve the problem of potential large fluctuations caused by the inversion of the migration matrix discussed in the beginning of Section 9.5. In this method, the matrix inversion is based on the iterative application of the Bayes theorem and the regularization parameter is the number of iterations. The unfolding iteration starts from the simulated distribution based on the parton-level angular information taken as prior. The posterior probability density function is derived from this prior and then used as prior in the next iteration. To realize this Bayesian iterative procedure, the RooUnfold tool is used [149].

Once the initial angular distribution iteratively unfolded, one can derive the polarization product $\alpha \cdot P$ from the forward-backward asymmetry or from a direct χ^2 fit to the angular distribution shape if defined with more than two bins. In the validation studies presented in the following sections, the two polarization extraction procedures are investigated with angular distributions defined using 2, 8 or 12 bins.

Convergence check

With the Bayesian unfolding, the only parameter one has to set is the number of iterations. To find the optimal value for this parameter, a series of convergence tests is performed using the baseline and re-weighted AcerMC samples. This optimal number of iterations is derived with respect to a well-defined convergence criterion which should be satisfied whatever the input value of the polarization: the unfolding procedure is considered to be converged when the change between two successive steps become lower than an absolute precision of 0.001.

The values of the polarization product $\alpha \cdot P$ extracted as a function of the number of iterations from the baseline AcerMC events selected with the Selection-1 and Selection-2 cuts are shown in Figure 9-14 for both the lepton and b-quark jet analyzers. The values obtained as a function of the number of iterations for the re-weighted AcerMC samples corresponding to the $\pm 10\%$ shifted polarizations at parton-level are presented in Figures 9-15 and 9-16 for the lepton and b-quark jet analyzers, respectively. These figures present the results extracted from the forward-backward asymmetry (left-hand side plots) and from the fit to the angular distribution shape (right-hand side plots) and for reconstructed angular distributions defined with 2 (open circles), 8 (closed circles) and 12 (open squares) bins (the distribution from which the parton-level polarization is derived is defined with 100 bins). The values associated to the Selection-1 events are given in black whereas the Selection-2 results are given in blue. In all plots, the red line represents the parton-level polarization and the shaded area around this line the convergence criterion of one per mill precision.

First of all, one can see that, whatever the spin analyzer or the selection level, the convergence is fast for the nominal samples while it is far slower for the $\pm 10\%$ re-weighted samples. The fast convergence of the baseline samples is due to the fact that the migration and efficiency corrections are calculated using the same simulation configuration. A second common feature is that the responses derived from the forward-backward asymmetry (left-hand side plots), although converging in all cases, are more dispersed with respect to the expected value than those given by the fit (right-hand side plots). The values provided by the forward-backward asymmetry are on the overall more accurate when using 8 bins (closed circles) than 2 or 12 bins. A final regularization parameter of 20 is chosen for the Bayesian unfolding procedure since it gives a general recovering within one per mill of the parton-level polarization whatever the spin analyzer, the selection level and the extraction procedure.

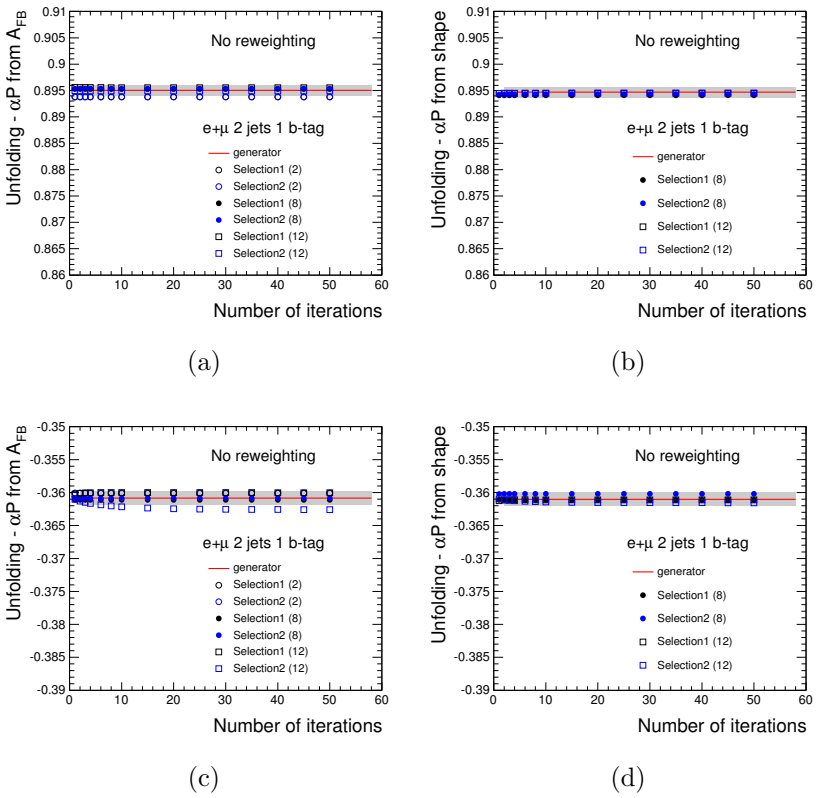

Figure 9-14: Values of the polarization observable, $\alpha \cdot P$, extracted with the Bayesian unfolding method and non re-scaled input polarizations as a function of the number of iterations from (a) the forward-backward asymmetry of the lepton analyzer, (b) the fit to the angular distribution of the lepton analyzer, (c) the forward-backward asymmetry of the b-quark jet analyzer and (d) the fit to the angular distribution of the b-quark jet analyzer. The baseline AcerMC sample is used and selected with the Selection-1 (black points) and Selection-2 (blue points) sets of cuts. The reconstructed angular distributions are defined with 2 (open circles), 8 (closed circles) and 12 (open squares) bins. The red lines represent the parton-level $\alpha \cdot P$ values derived using the same procedure than the unfolded ones and with distributions defined with 100 bins. The shaded areas correspond to the convergence criterion of 0.001 absolute precision.

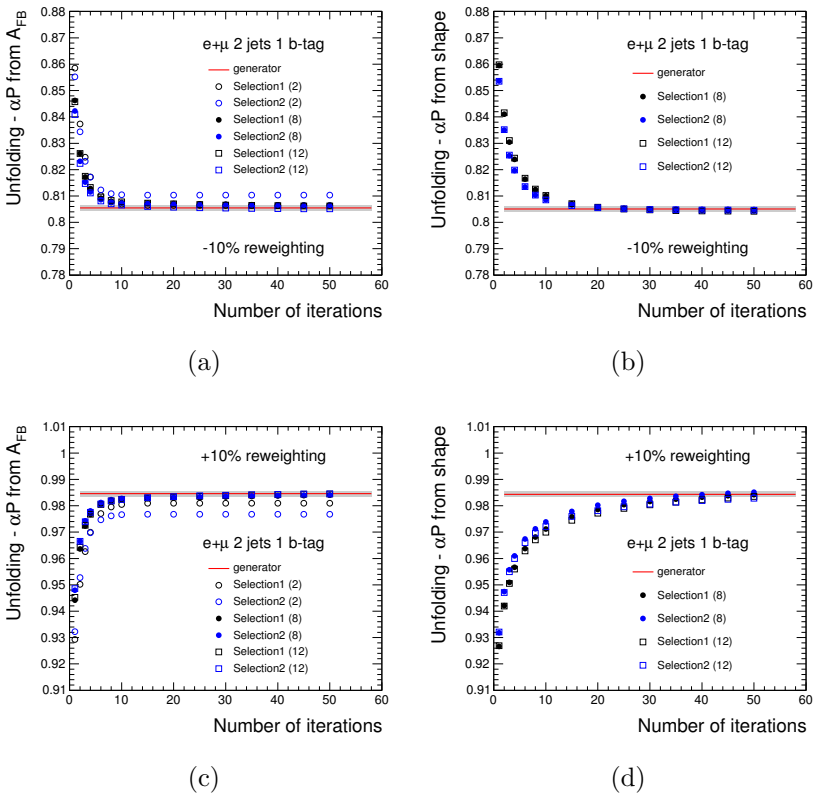

Figure 9-15: Values of the polarization observable, $\alpha \cdot P$, extracted with the Bayesian unfolding method and re-scaled input polarizations and for the lepton spin analyzer as a function of the number of iterations from (a) the forward-backward asymmetry with -10% re-scaling, (b) the distribution fit with -10% re-scaling, (c) the forward-backward asymmetry with $+10\%$ re-scaling and (d) the distribution fit with $+10\%$ re-scaling. The re-weighted AcerMC samples are used and selected with the Selection-1 (black points) and Selection-2 (blue points) sets of cuts. The reconstructed angular distributions are defined with 2 (open circles), 8 (closed circles) and 12 (open squares) bins. The red lines represent the parton-level $\alpha \cdot P$ values derived using the same procedure than the unfolded ones and with distributions defined with 100 bins. The shaded areas correspond to the convergence criterion of 0.001 absolute precision.

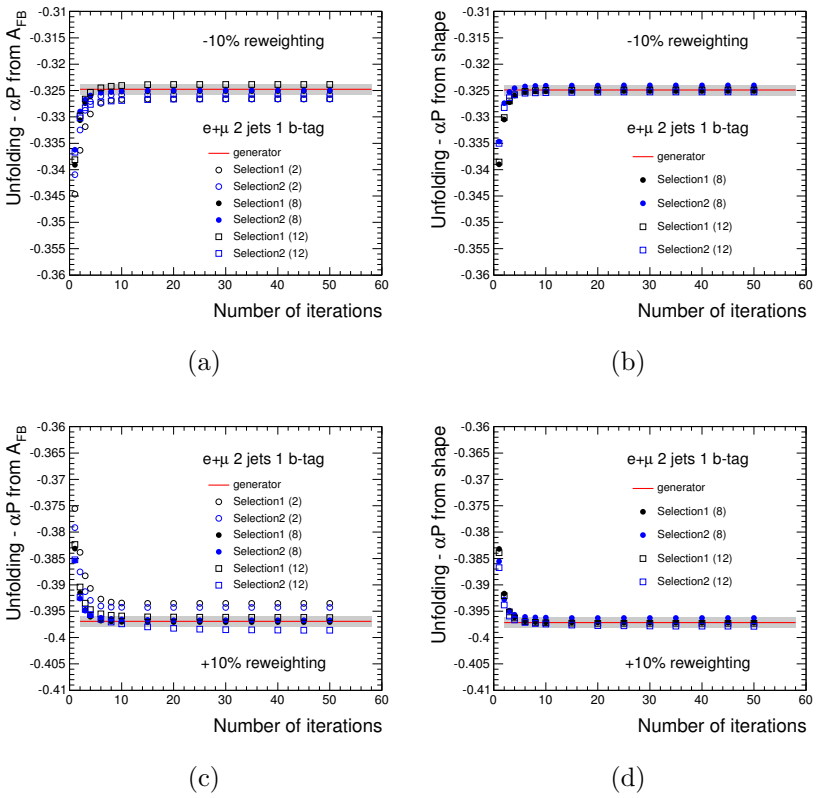

Figure 9-16: Values of the polarization observable, $\alpha \cdot P$, extracted with the Bayesian unfolding method and re-scaled input polarizations for the b-quark jet spin analyzer as a function of the number of iterations from (a) the forward-backward asymmetry with -10% re-scaling, (b) the distribution fit with -10% re-scaling, (c) the forward-backward asymmetry with $+10\%$ re-scaling and, (d) the distribution fit with $+10\%$ re-scaling. The re-weighted AcerMC samples are used and selected with the Selection-1 (black points) and Selection-2 (blue points) sets of cuts. The reconstructed angular distributions are defined with 2 (open circles), 8 (closed circles) and 12 (open squares) bins. The red lines represent the parton-level $\alpha \cdot P$ values derived using the same procedure than the unfolded ones and with distributions defined with 100 bins. The shaded areas correspond to the convergence criterion of 0.001 absolute precision.

Linearity check

Linearity checks are also performed for the iterative unfolding method using the same procedure as described in Section 9.5.1 for the validation of the ordinary unfolding method. These linearity tests are presented for the two extraction procedures (forward-backward asymmetry and direct χ^2 fit) from angular distributions reconstructed with 2 and 8 bins unfolded using 20 iterations. As discussed in the previous section, the best unfolding performances are obtained using 8 bins. The linearity results obtained with the 2-bin scheme are also reported here in order to have a comparison with the ordinary unfolding response.

The polarization observables, $\alpha \cdot P$, extracted from the iteratively unfolded reconstructed distributions are shown in Figure 9-17 as a function of the values extracted from the parton-level distributions for the two spin analyzers (lepton and b-quark jet) and for the two levels of selections (SELECTION-1 points in black and SELECTION-2 points in blue). Figure 9-17 presents the results extracted from the forward-backward asymmetries (left-hand side plots) and from the fit to the distributions (right-hand side plots) and for reconstructed angular distributions defined with 2 (open circles) and 8 (closed circles) bins. The response curves are fitted with a linear function $(\alpha \cdot P)_{response} = k(\alpha \cdot P)_{input} + c$ (solid lines), to be compared with the results expected for an accurate response (red dashed lines). The unfolding responses show a good linearity for both extraction procedures and both selection sets.

The results of the linear fit are summarized in Tables 9.4 and 9.5 for the tests with 2 and 8 bins, respectively. The values of the parameters k and c obtained using the 2-bin scheme are quite the same than those given by the ordinary unfolding method and reported in Table 9.3; this confirms the reliability of the basic matrix inversion algorithm in case of small off-diagonal matrix elements. When comparing the linearity results obtained with 2 and 8 bins from the forward-backward asymmetry (Tables 9.4 and 9.5), one can see that the 8-bin configuration gives a slightly better linearity with slightly smaller biases than the 2-bin configuration. In addition, when using 8 bins (Table 9.5), the responses derived with the Bayesian unfolding from the forward-backward asymmetry have a slightly better linearity and smaller biases (within 1-2%) than the ones derived from the direct fit.

In conclusion, from the simulation-based performance studies presented above, when using unfolding, the most accurate measurement of the polarization observable will be achieved from the forward-backward asymmetry of the angular distributions reconstructed with 8 bins and unfolded by using the iterative matrix inversion with Bayesian regularization. This conclusion is valid whatever the selected samples and whatever the spin analyzer.

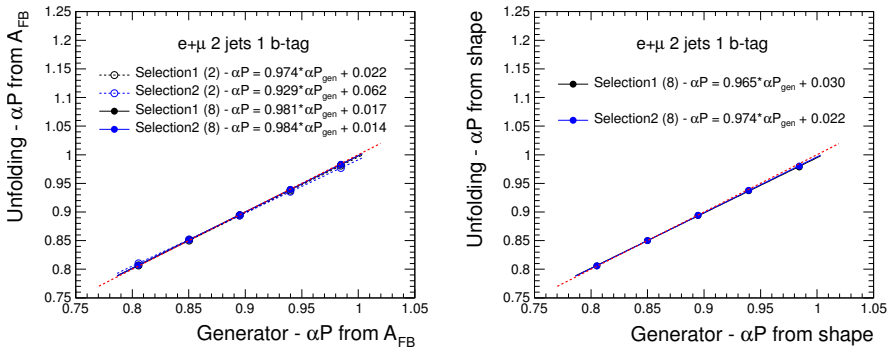

(a) (b)

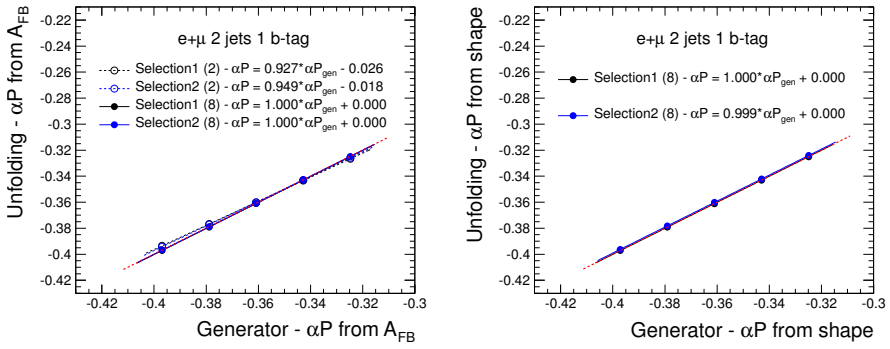

(c) (d)

Figure 9-17: Values of the polarization observable, $\alpha \cdot P$, extracted with the Bayesian unfolding method as a function of the parton-level values from (a) the forward-backward asymmetry of the lepton analyzer, (b) the fit to the angular distribution of the lepton analyzer, (c) the forward-backward asymmetry of the b-quark jet analyzer and (d) the fit to the angular distribution of the b-quark jet analyzer. The original and re-weighted AcerMC samples are used and selected with the Selection-1 (black points) and Selection-2 (blue points) sets of cuts. From the left to the right, the five points are derived from the samples with the value of $\alpha \cdot P$ shifted by -10%, -5%, 0%, $+5\%$ and $+10\%$. The reconstructed angular distributions are defined with 2 (open circles) and 8 (closed circles) bins and the parton-level distributions with 100 bins. The solid lines represent the linearity fits with the function $(\alpha \cdot P)_{response} = k(\alpha \cdot P)_{input} + c$ and the red dashed lines show the ideal case $(\alpha \cdot P)_{response} = (\alpha \cdot P)_{input}$.

Spin analyzer	SELECTION-1		SELECTION-2	
	k	c	k	c
lepton	0.974	0.022	0.929	0.062
b-quark jet	0.927	-0.026	0.949	-0.018

Table 9.4: Results of the linearity fit of the response curves shown in Figure 9-17 with the function $(\alpha \cdot P)_{response} = k(\alpha \cdot P)_{input} + c$. The response curves are extracted from the Bayesian iterative unfolding of the angular distributions reconstructed with 2 bins for the lepton and b-quark jet spin analyzers and for the SELECTION-1 and SELECTION-2 events. The polarization values, $\alpha \cdot P$, are extracted from the unfolded forward-asymmetry asymmetries.

Spin analyzer - Method	SELECTION-1		SELECTION-2	
	k	c	k	c
lepton - A_{FB}	0.981	0.017	0.984	0.014
lepton - shape	0.965	0.030	0.974	0.022
b-quark jet - A_{FB}	1.000	0.000	1.000	0.000
b-quark jet - shape	1.000	0.000	0.999	0.000

Table 9.5: Results of the linearity fit of the response curves shown in Figure 9-17, with the function $(\alpha \cdot P)_{response} = k(\alpha \cdot P)_{input} + c$. The response curves are extracted from the Bayesian iterative unfolding of the angular distributions reconstructed with 8 bins for the lepton and b-quark jet spin analyzers and for the SELECTION-1 and SELECTION-2 events. The polarization values, $\alpha \cdot P$, are extracted from both the forward-backward asymmetry and fit of the unfolded distributions.

Pull distributions

Pull distributions are constructed, as explained in Section 9.5.1, in order to validate the statistical error propagation in the iterative unfolding procedure. The pull distributions for the forward-backward asymmetries iteratively unfolded with the Bayesian regularization are shown in Figure 9-18. In all cases, the pull distributions agree well with standard normal distributions, leading to the conclusion that the statistical error is propagated properly in the iterative unfolding method.

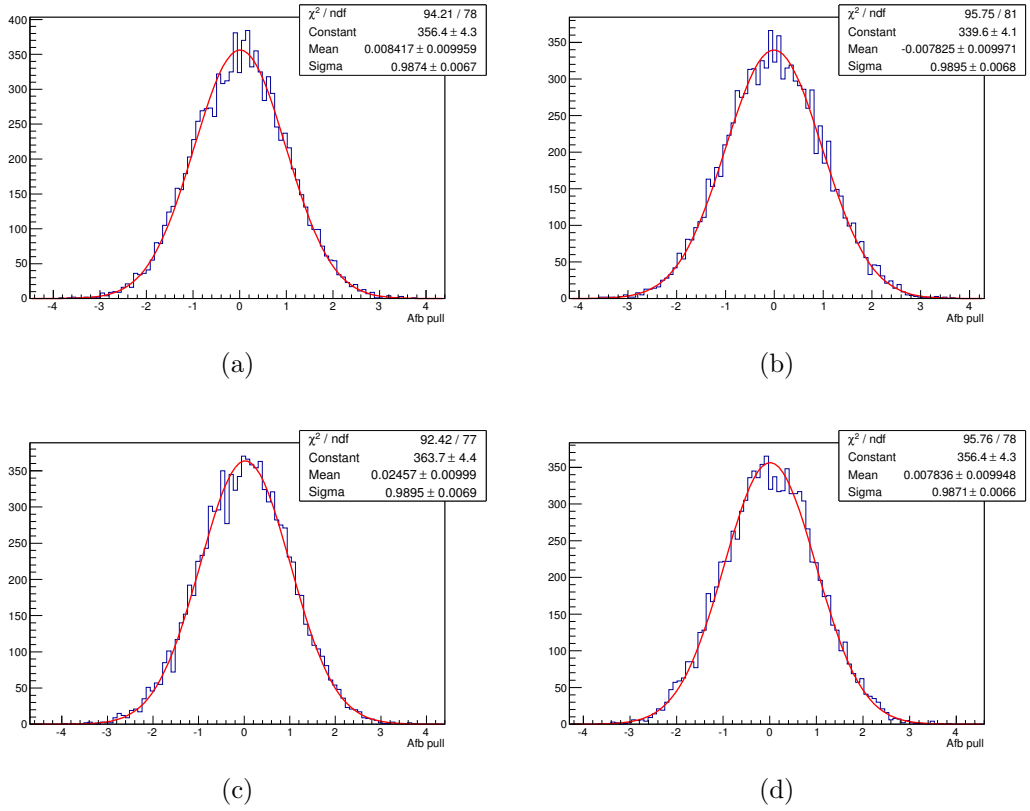

Figure 9-18: Pull distributions of the forward-backward asymmetries iteratively unfolded with the Bayesian regularization for (a) the lepton analyzer in the 2-bin scheme, (b) the b-quark jet analyzer in the 2-bin scheme, (c) the lepton analyzer in the 8-bin scheme and (d) the b-quark jet analyzer in the 8-bin scheme.

9.6 Folding method

Unlike the unfolding method that recovers the distribution from the reconstruction level back to parton level, the folding method predicts the distribution at reconstruction level by convolving the migration and efficiency effects to the theoretical distribution given by Equation 9.1. The folding method does need any inversion of the migration matrix.

As the measured angular distributions are reconstructed using a given finite number of bins, the folding method needs first to integrate the theoretical decay rate accordingly in order to get a set of coefficients $\{c_{0,k'},\ c_{1,k'}\}$, which depend only on the binning. The normalized fraction of events in the parton-level angular interval $[a_{k'}, b_{k'}]$ (bin labelled k') is expressed as follows:

$$\alpha_{k'}^{parton}(\alpha \cdot P) = \int_{a_{k'}}^{b_{k'}} \frac{1}{\Gamma}\frac{\mathrm{d}\Gamma}{\mathrm{d}\cos\theta}\mathrm{d}\cos\theta = \int_{a_{k'}}^{b_{k'}} \frac{1}{2}(1+\alpha\cdot P\cos\theta)\mathrm{d}\cos\theta. \tag{9.4}$$

One obtains after integration:

$$\alpha_{k'}^{parton}(\alpha \cdot P) = \frac{1}{2}\Delta_{1,k'} + \frac{1}{4}\Delta_{2,k'}\cdot\alpha\cdot P = c_{0,k'} + c_{1,k'}\cdot\alpha\cdot P \tag{9.5}$$

$$\text{with} \quad \Delta_{1,k'} = b_{k'} - a_{k'} \quad \textit{and} \quad \Delta_{2,k'} = b_{k'}^2 - a_{k'}^2. \tag{9.6}$$

The parameters $\{c_{0,k'}, c_{1,k'}\}$ are then convolved by the probability migration matrix R and by the efficiency corrections ϵ to get the normalized fractions α_k^{reco} of events falling in the angular bin labelled by the index k at reconstruction level:

$$\alpha_k^{reco}(\alpha \cdot P) = \sum_{k'=1}^{N_{bins}} (c_{0,k'} + c_{1,k'}\cdot\alpha\cdot P)\cdot\epsilon_{k'}\cdot R_{k,k'}. \tag{9.7}$$

Furthermore, introducing all the background contributions through simulated or data-driven templates as well as the total signal acceptance given by the Monte Carlo simulations to normalize the reconstructed event fractions α_k^{reco}, one can make an expected total angular distribution which is a function of the polarization parameter $\alpha\cdot P$. A binned maximum log-likelihood fit to the real data is then performed in order to extract $\alpha\cdot P$. Scale factors associated to the signal and background normalizations are also included in the fit as additional free parameters.

The likelihood function is given by the product of the Poisson distributions of the individual rates per selection (also called channel) and per distribution bin, the background rates being constrained by Gaussian priors:

$$L(\alpha\cdot P, \beta^s; \beta_j^b) = \prod_{i=1}^{N_{channels}} \prod_{k=1}^{N_{bins}} \frac{e^{-\mu_{ik}}\cdot\mu_{ik}^{n_{ik}}}{n_{ik}!} \cdot \prod_{j=1}^{N_{backgrounds}} G\left(\beta_j^b; 1, \Delta_j\right) \tag{9.8}$$

$$\text{with} \quad \mu_{ik} = \mu^s_{ik} + \sum_{j=1}^{N_{backgrounds}} \mu^b_{ijk} \quad , \quad \mu^s_{ik} = \beta^s \cdot \tilde{\nu}^s_i \cdot \alpha^s_{ik} \;\; and \;\; \mu^b_{ijk} = \beta^b_j \cdot \tilde{\nu}^b_{ij} \cdot \alpha^b_{ijk}. \quad (9.9)$$

This likelihood function includes for each channel (index i) and each bin (index k) a Poisson term in the observed number of events (n_{ik}) with the expectation value (μ_{ik}) defined as the sum of the expected contributions from signal (μ^s_{ik}) and all Monte Carlo or data-driven backgrounds (μ^b_{ijk} - the index j runs over the background processes). For a given process, the number of expected events in each channel and bin is given by the product of the predicted number of events ($\tilde{\nu}^s_i$ for signal or $\tilde{\nu}^b_{ij}$ for backgrounds) in the selected sample, a scale factor (β^s or β^b_j) and the fraction of events falling in this channel i and this bin k (α^s_{ik} and α^b_{ijk}), the normalization conditions for the sets of fractions for each channel and process being $\sum_{k=1}^{N_{bins}} \alpha^s_{ik} = 1$ for signal and $\sum_{k=1}^{N_{bins}} \alpha^b_{ijk} = 1$ for backgrounds.

The likelihood function is actually a function of the polarization parameter $\alpha \cdot P$, this parameter being implemented in the signal contribution by replacing the event fractions α^s_{ik} by the linear functions in $\alpha \cdot P$ expressed by Equation 9.7. The polarization observable will be thus determined from the fit to the observed distributions together with the scale factors β^s for the signal and β^b_j for the backgrounds.

Gaussian shapes centered at 1 and with a width of Δ_j are used to constrain the variation of the nuisance parameters β^b_j in order to account for prior knowledge of the background normalizations. The normalization correction factor β^s associated to the signal contribution, which is a completely free parameter of the fit, allows therefore to extract the production cross section in addition to the polarization observable which is related to the shape of the fitted angular distribution.

When performing the likelihood fit to the data, in addition to the selected signal sample, a control region is included in the likelihood function in order to have more constraints on the scale factors β^b_j associated to the backgrounds (mainly $t\bar{t}$ and $W + jets$). This control region is defined, as mentioned in Section 8.2.3, by selecting TAG events for which the invariant mass $m(l\nu b)$ is greater than 250 GeV. The likelihood function therefore includes two channels (index i in Equation 9.8), one corresponding to the signal channel and the other one to the control channel. For the signal channel, the event fractions associated to the signal process are parameterized as a function of the polarization observable as explained previously, while for the control channel, the signal event fractions are taken directly from the template distributions derived from simulations or data-driven methods.

The Gaussian constraints Δ_j used in the likelihood fit for the background normalizations are set to the theoretical cross section uncertainties (their values are discussed in Section 9.7.1). For W production in association with light jets, no Gaussian constraint is set, since the fit is not sensitive to this contribution at all. The contribution of the multijet background being already determined from data, no variations on the corresponding scale factor are allowed in the fit. The values for the constraints used in the fit are summarized in Table 9.6. For processes that are combined, the constraint

is evaluated by combining the theoretical cross section uncertainties in proportion to the contribution of each individual process in the selected event samples: a weighted uncertainty of 10% is thus obtained for the combination of the top quark production backgrounds ($t\bar{t}$, Wt and s-channel) and 8% is calculated for the combination of the Z+jets and diboson processes.

Background process	Uncertainty
$t\bar{t}$, Wt, s-channel	0.10
Z+jets, diboson	0.08
W+heavy flavor	0.50
W+light jets	0.00
Multijet	0.00

Table 9.6: Relative uncertainties on the background cross sections applied as Gaussian constraints (Δ) in the likelihood fit. For the combined ($t\bar{t}$, Wt, s-channel) and (Z+jets, diboson) processes, the overall constraints are evaluated by combining the individual theoretical cross section uncertainties in proportion to the contribution of each process in the selected event samples.

Linearity check

To validate the folding method, linearity checks are done based on the same procedure used to test the unfolding methods. These linearity checks are performed from the nominal and re-weighted AcerMC t-channel samples. No background contributions and hence no control channel are included in the likelihood fit and only the polarization observable is thus extracted from the fit (by construction, the signal scale factor is always equal to 1 since the folded theoretical distribution is normalized to the fitted angular distribution).

The polarization observables, $\alpha \cdot P$, extracted from the fit to the folded theoretical distributions are shown in Figure 9-19 as a function of the values directly extracted from the parton-level distributions for the two spin analyzers (lepton and b-quark jet) and for the two levels of selections (Selection-1 points in black and Selection-2 points in blue). The results are presented for distributions folded with 8 (open circles) and 12 (closed circles) bins. The response curves are fitted with a linear function $(\alpha \cdot P)_{response} = k(\alpha \cdot P)_{input} + c$ (solid lines) for comparison with the expected response (red dashed lines). For all studied configurations (spin analyzer, selection, binning), the folding response exhibits a very good response and no particular configuration has to be preferred contrary to the unfolding case.

The results of the linear fit are summarized in Table 9.7 for the 8-bin scheme. The corresponding linearity parameters are all within 0.5% with respect to the benchmark response (k=1 and c=0).

In conclusion, when using 8 bins to define the angular distributions, the folding method provides a more accurate response than the unfolding methods discussed

before: a more linear and a less biased response is indeed found from the various studies performed with simulated t-channel event samples.

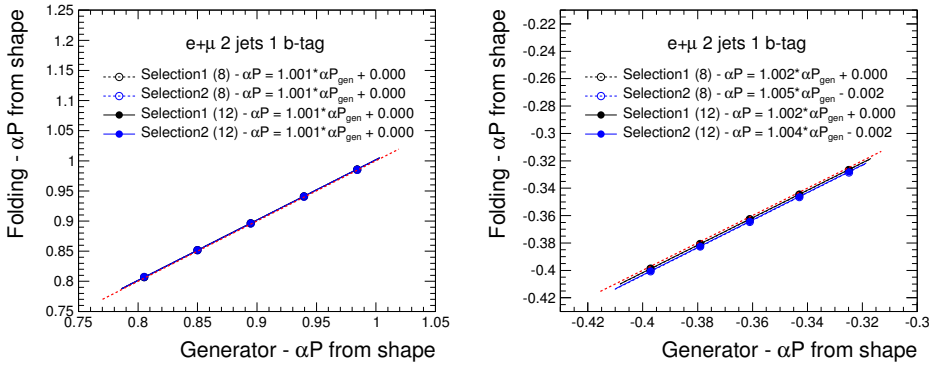

(a) (b)

Figure 9-19: Values of the polarization observable, $\alpha \cdot P$, extracted from the likelihood fit to the folded theoretical angular distributions as a function of the parton-level values for (a) the lepton analyzer and (b) for the b-quark jet analyzer. The original and re-weighted AcerMC samples are used and selected with the Selection-1 (black points) and Selection-2 (blue points) sets of cuts. From the left to the right, the five points are derived from the samples with the value of $\alpha \cdot P$ shifted by -10%, -5%, 0%, $+5\%$ and $+10\%$. The folded angular distributions are defined with 8 (open circles) and 12 (closed circles) bins and the parton-level distributions with 100 bins. The solid lines represent the linearity fits with the function $(\alpha \cdot P)_{response} = k(\alpha \cdot P)_{input} + c$ and the red dashed lines show the ideal case $(\alpha \cdot P)_{response} = (\alpha \cdot P)_{input}$.

Spin analyzer	Selection-1		Selection-2	
	k	c	k	c
lepton	1.001	0.000	1.001	0.000
b-quark jet	1.002	0.002	1.005	0.002

Table 9.7: Results of the linearity fit of the response curves shown in Figure 9-19, with the function $(\alpha \cdot P)_{response} = k(\alpha \cdot P)_{input} + c$. The response curves are extracted from the folding method in the 8-bin scheme with both the lepton and b-quark jet spin analyzers.

Pull distributions

Pull distributions are constructed, as explained in Section 9.5.1, in order to validate the statistical error propagation in the folding method. They are shown in Figure 9-20. In all cases, the pull distributions agree well with standard normal distributions, leading to the conclusion that the statistical error is propagated properly in the folding method.

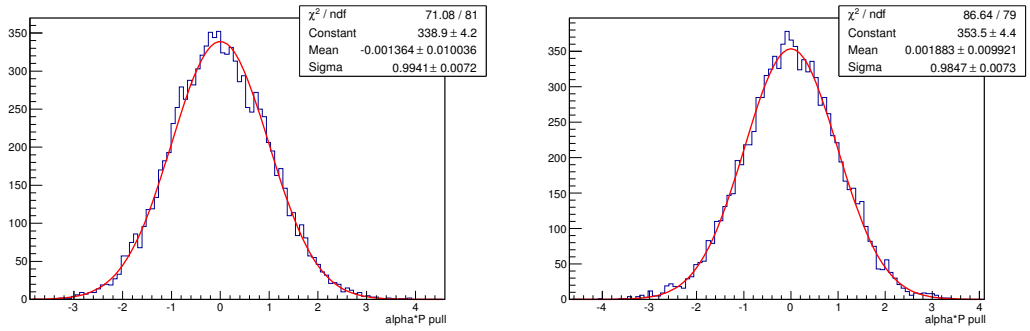

(a) (b)

Figure 9-20: Pull distributions of the folding method for (a) the lepton analyzer in the 8-bin scheme, (b) the b-quark jet analyzer in the 8-bin scheme,

9.7 Systematic uncertainties

Measurements have uncertainties from the statistical fluctuations in the recorded data as well as systematic uncertainties related to many aspects such as the misknowledge of the detector response and the theory that describes the physics processes. The statistical uncertainty could be reduced by recording more data, which is a question of time and luminosity. Various sources of systematic uncertainties, which affect the signal acceptance, the background rates and the distribution shapes, have to be considered properly in the measurements. Usually, the systematic uncertainty sources are classified into three categories: theoretical uncertainties (mis-modeling of the signal and background hard processes and showering/hadronization), detector uncertainties (mis-modeling of the detector response and object reconstruction, mis-calibration of the measured quantities) and data-driven background uncertainties (mis-measurement of the normalization). The impact of these various sources of uncertainties is determined using a frequentist method based on the generation of correlated pseudo-experiments.

9.7.1 Theoretical uncertainties

Theoretical cross section: It is an uncertainty due to the theoretical calculation of the cross sections corresponding to the various contributing processes. By looking at Equation 3.3, the theoretical uncertainty could come from the choice of the energy scales for the factorization and renormalization as well as from the parton distribution functions. This uncertainty impacts all simulated processes. For the top quark processes, the uncertainties on the theoretical cross sections calculated at approximate NNLO are used. These uncertainties are 11%, 10%, 8%, 5% for $t\bar{t}$, t-channel, Wt and s-channel [133, 52, 53, 54], respectively. Theorical uncertainties of 5% and 10% are assigned to the diboson and Z+jets processes, respectively. For the Z+jets process, an additional global 50% uncertainty due to the Berends scaling [150] and to the heavy flavor composition is also considered. The total uncertainty of 60% is

used in the unfolding measurements while the two contributions are kept splitted in the folding measurements (10% for the likelihood fit constraint and 50% in the pseudo-experiments). For the folding measurements, an uncertainty of 50% is used for the W+heavy flavor production; it combines in quadrature the 4% W+jets inclusive theory uncertainty with a 24% uncertainty per jet due to the Berends scaling and relative uncertainties of 50% and 24% on the $Wb\bar{b}$+$Wc\bar{c}$ and Wc flavor contributions, respectively. This uncertainty is totally implemented as constraint in the likelihood fit. For W+light jets contribution, a normalization uncertainty of 30%, only included in the pseudo-experiments, is considered; it combines the 4% W+jets inclusive theory uncertainty with the Berends scaling of 24% per jet. For the unfolding measurements, the uncertainties associated to the data-driven W+jets normalizations are used (see Section 9.7.3). When processes are combined, the cross section uncertainty of the combination is evaluated with respect to the proportion of each process in the sample. All these relative uncertainties on process normalizations are symmetrized.

Generator: The signal acceptances and background rates after reconstruction and event selection are different from one generator to another. For the main processes involving top quark productions, the uncertainty is estimated by comparing two different generators. For the t-channel process, the uncertainty is derived from the differences between AcerMC and PROTOS connected to the same parton shower Pythia. For $t\bar{t}$, the uncertainty is derived from the differences between MC@NLO and PowHeg connected to the same parton shower Herwig. The generator uncertainties are symmetrized. No systematic uncertainties associated to the parton showering and hadronization modeling are considered in the work reported in this thesis.

Initial and final state radiation (ISR/FSR): Both the initial and final state radiations can change the momentum of the particles produced by the hard process as discussed in Section 3.2. The uncertainty can be estimated from a generator tuned with more and less radiations. For all top quark processes, AcerMC+Pythia samples set with more and less ISR/FSR are used to estimate this uncertainty. The uncertainty is derived from the differences between the samples produced with more and less radiations divided by two and symmetrized.

W+jets shape variation: A shape uncertainty is assigned to the W+jets background based on the variation of several parameters in the generation of the W+jets event samples. The W+jets samples are reweighted according to the impact of the varied parameters. The uncertainty is taken from the differences between the reweighted and nominal samples.

9.7.2 Detector uncertainties

The uncertainties from the detector modeling are generally considered from three sources: the energy (momentum) scale, the energy (momentum) resolution and the efficiency corrections (scale factors) associated to the trigger, the reconstruction and the identification of the physics object. To estimate their impacts on the final measurements, the energy (momentum) or the correction factors are recalculated within 1σ with respect to their corresponding uncertainties and are thus converted into rate

or shape uncertainties for the signal and background contributions.

Integrated luminosity: The relative uncertainty on the integrated luminosity of the 2011 data is 1.8%; it is estimated by *van der Meer* scans as described in Section 5.5.

Lepton energy scale: The electron energy is a combination of the measurements from the tracking system and the electromagnetic calorimeter. The energy is then corrected by scale factors estimated from $Z \to ll$ data events as discussed in Section 5.1. The muon momentum is corrected according to the data-driven studies discussed in Section 5.2. For both electrons and muons, the correction scale factors shifted up and down by 1σ uncertainty are applied to recalculate the energy (momentum), leading to different event rates and angular distributions after selections.

Lepton energy resolution: The energy (momentum) resolution corrections are estimated to keep consistency between the data and simulations as discussed in Sections 5.1 and 5.2. By default, the energy (momentum) is smeared in the simulations for electrons (muons). By correcting the resolutions with 1σ of their uncertainties, the energy (momentum) of electrons (muons) is resmeared and the event rates after selections are recalculated.

Lepton reconstruction: The efficiency corrections due to trigger, reconstruction and identification are estimated in Sections 5.1 and 5.2 for electrons and muons, respectively. The correction factors are varied with 1σ according to their uncertainties in order to estimate the impact on the final measurements.

Jet energy scale: The energy of the jets is rescaled after the electromagnetic level and the hadronic-level calibrations as discussed in Section 5.3.2. The energy scale factors are shifted up and down within 1σ of their uncertainties in order to recalculate the jet energy.

Jet energy resolution: The jet energy resolution measured in the data agrees well within uncertainty with the simulated resolution. The jet energy in the simulated samples is thus by default not smeared. To estimate the uncertainty, the jet energy is smeared only within the resolution corrected by 1σ uncertainty.

Jet reconstruction efficiency: The jet reconstruction efficiency is defined as the fraction of probe track-jets matched to a calorimeter jet with a matching radius ΔR of 0.3. It is estimated using minimum bias and multijet events. The difference observed between the data and the simulations is applied to the simulated samples by randomly dropping jets from events according to the efficiency. After dropping jets in events, the changes with respect to the original simulated samples are taken as the uncertainty and symmetrized.

Jet vertex fraction: The cut on the jet vertex fraction is discussed in Section 8.1. A scale factor is introduced to complement the mismodeled simulation reflected by this cut. The corresponding uncertainty is estimated by varying the scale factor with 1σ of its uncertainty.

***B*-tagging efficiency:** Different b-tagging, c-tagging and mis-tagging efficiencies between the data and the simulations are found and scale factors are applied to the simulations in order to complement the disagreement. The corresponding uncertainties are translated to rate uncertainties by varying the scale factors with 1σ of their uncertainties.

Missing transverse momentum: The missing transverse momentum is calculated

from the reconstructed objects and from the additional cellout and softjet terms as written in Equation 5.31. The uncertainty coming from the reconstructed objects are automatically propagated in the calculation of the missing transverse momentum. The cellout and softjet contributions are treated in different ways. They are scaled up and down within 1σ in order to recalculate the missing transverse momentum.

9.7.3 Background uncertainties

QCD multijet background: The QCD multijet background is estimated using appropriate data-driven methods in dedicated control regions. Comparing the estimations obtained using different methods and control regions, one assigns an envelope of 50% uncertainty on the QCD multijet rate as described in Section 8.4.
W+jets background: The normalizations of the W+jets background processes are estimated from data in control regions. The estimated uncertainties, which include all the sources of uncertainties presented in this section, are discussed in details in Section 8.5. For the unfolding methods, a global normalization uncertainty of 14% is considered for the W+light jets process while a global uncertainty of 25% is used for the W+heavy jets processes.

9.7.4 Pseudo-experiments

In the framework of the frequentist interpretation, pseudo-experiments are used to realize the propagation of the systematic uncertainties to the measurement. The different sources of systematic uncertainties discussed in the previous sections cause variations on the signal acceptance, on the background rates as well as on the shape of the angular distributions. These effects are estimated by using systematically varied samples of simulated events and systematically varied normalization factors, in addition to the nominal ones, as inputs of the pseudo-experiments which are then varied accordingly through random drawings constrained by the corresponding uncertainties. By performing the polarization measurement from these pseudo-experiments (and additionally the cross section measurement with the folding method), one obtains an estimator of the probability density of all possible outcomes of the measurement; the standard deviation of this distribution is an estimator of the measurement uncertainty.

When performing pseudo-experiments based on the expected signal and background cross sections and on the expected signal polarization, the standard deviation of the distribution of the measured observable gives its expected uncertainty. When using the measured cross sections and polarization, the outcome of the pseudo-experiments provides in that case the (observed) uncertainty on the actual measurement.

In each pseudo-experiment, the expectation values ($\tilde{\nu}_j$) associated to the different processes (labelled by index j) are varied within their normalization uncertainties. This is performed by drawing for each process j a random number (β_j) according to a log-normal distribution with mean one and with the corresponding normalization systematic uncertainty (Δ_j) as width. Using a log-normal distribution has the advantage of avoiding unphysical negative β_j values. All the normalization variations

are additionally convolved with a variation due to the uncertainty on the integrated luminosity through the drawing of a common random number (γ). The Δ_j values correspond to the uncertainties on the theoretical cross section for the fully Monte Carlo processes and on the data-driven normalization for the QCD multijet and W+jets backgrounds. When using the folding method for the measurement, there is no smearing for the signal normalization since it is a free parameter of the likelihood fit. In the unfolding method, the signal normalization, which is not a free parameter of the measurement in that case, is varied within the theoretical cross section uncertainty of the t-channel process. The expectation values for the background ($\tilde{\nu}_j$) and signal ($\tilde{\nu}_s$) processes are then varied by including the up and down acceptance uncertainties ($\epsilon_{ij}^{+,-}$) associated to the different systematic sources (labelled by index i). This is done by drawing a Gaussian distributed random number (δ_i) for each type i of systematic uncertainty using a mean of zero and a width equal to one. To create the pseudo-experiment, the varied expectation values are then given by:

$$\tilde{\nu}_j^{pseudo} = \gamma \cdot \beta_j \cdot \tilde{\nu}_j \cdot \left[1 + \sum_i |\delta_i| \cdot \left(H(\delta_i) \cdot \epsilon_{ij}^{+} + H(-\delta_i) \cdot \epsilon_{ij}^{-}\right)\right] \tag{9.10}$$

where H denotes the Heaviside function. In the next step, the numbers of events (n_j) for the individual background and signal processes are determined from Poisson distributions with means $\tilde{\nu}_j^{pseudo}$. In the last step of the pseudo-experiment generation, the distribution of the angular observable used for the polarization measurement is obtained for each contributing process by drawing n_j times the angular observable according to the corresponding template distribution defined by a set $\{\alpha_{jk}^{pseudo}\}$ of normalized event fractions. The up and down uncertainties on the template angular shapes ($\Delta\alpha_{ijk}^{+,-}$) are included by varying bin-by-bin (labelled by index k) the nominal distributions in a similar way than for the expectation values and using the same systematic nuisance parameters (δ_i):

$$\alpha_{jk}^{pseudo} = \left[\alpha_{jk} + \sum_i |\delta_i| \cdot \left(H(\delta_i) \cdot \Delta\alpha_{ijk}^{+} + H(-\delta_i) \cdot \Delta\alpha_{ijk}^{-}\right)\right] \tag{9.11}$$

The pseudo-experiments generated as described above allow to estimate the statistical errors coming from the data; they are indeed included via the Poissonian drawings of the numbers of events n_j around the varied expectation values $\tilde{\nu}_j^{pseudo}$ (rate statistical variations) and via the drawings of the resulting numbers of events according to the varied angular templates (shape statistical variations). The errors due to the statistics of the Monte Carlo samples are additionally incorporated in the pseudo-experiments by drawing for each process a bin-by-bin random number according to a Gaussian distribution of mean one and of width equal to the statistical error associated to the angular bin, which is calculated from the root square of the quadratic sum of the event weights.

To extract the individual contributions to the total systematic uncertainty coming from the various sources described in Sections 9.7.1 to 9.7.3, pseudo-experiments are actually generated separately for each type of systematic uncertainty by giving as

input only the corresponding varied rates and shapes and by drawing only the associated random numbers. The individual systematic uncertainties are then derived from the standard deviation of the output distributions calculated with respect to the nominal measurement. The up and down uncertainties are estimated by separating events with respect to this reference, except the normalization uncertainties which are all symmetrized. The individual contributions of the statistical errors are also estimated from dedicated pseudo-experiments which include only the statistical variations. The statistical uncertainties are also calculated with respect to the nominal measurement and symmetrized. The total uncertainty is then derived by adding quadratically all the individual uncertainties.

9.7.5 Expected systematic uncertainties

The expected systematic uncertainties on the polarization observable, $\alpha \cdot P$, are estimated from pseudo-experiments generated using signal acceptances, background rates and angular distribution shapes given by the Monte Carlo event samples normalized with the expected (theoretical) cross sections for processes other than W+jets and QCD multijet. For the W+jets samples, the Monte Carlo distributions are re-normalized using the data-driven correction factors (see Section 8.5). For the QCD multijet events the normalizations (as well as the angular distributions for the muon channel) are taken from the data as explained in Section 8.4. For the signal process, the expected value for the polarization observable is directly implemented via the Monte Carlo angular distribution generated for the t-channel process. The systematic uncertainties are then included by varying the rates and shapes according to Equations 9.10 and 9.11 in order to produce pseudo-data from which the polarization observable is measured. The angular distribution corresponding to the pseudo-data is obtained by adding the varied signal and background contributions. The polarization observable is then extracted from this pseudo-data distribution using the unfolding and folding methods described in Sections 9.5 and 9.6 and the migration matrices and efficiencies presented in Section 9.4. With the unfolding procedure, the expected (non-varied) background contributions are subtracted from the pseudo-data distribution to extract the signal contribution to be deconvolved from the migration and efficiency effects. In the folding measurement, the convolved parton-level angular distribution, normalized to the expected signal acceptance, is added to the expected background contributions before being fitted to the pseudo-data distribution.

9.7.6 Observed systematic uncertainties

To estimate the observed systematic uncertainties, which correspond to the actual measurement of the polarization observable, a different approach should be considered since it is not possible to re-scale the original Monte Carlo signal angular distribution to take into account the measured polarization (this re-scaling procedure can only be done for a cross section measurement through the re-normalization of the signal and background contributions). In that case, the systematic uncertainties are included in the pseudo-experiments by varying the rates and shapes associated to the background

processes and by varying the efficiencies associated to the signal selection. No systematic variations are applied to the migration matrix to avoid duplication of some of the systematic effects on the signal response. The consequence of this choice is that the impacts on the migration matrix coming from systematic uncertainties associated to the detector modeling are under-estimated, while the uncertainties associated to the event generator are correctly handled. In general, the uncertainties are still reliable, since the migration effects are not large. For a polarization measurement with the folding method, the signal acceptance is also varied. A pseudo-background distribution is thus obtained by adding all the varied background contributions. With the unfolding method, the polarization observable is then extracted from the deconvolution of the signal distribution remaining after having subtracted the pseudo-background contribution from the real data. With the folding method, the polarization observable is extracted from the likelihood fit to the real data of the distribution obtained by adding to the pseudo-background the convolved parton-level distribution normalized to the varied acceptance. In addition, in this method, the signal and background contributions are re-normalized using the measured scale factors β_j^s and β_j^b which are also free parameters of the likelihood fit; the signal contribution is thus re-scaled to the measured cross section. In both methods, the same expected (not varied) migration matrices coupled to the varied efficiencies are used.

9.8 Polarization measurements

This section presents the results of the top quark polarization measurements performed with the unfolding and folding methods from the data (observed measurements) and from the Monte Carlo simulated events (expected measurements). The measured polarization observable is $\alpha \cdot P$ which combines the top quark degree of polarization with the spin analyzing power associated to the considered spin analyzer (lepton or b-quark). All results are present for the combination of the electron and muon channels.

9.8.1 Expected measurements

The expected measurements are extracted from the Monte Carlo simulation of the t-channel process as explained when presenting in Sections 9.5 and 9.6 the linearity checks carried out to validate the unfolding and folding methods. These expected polarizations correspond to the values derived from the Monte Carlo distributions provided by the baseline AcerMC event samples. To estimate the expected uncertainties, the background contributions are considered, as explained in Section 9.7.5, in order to propagate their associated systematic uncertainties to the expected measurement. The simulation event samples are selected with the Selection-1 and Selection-2 sets of cuts.

The expected results derived from the forward-backward asymmetry (2 bins) unfolded with a simple matrix inversion are listed Table 9.8 for the two spin analyzers and for the two selected samples; the results extracted using the iterative unfold-

ing method with the Bayesian regularization applied to angular distributions reconstructed with 2 or 8 bins are given in Table 9.9. The expected results obtained from the fit to the angular distribution shapes, defined with 8 bins, by using the Bayesian unfolding and folding methods are reported in Tables 9.10 and 9.11, respectively. In all the tables, the reported uncertainties (given in the parentheses) include both the systematic and statistical uncertainties.

From angular distributions defined with only 2 bins, the expected measurements based on the forward-backward asymmetry of the distributions unfolded with an ordinary matrix inversion (Table 9.8) or with an iterative Bayesian regularization (Table 9.9) give quite the same polarizations and systematic uncertainties (this is consistent with the comparison of the linearity results discussed in Section 9.5.2).

When using the Bayesian unfolding coupled to the forward-backward extraction procedure, the values listed in Table 9.9 show that, for the lepton spin analyzer, slightly lower expected systematic uncertainties are obtained with 8 bins (32%) than with 2 bins, while for the b-quark jet case, significantly larger systematic uncertainties are expected with the configuration of 8 bins (80-93% depending on the selection) with respect to the 2-bin scheme (72%). Therefore, with the b-quark jet spin analyzer, a better precision is expected with only 2 bins, while, as concluded in Section 9.5.2 from the linearity studies, a slightly better accuracy is expected with 8 bins. For the lepton analyzer, a better precision as well as a slightly better accuracy is expected with the 8-bin scheme.

If one compares the unfolding measurements obtained with the two different extraction procedures (forward-backward asymmetry with 8 bins in Table 9.9 and shape fit in Table 9.10), whatever the spin analyzer, a significant improvement on the expected precision is achieved with the forward-backward asymmetry with respect to the fit, since the calculation of the forward-backward asymmetry cancels some of the uncertainties. As concluded in Section 9.5.2 from the validation checks, a slightly better response is also expected with the forward-backward extraction.

For the measurements based on the fit of the angular distribution shape, the folding method (Table 9.11) always give expected measurements with a lower total uncertainty than the unfolding method (Table 9.10). With the lepton spin analyzer, precisions of about 24-28% and 45-46%, dependent on the selected samples, are expected from the folding and unfolding methods, respectively, whereas for the b-quark jet analyzer, precisions of about 58-66% and of the order of 170% are expected respectively for these two methods. The expected folding results are also more precise than the ones determined from the unfolded forward-backward asymmetry (Tables 9.8 and 9.9).

In conclusion, a largely better precision is therefore expected with the folding method, whatever the selection and spin analyzer. This complements the conclusion drawn in Section 9.6 from the validation tests which stipulates that the folding method leads to a better expected accuracy [1]. In all cases, a better precision is also expected for the lepton spin analyzer than for the b-quark jet analyzer. This is due to the

[1] Accuracy is the proximity of measurement results to the actual (true) value, while precision is only related to the uncertainty of the measurement no matter what the measured value is.

significantly worse reconstruction of the b-jet with respect to the charged lepton and also to the spin analyzing power of the b-quark (-0.41 at the tree level) which is largely lower than the maximal analyzing power of the charged lepton (1.0) and makes the angular templates less discriminating with respect to the backgrounds, compared to the lepton case.

The cross-check SELECTION-1 and the default SELECTION-2 selections give globally compatible expected measurements. In the next section, only the observed measurements corresponding to the default SELECTION-2 signal events will be presented, as they correspond to the larger signal-over-background ratio. In addition, this set of cuts has been used to extract the W boson polarization in the normal basis in order to search for CP-violation [73] (results presented in Section 3.6.4) and both analyses could be therefore more easily combined in the future.

The breakdowns of the relative contributions to the total expected statistical and systematic uncertainties for the measurements performed with the folding method and for the SELECTION-2 event samples are shown in Tables 9.12 and 9.13 for the lepton and b-quark jet spin analyzers, respectively.

For the lepton analyzer, the main sources of uncertainties come from the statistics (around 17% for the data statistics and 9% for the Monte Carlo statistics), the $t\bar{t}$ generator (about 12% on the average), the jet energy scale (around 8% on the average) and the jet energy resolution (9%). For the b-quark jet analyzer, these various contributions are much larger (around 40% for the data statistics, 20% for the simulation statistics, 24% on the average for the $t\bar{t}$ generator, 29% on the average for the jet energy scale and 8% for the jet energy resolution) with in addition a significant contribution coming from the t-channel generator (13%) and from the b-tagging (6%).

Spin analyzer	SELECTION-1	SELECTION-2
lepton	0.895 ($\pm$33.1%)	0.895 ($\pm$32.3%)
b-quark jet	-0.361 ($\pm$71.6%)	-0.363 ($\pm$71.5%)

Table 9.8: Expected top quark polarizations, $\alpha \cdot P$, extracted from the forward-backward asymmetry (2 bins) unfolded with a simple matrix inversion for the events selected with the SELECTION-1 and SELECTION-2 sets of cuts. The results are given for the lepton and b-quark jet spin analyzers. The relative uncertainties given in the parentheses include the statistical and systematic uncertainties; the up and down uncertainties are averaged.

Spin analyzer - Binning	SELECTION-1	SELECTION-2
lepton - 2 bins	0.894 (±33.1%)	0.894 (±32.4%)
lepton - 8 bins	0.895 (±32.3%)	0.895 (±32.2%)
b-quark jet - 2 bins	-0.360 (±71.9%)	-0.360 (±72.1%)
b-quark jet - 8 bins	-0.361 (±92.9%)	-0.361 (±80.3%)

Table 9.9: Expected top quark polarizations, $\alpha \cdot P$, extracted from the forward-backward asymmetry of the distributions (2 or 8 bins) unfolded iteratively with the Bayesian regularization for the events selected with the SELECTION-1 and SELECTION-2 sets of cuts. The results are given for the lepton and b-quark jet spin analyzers. The relative uncertainties given in the parentheses include the statistical and systematic uncertainties; the up and down uncertainties are averaged.

Spin analyzer	SELECTION-1	SELECTION-2
lepton	0.894 (±45.2%)	0.894 (±46.1%)
b-quark jet	-0.360 (±184%)	-0.360 (±166%)

Table 9.10: Expected top quark polarizations, $\alpha \cdot P$, extracted from a χ^2 fit to the angular distributions (8 bins) unfolded iteratively with the Bayesian regularization for the events selected with the SELECTION-1 and SELECTION-2 sets of cuts. The results are given for the lepton and b-quark jet spin analyzers. The relative uncertainties given in the parentheses include the statistical and systematic uncertainties; the up and down uncertainties are averaged.

Spin analyzer	SELECTION-1	SELECTION-2
lepton	0.896 (±23.5%)	0.896 (±27.8%)
b-quark jet	-0.362 (±65.6%)	-0.364 (±58.2%)

Table 9.11: Expected top quark polarizations, $\alpha \cdot P$, extracted from the likelihood fit to the folded theoretical angular distributions (8 bins) for the events selected with the SELECTION-1 and SELECTION-2 sets of cuts. The results are given for the lepton and b-quark jet spin analyzers. The relative uncertainties given in the parentheses include the statistical and systematic uncertainties; the up and down uncertainties are averaged.

9.8.2 Observed measurements

The observed measurements derived from the forward-backward asymmetry unfolded using the iterative method with Bayesian regularization applied to angular distributions reconstructed with 2 or 8 bins are given in Table 9.14 (the measurements provided by the ordinary unfolding procedure are not shown since they are quite equivalent to the 2-bin case). The observed results obtained from the fit to the angular distribution shapes, defined with 8 bins, by using the Bayesian unfolding and

Source	Relative uncertainties (%)	
Data statistics	+16.6	-16.6
Simulation statistics	+8.6	-8.6
Luminosity	+0.4	-0.4
Theory normalization	+3.7	-3.7
Multijet normalization	+1.0	-1.0
E_T^{miss}	+2.1	-3.7
Lepton reconstruction	+0.5	-0.5
Lepton energy scale	+0.9	-1.2
Lepton energy resolution	+0.5	-0.7
Jet energy resolution	+8.8	-9.7
Jet energy scale	+11.2	-6.5
Jet reconstruction	+0.3	-0.2
Jet vertex fraction	+0.2	-0.4
b-tagging factor	+2.1	-2.3
c-tagging factor	+0.4	-0.4
mis-tagging factor	+0.4	-0.3
ISR/FSR	+2.9	-4.2
t-channel generator	+7.0	-6.1
$t\bar{t}$ generator	+15.0	-10.9
W+jets shape variation	+0.5	-0.5
Total statistics	+18.7	-18.7
Total systematic	+22.6	-18.6
Total	+29.3	-26.4

Table 9.12: Breakdown of the relative contributions to the total expected uncertainty on the top quark polarization observable, $\alpha \cdot P$, extracted by using the folding method with the lepton spin analyzer. The events are selected with the SELECTION-2 set of cuts. The uncertainties are quoted in per cent.

folding methods are listed in Tables 9.15 and 9.16, respectively. In all the tables, the reported uncertainties (given in the parentheses) include both the systematic and statistical uncertainties. These measurements are presented for the SELECTION-2 signal samples.

Rather similar polarization values are found with the unfolding and folding methods. For the charged lepton, $\alpha \cdot P$ values ranging from 0.884 to 1.085 are measured (compared to the Standard Model value 0.895) whereas values between -0.460 and -0.280 are obtained for the b-quark jet (the Standard Model value is -0.361). On another hand, the associated total uncertainties are globally of the same order of magnitude than those estimated from the expectations: uncertainties ranging from 26 to 31% are derived for the lepton with the different methods; for the b-quark jet, the forward-backward asymmetry leads to a total uncertainty around 56% while the unfolding fit gives 177% and the folding fit 71%.

Source	Relative uncertainties (%)	
Data statistics	+40.1	-40.1
Simulation statistics	+22.0	-22.0
Luminosity	+0.3	-0.3
Theory normalization	+5.5	-5.5
Multijet normalization	+0.2	-0.2
E_T^{miss}	+7.2	-0.0
Lepton reconstruction	+0.7	-0.6
Lepton energy scale	+4.3	-2.9
Lepton energy resolution	+2.4	-0.2
Jet energy resolution	+8.2	-7.2
Jet energy scale	+20.8	-17.2
Jet reconstruction	+1.8	-1.8
Jet vertex fraction	+0.5	-0.0
b-tagging factor	+6.0	-5.1
c-tagging factor	+0.3	-0.2
mis-tagging factor	+0.6	-0.5
ISR/FSR	+0.4	-0.3
t-channel generator	+14.0	-12.5
$t\bar{t}$ generator	+20.2	-27.7
W+jets shape variation	+1.1	-1.0
Total statistics	+45.7	-45.7
Total systematic	+35.4	-36.6
Total	+57.8	-58.6

Table 9.13: Breakdown of the relative contributions to the total expected uncertainty on the top quark polarization observable, $\alpha \cdot P$, extracted by using the folding method with the b-quark jet spin analyzer. The events are selected with the SELECTION-2 set of cuts. The uncertainties are quoted in per cent.

Spin analyzer - Binning	SELECTION-2
lepton - 2 bins	0.886 ($\pm$25.8%)
lepton - 8 bins	0.884 ($\pm$27.9%)
b-quark jet - 2 bins	-0.397 ($\pm$55.7%)
b-quark jet - 8 bins	-0.460 ($\pm$56.2%)

Table 9.14: Observed top quark polarizations, $\alpha \cdot P$, extracted from the forward-backward asymmetry of the distributions (2 or 8 bins) unfolded iteratively with the Bayesian regularization for the events selected with the SELECTION-2 set of cuts. The results are given for the lepton and b-quark jet spin analyzers. The relative uncertainties given in the parentheses include the statistical and systematic uncertainties; the up and down uncertainties are averaged.

Spin analyzer	SELECTION-2
lepton	1.085 ($\pm$30.5%)
b-quark jet	-0.381 ($\pm$177%)

Table 9.15: Observed top quark polarizations, $\alpha \cdot P$, extracted from a χ^2 fit to the angular distributions (8 bins) unfolded iteratively with the Bayesian regularization for the events selected with the SELECTION-2 set of cuts. The results are given for the lepton and b-quark jet spin analyzers. The relative uncertainties given in the parentheses include the statistical and systematic uncertainties; the up and down uncertainties are averaged.

Spin analyzer	SELECTION-2
lepton	0.902 ($\pm$26.1%)
b-quark jet	-0.280 ($\pm$70.6%)

Table 9.16: Observed top quark polarizations, $\alpha \cdot P$, extracted from the likelihood fit to the folded theoretical angular distributions (8 bins) for the events selected with the SELECTION-2 set of cuts. The results are given for the lepton and b-quark jet spin analyzers. The relative uncertainties given in the parentheses include the statistical and systematic uncertainties; the up and down uncertainties are averaged.

The breakdowns of the relative contributions to the total observed statistical and systematic uncertainties for the measurements performed with the folding method and for the SELECTION-2 event samples are shown in Tables 9.17 and 9.18 for the lepton and b-quark jet spin analyzers, respectively.

The same dominant sources of uncertainties as for the expected measurements, which are the data and simulation statistics, the generators, the jet energy scale and resolution, are found for the polarization values measured from the data. For the charged lepton analyzer, one estimates 16% for the data statistics, 10% for the Monte Carlo statistics, 11% for the $t\bar{t}$ generator, 11% for the jet energy resolution and 4% on the average for the jet energy scale. For the b-tagged jet analyzer, these various contributions account for 50%, 31%, 22%, 21% and 17% on the average, respectively, with an additional significant contribution from b-tagging (7%).

Source	Relative uncertainties (%)	
Data statistics	+16.2	-16.2
Simulation statistics	+9.5	-9.5
Luminosity	+0.4	-0.4
Theory normalization	+3.3	-3.3
Multijet normalization	+0.9	-0.9
E_T^{miss}	+4.3	-2.7
Lepton reconstruction	+0.2	-0.5
Lepton energy scale	+2.0	-1.9
Lepton energy resolution	+0.7	-0.7
Jet energy resolution	+10.5	-11.0
Jet energy scale	+0.6	-8.1
Jet reconstruction	+0.2	-0.5
Jet vertex fraction	+0.1	-0.3
b-tagging factor	+2.4	-2.4
c-tagging factor	+0.3	-0.6
mis-tagging factor	+0.3	-0.6
ISR/FSR	+0.6	-1.0
t-channel generator	+3.9	-5.3
$t\bar{t}$ generator	+10.7	-11.4
W+jets shape variation	+0.6	-0.8
Total statistics	+18.8	-18.8
Total systematic	+16.8	-19.4
Total	+25.2	-27.0

Table 9.17: Breakdown of the relative contributions to the total observed uncertainty on the top quark polarization observable, $\alpha \cdot P$, extracted by using the folding method with the lepton spin analyzer. The events are selected with the SELECTION-2 set of cuts. The uncertainties are quoted in per cent.

9.8.3 Cross section measurements

The production cross section can be measured simultaneously with the polarization thanks to the folding method, since the normalization of the signal contribution is taken as a completely free parameter in the likelihood fit. The fit determines a scale factor (β^s) with respect to the Standard Model prediction. The cross section measured for t-channel production is thus derived by multiplying the fitted scale factor with the value used to normalize the simulated t-channel events (NNLO value 64.6 pb [52]). The observed systematic and statistical uncertainties estimated from the generation of pseudo-experiments are also re-scaled accordingly.

This section presents the production cross section measurements obtained for the signal events selected with the hard SELECTION-2 series of cuts. The measured (observed) cross section from the likelihood fit of the distribution of the charged lepton in the spectator basis is:

Source	Relative uncertainties (%)	
Data statistics	+50.4	-50.4
Simulation statistics	+30.8	-30.8
Luminosity	+0.3	-0.3
Theory normalization	+5.4	-5.4
Multijet normalization	+0.3	-0.3
E_T^{miss}	+0.1	-13.5
Lepton reconstruction	+0.7	-0.5
Lepton energy scale	+3.8	-4.7
Lepton energy resolution	+0.5	-3.7
Jet energy resolution	+21.3	-21.7
Jet energy scale	+10.3	-24.7
Jet reconstruction	+2.1	-2.0
Jet vertex fraction	+0.3	-0.8
b-tagging factor	+6.3	-7.5
c-tagging factor	+0.4	-0.2
mis-tagging factor	+0.8	-0.6
ISR/FSR	+2.8	-2.6
t-channel generator	+2.0	-0.3
$t\bar{t}$ generator	+22.3	-21.6
W+jets shape variation	+1.4	-1.4
Total statistics	+59.0	-59.0
Total systematic	+34.0	-43.2
Total	+68.1	-73.1

Table 9.18: Breakdown of the relative contributions to the total observed uncertainty on the top quark polarization observable, $\alpha \cdot P$, extracted by using the folding method with the b-quark jet spin analyzer. The events are selected with the SELECTION-2 set of cuts. The uncertainties are quoted in per cent.

$$(\sigma_t)_{obs} = 72.0 \pm 4.4(stat) \pm 12.5(syst)\ pb = 72.0 \pm 13.2\ pb. \tag{9.12}$$

The cross section measured from the likelihood fit of the distribution of the b-tagged jet in the spectator basis is:

$$(\sigma_t)_{obs} = 71.9 \pm 4.3(stat) \pm 12.0(syst)\ pb = 71.9 \pm 12.8\ pb. \tag{9.13}$$

One can notice that, unlike the polarization measurements, the cross section measurements are achieved with an equivalent precision for the two types of fitted angular distributions, a total uncertainty of 18% being expected for both of them (the observed uncertainties are also 18% in the two cases).

When fixing the shape parametrization of the signal contribution with the $\alpha \cdot P$ equal to the Standard Model values (i.e. the simulated template distribution is used

for the signal instead), cross sections with a very slighly lower total uncertainty are obtained: $\sigma_t = 72.0 \pm 12.8$ pb is extracted from the charged lepton distribution and $\sigma_t = 71.7 \pm 12.5$ pb from the distribution of the b-tagged jet.

All these cross sections values are in very good agreement with the Standard Model prediction calculated at approximate NNLO, $\sigma_t = 64.6^{+2.7}_{-2.0}$ pb [52]. This measurement improves the value published by the ATLAS collaboration from the analysis of the first 1 fb^{-1} of the 2011 data [144].

The likelihood fit implemented in the folding method allows also to extract the scale factors β_j^b associated to the background processes. These nuisance parameters are constrained within the theoretical uncertainties given in Table 9.6 and described in Section 9.6. The values obtained for the main background processes are listed in Table 9.19 together with their total uncertainties. They are given for the lepton spin analyzer (consistent values are found for the b-quark jet analyzer).

Compared to the theoretical uncertainties used as priors in the likelihood fit to constrain the backgrounds, the uncertainties obtained for the top quark background processes are of the same order of magnitude (12% versus 10% for the input constraint) while much smaller uncertainties are derived for the W + heavy flavor jet processes (14% instead of 50% for the input constraint). It should be noted for this process that the normalization factor and its associated uncertainty extracted with the folding method is in rather good agreement with the global correction factors estimated from the tag counting method presented in Section 8.5: 1.33±0.34 for the Wbb and Wcc components, and 1.32±0.28 for the Wc component.

Background process	β
$t\bar{t}$, Wt, s-channel	1.00 ± 0.12
W+heavy flavor	1.43 ± 0.20

Table 9.19: Scale factors β and their total uncertainties extracted for the combined ($t\bar{t}$, Wt, s-channel) and the W+heavy flavor processes. They come from the likelihood fit of the angular distributions reconstructed for the charged lepton.

9.9 Conclusion

This concluding section presents the polarization measurements extracted for the signal events selected with the tighter set of cuts (SELECTION-2) using the folding method which, as discussed in the previous sections, leads to the most accurate and precise expected measurements.

The expected and observed measurements of the top quark polarization observable associated to the charged lepton spin analyzer in the spectator basis are:

$$(\alpha_l \cdot P)_{exp} = 0.90^{+0.26}_{-0.24} \tag{9.14}$$

$$(\alpha_l \cdot P)_{obs} = 0.90^{+0.23}_{-0.24}. \tag{9.15}$$

The expected and observed measurements of the top quark polarization observable for the b-quark jet spin analyzer in the spectator basis are:

$$(\alpha_b \cdot P)_{exp} = -0.36^{+0.21}_{-0.21} \tag{9.16}$$

$$(\alpha_b \cdot P)_{obs} = -0.28^{+0.19}_{-0.21}. \tag{9.17}$$

These preliminary measurements on the top quark polarization observables, $\alpha_l \cdot P$ and $\alpha_b \cdot P$, are compatible with the Standard Model predictions within one standard deviation.

From the measurement performed with the charged lepton analyzer, which is the most precise one, we can extract the top quark degree of polarization P by assuming the value predicted by the Standard Model for the spin analyzing power whose calculated value at NLO is 0.998 [72]. One obtains:

$$(P)_{obs} = 0.90^{+0.23}_{-0.24}. \tag{9.18}$$

On the other hand, from the measurements given by the two spin analyzers, one can also extract the value of the ratio between the charged lepton and b-quark spin analyzing powers. One gets for this observable:

$$\left(\frac{\alpha_b}{\alpha_l}\right)_{obs} = -0.31^{+0.23}_{-0.24}. \tag{9.19}$$

This result is in agreement with the value predicted by the Standard Model at NLO which is -0.39 (the spin analyzing power calculated at NLO is 0.998 for the lepton [72] and -0.39 for the b-quark [151]).

Chapter 10

Conclusion

After the observation of the single top quark t-channel production at the LHC [152, 60], precise measurements on single top quarks become of crucial interest. These measurements cover the top-antitop quark cross section ratio, the differential cross section, the top quark mass and the polarization observables. In particular, via the electroweak interaction, the single top quark t-channel production mode provides a chance to measure the degree of the top quark polarization P, which will contribute to constrain the Wtb anomalous couplings beyond the Standard Model left-handed vector coupling.

In this document, the first measurements on top quark polarization performed with the ATLAS detector are presented. The studies started from the parton level, where different anomalous couplings are tested using the PROTOS generator, in order to clarify the impact of the presence of the anomalous couplings in the production and decay Wtb vertices. Following this, at the reconstruction level, the events are selected aiming at isolating the single top quark t-channel production, and the relevant background contamination is estimated to decompose the non-polarized events from the data. Benefiting from the data samples with highly purified signal events, the unfolding and folding methods are constructed to measure the polarization. Various tests and checks on the methods with different extraction approaches (from the forward-backward asymmetry or a direct χ^2 fit) have been done for both lepton and b-quark spin analyzers. With the comparison on the expected measurements given by different methods, the folding method is chosen thanks to its most accurate response and the smallest expected uncertainties. The first preliminary values for the top quark polarization product $(\alpha \cdot P)$ are thus derived. By assuming the Standard Model value for the spin analyzing power α, the degree of top quark polarization is obtained using lepton as the spin analyzer:

$$(P)_{obs} = 0.90^{+0.23}_{-0.24}. \tag{10.1}$$

This result is compatible with the Standard Model prediction. Furthermore, the ratio $\frac{\alpha_b}{\alpha_l}$ between the b-quark and lepton spin analyzing powers is also derived.

In the future, all the measured polarization parameters can be used in a global fit together with the measurements of the W polarization as well as the single top quark

cross section, in order to strongly constrain the anomalous Wtb couplings.

Appendix A

Simulations with PROTOS

A.1 Energy configuration

As described in Section 7.3.4, samples are generated with the PROTOS generator configured with the Standard Model couplings at the center of mass energies of $7\,TeV$, $8\,TeV$ and $14\,TeV$. The distributions of the transverse momentum and of the pseudorapidity associated to the spectator and top quarks are shown in Figure A-1. The distributions of the same kinematic variables corresponding to the decay products of the top quark (W boson, b-quark, charged lepton and neutrino) are shown in Figures A-2 and A-3.

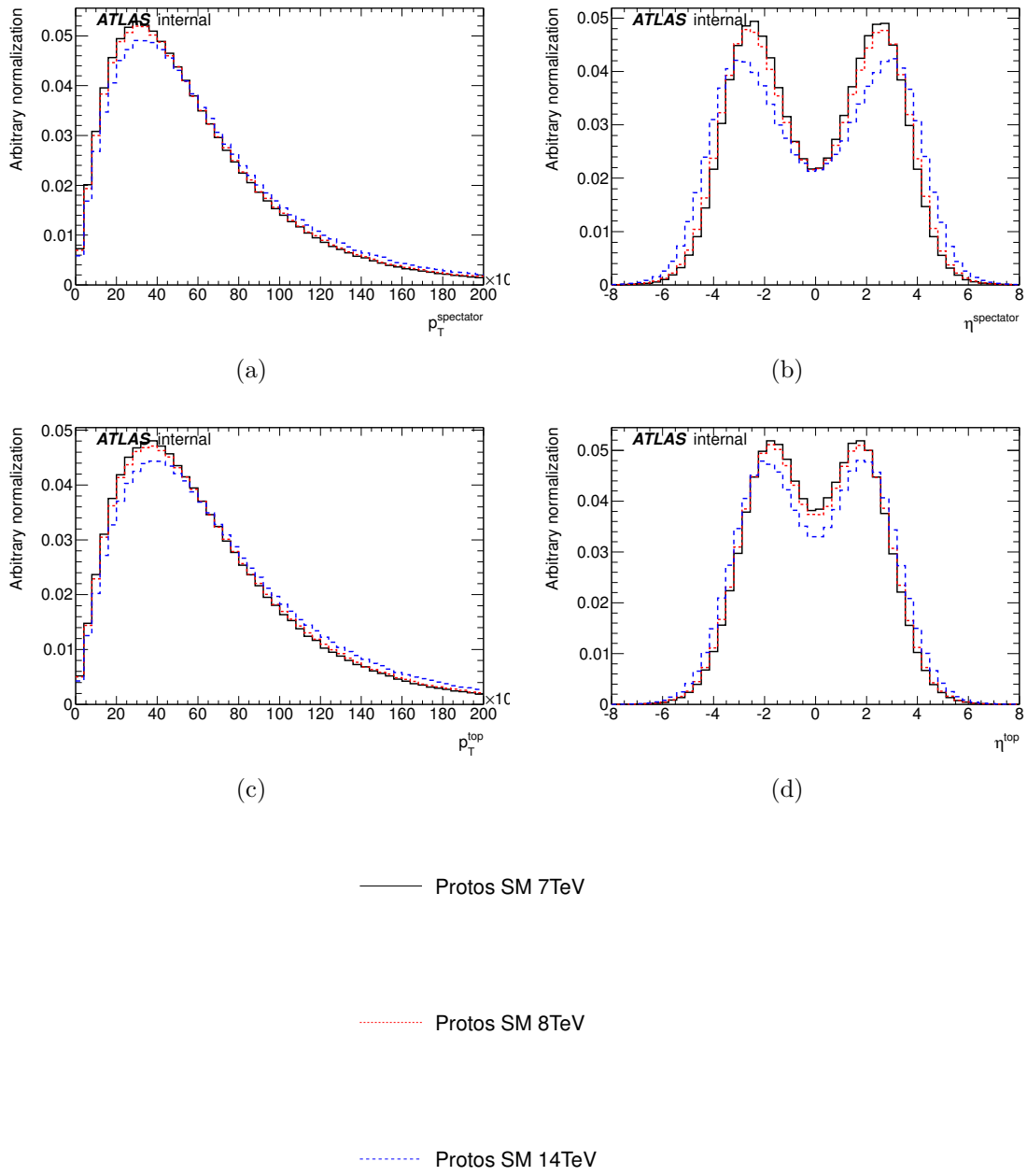

Figure A-1: Comparison of the parton-level kinematic distributions for PROTOS events produced with the Standard Model couplings at the center of mass energies of 7 TeV (black solid line), 8 TeV (red dashed line) and 14 TeV (blue dashed line) (a) spectator quark transverse momentum, (b) spectator quark pseudorapidity, (c) top quark transverse momentum and (d) top quark pseudorapidity. The distributions are shown for the electron channel.

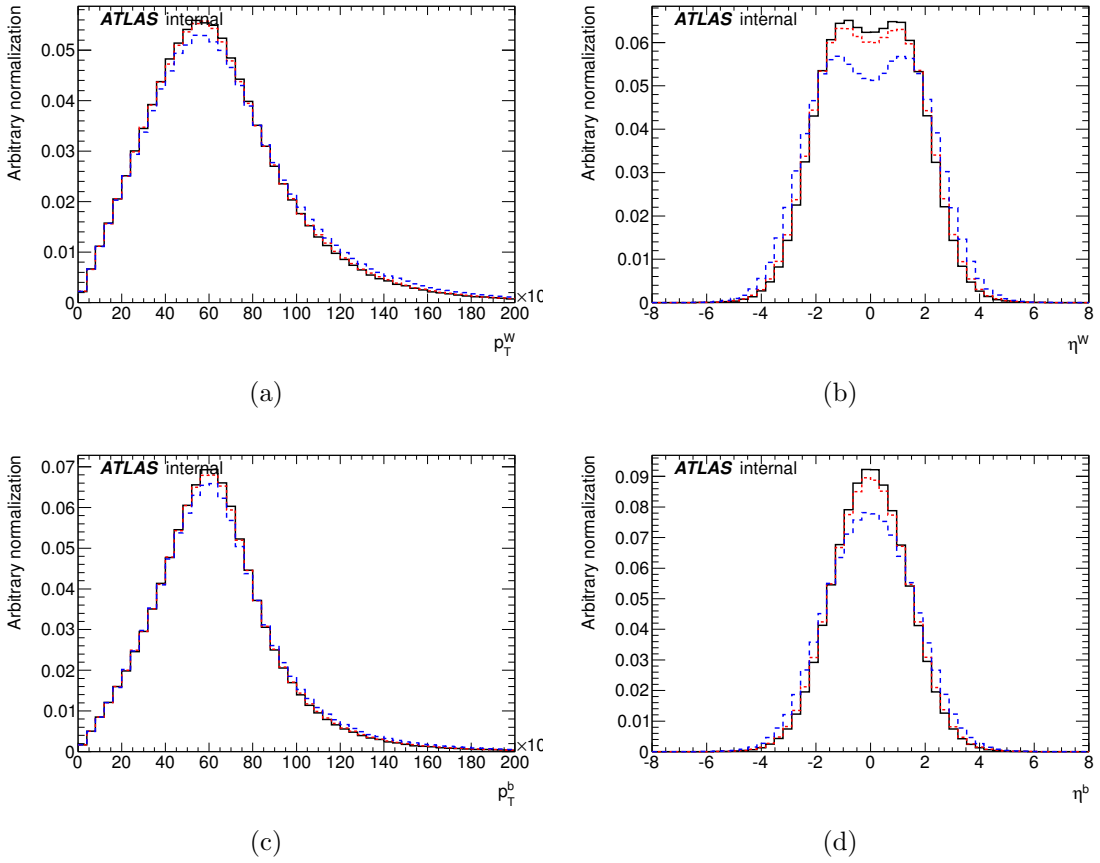

(a) (b)

(c) (d)

Figure A-2: Comparison of the parton-level kinematic distributions for PROTOS events produced with the Standard Model couplings at the center of mass energies of 7 TeV (black solid line), 8 TeV (red dashed line) and 14 TeV (blue dashed line) (a) W boson transverse momentum, (b) W boson pseudorapidity, (c) b-quark transverse momentum and (d) b-quark pseudorapidity. The distributions are shown for the electron channel.

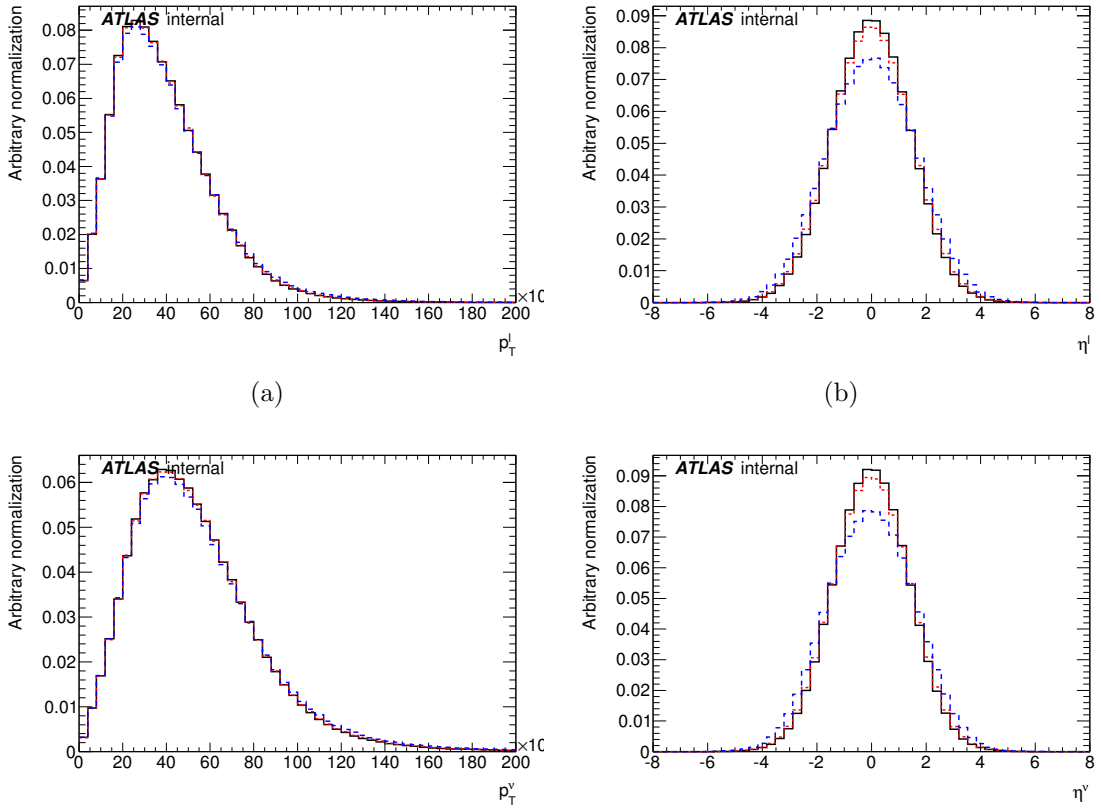

(a) (b)

(c) (d)

Figure A-3: Comparison of the parton-level kinematic distributions for PROTOS events produced with the Standard Model couplings at the center of mass energies of 7 TeV (black solid line), 8 TeV (red dashed line) and 14 TeV (blue dashed line) (a) lepton transverse momentum, (b) lepton pseudorapidity, (c) neutrino transverse momentum and (d) neutrino pseudorapidity. The distributions are shown for the electron channel.

Appendix B

Event selection

B.1 PRETAG kinematic distributions

The distributions of the transverse momentum and of the pseudorapidity of the physics objects (lepton, leading and sub-leading jets) as obtained in the PRETAG samples are shown in Figure B-1 and B-2 for the electron and muon channels, respectively.

B.2 TAG kinematic distributions

The distributions of the transverse momentum and of the pseudorapidity of the physics objects (lepton, b-tagged and light jets) as obtained in the TAG samples are shown in Figure B-3 and B-4 for the electron and muon channels, respectively Additionally, the kinematic distributions associated to the reconstructed W boson are shown in Figure B-5.

To check the kinematic modeling on the variables used in SELECTION-1 and SELECTION-2 listed in Section 8.2.2, Figure B-6 and B-7 show their distributions.

B.3 Signal kinematic distributions

The kinematic distributions of the the physics objects for the SELECTION-1 samples in the electron and muon channels are shown in Figure B-8 and Figure B-9, respectively. The kinematic distributions of the the physics objects for the SELECTION-2 samples in the electron and muon channels are shown in Figure B-10 and Figure B-11, respectively. The physics objects cover the lepton, the b-tagged jet and the non-tagged (light) jet.

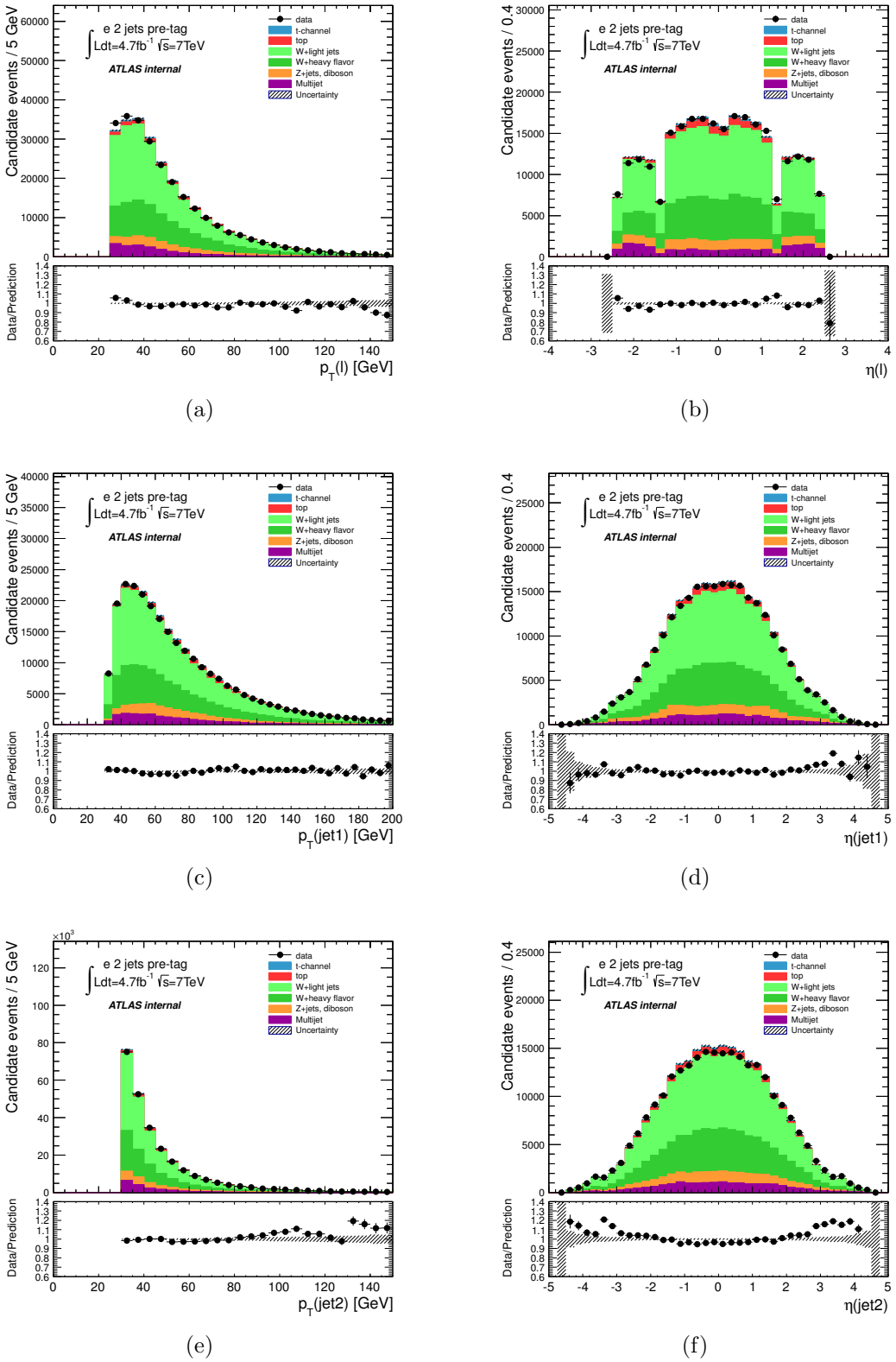

Figure B-1: Kinematic distributions of the PRETAG sample for the electron channel. (a) electron transverse momentum, (b) electron pseudorapidity, (c) leading jet transverse momentum, (d) leading jet pseudorapidity, (e) sub-leading transverse momentum and (f) sub-leading jet pseudorapidity.

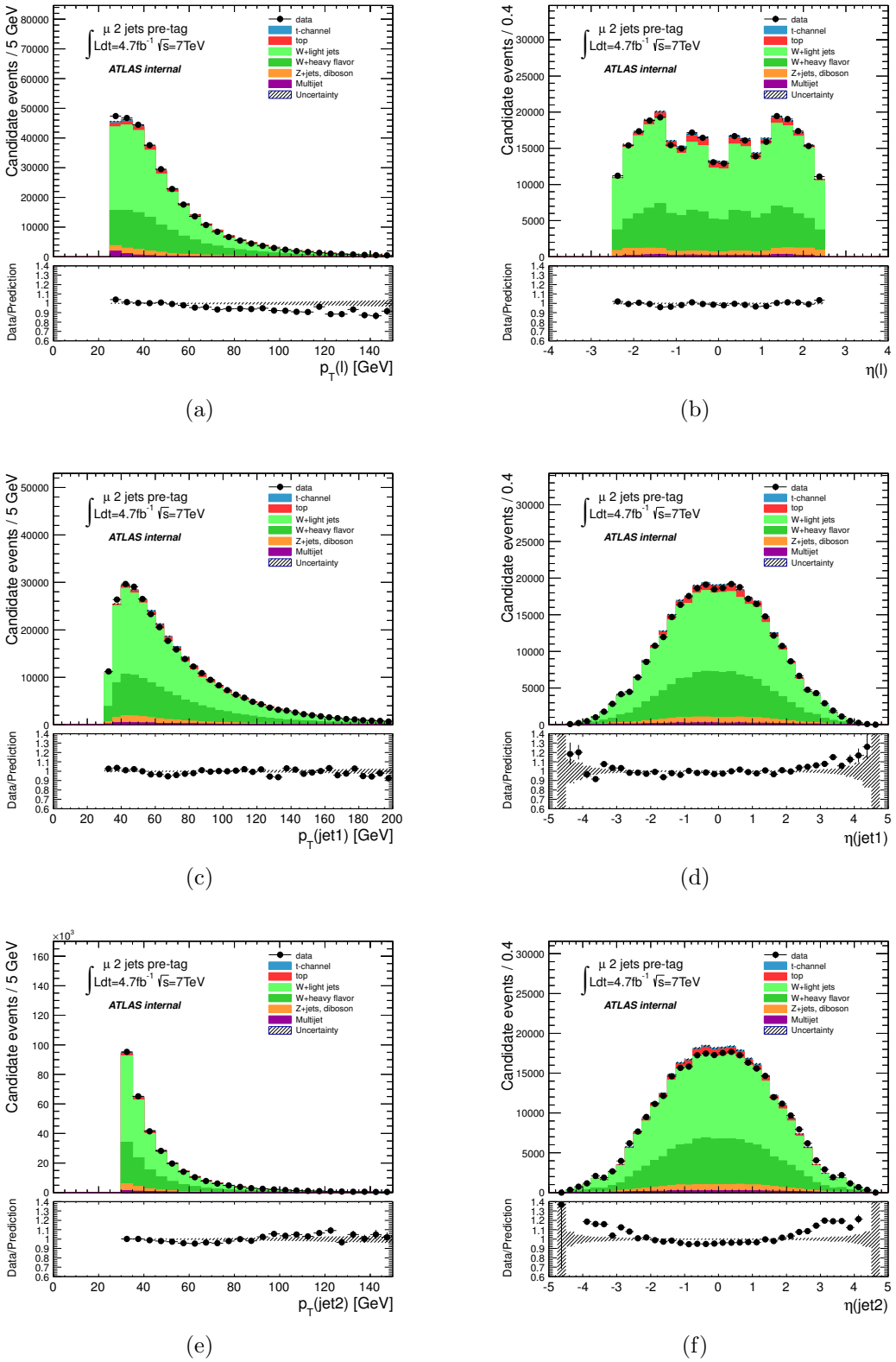

Figure B-2: Kinematic distributions of the PRETAG sample for the muon channel. (a) muon transverse momentum, (b) muon pseudorapidity, (c) leading jet transverse momentum, (d) leading jet pseudorapidity, (e) sub-leading jet transverse momentum and (f) sub-leading jet pseudorapidity.

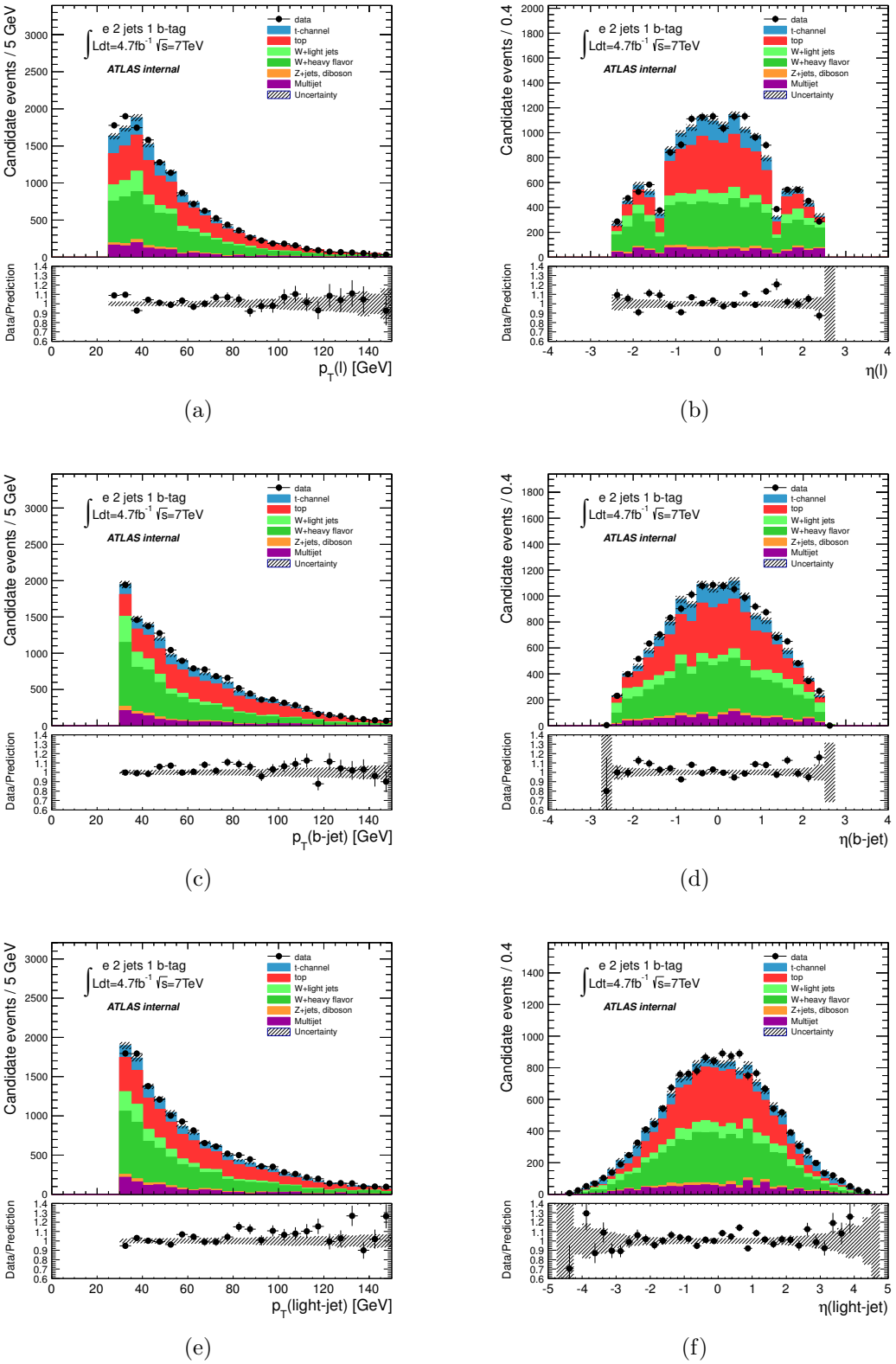

Figure B-3: Kinematic distributions of the TAG sample for the electron channel. (a) electron transverse momentum, (b) electron pseudorapidity, (c) b-tagged jet transverse momentum, (d) b-tagged jet pseudorapidity, (e) light jet transverse momentum and (f) light jet pseudorapidity.

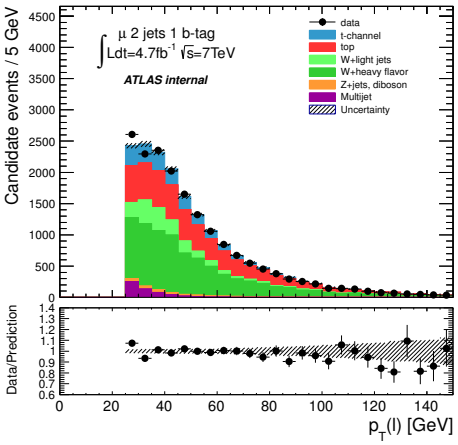

(a)

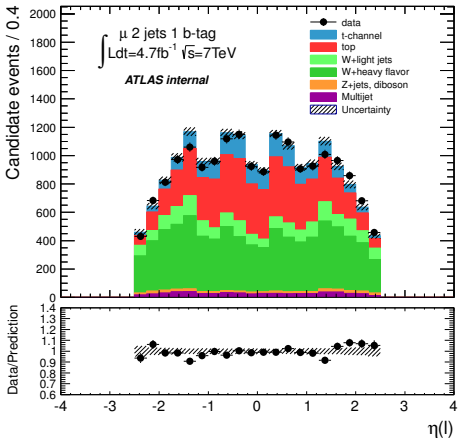

(b)

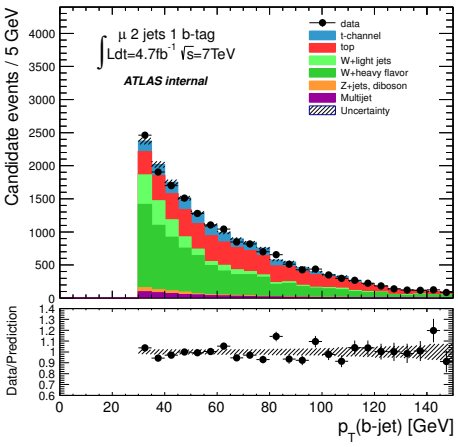

(c)

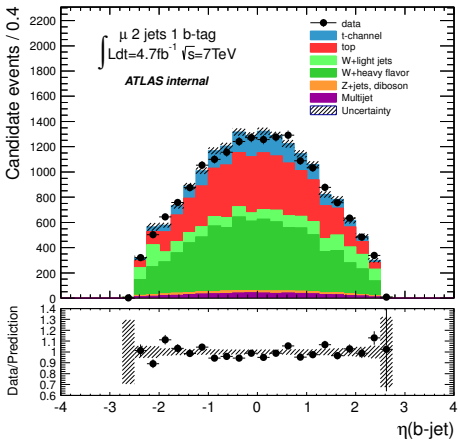

(d)

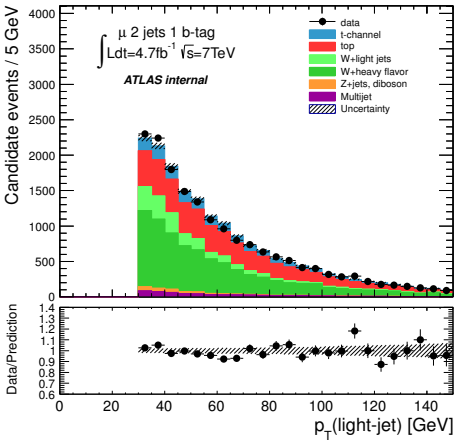

(e)

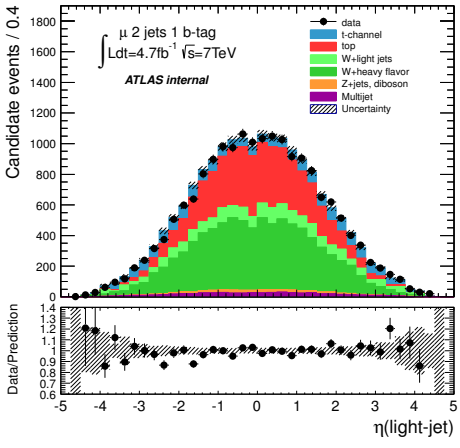

(f)

Figure B-4: Kinematic distributions of the TAG sample for the muon channel. (a) muon transverse momentum, (b) muon pseudorapidity, (c) b-tagged jet transverse momentum, (d) b-tagged jet pseudorapidity, (e) light jet transverse momentum and (f) light jet pseudorapidity.

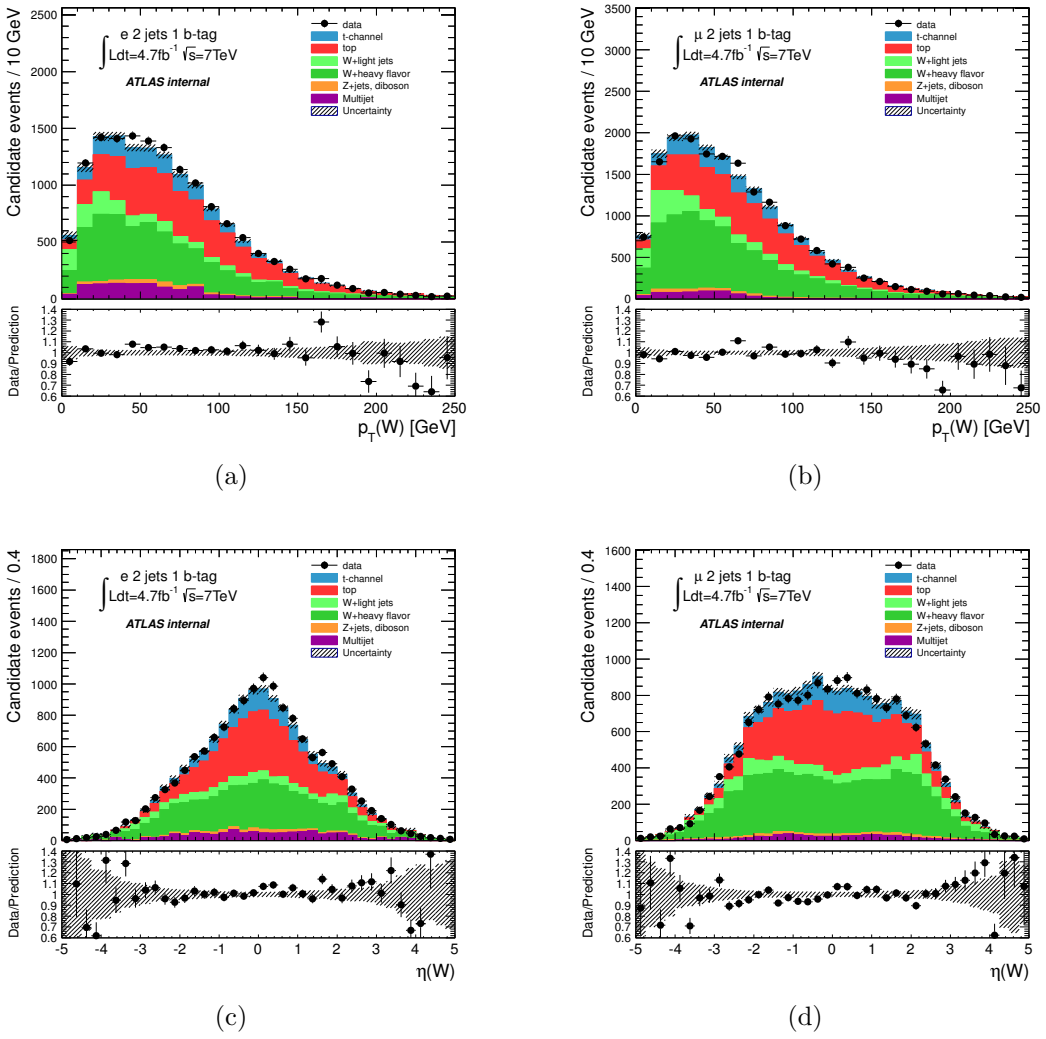

Figure B-5: Kinematic distributions of the reconstructed W boson in the TAG sample for both electron and muon channels. (a) transverse momentum for the electron channel, (b) transverse momentum for the muon channel, (c) pseudorapidity for the electron channel and (d) pseudorapidity for the muon channel.

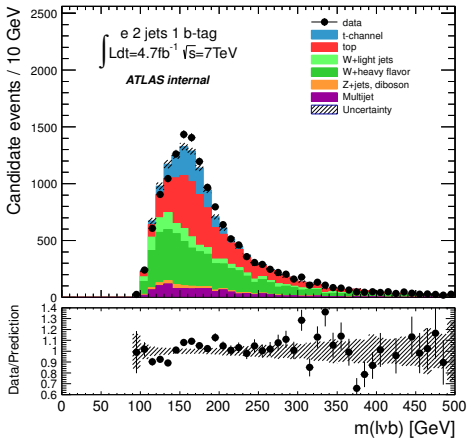

(a)

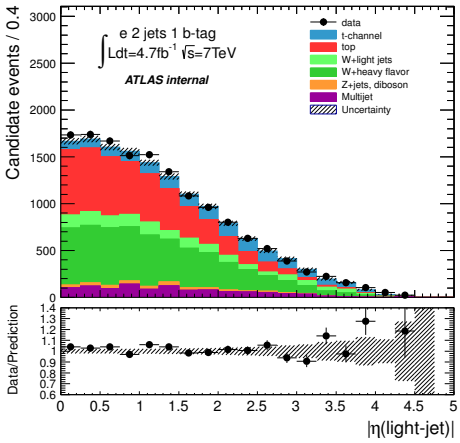

(b)

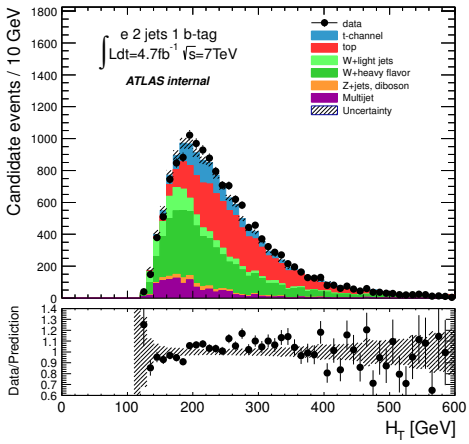

(c)

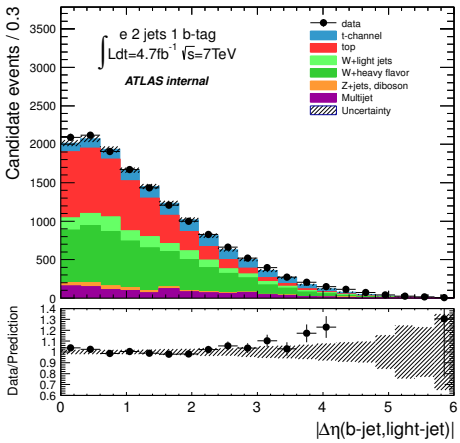

(d)

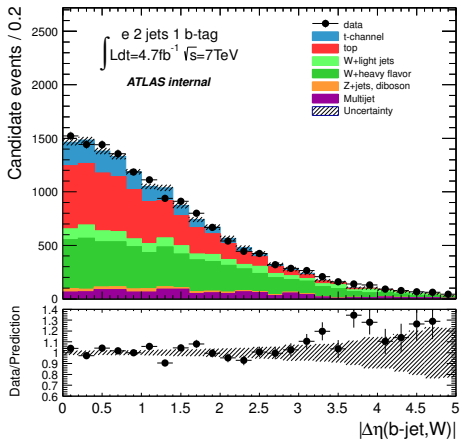

(e)

Figure B-6: Distributions of the variables used in the SELECTION-1 and SELECTION-2 sets of cuts produced with the TAG sample for the electron channel. (a) invariant mass of the lepton, neutrino and b-jet, (b) light jet pseudorapidity, (c) scalar sum of the transverse momenta of the jets, the lepton combined with the transverse missing momentum, (d) $\Delta\eta$ between the b-tagged jet and the light jet and (e) $\Delta\eta$ between the b-tagged jet and the W boson.

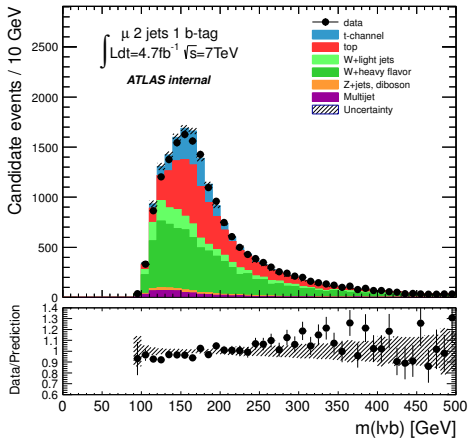

(a)

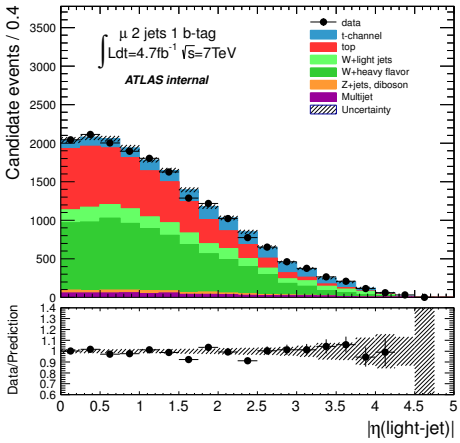

(b)

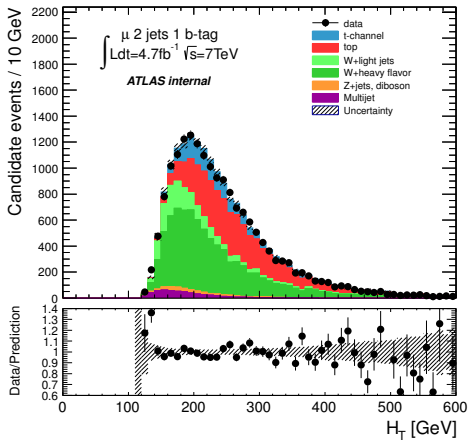

(c)

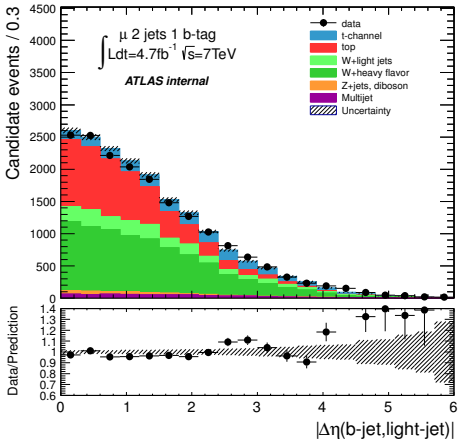

(d)

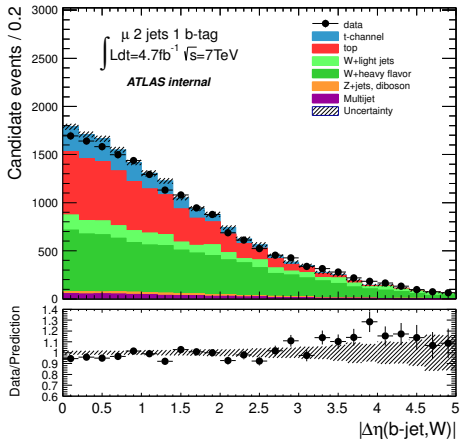

(e)

Figure B-7: Distributions of the variables used in the SELECTION-1 and SELECTION-2 sets of cuts produced with the TAG sample for the muon channel. (a) invariant mass of the lepton, neutrino and b-jet, (b) light jet pseudorapidity, (c) scalar sum of the transverse momenta of the jets and the lepton combined with the transverse missing momentum, (d) $\Delta\eta$ between the b-tagged jet and the light jet and (e) $\Delta\eta$ between the b-tagged jet and the W boson.

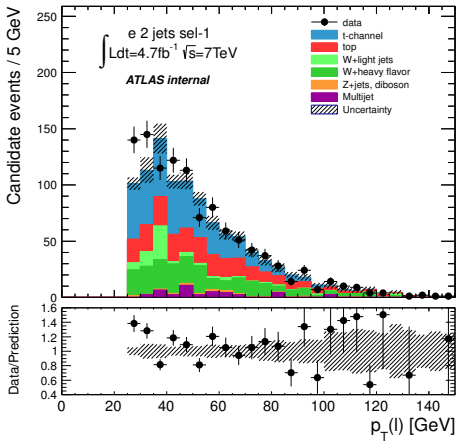

(a)

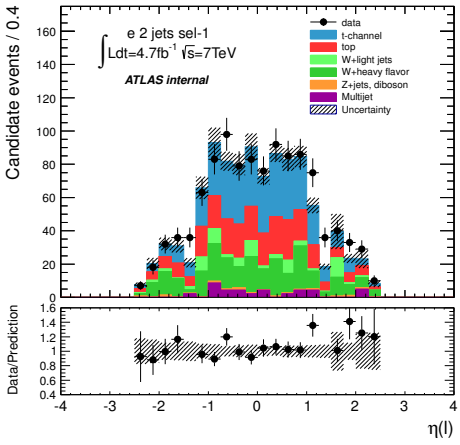

(b)

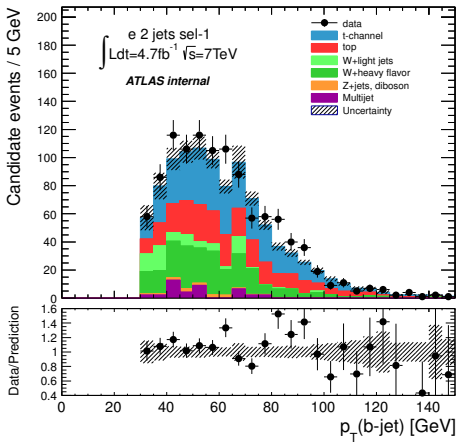

(c)

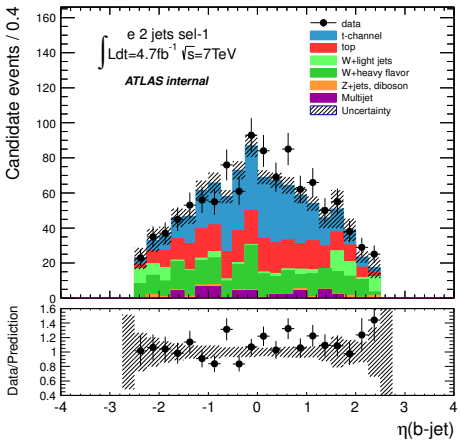

(d)

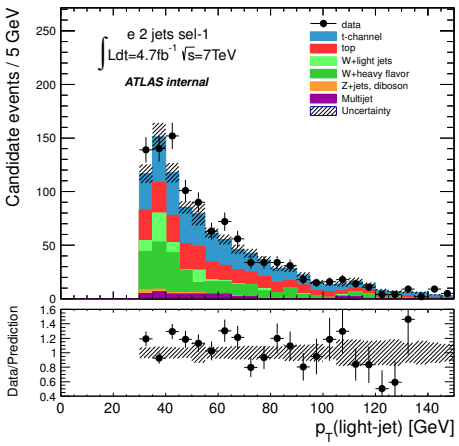

(e)

Figure B-8: Kinematic distributions of the SELECTION-1 sample for the electron channel. (a) electron transverse momentum, (b) electron pseudorapidity, (c) b-tagged jet transverse momentum, (d) b-tagged jet pseudorapidity and (e) light jet transverse momentum.

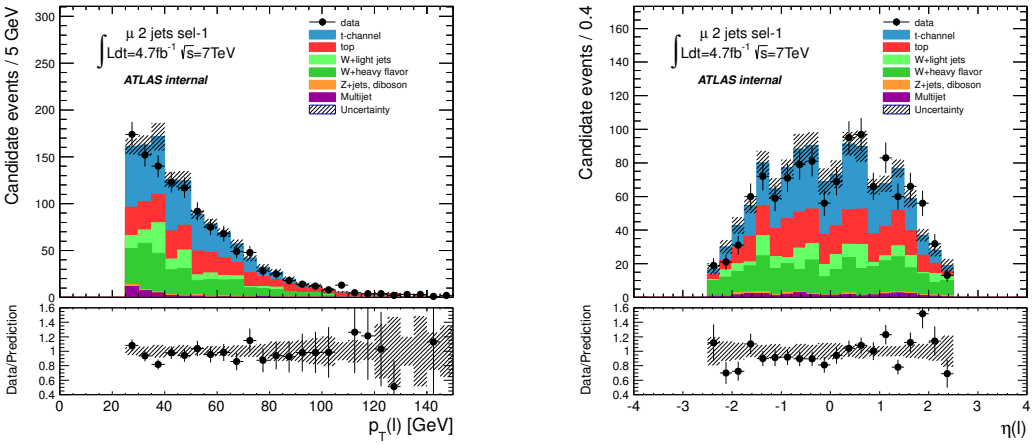

(a)

(b)

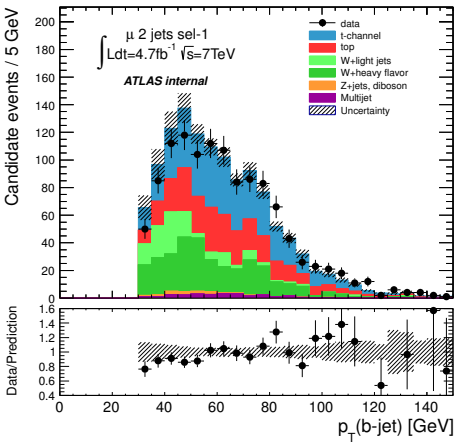

(c)

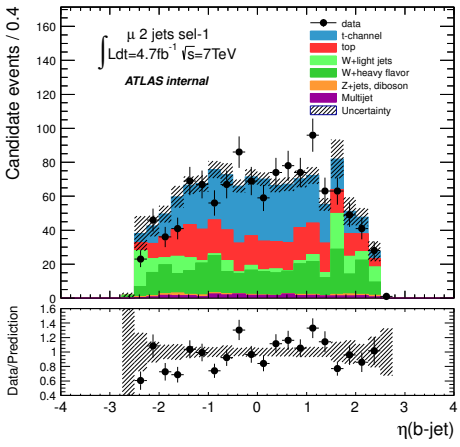

(d)

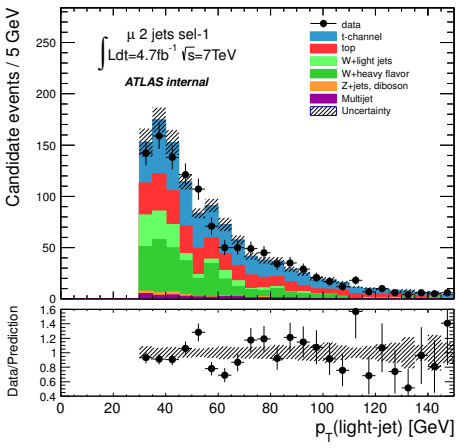

(e)

Figure B-9: Kinematic distributions of the SELECTION-1 sample for the muon channel. (a) muon transverse momentum, (b) muon pseudorapidity, (c) b-tagged jet transverse momentum, (d) b-tagged jet pseudorapidity and (e) light jet transverse momentum.

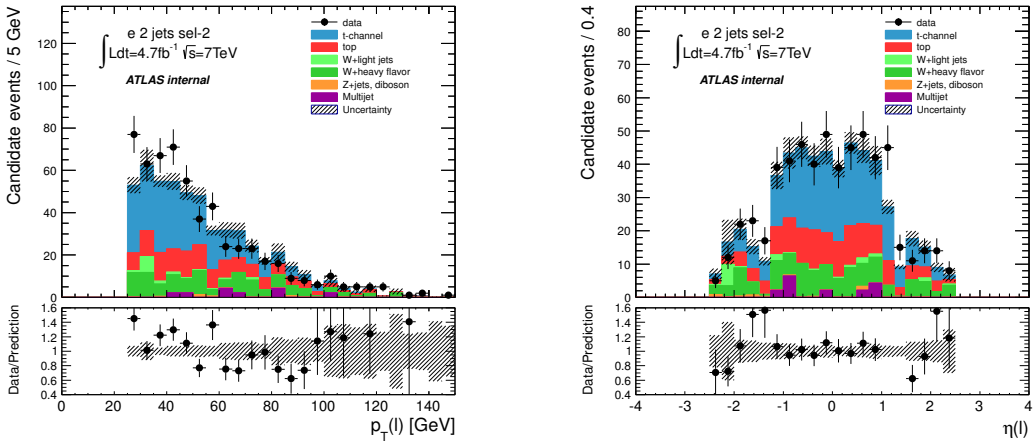

(a)

(b)

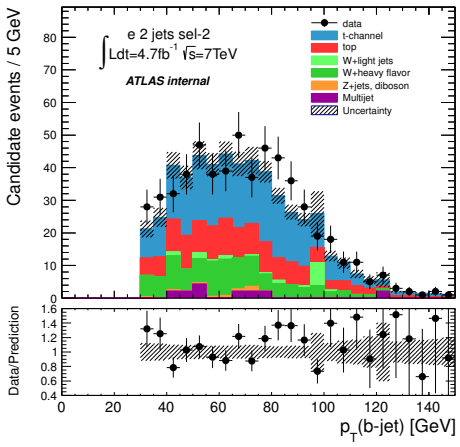

(c)

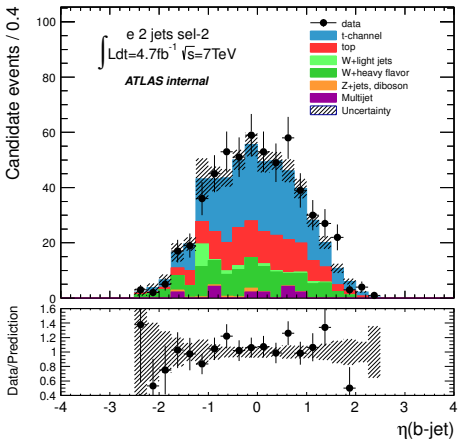

(d)

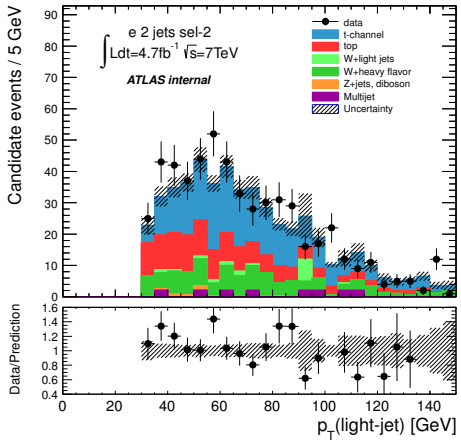

(e)

Figure B-10: Kinematic distributions of the SELECTION-2 sample for the electron channel. (a) electron transverse momentum, (b) electron pseudorapidity, (c) b-tagged jet transverse momentum, (d) b-tagged jet pseudorapidity and (e) light jet transverse momentum.

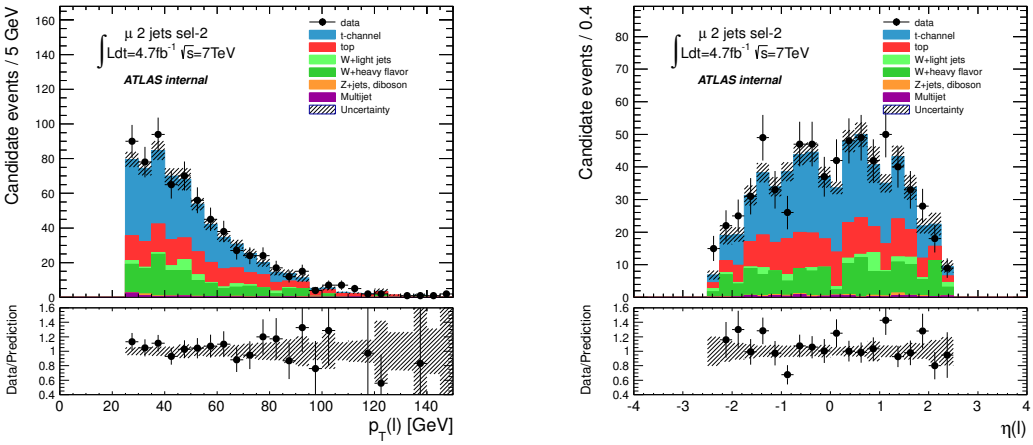

(a)

(b)

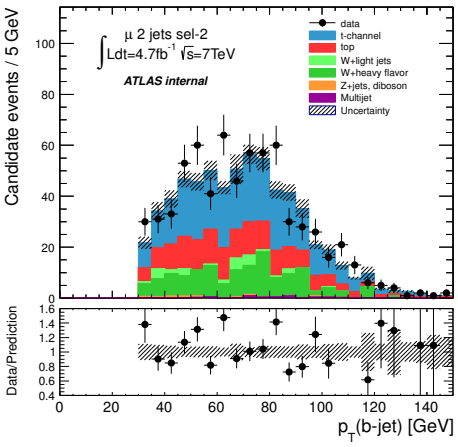

(c)

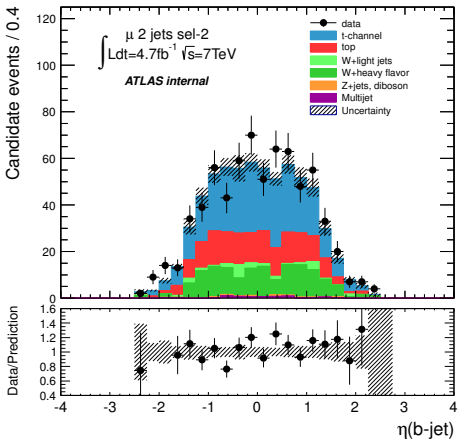

(d)

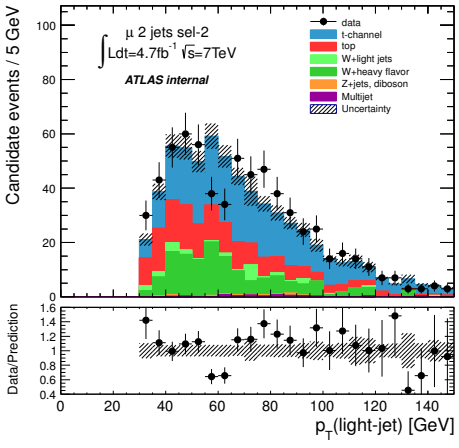

(e)

Figure B-11: Kinematic distributions of the SELECTION-2 sample for the muon channel. (a) muon transverse momentum, (b) muon pseudorapidity, (c) b-tagged jet transverse momentum, (d) b-tagged jet pseudorapidity and (e) light jet transverse momentum.

Bibliography

[1] Max Planck. Entropy and Temperature of Radiant Heat, Annalen der Physik, vol. 1. no 4. April, pg. 719-37. 1900.

[2] Albert Einstein. Über einen die Erzeugung und Verwandlung des Lichtes betreffenden heuristischen Gesichtspunkt (a translation: On a Heuristic Viewpoint Concerning the Production and Transformation of Light), Annalen der Physik 322(6), 132–148 (1905). 1905.

[3] Louis de Broglie. Recherches sur la théorie des quanta (Researches on the quantum theory), Thesis, Paris, 1924, Ann. de Physique (10) 3, 22 (1925). 1924.

[4] J. Beringer et al. (Particle Data Group). The Review of Particle Physics, Phys. Rev. D86, 010001 (2012). 2012.

[5] S. Weinberg. A model of leptons, Phys. Rev. Lett. 19 (1967) 1264-1266. 1967.

[6] S. L. Glashow. Partial symmetries of weak interactions, Nucl. Phys. 22 (1961) 579-588. 1961.

[7] A. Salam. Weak and electromagnetic interactions, Proceedings of the 8th Nobel Symposium on Elementary Particle Theory, Relativistic Groups and Analyticity, Stockholm, Sweden, 1968, edited by N. Svartholm, p. 367-377. 1968.

[8] Z. Sullivan. Fully differential W production and decay at next-to-leading order in QCD, Phys. Rev. (2002) 075011, arXiv:hep-ph/0207290 [hep-ph]. 2002.

[9] D. Duffty, Z. Sullivan. Model independent reach for W-prime bosons at the LHC, Phys. Rev. D86 (2012) 075018, arXiv:1208.4858 [hep-ph]. 2012.

[10] C. Cheung, A. L. Fitzpatrick, L. Randall. Sequestering CP Violation and GIM-Violation with Warped Extra Dimensions, JHEP 0801 (2008) 069, arXiv:0711.4421 [hep-th]. 2008.

[11] A. L. Fitzpatrick, G. Perez, L. Randall. Flavor anarchy in a Randall-Sundrum model with 5D minimal flavor violation and a low Kaluza-Klein scale, Phys. Rev. Lett. 100 (2008) 171604, arXiv:0710.1869 [hep-ph]. 2008.

[12] C. Bini, R. Contino, N. Vignaroli. Heavy-light decay topologies as a new strategy to discover a heavy gluon, JHEP 1201 (2012) 157, arXiv:1110.6058 [hep-ph]. 2012.

[13] N. Vignaroli. Discovering the composite Higgs through the decay of a heavy fermion, JHEP 1207 (2012) 158, arXiv:1204.0468 [hep-ph]. 2012.

[14] N. Vignaroli. $\Delta F = 1$ constraints on composite Higgs models with LR parity, Phys. Rev. D 86 (2012) 115011, arXiv:1204.0478 [hep-ph]. 2012.

[15] Nicola Cabibbo. Unitary Symmetry and Leptonic Decays, Phys. Rev. Lett. 10 531 (1963). 1963.

[16] Makoto Kobayashi, Toshihide Maskawa. CP-Violation in the Renormalizable Theory of Weak Interaction, Prog. Theor. Phys 49, 652 (1973). 1973.

[17] T. M. P. Tait. SIGNALS FOR THE ELECTROWEAK SYMMETRY BREAKING ASSOCIATED WITH THE TOP QUARK, Ph.D. Thesis, MSUHEP-90622, arXiv:hep-ph/9907462v1. 1999.

[18] C. N. Yang, R. L. Mills. Conservation of Isotopic Spin and Isotopic Gauge Invariance, Phys. Rev. 96, 191–195 (1954) . 1954.

[19] F. Englerts, R. Brout. Broken Symmetry and the Mass of Gauge Vector Mesons, Phy. Rev. Lett., 13:321-232, 1964. 1964.

[20] P. W. Higgs. Broken Symmetries and the Masses of Gauge Bosons. Phy. Rev Lett., 13:508-509, 1964. 1964.

[21] Ling-Lie Chau, Wai-Yee Keung. Comments on the Parametrization of the Kobayashi-Maskawa Matrix, Phys. Rev. Lett. 53, 1802–1805 (1984). 1984.

[22] Lincoln Wolfenstein. Parametrization of the Kobayashi-Maskawa Matrix, Phys. Rev. Lett. 51, 1945–1947 (1983). 1983.

[23] A.J. Buras et al. Waiting for the Top Quark Mass, $K^+ \to \pi^+ \nu\bar{\nu}$, $B_s^0 - \bar{B}_s^0$ Mixing and CP Asymmetries in B-Decays, Phys.Rev.D50:3433-3446,1994, arXiv:hep-ph/9403384. 1994.

[24] J. Charles, et al. CP Violation and the CKM Matrix: Assessing the Impact of the Asymmetric B Factories, Eur.Phys.J.C41:1-131,2005, arXiv:hep-ph/0406184. 2005.

[25] A. Hocker et al. A New Approach to a Global Fit of the CKM Matrix, Eur.Phys.J.C21:225-259,2001, arXiv:hep-ph/0104062. 2001.

[26] The UTfit Collaboration. The 2004 UTfit Collaboration Report on the Status of the Unitarity Triangle in the Standard Model, JHEP0507:028,2005, arXiv:hep-ph/0501199. 2005.

[27] The UTfit Collaboration. Model-independent constraints on Delta F=2 operators and the scale of New Physics, JHEP 0803:049,2008, arXiv:0707.0636 [hep-ph]. 2008.

[28] The ATLAS Collaboration. Observation of a New Particle in the Search for the Standard Model Higgs Boson with the ATLAS Detector at the LHC, Phys. Lett. B 716 (2012) 1-29, arXiv:1207.7214. 2012.

[29] The CMS Collaboration. Observation of a new boson at a mass of 125 GeV with the CMS experiment at the LHC, Phys. Lett. B 716 (2012) 30, arXiv:1207.7235v2. 2012.

[30] The ATLAS Collaboration. Study of the spin of the new boson with up to 25 fb^{-1} of ATLAS data, ATLAS-CONF-2013-040. 2013.

[31] The CMS Collaboration. Study of the mass and spin-parity of the Higgs boson candidate via its decays to Z boson pairs, CMS-HIG-12-041, arXiv:1212.6639. 2012.

[32] CMSnoop R. J. Barlow. Event classification using weighting methods , J. Comput. Phys. 72 (1987) 202. http://dx.doi.org/10.1016/0021-9991(87)90078-7 texttt doi:10.1016/0021-9991(87)90078-7. 1987.

[33] Siegfried Bethke. Experimental Tests of Asymptotic Freedom, Prog.Part.Nucl.Phys.58:351-386,2007, arXiv:hep-ex/0606035. 2007.

[34] R. P. Feynman. The Behavior of Hadron Collisions at Extreme Energies. High Energy Collisions: Third International Conference at Stony Brook, N.Y. Gordon & Breach. pp. 237–249. ISBN 978-0-677-13950-0. 1969.

[35] J. M. Butterworth, G. Dissertori, G. P. Salam. Hard Processes in Proton-Proton Collisions at the Large Hadron Collider, arXiv:1202.0583 [hep-ex]. 2012.

[36] Torbjorn Sjostrand, Stephen Mrenna, Peter Skands. PYTHIA 6.4 Physics and Manual, JHEP 0605:026,2006, arXiv:hep-ph/0603175. 2006.

[37] G.Corcellaet al. HERWIG 6.5: an event generator for Hadron Emission Reactions With Interfering Gluons (including supersymmetric processes), JHEP 0101:010,2001, arXiv:hep-ph/0011363. 2002.

[38] R. Ellis, W. Stirling, B. Webber. QCD and Collider Physics. Cambridge University Press, Cambridge, UK, 1996. 1996.

[39] . `http://www.phys.psu.edu/~cteq/`. .

[40] . `https://www.desy.de/h1zeus/combined_results/index.php?do=proton_structure`. .

[41] . `http://durpdg.dur.ac.uk/hepdata/mrs.html`. .

[42] . http://nnpdf.hepforge.org/. .

[43] G. Altarelli and G. Parisi. Asymptotic Freedom in Parton Language, Nucl.Phys. B126 (1977) 298. 1977.

[44] M. Klein et al. On The Decay Of The Top Quark, Phys.Lett. B153 (1985) 341. 1985.

[45] M. Aliev et al. HATHOR - HAdronic Top and Heavy quarks cross section calculatoR. Comput. Phys. Commun.182 (2011) 1034-1046, arXiv:1007:1327 [hep-ph]. 2011.

[46] A.D. Martin et al. Parton distributions for the LHC, Eur. Phys. J. C63 (2009) 189-285, arXiv: 0901.0002 [hep-ph]. 2009.

[47] A.D Martin et al. Uncertainties on alpha_S in global PDF analyses and implications for predicted hadronic cross sections, Eur. Phys. J. C64 (2009) 653-680, arXiv:0905.3531 [hep-ph]. 2009.

[48] M. Cacciari et al. Top-pair production at hadron colliders with next-to-next-to-leading logarithmic soft-gluon resummation, to appear in Phys. Lett. B, arXiv:1111.5869 [hep-ph]. 2011.

[49] M. Czakon and A. Mitov. Top++: a program for the calculation of the top-pair cross-section at hadron colliders, arXiv:1112.5675 [hep-ph]. 2011.

[50] The ATLAS Collaboration. Measurement of the top quark pair production cross section in the single-lepton channel with ATLAS in proton-proton collisions at 8 TeV using kinematic fits with b-tagging, ATLAS-CONF-2012-149. 2012.

[51] S. S. D. Willenbrock, D. A. Dicus. Production of heavy quarks from W-gluon fusion, Phys. Rev. D 34 155 (1986). 1986.

[52] Nikolaos Kidonakis. Next-to-next-to-leading-order collinear and soft gluon corrections for t-channel single top quark production, Phys. Rev. D 83, 091503(R) (2011). 2011.

[53] Nikolaos Kidonakis. Two-loop soft anomalous dimensions for single top quark associated production with a W^- or H^-, Phys. Rev. D 82, 054018 (2010). 2010.

[54] Nikolaos Kidonakis. Next-to-next-to-leading logarithm resummation for s-channel single top quark production, Phys. Rev. D 81, 054028 (2010). 2010.

[55] Nikolaos Kidonakis. Single top quark production at the Fermilab Tevatron: Threshold resummation and finite-order soft gluon corrections, Phys. Rev. D 74, 114012 (2006). 2006.

[56] D0 Collaboration. Observation of the Top Quark, Phys. Rev. Lett. 74, 2632 (1995). 1995.

[57] CDF Collaboration. Observation of Top Quark Production in $\bar{p}p$ Collisions with the Collider Detector at Fermilab, Phys. Rev. Lett. 74 2626 (1995). 1995.

[58] D0 Collaboration. Observation of Single Top-Quark Production, Phys. Rev. Lett. 103 092001 (2009). 2009.

[59] CDF Collaboration. Observation of Electroweak Single Top-Quark Production, Phys. Rev. Lett. 103 092002 (2009). 2009.

[60] The CMS Collaboration. Measurement of the single-top-quark t-channel cross section in pp collisions at $\sqrt{s} = 7\ TeV$, JHEP12(2012)035. 2012.

[61] The ATLAS Collaboration. Measurement of t-Channel Single Top-Quark Production in pp Collisions at $\sqrt{s} = 8\ TeV$ with the ATLAS detector, ATLAS-CONF-2012-132. 2012.

[62] The CMS Collaboration. Measurement of the single-top-quark t-channel cross section in pp collisions at $\sqrt{s} = 8\ TeV$, CMS PAS TOP-12-011. 2012.

[63] The ATLAS Collaboration. Evidence for the associated production of a W boson and a top quark in ATLAS at $\sqrt{s} = 7\ TeV$, Phys. Lett. B 716 (2012) 142-159. 2012.

[64] The CMS Collaboration. Evidence for Associated Production of a Single Top Quark and W Boson in pp Collisions at $\sqrt{s} = 7\ TeV$, PRL 110, 022003 (2013). 2013.

[65] The ATLAS Collaboration. Search for s-channel Single Top-Quark Production in pp Collisions at $\sqrt{s} = 7\ TeV$, ATLAS-CONF-2011-118. 2011.

[66] G.L. Kane, G.A. Ladinsky, C-P. Yuan. Using the top quark for testing standard-model polarization and CP predictions, Phys. Rev. D 45 (1992) 124. 1992.

[67] J.A. Aguilar-Saavedra. A minimal set of top anomalous couplings, Nucl. Phys. B 812 (2009) 181, arXiv:0811.3842 [hep-ph]. 2009.

[68] The D0 Collaboration. Search for anomalous Wtb couplings in single top quark production in $p\bar{p}$ collisions at $\sqrt{s} = 1.96\ TeV$, Phys. Lett. B 708 (2012) 21-26. 2012.

[69] A. Czarnecki, J. G. Körner, J. H. Piclum. Helicity fractions of W bosons from top quark decays at next-to-next-to-leading order in QCD, Phys. Rev. D 81, 111503(R) (2010). 2010.

[70] The CMS Collaboration. Measurement of W-helicity fractions in single top events topology, CMS PAS TOP-12-020. 2013.

[71] The D0 Collaboration. Combination of searches for anomalous top quark couplings with 5.4 fb^{-1} of ppbar collisions, Phys. Lett. B 713 (2012) 3 165-171. 2012.

[72] J. A. Aguilar-Saavedra, J. Bernabeu. W polarisation beyond helicity fractions in top quark decays, arXiv:1005.5382v2 [hep-ph]. 2010.

[73] The ATLAS Collaboration. Search for CP violation in single top quark events in *pp* collisions at $\sqrt{s} = 7\ TeV$ with the ATLAS detector, ATLAS-CONF-2013-032. 2013.

[74] G. Mahlon, S. Parke. Improved Spin Basis for Angular Correlation Studies in Single Top Quark Production at the Tevatron, Phys.Rev.D55:7249-7254,1997, arXiv:hep-ph/9611367. 1997.

[75] Reinhard Schwienhorst et al. Single top quark production and decay in the t channel at next-to-leading order at the LHC, Phys. Rev. D 83, 034019 (2011). 2011.

[76] J. A. Aguilar-Saavedra. Single top quark production at LHC with anomalous Wtb couplings, Nucl.Phys.B804:160-192,2008, arXiv:0803.3810 [hep-ph]. 2008.

[77] G. Burdman, B. A. Dobrescu, E. Pontón. Resonances from two universal extra dimensions, Phys. Rev. D74 (2006) 075008, arXiv:hep-ph/0601186 [hep-ph]. 2006.

[78] J. C. Pati and A. Salam. Lepton Number as the Fourth Color, Phys. Rev. D10 (1974) 275–289. 1974.

[79] E. Malkawi, T. M. Tait, C. Yuan. A Model of Strong Flavor Dynamics for the Top Quark, Phys. Lett. B385 (1996) 304, arXiv:hep-ph/9603349 [hep-ph]. 1996.

[80] The ATLAS Collaboration. Search for $W' \to t\bar{b}$ in proton-proton collisions at a centre-of-mass energy of $\sqrt{s} = 8\ TeV$ with the ATLAS detector, ATLAS-CONF-2013-050. 2013.

[81] The ATLAS Collaboration. Search for single b^*-quark production with the ATLAS detector at $\sqrt{s} = 7\ TeV$, Phys. Lett. B 721 (2013) 171-189, arXiv:1301.1583. 2013.

[82] S. L. Glashow, J. Iliopoulos, L. Maiani. Weak Interactions with Lepton-Hadron Symmetry, Phys. Rev. D 2, 1285–1292 (1970). 1970.

[83] J. A. Aguilar-Saavedra. Top flavour-changing neutral interactions: theoretical expectations and experimental detection, Acta Phys.Polon.B35:2695-2710,2004, arXiv:hep-ph/0409342. 2004.

[84] The ATLAS Collaboration. Search for FCNC single top-quark production at $\sqrt{s} = 7\ TeV$ with the ATLAS detector, Physics Letters B 712 (2012) 351-369, arXiv:1203.0529. 2012.

[85] The ATLAS Collaboration. A search for flavour changing neutral currents in top-quark decays in pp collision data collected with the ATLAS detector at $\sqrt{s} = 7\ TeV$, JHEP 1209 (2012) 139, arXiv:1206.0257. 2012.

[86] M. Hosch, K. Whisnant, B.-L. Young. Direct Top Quark Production at Hadron Colliders as a Probe of New Physics, Phys.Rev. D56 (1997) 5725-5730, arXiv:hep-ph/9703450. 1997.

[87] T. Tait and C.-P. Yuan. Anomalous t-c-g coupling: The connection between single top quark production and top quark decay, Phys. Rev. D 55, 7300–7301 (1997). 1997.

[88] The ATLAS Collaboration. ATLAS DETECTOR AND PHYSICS PERFORMANCE, Technical Design Report, CERN/LHCC 99-14. 1999.

[89] The CMS Collaboration. CMS Physics TDR, CERN-LHCC-2006-001. 2006.

[90] The ALICE Collaboration. ALICE Technical Proposal for A Large Ion Collider Experimentat the CERN LHC, CERN/LHCC/95–71. 1995.

[91] The LHCb collaboration. LHCf experiment : Technical Design Report, CERN-LHCC-2006-004. 2006.

[92] The TOTEM Collaboration. TOTEM Technical Design Report, CERN-LHCC-2004-002. 2004.

[93] The LHCf collaboration. LHCf experiment : Technical Design Report, CERN-LHCC-2006-004. 2006.

[94] The MoEDAL collaboration. MoEDAL Technical Design Report, CERN-LHC-2009-006. 2009.

[95] The ATLAS Collaboration. The ATLAS Experiment at the CERN Large Hadron Collider, JINST 3 (2008) S08003. 2008.

[96] The ATLAS Collaboration. ATLAS inner detector : Technical Design Report, 1, ATLAS-TDR-4 ; CERN-LHCC-97-016. 1997.

[97] M. Aharrouche et al. Response uniformity of the ATLAS liquid argon electromagnetic calorimeter, Nucl. Instrum. Meth. A 582 (2007) 429. 2007.

[98] J. Colas et al. Position resolution and particle identification with the ATLAS EM calorimeter, Nucl. Instrum. Meth. A 550 (2005) 96. 2005.

[99] M. Aharrouche et al. Energy linearity and resolution of the ATLAS electromagnetic barrel calorimeter in an electron test-beam, Nucl. Instrum. Meth. A 568 (2006) 601. 2006.

[100] B. Dowler et al. Performance of the ATLAS hadronic end-cap calorimeter in beam tests, Nucl. Instrum. Meth. A 482 (2002) 94. 2002.

[101] A.E. Kiryunin et al. GEANT4 physics evaluation with testbeam data of the ATLAS hadronic end-cap calorimeter, Nucl. Instrum. Meth. A 560 (2006) 278. 2006.

[102] C. Cojocaru et al. Hadronic calibration of the ATLAS liquid argon end-cap calorimeter in the pseudorapidity region $1.6 < |\eta| < 1.8$ in beam tests, Nucl. Instrum. Meth. A 531 (2004) 481. 2004.

[103] C. Cojocaru et al. Muon results from the EMEC/HEC combined run corresponding to the ATLAS Pseudorapidity Region $1.6 < |\eta| < 1.8$, ATLAS Note ATL-LARG-2004-006, http://cdsweb.cern.ch/record/732313. 2004.

[104] J.C. Armitage et al. Electron signals in the forward calorimeter prototype for ATLAS, 2007 JINST 2 P11001. 2007.

[105] J.P. Archambault et al. Energy calibration of the ATLAS liquid argon Forward Calorimeter, 2008 JINST 3 P02002. 2008.

[106] The ATLAS collaboration. Electron performance measurements with the ATLAS detector using the 2010 LHC proton-proton collision data, Eur. Phys. J. C72 (2012) 1909. 2012.

[107] The ATLAS collaboration. Expected electron performance in the ATLAS experiment, ATL-PHYS-PUB-2011-006. 2011.

[108] F.Djama. Using $Z^0 \to e^+e^-$ for Electromagnetic Calorimeter Calibration, ATL-LARG-2004-008. 2004.

[109] The ATLAS Collaboration. Expected Performance of the ATLAS Experiment, Detector, Trigger and Physics, CERN-OPEN-2008-020. 2008.

[110] The ATLAS collaboration. Muon Performance in Minimum Bias pp Collision Data at $\sqrt{s} = 7\ TeV$ with ATLAS, ATLAS-CONF-2010-036. 2010.

[111] R. Clifft and A. Poppleton. iPatRec: Inner Detector pattern-recognition and track-fitting, ATL-SOFT-94-009. 1994.

[112] The ATLAS collaboration. A measurement of the muon reconstruction efficiency in 2010 ATLAS data using J/ψ decays, ATLAS-CONF-2012-125. 2012.

[113] The ATLAS collaboration. Muon reconstruction efficiency in reprocessed 2010 LHC proton-proton collision data recorded with the ATLAS detector, ATLAS-CONF-2011-063. 2011.

[114] The ATLAS collaboration. ATLAS Muon Momentum Resolution in the First Pass Reconstruction of the 2010 $p-p$ Collision Data at $\sqrt{s} = 7\ TeV$, ATLAS-CONF-2011-046. 2011.

[115] The ATLAS collaboration. Study of the Material Budget in the ATLAS Inner Detector with K_s^0 decays in collision data at $\sqrt{s} = 900\ GeV$, ATLAS-CONF-2010-019. 2010.

[116] The ATLAS collaboration. J/ψ Performance of the ATLAS Inner Detector, ATLAS-CONF-2010-078. 2010.

[117] The ATLAS collaboration. Tracking Studies for b-tagging with 7 TeV Collision Data with the ATLAS Detector, ATLAS-CONF-2010-070. 2010.

[118] The ATLAS collaboration. Studies of the performance of the ATLAS detector using cosmic-ray muons, Eur.Phys.J. C71 (2011) 1593, CERN-PH-EP-2010-070, arXiv:1011.6665. 2011.

[119] W. Lampl et al. Calorimeter clustering algorithms: description and performance, ATL-LARG-PUB-2008-002, CERN, Geneva, April, 2008. 2008.

[120] Matteo Cacciari, Gavin P. Salam, Gregory Soyez. The anti-kt jet clustering algorithm, JHEP 0804:063,2008, arXiv:0802.1189 [hep-ph]. 2008.

[121] M. Cacciari and G. P. Salam. Dispelling the N^3 myth for the k_t jet-finder, Phys. Lett. B 641 (2006) no. 1, 57-61. 2006.

[122] M. Cacciari et al. http://fastjet.fr/. .

[123] The ATLAS Collaboration. Jet energy scale and its systematic uncertainty in proton-proton collisions at $\sqrt{s} = 7\ TeV$ with ATLAS 2010 data, ATLAS-CONF-2011-032. 2011.

[124] The ATLAS Collaboration. Performance of missing transverse momentum reconstruction in proton-proton collisions at 7 TeV with ATLAS, Eur.Phys.J.C 72 (2012) 1844, CERN-PH-EP-2011-114, arXiv:1108.5602 [hep-ex]. 2012.

[125] The ATLAS collaboration. Improved luminosity determination in pp collisions at $\sqrt{s} = 7\ TeV$ using the ATLAS detector at the LHC, CERN-PH-EP-2013-026, arXiv:1302.4393 [hep-ex]. 2013.

[126] S. van der Meer. Calibration of the effective beam height in the ISR, CERN-ISR-PO-68-31. 1968.

[127] C. Rubbia. Measurement of the luminosity of pp collider with a (generalized) van der Meer method, CERN-pp-Note-38. 1977.

[128] B. P. Kersevan and R. Elzbieta-Was. The Monte Carlo Event Generator AcerMC version 3.5 with interfaces to PYTHIA 6.4, HERWIG 6.5 and ARIADNE 4.1, arXiv:0405247 [hep-ph]. 2008.

[129] A. Sherstnev and R. Thorne. Different PDF approximations useful for LO Monte Carlo generators, arXiv:0807.2132 [hep-ph]. 2008.

[130] B. P. Kersevan I. Hinchliffe. A Consistent Prescription for the Production Involving Massive Quarks in Hadron Collisions, JHEP 0609:033,2006, arXiv:hep-ph/0603068. 2006.

[131] Paolo Nason. A New Method for Combining NLO QCD with Shower Monte Carlo Algorithms, JHEP 0411:040,2004, arXiv:hep-ph/0409146. 2004.

[132] Hung-Liang Laiet al. New parton distributions for collider physics, Phys.Rev.D82:074024,2010, arXiv:1007.2241 [hep-ph]. 2010.

[133] M. Aliev et al. Calculation at approximate NNLO in QCD using Hathor 1.2, Comput.Phys.Commun.182:1034-1046,2011. 2011.

[134] M.L. Manganoet al. ALPGEN, a generator for hard multiparton processes in hadronic collisions, JHEP 0307 (2003) 001, arXiv:hep-ph/0206293. 2003.

[135] J. Pumplinet al. New Generation of Parton Distributions with Uncertainties from Global QCD Analysis, JHEP 0207:012,2002, arXiv:hep-ph/0201195. 2002.

[136] The ATLAS Collaboration. The ATLAS Simulation Infrastructure, Eur.Phys.J.C70:823-874,2010, arXiv:1005.4568 [physics.ins-det]. 2010.

[137] S. Agostinelli et al. Geant4—a simulation toolkit, Nuclear Instruments and Methods in Physics Research A 506 (2003) 250-303. 2003.

[138] J. Allison et al. Geant4 developments and applications, IEEE Transactions on Nuclear Science 53 No. 1 (2006). 2006.

[139] The ATLAS Collaboration. Improved luminosity determination in *pp* collisions at $\sqrt{s} = 7\ TeV$ using the ATLAS detector at the LHC, CERN-PH-EP-2013-026, arXiv:1302.4393 [hep-ex]. 2013.

[140] M R Whalleyet al. Contributed to HERA and the LHC: A Workshop on the Implications of HERA and LHC Physics, arXiv:hep-ph/0508110. 2005.

[141] The ATLAS collaboration. Proposal and Motivations for 2011 Trigger Menu, ATL-COM-DAQ-2011-007. 2011.

[142] The ATLAS collaboration. *b*-Tagging Algorithms and their Performance at ATLAS, arXiv:0809.4896 [hep-ex]. 2008.

[143] The ATLAS collaboration. Measurement of t-Channel Single Top Quark Production cross section with *pp* Collisions using a Cuts-Based Approach, ATL-COM-PHYS-2012-1430. 2012.

[144] The ATLAS collaboration. Measurement of the *t*-channel single top-quark production cross section in pp collisions at $\sqrt{s} = 7\ TeV$ with the ATLAS detector, Phys. Lett. B 717 (2012) 330-350, arXiv:1205.3130. 2012.

[145] The ATLAS Collaboration. Object selection and calibration, background estimations and MC samples for the Autumn 2012 Top Quark analyses with 2011 data, ATL-COM-PHYS-2012-1197. 2012.

[146] E. Barberis et al. The Matrix Method and its Error Calculation, D0-NOTE 4564. 2004.

[147] The ATLAS Collaboration. Object selection and calibration, background estimations and MC samples for the Winter 2012 Top Quark analyses with 2011 data, ATL-COM-PHYS-2012-224. 2012.

[148] G. Mahlon, S. Parke. Single Top Quark Production at the LHC: Understanding Spin, Phys.Lett. B476 (2000) 323-330. 2000.

[149] Tim Adye. Unfolding algorithms and tests using RooUnfold, arXiv:1105.1160 [physics.data-an]. 2011.

[150] F. A. Berends et al. Multi-jet production in W, Z events at p anti-p colliders, Phys. Lett. B224 (1989) 237. doi:10.1016/0370-2693(89)91081-2. 1989.

[151] A. Brandenburg et al. QCD-corrected spin analysing power of jets in decays of polarized top quarks, Phys.Lett. B539 (2002) 235-241, arXiv:hep-ph/0205023. 2002.

[152] The ATLAS Collaboration. Measurement of the t-channel single top-quark production cross section in pp collisions at $\sqrt{s} = 7\ TeV$ with the ATLAS detector, Physics Letters B 717 (2012) 330–350. 2012.

Top polarization measurement in single top quark production with the ATLAS detector

Abstract

The top quark polarization in electroweak single top quark production allows to probe the structure of the Wtb vertex and in particular to test the left-handed vector coupling of the Standard Model and to search for anomalous right-handed and tensor couplings. This thesis reports the measurement of the single top quark polarization from the 4.7 fb^{-1} data recorded in 2011 by the ATLAS detector at the LHC in proton-proton collisions at the center of mass energy of 7 TeV. The polarization is extracted from angular distributions reconstructed in a specific spin basis for t-channel single top quark events. The theoretical context of the top quark production in hadron colliders via the strong and electroweak interactions is first introduced. Then the detector, the reconstruction performances of the final state physics objects as well as the selections of events having a single top quark t-channel signature are described. The unfolding and folding methods used to extract the top quark polarization are presented and tested with different configurations in the next part of the thesis. Finally, the measured polarizations are examined with their estimated systematic uncertainties coming from the theory, the detector response and modeling as well as from the statistics of the data and simulation event samples. This thesis reports the first measurement with the ATLAS detector of the single top quark polarization. The obtained results are compatible with the Standard Model predictions and will contribute to constrain the anomalous Wtb couplings.

Mesure de la polarisation dans la production électrofaible de quark top avec le détecteur ATLAS

Résumé

La polarisation des quarks top produit par interaction électrofaible permet de sonder la structure du vertex Wtb et en particulier de tester le couplage vecteur gauche prévu dans le cadre du Modèle Standard et de rechercher les couplages anormaux droit et tenseur introduits par plusieurs théories au-delà du Modèle Standard. Cette thèse présente la mesure de la polarisation des quarks top produits par interaction électrofaible à partir des données correspondantes à une luminosité integrée de $4,7\ fb^{-1}$ enregistrées en 2011 par le détecteur ATLAS dans les collisions proton-proton du LHC à l'énergie centre de masse de $7\ TeV$. La polarisation est extraite des distributions angulaires reconstruites dans une base de spin spécifique pour les événements de production de quark top en voie-t. Le contexte théorique de production de quarks top par interactions forte et électrofaible dans les collisionneurs hadroniques est tout d'abord introduit. Ensuite, le détecteur, les performances de reconstruction des objets physiques ainsi que la sélection des événements avec une signature de top quark électrofaible en voie-t sont décrits. Les méthodes de déconvolution et de convolution utilisées pour extraire la polarisation sont ensuite présentées et testées avec différentes configurations. Les résultats obtenus ainsi que les incertitudes théoriques, expérimentales et statistiques sont finalement examinées. Cette thèse présente la première mesure avec le détecteur ATLAS de la polarisation des quarks top électrofaibles. Les résultats obtenus sont compatibles avec les prédictions du Modèle Standard et contribueront à contraindre de manière significative les couplages Wtb anormaux.